2018

Diffuse Optical Cerebral Diagnostics For Real-Time Guidance During Pediatric Surgery And Resuscitation

Tiffany Ko
University of Pennsylvania, tiko@seas.upenn.edu

Recommended Citation

Ko, Tiffany, "Diffuse Optical Cerebral Diagnostics For Real-Time Guidance During Pediatric Surgery And Resuscitation" (2018). *Publicly Accessible Penn Dissertations*. 3138.
https://repository.upenn.edu/edissertations/3138

Diffuse Optical Cerebral Diagnostics For Real-Time Guidance During Pediatric Surgery And Resuscitation

Abstract

Adequate oxygen and blood flow are vital for the developing pediatric brain. Herein, we apply quantitative diffuse optical techniques, frequency-domain diffuse optical spectroscopy (FD-DOS) and diffuse correlation spectroscopy (DCS), to non-invasively characterize cerebral oxygenation (StO2), blood flow (CBF), and oxygen metabolism (CMRO2) in pediatric animal models of hypoxic-ischemic injury.

In a neonatal swine model ($n=8$) of congenital cardiac defect repair, we performed a two-part study which validated non-invasive diffuse optical measurements and uncovered significant limitations in the guidance of deep hypothermia using temperature during cardiopulmonary bypass. First, non-invasive CMRO2 was validated against invasive methods over wide temperature ranges (18-37°C). Non-invasive measurements of CBF ($p<0.001$) and CMRO2 ($p<0.001$) were significantly associated with invasive measurements. Furthermore, a significant hysteresis ($p=0.001$) of cerebral metabolic temperature-dependence during cooling versus rewarming with respect to NPT is “fixed” with the use of ICT ($p>0.5$).

Second, we compared non-invasively measured cerebral metabolic parameters between cohorts who underwent deep hypothermia with or without circulatory arrest (DHCA; $n=8$). Cerebral metabolic temperature-dependence with respect to ICT in DHCA animals demonstrated significantly diminished temperature sensitivity during rewarming ($p<0.001$; i.e., following reperfusion) compared to during cooling. Direct non-invasive CMRO2 measurement is an improved surrogate of cerebral status over temperature and enables individualized management of deep hypothermia and circulatory arrest.

In another study of asphyxia-induced pediatric cardiac arrest and cardiopulmonary resuscitation (CPR), non-invasive measures of StO2, oxy-hemoglobin concentration ([HbO2]) and total hemoglobin concentration (THC) at 10-minutes of CPR were significantly associated with return of spontaneous circulation (ROSC). The absolute change in [HbO2] from 1-minute of CPR (Δ[HbO2]CPR) was the optimal predictor of ROSC, with a mean (SD) AUC of 0.91 (0.07) across the first 10 minutes of CPR, evaluated at 1-minute intervals. Furthermore, separate high sensitivity and specificity threshold for ROSC were established.

These results show, in several contexts, that non-invasive FD-DOS/DCS neuromonitoring provides unique physiological information about the developing pediatric brain that enables individualized identification of critical neurological risk periods and real-time guidance of clinical care.

Degree Type

Dissertation

Degree Name

Doctor of Philosophy (PhD)

Graduate Group

Bioengineering

First Advisor

Arjun G. Yodh

Second Advisor

Daniel J. Licht

Keywords

cardiopulmonary bypass, cardiopulmonary resuscitation, cerebral metabolism, diffuse optics, hypothermia, pediatrics

Subject Categories

Biomedical

DIFFUSE OPTICAL CEREBRAL DIAGNOSTICS FOR REAL-TIME GUIDANCE DURING PEDIATRIC SURGERY AND RESUSCITATION

Tiffany S. Ko

A DISSERTATION

in

Bioengineering

Presented to the Faculties of the University of Pennsylvania

in

Partial Fulfillment of the Requirements for the

Degree of Doctor of Philosophy

2018

Supervisor of Dissertation

Arjun G. Yodh, Ph.D.
James M. Skinner Professor of Science
Department of Physics and Astronomy

Co-Supervisor of Dissertation

Daniel J. Licht, M.D.
Associate Professor of Neurology and Pediatrics
Children's Hospital of Philadelphia

Graduate Group Chairperson

Ravi Radhakrishnan, Ph.D., Professor of Bioengineering

Dissertation Committee

David F. Meaney, Ph.D., Professor, Department of Bioengineering

Todd J. Kilbaugh, M.D., Associate Professor, Anesthesiology and Critical Care, *CHOP*

DIFFUSE OPTICAL CEREBRAL DIAGNOSTICS FOR REAL-TIME GUIDANCE DURING PEDIATRIC SURGERY AND RESUSCITATION

ACKNOWLEDGEMENTS

This educational journey was made possible by many individuals, past and present. First and foremost, I would like to thank my family (Feng-ou “Frank” Ko, Dr. Karen Liu, William Ko) and my partner Laura Kabelitz for their tireless encouragement, Dr. Constantine Mavroudis and Dr. Todd Kilbaugh for their foresight, excellent sense of humor and for the design and implementation of experimental protocols underlying the animal models presented, and Dr. Wesley Baker and my advisers Prof. Arjun Yodh and Dr. Daniel Licht for their patience, knowledge and mentorship. Through thick and thin, these individuals (plus my pups, Tonka and Tova) provided every form of support a graduate student could ask for and more. But, to be sure, they were not alone.

From the start, I am grateful to the Bioengineering department (Prof. Brian Litt, Prof. Beth Winkelstein, Kathleen Venit) and the HHMI Interfaces Program and its administration (Dr. Ann Tiao, Dr. Jim Gee, Dr. Andrew Maidment, Prof. Jim Delikatny, Dr. Nick Bryan) for bringing me to Penn and offering me the medical education of an engineer’s lifetime; without which, I would never have found this path. Tangentially, I would also like to thank my Perelman School of Medicine classmates for their comradery and friendship and for the opportunity to serve in the Penn Med LGBTPM+ student organization. These experiences helped form my investigational outlook and provided the opportunity to work and learn alongside future and current attending physicians. Importantly, through the HHMI curriculum, I met Dr. Licht.

In addition to welcoming me into his research lab, Dr. Licht has been unwavering and enthusiastic in his support of my endeavors and provided me with countless opportunities for clinical research and professional development, including the presented work. Over the years, he has repeatedly shown me how powerful communication, kindness and open-mindedness can be in creating an environment where everyone feels respected, welcome and able to contribute. In this vein, Dr. Licht and Dr. Yodh have been ideal role models in their cultivation of the spirit of collaboration.

As a member of Dr. Yodh's lab, I was lucky to be a part of another wonderful research group where he has tirelessly provided opportunities for personal and professional development. The present work incorporates insights from constructive discussions and collaborations with Dr. Yodh and lab group members as well as Dr. Yodh's previous trainees (Prof. Rickson Mesquita, Prof. Turgut Durduran) and other visiting researchers (Dr. Shih-Yu Tzeng, Dr. Zhe Li, Dr. Detian Wang, Rodrigo Forti). In conjunction with Dr. Licht, I was also afforded invaluable mentoring opportunities of undergraduate students (Vincent Morano, Alexander Schmidt, Elizabeth Bixler) who also directly supported the present work.

In sum, I am forever grateful to Dr. Yodh and the Biomedical Optics Group members (Dr. Wesley Baker, Dr. Jennifer Lynch, Dr. David Busch, Dr. Erin Buckley, Dr. Jeffrey Cochran, Dr. Han Ban, Dr. Venki Kavuri, Dr. Ashwin Parthasarathy, Dr. Lian He, Dr. Lin Wang, Dr. Brian White, Dr. Yi Hong Ong, Kenneth Abramson, Sanghoon "Bryan" Chong, Dr. Karla Bergonzi), Dr. Licht and the members of the June and Steve Wolfson Laboratory for Clinical and Biomedical Optics at the Children's Hospital of Philadelphia (Dr. Constantine Mavroudis, Dr. Ann McCarthy, Dr. Maryam Naim, Dr. Rui Xiao, Madeline Winters, John Newland, Kobina Mensah-Brown, Timothy Boorady, Mahima Devarajan, Marin Jacobwitz, Jonah Padawer), and Dr. Kilbaugh and his collaborators and research group members (Dr. Ryan Morgan, Dr. Andrew Lautz, Dr. Robert Sutton, Dr. Robert Berg, Dr. Vinay Nadkarni, Dr. Alexandra Marquez, Yuxi Lin, Sejin "Seth" Jeong, William Landis). This immense team has taught me everything I know about applying diffuse optics to medicine and has directly supported the present work with constructive discussions, technical guidance, a wealth of ThorLabs snacks, and countless hours of patient dedication. I am particularly grateful to those included individuals who helped move a mountain of my personal effects when I needed it most.

This work stands on the shoulders of giants and would not have been possible without the history of innovation at Penn, by Drs. Britton Chance and Arjun Yodh, and at CHOP, by Drs. Dean Kurth and William Greeley. Their foundational work continues to light the way for the clinical application of frequency-domain diffuse optical spectroscopy and diffuse correlation spectroscopy as a combined diagnostic measurement of cerebral oxygen metabolism in children. The presented work was also made possible by the veterinary staff at the Children's Hospital of Philadelphia (CHOP), as well as the financial support of Dr. J. William Gaynor, Dr. Yodh, Dr. Licht, and Dr. Kilbaugh and an F31 pre-doctoral training grant (HD085731) from the Eunice Kennedy Shriver National Institute of Child Health (NICHD) at the National Institutes of Health.

To conclude, I am overwhelmingly grateful for everyone's patience. To the reader, I appreciate the opportunity to share my work with you and welcome your correspondence.

ABSTRACT

DIFFUSE OPTICAL CEREBRAL DIAGNOSTICS FOR REAL-TIME GUIDANCE DURING PEDIATRIC SURGERY AND RESUSCITATION

Tiffany S. Ko

Arjun G. Yodh

Daniel J. Licht

Adequate oxygen and blood flow are vital for the developing pediatric brain. Herein, we apply quantitative diffuse optical techniques, frequency-domain diffuse optical spectroscopy (FD-DOS) and diffuse correlation spectroscopy (DCS), to non-invasively characterize cerebral oxygenation (StO_2), blood flow (CBF), and oxygen metabolism ($CMRO_2$) in pediatric animal models of hypoxic-ischemic injury.

In a neonatal swine model (n=8) of congenital cardiac defect repair, we performed a two-part study which validated non-invasive diffuse optical measurements and uncovered significant limitations in the guidance of deep hypothermia using temperature during cardiopulmonary bypass. First, *non-invasive* $CMRO_2$ was validated against *invasive* methods over wide temperature ranges (18-37°C). Non-invasive measurements of CBF ($p<0.001$) and $CMRO_2$ ($p<0.001$) were significantly associated with invasive measurements. Furthermore, a significant hysteresis ($p=0.001$) of cerebral metabolic temperature-dependence during cooling versus rewarming with respect to NPT is “fixed” with the use of ICT ($p>0.5$).

Second, we compared non-invasively measured cerebral metabolic parameters between cohorts who underwent deep hypothermia with or without circulatory arrest (DHCA; n=8). Cerebral metabolic temperature-dependence with respect to ICT in DHCA animals demonstrated significantly diminished temperature sensitivity during rewarming ($p<0.001$; *i.e.*, following reperfusion) compared to during cooling. Direct non-invasive $CMRO_2$ measurement is an improved surrogate of cerebral status over temperature and enables individualized management of deep hypothermia and circulatory arrest.

In another study of asphyxia-induced pediatric cardiac arrest and cardiopulmonary resuscitation (CPR), non-invasive measures of StO_2, oxy-hemoglobin concentration ($[HbO_2]$) and total hemoglobin concentration (THC) at 10-minutes of CPR were significantly associated with return of spontaneous circulation (ROSC). The absolute change in $[HbO_2]$ from 1-minute of CPR ($\Delta[HbO_2]_{CPR}$) was the optimal predictor of ROSC, with a mean (SD) AUC of 0.91 (0.07) across the first 10 minutes of CPR, evaluated at 1-minute intervals. Furthermore, separate high sensitivity and specificity threshold for ROSC were established.

These results show, in several contexts, that non-invasive FD-DOS/DCS neuromonitoring provides unique physiological information about the developing pediatric brain that enables individualized identification of critical neurological risk periods and real-time guidance of clinical care.

TABLE OF CONTENTS

LIST OF FIGURES

LIST OF TABLES

LIST OF ABBREVIATIONS AND SYMBOLS

AHA	American Heart Association
CARES	Cardiac Arrest Registry to Enhance Survival database
CDC	US Centers for Disease Control and Prevention
CHOP	Children's Hospital of Philadelphia
CoSTR	Consensus on Science with Treatment Recommendations
FDA	Food and Drug Administration
ILCOR	International Liaison Committee on Resuscitation
	(Unit)
A-B-C	“Airway”-“Breathing”-“Circulation” sequence of BLS CPR
ABP	arterial blood pressure (mmHg)
ACT	activated clotting time (s)
AED	automated external defibrillator
AoP	aortic pressure (mmHg)
AP	anteroposterior
AUC	area under the curve
BFI	blood flow index (cm^2/s)
BLS	basic life support
C-A-B	“Circulation”-“Airway”-“Breathing” sequence of BLS CPR
CaO_2	arterial blood concentration of oxygen (mL O_2/dL blood)
CBF	cerebral blood flow (mL blood/min/100g)
CHD	congenital heart defects
$CMRO_2$	cerebral metabolic rate of oxygen (mL O_2/min/100g)
$CMRO_{2,i}$	absolute index of non-invasive $CMRO_2$ (cm^2/s*mL O_2/dL blood)

CoPP	coronary perfusion pressure (mmHg)
CPB	cardiopulmonary bypass
CPR	cardiopulmonary resuscitation
CW NIRS	continuous-wave near-infrared spectroscopy
DBP	diastolic arterial blood pressure (mmHg)
DCS	diffuse correlation spectroscopy
DG-CPR	depth-guided, AHA guideline CPR
DH	deep hypothermic
DHCA	deep hypothermic circulatory arrest
DOS	diffuse optical spectroscopy
DPF	differential pathlength factor
ECG	electrocardiogram
ECLS	extracorporeal life support
EEG	electroencephalography
EMS	emergency medical services
$ETCO_2$, $EtCO_2$	end-tidal carbon dioxide (mmHg)
FD-DOS	frequency-domain diffuse optical spectroscopy
FiO_2	fraction of inspired oxygen (%)
Fr	French
Glu	glucose (μmol/L)
[Hb]	deoxy-hemoglobin concentration (μmol/L)
$[HbO_2]$	oxy-hemoglobin concentration (μmol/L)
Hct	blood hematocrit fraction (%)
HD-CPR	hemodynamic-directed CPR

[Hgb]	hemoglobin concentration in blood (g Hgb/dL blood)
HLHS	hypoplastic left heart syndrome
ICT	intracranial brain temperature (°C)
ICU	intensive care unit
IHCA	in-hospital cardiac arrest
iNO	inhaled nitric oxide
IQR	interquartile range
Lac	lactate (mmol/L)
MCHC	mean corpuscular hemoglobin concentration (g Hgb/mL blood)
MRI	magnetic resonance imaging
NIR	near-infrared
NIRS	near-infrared spectroscopy
NPT	nasopharyngeal temperature (°C)
OEF	oxygen extraction fraction
OHCA	out-of-hospital cardiac arrest
PALS	Pediatric Advanced Life Aupport
PbtO2, $PbtO_2$	intracranial brain tissue oxygen tension (mmHg)
PCPC	Pediatric Cerebral Performance Category
PET	positron emission tomography
PEWS	Pediatric Early Warning Scores
pIHCA	pediatric in-hospital cardiac arrest
PMT	photomultiplier tube detectors
pOHCA	pediatric out-of-hospital cardiac arrest
RaP	right atrial pressure (mmHg)

rCBF	relative cerebral blood flow
rCBF DCS	relative CBF from diffuse correlation spectroscopy (%)
rCBF LD	relative CBF from invasive laser Doppler (%)
ROC	receiver-operating-characteristic
ROSC	return of spontaneous circulation
rSO_2	CW NIRS measurement of cerebral regional oxygen saturation (%)
SaO2, SaO_2	arterial oxygen saturation (%)
SCP	selective cerebral perfusion
SD	standard deviation
SE	standard error
$SjvO_2$	internal jugular venous oxygen saturation (%)
SpO2, SpO_2	peripheral saturation (%)
SRS	spatially-resolved spectroscopy
$SssO_2$	sagittal sinus oxygen saturation (%)
StO_2	cerebral tissue oxygenation (%)
TCD	transcranial Doppler ultrasound
THC	total hemoglobin concentration
VF	ventricular fibrillation

SYMBOLS

A	Amplitude (**Chapter 1**); Arrhenius Equation pre-exponential factor (**Chapter 2, 3**)
a	linear mixed-effects model slope effect
α	ratio of moving scatterers to total scatterers in the optical cross-section

b	linear mixed-effects model intercept effect (**Chapter 2, 3**); scattering power (**Chapter 4**)
$cal_A(r)$	amplitude calibration coefficient at position r
$cal_\phi(r)$	phase calibration coefficient at position r
D	tissue photon diffusion coefficient expressed
D_B	effective diffusion coefficient of moving scatterers
$E(\vec{r},t)$	temporal electric-field
E_a	activation free energy barrier
ϵ	extinction coefficients
γ	optical venous fraction
θ	phase
$G_1(\vec{r},\tau)$	temporal electric-field autocorrelation function
$g_1(\vec{r},\tau)$	normalized temporal electric field autocorrelation function
$g_2(\vec{r},\tau)$	normalized temporal intensity autocorrelation function
k	"wavevector" (**Chapter 1**); rate of reaction (**Chapter 2**)
k_0	wavenumber, i.e., inverse of optical wavelength
k_i	imaginary component of wavevector k
k_r	real component of wavevector k
l_{tr}	photon mean free path
λ	wavelength (nm)
Λ	speckle contrast of the intensity speckle fluctuations
μ_a	tissue absorption coefficient (1/cm)
μ_s	tissue scattering coefficient (1/cm)
μ_s'	tissue reduced scattering coefficient (1/cm)

Q_{10}	Van't Hoff temperature coefficient
R	Diffuse reflectance (W/cm^2**; Chapter 1**); universal gas constant (8.3144598 joules/K/mol; **Chapter 2, 3**); Pearson's correlation coefficient (**Chapter 4**)
R_{eff}	effective reflection coefficient at the boundary
R^2	coefficient of determination
r	source-detector separation distance (cm)
$\vec{r}$	position
S	concentration of radiant source power (W/cm^3; **Chapter 1**); spatially-resolved spectroscopy (SRS) slope (**Chapter 1, 4**)
t	time (s or min)
$t_{\mathrm{HbO_2,MIN}}$	time-to-minimal [HbO_2] depletion (min)
$t_{\mathrm{OEF,MAX}}$	time-to-maximal oxygen extraction (min)
τ	correlation delay-time (s)
T	temperature (°C or K)
Φ	photon fluence rate (W/cm^2)
v	speed of light in the medium (m/s)
ω	angular frequency (rad/s)
z_b	extrapolated-zero boundary distance

CHAPTER 1: BACKGROUND AND SIGNIFICANCE

Few things in life are more vital or more complex than the human brain. Before birth or sentience, our immature brain is already hard at work laying the foundations for centralized processing hubs and the connecting neuronal signaling super highways underlying our capacity for thought, sensation, memory and function. Innate primitive reflexes and early structural differentiation of the auditory, visual and sensorimotor cortices provide the means and the feedback necessary to begin to perceive and interact with the world around us.

Early neuroprotection is critical to long-term quality of life. It is a particularly urgent concern in populations of children with increased vulnerability to neurological injury, as can arise during surgery or cardiac arrest. Unfortunately, non-invasive diagnostic techniques for continuous and safe monitoring of the developing pediatric brain during critical periods of risk are limited. The research in this thesis leverages the relatively low absorption of biological tissue in the near-infrared (NIR) for non-invasive monitoring of the brain. Specifically, diffuse optical monitoring and imaging with NIR light enables non-invasive, continuous quantification of cerebral hemodynamics, *i.e.*, quantification of cerebral blood volume, blood oxygenation, and tissue metabolism.

In this introduction, we first provide an overview of the theoretical basis and instrumentation necessary for diffuse optical measurements (**Chapter 1, Section A**). We next provide a brief review of the neurological outcomes and risk factors faced by neonates with severe congenital heart disease. We then present a framework for how diffuse optical measurements may be applied during intraoperative cardiac repair to mitigate these risks (**Chapter 1, Section B**). Finally, we provide a similar overview for pediatric cardiac arrest and resuscitation (**Chapter 1, Section C**). In subsequent chapters, the novel clinical diagnostic capabilities of this optical modality are validated and are utilized to characterize brain alterations in pediatric swine models of neonatal cardiac repair (**Chapter 2** and **3**) and in pediatric swine models of cardiac arrest and cardiopulmonary resuscitation (CPR; **Chapter 4**). To conclude this work, we summarize our findings, their limitations, and our future outlook (**Chapter 5**).

A. Diffuse Optical Monitoring of Cerebral Hemodynamics

In biological tissue, the propagation of NIR light (wavelengths from 650 to 1000 nm) is well-modeled as a diffusive process due to the predominance of tissue scattering over tissue absorption. The resulting "transparency" permits photons to travel through large chunks of tissue (*e.g.,* 1 to 10 cm) in the infant head in reflectance geometry.[1–5] Typically, a compact optical probe is used to place non-invasive NIR light sources on the surface of the skin and to collect the photons that propagate from the source and through the tissue at a separate detector position (*e.g.,* 2.5 cm away from the source on the tissue surface). As the photons travel through tissue, they are scattered and absorbed. In this way, physiological information about the tissue is imprinted into the transmitted NIR light. By examining the differential spectral changes of the detected light with respect to wavelength, source-detector separation, and other factors, we can characterize tissue properties.

Modeling tissue as a homogenous turbid medium, the photon fluence rate (Φ, W/cm^2) at a position, $\vec{r}$, is described by the Photon Diffusion Equation:[6–10]

$$\frac{\partial\Phi(\vec{r},t)}{\partial t} = vS(\vec{r},t) + D\nabla^2\Phi(\vec{r},t) - v\mu_a\Phi(\vec{r},t). \qquad (1.1)$$

Here t represents time, $S(\vec{r},t)$ represents the source light distribution, v is the speed of light in the medium, μ_s' is the tissue reduced scattering coefficient, μ_a is the tissue absorption coefficient, and D is the tissue photon diffusion coefficient expressed, *i.e.,* $D = v[3(\mu_s' + \mu_a)]^{-1}$. A key assumption for this formulation is that the source light and light radiance are predominantly isotropic, $\mu_s' \gg \mu_a$, and the typical photon path length travelled through the tissue is significantly greater than the mean free path ($l_{tr} = 1/(\mu_a + \mu_s') \sim 1/\mu_s'$; *i.e.*, one random-walk step).

Thus μ_s' and μ_a are the defining optical properties unique to the turbid medium being measured. These parameters are the sources of information from which physiologic information may be quantified. In essence, μ_s' and μ_a correspond to the distance traveled by a photon in tissue before it has had its direction randomized ($1/\mu_s'$, by reduced scattering) or has been absorbed ($1/\mu_a$), respectively; more precisely, these are "exponential" decay lengths for the above processes. Sources of scattering in biological tissue are varied and largely delineated by composition rather than function; significant scatterers include collagen and other fibrous tissues, bone, lipid and cells with large concentrations of mitochondria or lysosomes.[11] Sources of absorption (*i.e.,* tissue chromophores) are better-defined and limited to a few major contributors. Water is the primary absorber, however, a substantial decrease in absorption between 300 to 1000nm permits spectroscopic examination of other chromophores. Importantly, in the NIR window between 650 to 1000nm, oxy- and deoxy-hemoglobin are prominent absorbers with differential spectral behavior that permits separation of their respective contributions. By combining measurements of absorption (μ_a) at multiple wavelengths across this range, the concentrations of oxy- and deoxy-hemoglobin can be quantified, and the relative oxygenation of cerebral tissue hemoglobin determined. All approaches to derive these types of information involve "fitting" measured data to theoretical models. To this end, solutions to the photon diffusion equation (**Equation 1.1**) are next described.

A.1. Frequency-Domain, Infinite Homogenous Medium, Solution

In this work, frequency-domain techniques are employed to quantify the absolute optical properties (μ_a, $\mu_s{}'$) of tissue. Assuming the existence of a stationary, sinusoidally amplitude-modulated point source with angular frequency ω in a highly scattering medium, the fluence rate of resulting diffusing photon density waves in the medium can be separated into DC and AC components

$$\Phi(\vec{r},t) = \Phi_{\mathrm{DC}}(\vec{r}) + \Phi_{\mathrm{AC}}(\vec{r})e^{i\omega t}. \tag{1.2}$$

Substitution of the AC component into the Photon Diffusion Equation yields a closed-form analytical solution for the fluence rate at position $\vec{r}$ in an infinite homogenous medium with the point source placed at the origin:

$$\Phi_{\mathrm{AC}}(\vec{r}) = \frac{vS_{AC}}{4\pi Dr}e^{ikr}, \tag{1.3}$$

The variable $r = |\vec{r}|$ and the real and imaginary components of the “wavevector,” $k = k_r + ik_i$, are fully expressed as:

$$k_r = \sqrt{\frac{v\mu_a}{2D}\left(\sqrt{1+\left[\frac{\omega}{v\mu_a}\right]^2} - 1\right)}\ ; \tag{1.4}$$

$$k_i = \sqrt{\frac{v\mu_a}{2D}\left(\sqrt{1+\left[\frac{\omega}{v\mu_a}\right]^2} + 1\right)}. \tag{1.5}$$

The fluence rate can then be expressed as $\Phi_{\mathrm{AC}}(\vec{r}) = A(r)e^{i\theta(r)}$ and real and imaginary components determined by concurrent measurements of the amplitude $A(r)$ and phase $\theta(r)$. μ_a and μ_s' at a single optical wavelength may be obtained by fitting the data using, for example, multiple measurements of the fluence rate at varying r or ω.

A.2. Frequency-Domain, Semi-Infinite Homogenous Medium, Solution

For clinical applications of the frequency-domain technique, a reflectance geometry is often employed in order to perform measurements on the surface of the skin.[9,12–16] As a result, a boundary condition must be imposed and assumptions must be made regarding propagation of diffuse light across the boundary (*i.e.*, the surface of the skin). Modeling underlying tissue as a semi-infinite homogenous medium with boundary surface at $z = 0$, we must first account for the fact that our fiber source, in practice, is usually not an isotropic point source. However, it is well approximated by a point source at a depth within the medium of roughly the mean free path of a photon ($z = l_{tr}$), directly below the boundary location of the incident source. The boundary condition for light fluence at the interface requires an additional so-called extrapolated-zero boundary condition approximation where, at a certain distance ($z = -z_b$), the fluence rate from the light source falls to zero:[17]

$$z_b \sim \frac{2}{3} l_{tr} \left(\frac{1 + R_{eff}}{1 - R_{eff}} \right). \tag{1.6}$$

R_{eff} is the effective reflection coefficient at the boundary to account for index of refraction mismatches between tissue and air or a measurement probe. Given refractive indices of the tissue (n) and the outside medium (n_{out}), $R_{eff} \sim -1.440(n/n_{out})^{-2} + 0.701(n/n_{out})^{-1} + 0.668 + 0.0636(n/n_{out})$.[18]

With the extrapolated-zero boundary condition, the method of images (**Figure 1.1**) can be used to solve the semi-infinite medium problem. The "method of images" introduces a "negative" light source with identical but opposite fluence to the point light source within the medium but placed at a position $z = -z_s = -(2z_b + l_{tr})$ that is the mirrored location of l_{tr} across z_b. Combining the fluence rate solutions for point sources

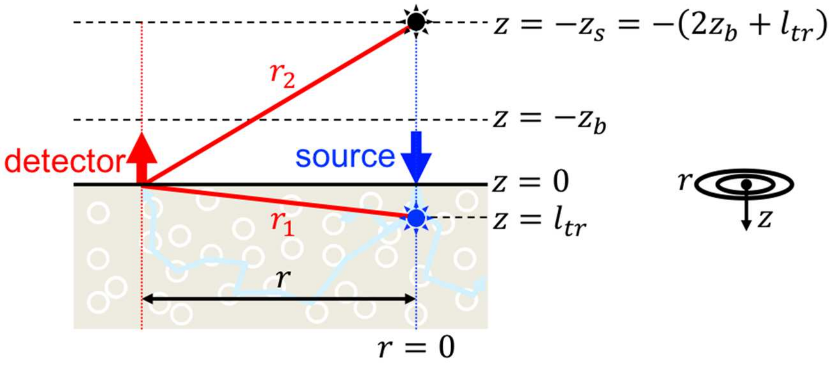

Figure 1.1 Extrapolated-Zero Boundary and the Method of Images: Modeling tissue (*shaded*) as a semi-infinite homogenous medium, an extrapolated-zero boundary condition is imposed at $z = -z_b$ using the method of images. At a depth $z = l_{tr}$ (*i.e.*, one random-walk step) the source may be well-approximated as an isotropic point source (*blue star*). The zero boundary is achieved by then placing a "negative" light source (*black star*) of equal but opposite source fluence at $z = -z_s$, the mirrored location of $z = l_{tr}$ across $z = -z_b$. This is used to solved for the detected fluence rate ($\Phi_{AC}(\vec{r})$) at a distance r from the source on the surface of the medium.

in an infinite medium at both source locations yields the semi-infinite homogeneous solution:

$$\Phi_{\mathrm{AC}}(\vec{r}) = \frac{vS_{AC}}{4\pi D}\left(\frac{e^{ikr_1}}{r_1} - \frac{e^{ikr_2}}{r_2}\right), \tag{1.7}$$

where $r_1 = \sqrt{r^2 + l_{tr}^2}$ is the Euclidean distance from the detector position to the point source in the medium, and $r_2 = \sqrt{r^2 + (2z_b + l_{tr})^2}$ is the Euclidean distance from the detector position to the mirrored negative point source.

When the source-detector separation $r \gg l_{tr}$, the solution simplifies to:

$$\Phi_{\mathrm{AC}}(\vec{r}) = \frac{vS_{AC}}{4\pi D}\left(\frac{e^{-kr}}{r^2}\right)\left(2k\left(l_{tr}z_b + z_b^2\right)\right). \tag{1.8}$$

Like the infinite solution, the fluence rate can then be expressed as $\Phi_{\mathrm{AC}}(\vec{r}) = A(r)e^{i\theta(r)}$ and the following linear expressions with respect to source-detector separation (r) may be derived:

$$\ln(A(r)r^2) = -k_i r + A_0; \tag{1.9}$$

$$\phi(r) = k_r r + \phi_0. \tag{1.10}$$

These relationships provide the means to extract optical properties μ_a and $\mu_s{}'$ by measuring $A(r)$ and $\phi(r)$ at multiple source-detector separations and then performing linear regression to determine slopes k_i and k_r, respectively. μ_a and $\mu_s{}'$ are readily determined from **Equations 1.4** and **1.5** whereby.

$$\mu_a = \frac{\omega}{2v}\left(\frac{k_i}{k_r} - \frac{k_r}{k_i}\right); \tag{1.11}$$

$$\mu_s' = \frac{2v}{3\omega} k_i k_r. \tag{1.12}$$

It is fair to say that variants of this methodology are used for the majority of "monitoring" measurements in the field. This methodology is a core part of the central analyses performed throughout this thesis in order to extract the absolute tissue optical properties of the brain in pediatric swine.

A.3. Calibration of Frequency-Domain Measurements

In practice, a calibration procedure must also be performed in order to simultaneously measure at multiple source-detector separations.[19] This is due to the variability in coupling of different source and detection elements to the surface of the skin. The calibration procedure calculates a correction factor for each source-detector pair by using a tissue-mimicking calibration phantom with known optical properties. Due to optical hardware issues that limit the dynamic range of detection, and the associated increase in measurement error as limits of detection are reached, it is desirable for the calibration phantom to have similar optical properties to the tissue being measured.

Amplitude and phase calibration coefficients must be individually calculated for each wavelength of characterization. On a calibration phantom with properties $\mu_{a,CAL}$ and

$\mu'_{s,CAL}$ for any given wavelength, $k_{i,CAL}$ and $k_{r,CAL}$ may be calculated from **Equation 1.4** and **1.5**. Then, the expected amplitude $A_e(r)$ and phase $\phi_e(r)$ may be calculated as

$$A_e(r) = e^{A_0}\left(\frac{e^{-k_{i,CAL}r}}{r^2}\right); \tag{1.13}$$

$$\phi_e(r) = k_{r,CAL}r + \phi_0. \tag{1.14}$$

Given the actual raw measurements of amplitude and phase ($A(r)$, $\phi(r)$, respectively), the amplitude and phase calibration coefficients $cal_A(r)$ and $cal_\phi(r)$ are calculated as:

$$cal_A(r) = \frac{A_e(r)}{A(r)} = \frac{e^{A_0}}{A(r)}\left(\frac{e^{-k_{i,CAL}r}}{r^2}\right); \tag{1.15}$$

$$cal_\phi(r) = \phi_e(r) - \phi(r) = k_{r,CAL}r + \phi_0 - \phi(r). \tag{1.16}$$

In theory A_0 and ϕ_0 represent the amplitude and phase of the source light; in practice these are typically calculated from the raw measurements of the first source-detector separation r_1, such that the calibration coefficients $cal_A(r_1) = 1$ and $cal_\phi(r_1) = 0$.

To solve for optical properties from measurements of amplitude and phase ($A(r)$, $\phi(r)$, respectively) on tissue, $A_e(r)$ and $\phi_e(r)$ should be calculated by applying the calibration coefficients and fitting a linear regression with respect to r to solve for k_i and k_r, respectively. Subsequently, μ_a and $\mu_s{}'$ may be extracted as described above in **Equations 1.9-12**.

A.4. Frequency-Domain Diffuse Optical Spectroscopy Analysis

Multi-distance, frequency-domain diffuse optical spectroscopy (FD-DOS) uses the wavelength-dependent absorption and scattering coefficients, quantified above, to determine concentrations of chromophores in tissue. The instrumentation and analysis are described in detail throughout the work. In brief, using the well-known extinction coefficients (ϵ) of water, oxy- and deoxy-hemoglobin (H_2O, HbO_2, and Hb, respectively),[20] and assuming a constant cerebral water volume fraction (often 0.75) and negligible contributions from lipid, the measured absorption coefficients (μ_a) across multiple wavelengths (λ) may be used to create a linear system of equations where:[9,13,14,21]

$$\mu_a(\lambda) = \epsilon_{HbO_2}(\lambda)[HbO_2] + \epsilon_{Hb}(\lambda)[Hb] + 0.75\mu_{a,H_2O}(\lambda). \tag{1.17}$$

Absolute concentrations of oxy-hemoglobin ($[HbO_2]$, μmol/L) and deoxy-hemoglobin ([Hb], μmol/L) in cerebral tissue may then be resolved. The total hemoglobin concentration (THC, μmol/L) and cerebral tissue oxygen saturation (StO_2, %) are subsequently calculated as:

$$THC = [HbO_2] + [Hb]; \tag{1.18}$$

$$StO_2 = \frac{[HbO_2]}{THC} \times 100\% \tag{1.19}$$

Validation of frequency-domain quantification of StO_2 has been performed in both animal models[22] and in neonates.[23] It has since been widely applied in vulnerable pediatric populations to examine alterations in cerebral hemodynamics.[24]

A.5. Continuous-Wave Near Infrared Spectroscopy (CW NIRS)

The vast majority of clinical instruments that measure cerebral tissue oxygen saturation are based on the diffuse optical technique called continuous-wave near-infrared spectroscopy (CW NIRS). In this work this is referred to as CW NIRS. Note, because the “continuous-wave” aspect is generally not discussed in clinical communities, this technique is also known as just “NIRS.” Further, while the term “near-infrared spectroscopy (NIRS)” is technically equivalent to the terminology “diffuse optical spectroscopy (DOS),” NIRS is used almost exclusively to describe instrumentation which employs a continuous-wave light source. (CW light sources have an intensity that is constant in time; CW NIRS does not carry phase information.)

It is important to realize that the use of CW light sources to measure tissue oxygen saturation (CW NIRS) requires assumptions about patient characteristics at baseline. CW NIRS does not capture enough information to resolve both absorption and scattering coefficients. As a result, in this work, the terminology "diffuse optical spectroscopy (DOS)" has been reserved for reference to quantitative diffuse optical techniques (*i.e.*, more quantitative than CW NIRS), which permit calculation of absolute optical properties from data. Herein, we describe some of the ways that CW NIRS data is analyzed and its critical limitations.

Differential Pathlength Method

Due to the relatively low-cost barriers to adoption, early clinical cerebral oximeters predominantly used what is known as the "differential pathlength method."[25] In turbid (highly scattering) homogeneous medium, changes in the intensity may be expressed using the so-called modified Beer-Lambert Law:

$$\Delta OD(t) = -\log\left(\frac{I(t)}{I_0}\right) = (r \cdot DPF)\left[\Delta\mu_a(t) + \left(\frac{\mu_{a,0}}{\mu'_{s,0}}\right)\Delta\mu'_s(t)\right], \tag{1.20}$$

where ΔOD is the change in optical density from baseline ($t = 0$), r is the source-detector separation, DPF is the differential pathlength factor, I_0, $\mu_{a,0}$, and $\mu'_{s,0}$ are the intensity, absorption and reduced scattering at baseline, respectively, and $I(t)$ is the intensity at time t. For a semi-infinite homogenous medium, when $r \gg (l_{tr} + 2z_b)$, *i.e.*, the "large r" approximation, the DPF may be expressed as[26]

$$DPF = \frac{3r\mu'_s}{2\left(r\sqrt{3\mu_{a,0}\mu'_s} + 1\right)}. \tag{1.21}$$

This result essentially comes from a Taylor expansion of the optical density with respect to small changes in absorption and scattering. By assuming that tissue scattering remains constant over time ($\Delta\mu_s'(t) \cong 0$), all changes in intensity may be equated to changes in absorption: $\Delta OD(t) = r \cdot DPF \cdot \Delta\mu_a(t)$. This expression differs from the traditional Beer-Lambert Law in "optically-thin" media because, in tissue, the photon path becomes highly scattered and therefore cannot be measured in direct transmission geometry from the source to the detector (distance r). To account for the increase in photon pathlength due to scattering, the source-detector separation (r) is multiplied by the DPF to reflect the *average* photon pathlength in tissue for that particular source-detector separation and background optical properties.

What makes the differential pathlength method attractive can also make it inaccurate. Using baseline assumptions of μ_a and μ_s', a simple measurement of intensity can resolve changes in μ_a for determination of changes in [HbO_2] and [Hb]. This method is generally robust to changes in scattering, due to the $\mu_{a,0}/\mu_{s,0}' \cong 0.01$ multiplicative term in **Equation 1.20**; the relative error in absorption due to scattering changes is thus comparable to the relative change in scattering. Unfortunately, the DPF method cannot quantify baseline optical properties. As will be discussed in this thesis, baseline scattering and absorption properties can have significant inter-subject variability (with a coefficient of variation between 10% and 20%). Furthermore, hypoxic-ischemic conditions also significantly affect tissue scattering and absorption. Examining **Equation 1.20** and **1.21**, if a constant DPF and scattering coefficient (μ_s') over time are erroneously assumed, when scattering does in-fact increase, a larger $\Delta\mu_a$ is erroneously calculated. Also, both expressions are dependent on the source-detector separation (r) which is sensitive to accurate positioning and coupling of these optical elements to the surface of the skin. As a result, clinical oximeters which employed the DPF method will often produce highly inconsistent trends across patients and are further impacted by physiologic changes which affect scattering.[27]

Spatially-Resolved Spectroscopy (SRS)

The most recent generation of FDA approved cerebral CW NIRS oximeters employ the technique of spatially-resolved spectroscopy (SRS).[7,28,29] This techniques relies on deriving a theoretical linear relationship between the detected diffuse reflectance and source-detector separation from which optical properties may be empirically resolved with linear fitting. The use of multiple separations partially mitigates the influence of tissue-coupling errors and allows for improved cerebral sensitivity compared to the DPF method.

To derive the CW diffuse reflectance, we start with the solution for the fluence rate in a semi-infinite homogenous medium for continuous light instead of in the frequency-domain (**Equation 1.7**). The same method of images (**Figure 1.1**) may be employed to solve for the CW fluence rate (Φ_{CW}, W/cm^2) at a distance r from an isotropic point source:[7]

$$\Phi_{\mathrm{CW}}(r) = \frac{1}{4\pi D}\left(\frac{e^{-\mu_{eff} r_1}}{r_1} - \frac{e^{-\mu_{eff} r_2}}{r_2}\right), \tag{1.22}$$

where $\mu_{eff} = \sqrt{3\mu_a(\mu_a + \mu_s')}$, and, as before, $D = v[3(\mu_s' + \mu_a)]^{-1}$, $r_1 = \sqrt{l_{tr}^2 + r^2}$, and $r_2 = \sqrt{r^2 + (2z_b + l_{tr})^2}$. Using Fick's First Law of Diffusion, the CW fluence rate may be used to derive the steady-state diffuse reflectance ($\mathrm{R}_{CW}(r)$, W/cm^2) measured at this position from a source with intensity I_0:[7,28]

$$\mathrm{R}_{CW}(r) = \frac{I_0}{4\pi}\left[l_{tr}\left(\mu_{eff} + \frac{1}{r_1}\right)\frac{e^{-\mu_{eff} r_1}}{r_1^2} + (l_{tr} + 2z_b)\left(\mu_{eff} + \frac{1}{r_2}\right)\frac{e^{-\mu_{eff} r_2}}{r_2^2}\right]. \tag{1.23}$$

Assuming much greater source-detector separations than the mean transport free path ($r \gg l_{tr}$), it follows that $r_1 \cong r_2 \cong r$. Adding the assumption of scattering predominance over absorption ($\mu_s' \gg \mu_a$), **Equation 1.23** reduces to[26]

$$\mathrm{R}_{CW}(r) = C\left[\left(\sqrt{3\mu_a\mu_s'} + \frac{1}{r}\right)\frac{e^{-\sqrt{3\mu_a\mu_s'}r}}{r^2}\right], \tag{1.24}$$

where $C = I_0(l_{tr} + z_b)/2\pi$ becomes a scalar constant with respect to r. The expression may be rearranged as

$$\ln(\mathrm{R}_{CW}(r)\cdot r^2) = -r\sqrt{3\mu_a\mu_s'} + \left[\ln\left(\frac{r\sqrt{3\mu_a\mu_s'}+1}{r}\right) + \ln(C)\right]. \tag{1.25}$$

Given typical optical properties of μ_a in the range of 0.1-0.2 cm^{-1}, μ_s' in the range of 5 to 15 cm^{-1}, source-detector separations (SDS) r>2cm, it follows that $r\sqrt{3\mu_a\mu_s'} \gg 1$. This assumption reduces the bracketed expression on the right-hand side of **Equation 1.25** to a scalar constant that is independent of r. Thus, a linear fitting of $\ln(\mathrm{R}_{CW}(r)\cdot r^2)$ with respect to r, gives a fitted slope, $S = -\sqrt{3\mu_a\mu_s'}$, which can be used to solve for μ_a (using an assumed μ_s') according to the relationship

$$\mu_a = \frac{S^2}{3\mu_s'}. \tag{1.26}$$

For selected optical properties across the physiologic range, we show the numerically-calculated percentage error in S^2 for pediatric- and adult-sized probes (SDS = 0.9 and 2.5cm; SDS = 1.5 and 5cm; respectively; see **Figure 1.2**) using the SRS linear-fitting method. These errors were calculated by computing the slope S of $\ln(\mathrm{R}_{CW}(r)\cdot r^2)$, from **Equation 1.25**, with respect to r for each probe. The error of the fitted S^2 is then calculated with respect to the "true" S^2, computed as $3\mu_a\mu_s'$. We see that, for a subset of larger physiologic optical properties and larger source-detector

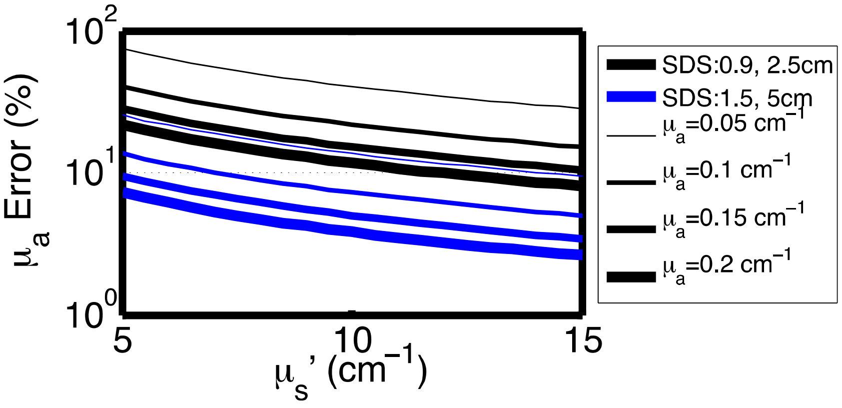

Figure 1.2. Slope Error in Determination of μ_a using Spatially Resolved Spectroscopy (SRS): Using continuous-wave SRS, absorption is equated to a fitted linear slope $\mu_a \sim S^2$ by assuming $r\sqrt{3\mu_a\mu_s'} \gg 1$, where r is the source-detector separation (SDS). The percentage error in S^2 is plotted with respect to two different probe layouts: pediatric (SDS = 0.9 and 2.5 cm; *black lines*) and adult (SDS =1.5 and 5cm; *blue lines*). We see retention of error (>1%) at all physiologic levels of scattering and absorption ($\mu_s' = 5 - 15\ \mathrm{cm}^{-1}$, *horizontal axis*; $\mu_a = 0.05 - 0.2\ \mathrm{cm}^{-1}$, *line thickness*), with worse error with the diminishing value of $\mu_a\mu_s'$.

separations, SRS can produce a fairly accurate (<10% error) extraction of the fitted slope, which in turn translates into a fairly accurate extraction of absorption (μ_a). However, this result relies on the fact that scattering (μ_s') was accurately assumed. The CW SRS assumption of a constant, population "average" scattering causes additional errors in the quantification of μ_a which may be attributed to inter-subject variability as well as dynamic changes in μ_s' over time.

Errors in the assumption of μ_s' introduces additional errors in μ_a. This magnitude of error can be quickly deduced from **Equation 1.26** whereby if we assume that $true(\mu_a) \cdot true(\mu_s') = S^2 = calculated(\mu_a) \cdot assumed(\mu_s')$, expression of the error of SRS-calculated μ_a follows as:

$$\frac{calculated(\mu_a)}{true(\mu_a)} = \frac{true(\mu_s')}{assumed(\mu_s')}. \tag{1.27}$$

Underestimation in baseline μ_s' properties results in an overestimation of μ_a. An increase in $true(\mu_s')$ would result in an erroneous and proportional increased in $calculated(\mu_a)$.

Notably, this cursory scattering error assessment does not consider the additional impact on the accuracy of SRS linear fitting with respect to source-detector separation when scattering changes. We perform a more complete analysis of physiologic error with respect to μ_s' in **Chapter 4**. With this understanding of error dependency in CW NIRS instruments in clinical use, we can better identify when and how measurements of cerebral hemodynamics by CW NIRS are most susceptible to error.

A.6. Diffuse Correlation Spectroscopy (DCS)

Diffuse correlation spectroscopy (DCS) is a time-domain diffuse optical technique that derives a cerebral blood flow index (BFI, cm^2/s) from quantification of the rapid speckle intensity fluctuations of multiply scattered coherent NIR light induced by red blood cell motion.[30–32] With much similarity to the diffusion of photons, the temporal electric-field ($E(\vec{r},t)$) autocorrelation function ($G_1(\vec{r},\tau) = \langle E^*(\vec{r},t)\cdot E(\vec{r},t+\tau)\rangle^2$) also diffuses through tissue.

Its transport dynamics are described by the correlation diffusion equation:

$$-vS(\vec{r}) = \left[\dot{\nabla}\cdot D(\vec{r})\nabla - v\mu_a(\vec{r}) - \frac{\alpha}{3}v\mu_s' k_0^2\langle\Delta\vec{r}^2(\tau)\rangle\right]G_1(\vec{r},\tau). \tag{1.28}$$

Notice, this formulation is like the photon equation for CW light. However, the correlation function is expressed as a function of position $\vec{r}$ and correlation delay-time τ. k_0 is the wavenumber (*i.e.*, inverse of optical wavelength) in tissue, α is the ratio of moving scatterers to total scatterers in the optical cross-section, D is the photon diffusion coefficient from the photon diffusion equation, and μ_a and μ_s' also appear as previously defined. Interestingly, the factor $\langle\Delta\vec{r}^2(\tau)\rangle$ also appears as an absorption term which contributes to decreased correlation; this factor is defined as the mean-square displacement of the scatterers after a delay-time τ. $\langle\Delta\vec{r}^2(\tau)\rangle$ is often set to be $6D_B\tau$, where D_B is the effective diffusion coefficient of moving scatterers; this approach assumes the movement of the scatterers in tissue (red blood cells) is well approximated by an effective Brownian model. Using a similar method of an extrapolated-zero boundary condition and the method of images discussed in Section A.2 (above), the solution for $G_1(\vec{r},\tau)$ in a semi-infinite homogeneous medium may be expressed as:

$$G_1(\vec{r},\tau) = \frac{3\mu_s' S_0}{4\pi}\left(\frac{e^{-\kappa(\tau)r_1}}{r_1} - \frac{e^{-\kappa(\tau)r_2}}{r_2}\right), \tag{1.29}$$

where $\kappa(\tau) = \left(\frac{v}{D}\left[\mu_a + \frac{\alpha}{3}\mu_s' k_0^2\right](6D_B\tau)\right)^{\frac{1}{2}}$.

The blood flow index (BFI) measured by DCS is the combined coefficient αD_B. Using high-speed instrumentation to quantify the normalized intensity autocorrelation function ($g_2(\vec{r},\tau)$) of arriving photons at the detector, the normalized electric field autocorrelation function ($g_1(\vec{r},\tau)$) can be calculated via the Seigert relation ($g_2(\tau) = 1 + \beta|g_1(\tau)|^2$). $\beta = \Lambda^2$, where Λ is the speckle contrast of the intensity speckle fluctuations. The calculated $g_1(\vec{r},\tau)$ curve may then be fit using a least-squares minimization algorithm to empirically derive αD_B~BFI.

Due to the direct dependence of the autocorrelation function on μ_a and μ_s' (**Equation 1.29**), the quantification of BFI is thus dependent, as was the quantification of [HbO$_2$] and [Hb], on accurate measurement of these optical properties. If μ_a and μ_s' are not quantified, then they must be assumed to derive a BFI. This results in significant errors in both absolute BFI and its relative changes.[33] In this work, concurrent FD-DOS measurements are carried out to quantify μ_a and μ_s' in the same tissue volume measured by DCS for improved physiologic accuracy of BFI.

An example of the fitted g_1 curve as a function of delay time τ demonstrates (**Figure 1.3**) the effects of cooling to deep hypothermia and deep hypothermic circulatory

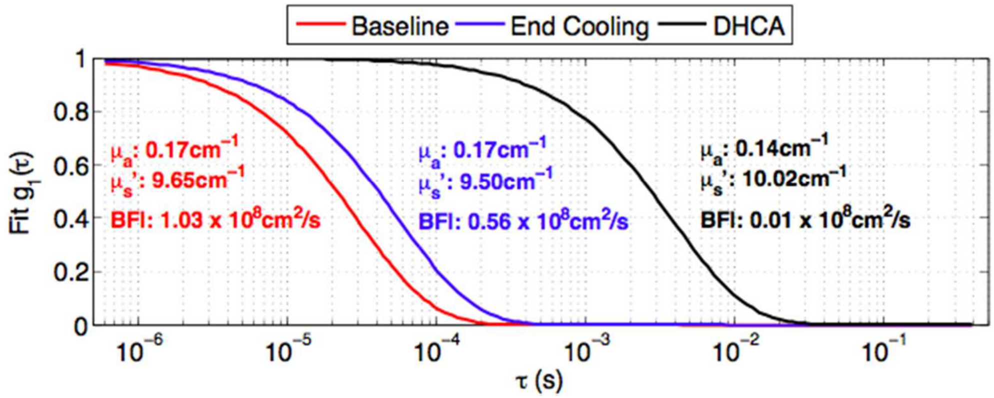

Figure 1.3. Normalized electric field autocorrelation function (g_1) exhibits slower decay as the blood flow in tissue declines. The fitted autocorrelation function is shown for measurements acquired at baseline on cardiopulmonary bypass (*red*), during deep hypothermia (*blue*), and during deep hypothermic circulatory arrest (DHCA; *black*). Optical absorption and scattering properties (μ_a and μ_s') and fitted blood flow index (BFI) values, which corresponds to cerebral blood flow, at each time-point are displayed.

arrest (DHCA) on g_1, on the optical absorption and scattering coefficients, and on the BFI (*see* **Chapter 2** and **3**). Examining BFI relative to baseline, we are able to show a ~50% decrease in cerebral blood flow as a result of cooling and >99% decrease during DHCA when all blood has been vacuumed from the body and there are no sources of cerebral perfusion. These results help demonstrate that, unlike measures of cerebral blood velocity from transcranial Doppler ultrasound,[34] DCS quantification of BFI is not impacted by low flow; i.e., DCS is sensitive to very small flows.

BFI measured by DCS has been clinically validated against Xenon CT,[35] transcranial Doppler ultrasound,[36,37] phase-contrast,[38,39] arterial spin labeling MRI,[40] and fluorescent microspheres.[41] It has been repeatedly shown to be an accurate surrogate of relative cerebral blood flow (rCBF). Moreover, quantitative relationships have been explored in order to translate BFI into physiologic units (ml/min/kg) of cerebral blood flow in children.[38,39] The impact of deep hypothermia on quantification of BFI and validation

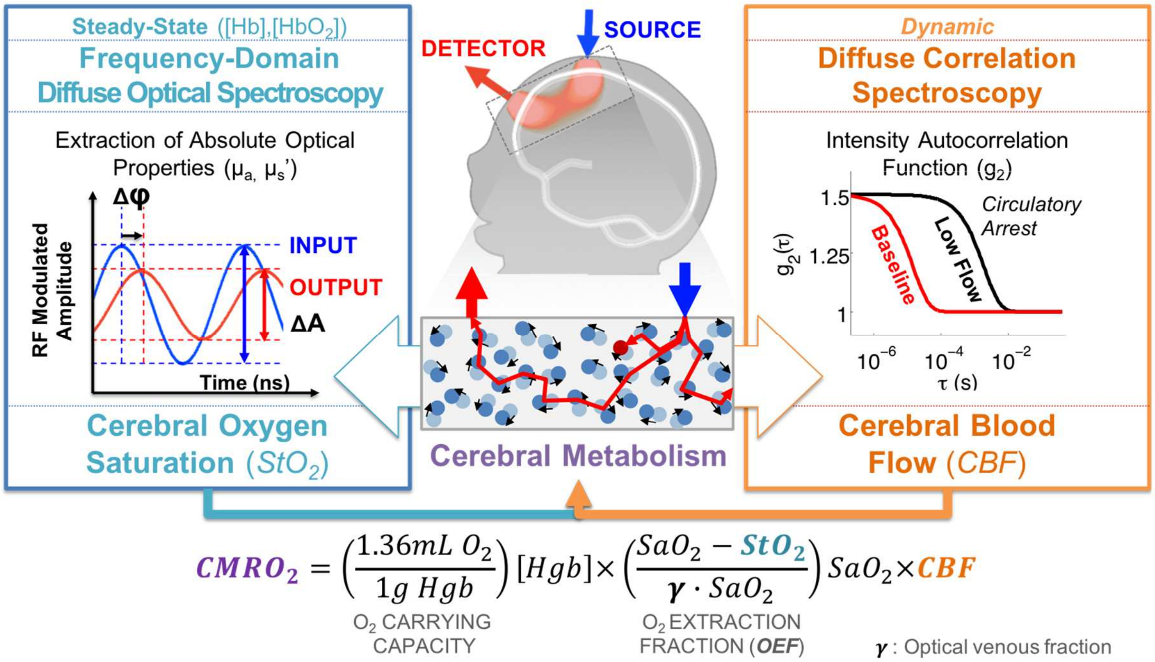

$$\boldsymbol{CMRO_2} = \left(\frac{1.36mL\ O_2}{1g\ Hgb}\right)[Hgb]\times\left(\frac{SaO_2 - \boldsymbol{StO_2}}{\boldsymbol{\gamma}\cdot SaO_2}\right)SaO_2\times\boldsymbol{CBF}$$

Figure 1.4. Non-Invasive Measurement of Cerebral Metabolism: Combining frequency-domain diffuse optical spectroscopy (FD-DOS) measures of cerebral tissue oxygen saturation (StO_2) and diffuse correlation spectroscopy (DCS) measures of cerebral blood flow (CBF), the cerebral metabolic rate of oxygen ($CMRO_2$) can be calculated using the known O_2 carrying capacity of hemoglobin, the hemoglobin concentration in blood ([Hgb]), the arterial oxygen saturation (SaO_2), and an assumption of the optical venous fraction (γ).

against invasive measures of rCBF by laser Doppler flowmetry is an important aspect of **Chapter 2**.

A.7. Diffuse Optical Measurements of Cerebral Oxygen Metabolism

Concurrent measures of cerebral oxygenation by FD-DOS and cerebral blood flow (CBF) by DCS, permit the combined calculation of the cerebral metabolic rate of oxygen ($CMRO_2$). While the methodology is reviewed in detail later in the methods of **Chapter 2**, here we provide a brief overview of it in **Figure 1.4**.

To perform FD-DOS measurements, our clinical diffuse optical instrument (**Figure 1.5, B**) incorporates a commercially available frequency-domain instrument

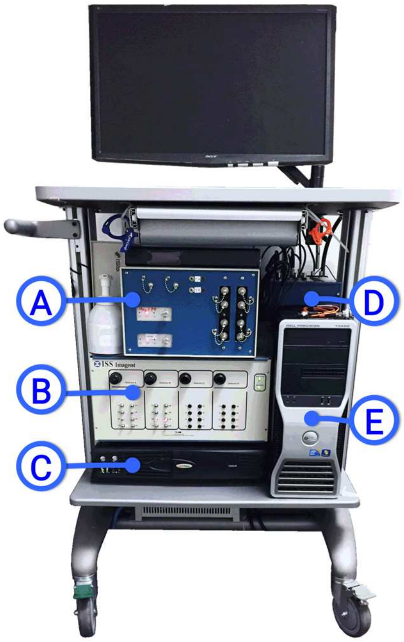

Figure 1.5. Clinical Diffuse Optical Instrumentation: Our diffuse optical instrument features a custom, laboratory built DCS instrument (A), a commercial FD-DOS instrument (B), an uninterruptible power supply to permit instrument portability (C), a digital data acquisition board (D) and a desktop control computer (E). The portability of instrumentation has permitted instruments at the bedside in the operating room and intensive care units.

(Imagent; ISS Inc., Champagne, IL, USA) that has been customized with four laser diodes at four distinct wavelengths in the NIR window (690nm, 725nm, 785nm, 830m). Via customized fiber optic measurement probes, the source light is transmitted to the tissue surface and detected photons are transmitted back to two high-sensitivity photomultiplier tube (PMT) detectors. The emission of these lasers and the detector are both sinusoidally intensity-modulated at 110MHz.

The duplicated sources for each wavelength of emission allows for placement at up to four difference source positions. The lasers are multiplexed such that only one of the sixteen sources is turned on at any given time. Time multiplexing of these sources then permits separated measurements at each wavelength and source position. A full cycle of measurements from all sources is acquired at a rate of 10 Hz. The instrument also features automated optimization of PMT gain which ensures that the PMT is acquiring the highest sensitivity signal permitted without saturation.

The DCS instrumentation (**Figure 1.5, A**) employs long-coherence length (>10m) lasers sources (RCL-080-785S; CrystaLaser, Inc, Reno, NV, USA) and single-photon-counting avalanche photodiode detectors (SPCM-AQ4C; Excelitas Technologies, Corp., Waltham, MA, USA), operating in Geiger mode, to detect and time the arrival of photons in each “speckle.” These photons have traveled through the brain.

A high-speed correlator board (FLEX03OEM-8CH; Correlator.com, NJ, USA) is used to measure the intensity autocorrelation function. It is computed for delay times ranging from 200ns to 1s. This permits empirical computation of a cerebral BFI from fitting to data (as described), which typically ranges from $1\text{x}10^{-9}$ to $5\text{x}10^{-8}$ cm/s^2 under normal physiologic conditions. However, during extreme physiological conditions such as circulatory arrest, significantly lower values are measured.

The FD-DOS instrument and DCS instrument are both connected to a digital data acquisition board and desktop computer which facilitate multiplexing of FD-DOS and DCS measurements (**Figure 1.5, D** and **E**). Due to the overlapping sensitivity of FD-DOS detectors to DCS sources and vice-versa, these different measurement modalities must also be multiplexed in time. The tuning of timing parameters is often dependent on study design. The DCS measurement is the more sensitive and “light-starved” due to the need for single-mode detection fibers to maintain coherence of detected photons. Thus, when allowable, it is beneficial to acquire more DCS measurements to increase signal-to-noise of the measurement. When examining physiologic signals with slower temporal components (>1 minute) the DCS instrument was allowed to integrate for 3 seconds per frame before switching to a 1 second measurement frame of FD-DOS. However, in the context of rapid physiologic changes (*i.e.*, cardiopulmonary resuscitation), the integration time of the DCS signal was decreased to 500ms to permit increased time resolution.

Including delays for switching between the modalities, an approximate combined FD-DOS/DCS sampling rate of 0.16Hz during cardiopulmonary bypass experiments presented in **Chapter 2** and **3**. The sampling rate was 0.3Hz in the resuscitation work presented in **Chapter 4**.

The technique of combining DOS and DCS to perform all-optical cerebral metabolic measurements has the tremendous advantage of a compact patient interface.[42–44] This is critical when working with newborns and infants where not only is the head small, the skull is still hardening, and in some cases, the skull has yet to cover regions of the central fissure. Optical metabolic imaging has been applied with great promise in a variety of clinical contexts. In Francescini et al., the measurement of $CMRO_2$ in infants demonstrated increasing THC and $CMRO_2$ with age despite stable StO_2; this likely reflects increasing metabolic demands of brain maturation that could not have been accessible without the concurrent DCS measurement of CBF.[45] Using an earlier version of our clinical instrument, Durduran et al., demonstrated a lack of change in $CMRO_2$ during hypercapnia in neonates with severe congenital heart defects. This work verified the expected physiologic response and demonstrated that optical measurements could be used to interrogate whether this proper autoregulatory response was present. This technique has clearly demonstrated improved patient accessibility over existing clinical modalities.

By extending this work to continuous monitoring during procedural interventions, we demonstrate that, in addition to logistical benefits, the high temporal resolution of optical methods allows for the development of novel diagnostic measures of cerebral status. Cerebral status information, in turn, could facilitate real-time guidance during neonatal cardiac surgery and resuscitation and improve neurological outcomes in these high-risk pediatric populations.

B. Mitigating Pediatric Brain Injury During Hypothermic Cardiopulmonary Bypass

B.1. Post-Operative Neurological Injury in CHD Neonates

Congenital heart defects (CHD) occur in approximately 8 of every 1,000 live births worldwide and are the most common congenital birth defect.[46] Approximately 1 in 3 of these newborns are affected by severe CHD, or life-threatening lesions requiring immediate surgical intervention in the first weeks of life.[47] Despite considerable increases in survival over the last two decades, the ~40% incidence of newly acquired post-operative neurological injury,[48,49] specifically white matter injury, has remained largely unchanged and poses a significant challenge to short-term morbidity and long-term neurodevelopment.[47,50] In recent results, at 1 year of age, children who underwent two-ventricle repair at less than 9 months of age continue to exhibit significant reductions in white matter volume that accounted for 75% of total reduction in brain volume compared to healthy age-matched controls.[51] White matter volume was also significantly associated with standardized measures of language and communication development which were below the 50th percentile. Within the first 3 years of life, in absence of known genetic syndrome, 35% experience significant neurodevelopmental delays,[52] and at school-age, 23% report impaired psychosocial functioning.[53] Neuroprotective strategies to identify and address operative risk factors for neurological injury in these neonates are urgently needed to prevent early injury with potentially catastrophic long-term reductions in quality of life.

Beca et al., identified that infants with severe CHD that required surgical repair of the aortic arch had more than 4-fold increase in risk of acquired post-operative white matter injury.[54] In these patients, duration of cardiopulmonary bypass (CPB) and the use of deep hypothermic circulatory arrest (DHCA) were identified as operative risk factors; (1) for each 1-minute increase in CPB duration, risk of injury increased by 2%, and (2) risk of injury increased 5-fold with the use of DHCA.

While recent dialogue surrounding the association of perioperative risk factors and long-term neurodevelopmental outcomes has emphasized the importance of non-modifiable patient characteristics and socio-economic factors,[49,54,55] the occurrence and impact of severe hypoxic-ischemic insults[56–58] during surgical correction remain unquantified in increasingly vulnerable patients due to the lack of routine intraoperative neuromonitoring.[59] Moreover, the findings that intraoperative cerebral oxygen saturation is associated with both white matter injury[60] and neurodevelopmental outcomes at 1 year of age[61], and that deficits in both total brain volume and white matter volume are significantly associated with cognitive, motor and executive function in adolescence,[62] indicate the value of developing neuromonitoring strategies for individual optimization of intraoperative risk factors to address discriminant neurological injury in high-risk individuals.[63]

B.2. Intraoperative Risk Factors for Post-Operative Neurological Injury

Extracorporeal Cardiopulmonary Bypass (CPB) Support

Cardiopulmonary bypass (CPB) support provides perfusion, gas exchange, and temperature management of the patient during surgical repair, but, in the process, it exposes the perfusing blood to an artificial environment that contrasts starkly with the smooth vascular endothelium in the body.[64] The use of CPB in neonates inherently causes 2 to 3-fold hemo-dilution due to the volume of blood in the CPB circuit compared to the neonate’s corporeal volume; by contrast, in adults, the CPB circuit volume is only 1/3 to 1/4 of patient volume. Thus, it should not be surprising that placement of an infant on extracorporeal CPB support is associated with several well-documented physiologic mechanisms which increase the risk of neurological injury.[65] These include systemic release of inflammatory mediators,[66,67] hydropic degeneration of cellular membranes,[68] tissue edema,[69] and risks of cerebral hyperthermia[70,71] and ischemia-reperfusion injury.[72] Advances in management of CPB support have endeavored to address these mechanistic risks, and routine neuromonitoring appears to be necessary in this context to address the uncertainty of the effects on cerebral perfusion and oxygenation.

Deep Hypothermia & Temperature Management

Deep hypothermia (DH), or the profound lowering of body temperature to below 20°C is commonly used during CPB to improve vital organ tolerance to procedural ischemia by suppressing metabolic demand.[73,74] While this technique is largely recognized to be beneficial and has been used in neonates for more than four decades,[75] standardized guidance about the management of cooling and rewarming to prevent neurological injury was only released in 2015. This guidance focused on adult care; pediatrics studies were only cited twice.[76,77] For infants, both target temperature for optimal neuroprotection and the site of temperature measurement remain controversial.[74,78] The most widely cited reports characterizing the temperature dependence of cerebral metabolism (which is the primary therapeutic target of DH) during CPB in children[79] by Greeley et al., and in adults[80,81] by Croughwell et al. and McCullough et al., suffer from uncertainty due to lack of true brain temperature determination.

In prominent surgical textbooks describing neonatal cardiac repair,[74,82] nasopharyngeal and esophageal temperatures are used for guidance of deep hypothermia. Indeed, these temperature measurement locations are the same at our institution, wherein the target temperature is 18°C.[83] Nasopharyngeal temperature is also commonly reported in studies to assess the depth of hypothermia.[83–85] Both nasopharyngeal and tympanic membrane temperatures are recommended over bladder or rectal temperatures to avoid the potential of cerebral hyperthermia during rewarming.[74] However, even without exogenous temperature alterations, inconsistent agreement with brain temperature has been reported for both anatomical locations in children and animal models.[86–89] Moreover, in the context of subsequent ischemia during deep hypothermic circulatory arrest (DHCA), the extent of ischemic neuronal injury has been shown to be highly brain temperature-dependent.[90] Thus the precise determination of brain temperature, or residual metabolism, is critical to ensure neuroprotection. Unfortunately, the existing clinical modalities suitable for continuous intraoperative monitoring are limited. This knowledge gap is and these limitations represent the primary motivation for the work presented in **Chapter 2**. Feasible intraoperative modalities and their limitations will also be discussed further below (**Section B.3**).

Deep Hypothermic Circulatory Arrest (DHCA)

Reconstruction of the aortic arch is an essential aspect of surgical intervention of several neonatal cardiac defects. These include interrupted aortic arch, aortic arch hypoplasia, and univentricular lesions (*e.g.,* hypoplastic left heart syndrome, HLHS), the lesion type with the greatest burden of post-operative neurological morbidity.[82] Standard cannulation techniques for cardiopulmonary bypass (CPB) require an intact aortic arch to maintain cerebral and corporeal perfusion; however, this precludes the conduct of surgical aortic arch reconstruction. In neonates where circulatory arrest is deemed necessary for repair, deep hypothermia, as described above, is induced to mitigate hypoxic-ischemic injury during circulatory arrest. Extended durations of DHCA (durations > 41 minutes) have significantly worse neurodevelopmental outcomes at school age.[91] Alternatively, to provide continuous perfusion and cooling to just the brain, selective cerebral perfusion (SCP) may be established via the right innominate and vertebral arteries after only a brief period (~15 minutes) of circulatory arrest.[92,93] The brain may then be continuously cooled and perfused at low flow (10-30 mL/min/kg) with ongoing arch correction in the thoracic cavity. Selection between DHCA versus SCP, or other similar "low-flow" perfusion strategies, remains a contentious topic among pediatric cardiac surgeons and is largely determined by institution of practice.[94] For DHCA durations <40 minutes, rates of seizure were comparable to neonates and infants wherein DHCA was not used.[95] In fact, in a relatively recent prospective randomized control study published by Algra et al., DHCA and SCP exhibited almost identical incidence of post-operative neurological white matter injury.[96] DHCA is currently used at our institution and is the focus of **Chapter 3**. Intraoperative monitoring of cerebral perfusion and metabolism has the potential to offer an objective measure of cerebral health that will permit individual-level, rather than institutional-level, optimization of management and neurological outcomes.

B.3. Intraoperative Neuromonitoring

The use of multimodal intraoperative neuromonitoring has provided substantial evidence for positive impact on neurological outcomes following adult and pediatric cardiac surgery.[97,98] In a study of 250 children undergoing surgical repair of congenital cardiac defects, Austin et al.[97] used concurrent electroencephalography (EEG), transcranial Doppler ultrasound (TCD), and continuous-wave cerebral near-infrared spectroscopy (NIRS; *i.e.*, a diffuse optical technique); in this study, an interventional algorithm designed to address deficiencies in cerebral perfusion and oxygenation had a beneficial impact on the incidence of postoperative neurologic sequelae and hospital length-of-stay. Strikingly, NIRS cerebral oximetry and TCD measurement of blood flow velocity in the middle cerebral artery could account for 58% and 37% of abnormalities detected, respectively, leaving only 5% EEG-related. Neuromonitoring-based intervention resulted in significant improvement, from 26% incidence of neurological complications to 6%. This result is comparable to the 7% seen in children where no abnormalities were detected. Additional critical review has estimated that 90% of cerebral abnormalities may be detected via NIRS and 10% via TCD.[25] These and more recent findings of predictive value in adverse neurological outcomes at 1 year of age have led to increased adoption of intraoperative NIRS-derived cerebral regional oxygen saturation (rSO_2) monitoring;[61,92,99,100] however, logistical difficulty with placement and operation during the course of surgery has prevented similar adoption of TCD.[101]

While valuable for trend monitoring, intraoperative NIRS has both measurement limitations and variability (*see above*, **Section A.5**). These issues are widely reported, and the technology also precludes clinical interpretation based on absolute values of any of the parameters it probes, particularly in the context of cardiopulmonary bypass and circulatory arrest.[27,102–104] Errors in NIRS quantification of rSO_2 are introduced from assumed baseline properties, which include a population-derived scattering coefficient that may vary ~50% between neonatal subjects, especially in high-risk populations with diverse presentations.[5,45,105] Moreover, profound physiologic changes during CPB (*e.g.*, hydropic degeneration in the brain leading to fluctuations in osmolarity[68,106]) and cooling of the dermis and subdermis[107] impact tissue scattering and cause additional errors in this method of quantification. In many clinical systems, the limited optical power of light-emitting diode sources is susceptible to low optical signal at the limits of detection in the presence of abnormally elevated hematocrit levels or darker skin pigmentation.[108] Despite these shortfalls, rapid adoption of commercial NIRS systems has taken place due to critical clinical needs and is encouraging for future acceptance of more advanced diffuse optical instrumentation that directly address existing limitations of NIRS (CW NIRS).

B.4. Improved Clinical Accuracy Using Quantitative Diffuse Optical Monitoring

As described in **Section A** (above), frequency- and time-domain diffuse optical spectroscopy, characterize scattering effects directly, and enable continuous *absolute* quantification of oxy- and deoxy-hemoglobin concentration for calculation of cerebral tissue oxygen saturation (StO_2).[53] Increased feasibility testing of DOS absolute quantification in clinical pediatric settings has been reported since initial measurements in 35 healthy newborn infants by Duncan et al., in 1995,[3] over two decades ago, and then in neonates undergoing surgical cardiac repair by Watzman and Kurth et al. in 2000 at our institution.[23] Absolute quantification has enabled cross-sectional comparisons with exciting new insights in this high-risk population by Lynch et al., regarding the critical decline of StO_2 in the pre-operative period and correlations with subsequent neurological injury.[109,110] The use of coherent laser sources, radio frequency-modulation, and more sensitive optical detectors extend conventional NIRS limits of detection and permit more accurate and sensitive spectroscopic analysis.[27] Furthermore, frequency-domain DOS (FD-DOS) quantification of StO_2 does not exhibit temperature sensitivity during deep hypothermia.[111]

However, even with improved quantification, intraoperative cerebral saturation monitoring alone does not fully capture dynamic information regarding cerebral oxygen delivery. This is important when identifying the cause of abnormal readings and for determining the appropriate intervention, if any. In the context of deep hypothermic cardiopulmonary bypass, depressed StO_2, a result of increased oxygen extraction, may reflect increased cerebral metabolism and cerebral inflammation when cerebral blood flow is concurrently elevated. Alternatively, if cerebral blood flow is depressed, the condition may not be pathologic as long as total oxygen metabolism is comparable to a healthy baseline. Quantification of cerebral blood flow enables more accurate formulation of critical differential diagnoses.

TCD measures of blood flow-velocity have been effectively used as a surrogate for cerebral blood flow (CBF) and for emboli detection in clinical research settings. However the variable integrity of the developing neonatal skull is a significant challenge for stable probe placement during the course of surgery.[25,74]

Diffuse correlation spectroscopy (DCS; *see above* **Section A.6**) is a relatively novel technique for non-invasive measurement of CBF which has been cross-validated against numerous clinical imaging modalities.[35–41] As a stand-alone modality, DCS measurements of CBF exhibit shortcomings which are comparable to those of conventional NIRS and measurement of rSO_2. It has been shown that DCS measurement error of CBF is susceptible to assumption errors of optical scattering.[33] As a result, the use of concurrent absolute FD-DOS quantification of optical scattering and absorption properties enables more accurate DCS measurement of CBF. These advanced modalities may be combined into a single compact measurement probe, equivalent in size to conventional NIRS forehead probes, but now equipped with the capability of non-invasive cerebral *metabolic* monitoring in neonates.[40,45] With adjunct blood gas monitoring of arterial oxygen saturation (SaO_2) and hematocrit (Hct), continuous measurements of cerebral oxygen saturation via FD-DOS and cerebral blood flow via DCS may be combined into a real-time measure of cerebral metabolic rate of oxygen ($CMRO_2$; **Chapter 2, Section C.5**). This is a significant logistical advantage for using DCS over TCD monitoring in the operating room. Importantly, a good correlation between DCS cerebral blood flow index and TCD blood flow-velocity have recently been reported in neonates during cardiopulmonary bypass and deep hypothermia.[37] In this thesis, we extend these novel techniques to validate continuous quantification of cerebral oxygen *metabolism* during deep hypothermia to enable more accurate and rapid identification of pathologic mismatches in oxygen demand and supply.

B.5. Significance & Innovation

Recent reports have demonstrated the feasibility of FD-DOS and DCS in the neonatal cardiac intraoperative environment.[37,112] However, the validity of DCS quantification of cerebral blood flow or in the combined FD-DOS/DCS quantification of $CMRO_2$ has not been tested (or explored) during the profound physiologic changes induced by deep hypothermia and subsequent rewarming to normothermia. In **Chapter 2**, titled “Non-invasive optical neuromonitoring of the temperature- dependence of cerebral oxygen metabolism during deep hypothermic cardiopulmonary bypass in neonatal swine,” we pursue two primary objectives. First, using concurrent measures of non-invasive and invasive sampling of oxygen extraction fraction (OEF), CBF, and $CMRO_2$, we validate the non-invasive optical instrumentation during the induction of and recovery from deep hypothermic cardiopulmonary bypass. Secondly, we examine the sufficiency of conventional nasopharyngeal temperature guidance of deep hypothermia to reflect intracranial brain temperature and metabolism. The combination of continuous non-invasive nasopharyngeal and invasive intracranial temperature sampling, as well as continuous non-invasive metabolic quantification, permits unprecedented high-resolution characterization of the temperature-dependence of cerebral oxygen metabolism during cooling and rewarming as well as examination of agreement with broadly-applied Arrhenius-type models[113–116] of reaction-rate dependence. Our results provide valuable insights regarding the clinical variability of metabolism with respect to nasopharyngeal temperature, as well as validation data to support the use of quantitative diffuse optical measurement of cerebral metabolism to effectively address this variability.

We thus can move forward to the next step of our investigation, with improved confidence in our quantitative metabolic measures, and the insight that accurate characterization of metabolic temperature dependence necessitates the use of invasive intracranial temperature. Further, individualized optimization of surgical management requires quantification of expected effect sizes in order to determine diagnostic thresholds which delineate those with increased risk. In **Chapter 3**, titled "Impact of deep hypothermic circulatory arrest on non-invasive diffuse optical measurement of cerebral oxygen metabolism in neonatal swine," we extend our study to examine cerebral metabolism in an additional cohort of neonatal swine (n=10) who were randomized to receive 40 minutes of deep hypothermic circulatory arrest (DHCA) versus deep hypothermic continuous perfusion (DHCP); note, animals who had been included in the initial validation stage of the study were limited to those in the DHCP group.

Continuous metabolic quantification during circulatory arrest permitted novel quantification of the timing of oxygen availability via the concentration of oxy-hemoglobin [HbO_2], the timing of oxygen extraction via the calculated oxygen extraction fraction (OEF), and insights into the persisting impact of circulatory arrest on cerebral oxygen metabolism during the rewarming period as reflected by comparison of metabolic temperature-dependence in the cooling period, prior to arrest, versus the rewarming period, following arrest. Quantification of the effects of DHCA on cerebral oxygen metabolism provides improved understanding of the timing and magnitude of metabolic shifts, including from aerobic to anaerobic respiration during prolonged arrest, as well as the sufficiency of reperfusion to replenish depleted oxygen following circulatory arrest.

Future examination of how these parameters are associated with neurological outcomes may lead to the identification of critical thresholds to prevent neurological risk.

C. Neurological Predictors of CPR Outcome following Pediatric Respiratory-Mediated Cardiac Arrest

Children who suffer cardiac arrest face high rates of mortality and neurological morbidity. Herein, we examine outcomes following pediatric cardiac arrest, risk factors, and the potential role of non-invasive neuromonitoring to address these risk factors.

C.1. Neurological Morbidity and Mortality following Pediatric Cardiac Arrest, Risk Factors, and the Role of Cardiopulmonary Resuscitation (CPR)

Over the last 15 years, survival has significantly improved from ~30% to over 45%[117–120] for children of all ages (<19 years) who suffer in-hospital cardiac arrest (IHCA). However, for those who suffer out-of-hospital cardiac arrest (OHCA), despite improved CPR quality over time,[121] there has been only limited evidence of improved survival for adolescents (aged 12-18 years)[122] but not for infants (<1 year) or for children (1-11 years).[122,123] Infants and children, who represent ~50% and 25%, respectively, of all pediatric cardiac arrests,[119,122–126] face bleak rates (~3.5 and 10%, respectively) of survival to hospital discharge with little improvement in the last 5 years.[127,128]

The discrepancy between pediatric IHCA (pIHCA) and OHCA (pOHCA) also extends to neurological outcomes and morbidity. Over 60% of pIHCA survivors achieve favorable neurological outcomes, defined as a Pediatric Cerebral Performance Category (PCPC) of 1 (normal age-appropriate neurodevelopmental function), 2 (mild disability) or 3 (moderate disability), as opposed to 4 (severe disability), 5 (comatose/vegetative), or 6 (death), with no significant differences across age groups.[117,119,126,129] In comparison, only one-third of pOHCA survivors achieve favorable neurological outcomes.[124,130] In a 2015 report summarizing n=1980 children (<18 years) who experienced an OHCA and factors associated with their outcomes, 69.8% were young children (<7 years) who constituted only 32.0% of survivors.[123] A multivariate model accounting for sex, race, historical timing, and first monitored rhythm showed a highly significant age group bias ($p<0.001$) where children younger than 7-years of age were less than half as likely to have favorable neurological outcomes compared to older children aged 13 to 17-years. Critically, accounting for age group, the presence of a shockable first monitored rhythm conveyed a 6.8-fold increase ($p<0.001$) in favorable neurological outcomes over non-shockable rhythms (*e.g.*, asystole). The distinct and persisting risk factors of OHCA highlighting young age and first-presentation with a non-shockable cardiac rhythm[121,123,125,130] strongly indicates that young children may have physiologically discrepant mechanisms which affect their response to cardiac arrest as well as their ability to recover from arrest. We carefully consider these characteristic features in the selection of our physiological model to permit an accurate representation of this at-risk population.

While beyond the immediate scope of the presented work, we highlight another important, persisting and modifiable risk factor which distinguishes children who suffer an OHCA in the United States and impacts both chances of bystander CPR and subsequent neurologically intact survival: *race*. In a recent study examining pOHCA in 3,900 children occurring in 2013-2015 from the Cardiac Arrest Registry to Enhance Survival (CARES) database of the US Centers for Disease Control and Prevention (CDC), 56.3% of white children received bystander CPR compared to 39.4% of black children and 44.0% of other racial backgrounds (*i.e.*, *black and other non-white children were 30% and 22% less likely to receive bystander CPR*, respectively).[131] Receiving bystander CPR translated into a 1.5-fold (95% CI: 1.2, 2) increase in survival with favorable neurological outcomes. In total, even adjusting for the occurrence of bystander

CPR, age, sex, witnessed arrest, arrest location, rhythm type, and defibrillation, black, Hispanic and other races/ethnicities were 32%, 9%, and 13% less likely than white children to achieve survival with favorable neurological outcomes. Though a cursory glance might suggest innate racial or genetic health disparities, these statistics do *not* account for provider bias or timing characteristics critical to survival (*e.g.*, time to initiation of compressions). In comparison, a recent study of 29,577 children with IHCA from 1997 to 2012 in the United States also observed a racial discrepancy where survival was 8.8% and 12.8% less likely in black and other non-white children compared to white children.[120] In a smaller study of pIHCA in 3,701 children occurring in 2006, adjustment for age, sex, hospital location, comorbidities, and cardiac factors resulted in no racial disparities in incidence or survival.[132] Racial disparities in the out-of-hospital setting are not unique to children,[133] and deserve continued attention by all communities inside and outside of academia.[134]

Despite the many discrepant risk factors between pIHCA and pOHCA, a common connection is timing. The 3-phase time-sensitive model of physiologic response following cardiac arrest, as described by Weisfeldt and Becker,[135] may underlie a striking U-curve relationship, uncovered by Tijssen et al., between pOHCA scene time (*i.e.*, the amount of time spent by first-responders at the scene prior to departing towards a hospital) and survival to hospital discharge.[122] Both a scene time <10 minutes or >35 minutes conveyed decreased chances of survival compared to 10-35 minutes. This was attributed to the lack of intervention (*e.g.*, defibrillation, intravenous fluid administration) for a “scoop and run” encounter associated with <10 minutes, versus detrimental or futile over-intervention (*e.g.*, placement of an invasive airway) that delayed re-establishment of perfusion when scene times exceeded 35 minutes. Given an average emergency medical services (EMS) response time of 5 to 5.5 minutes[121,122] following a 9-1-1 call, the timeline of survival risk is well-aligned with pIHCA. For pIHCA occurring in an intensive care unit (ICU; 96% of pIHCA[136]), cardiopulmonary resuscitation (CPR) times exceeding 30 minutes had a decreased survival rate of 28% compared to 45% overall survival.[119] The median [IQR] CPR time in survivors of pIHCA was found to be 15 [7-36] minutes versus 29 [15-49] minutes in non-survivors within a cohort of 880 children.[129] The achievement of return of spontaneous circulation (ROSC; *i.e.*, restarting of the heart) within 30 minutes of arrest appears critical to survival, though not the only determinant. Compared to the respective infant and children OHCA survival rates of ~3.5% and 10% discussed above, infants and children who suffered OHCA but achieved ROSC prior to hospital arrival had increased survival rates of 28.6% and 47.1%, respectively;[121] these statistics are more concordant with survival in pIHCA (~45%).

In addition to timing, quality of CPR is also divisive for survival, both in-hospital and out-of-hospital, and, potentially, a more modifiable risk factor.[121,137] Notably, the pIHCA survival rate of subjects with CPR times ranging from 16-35 minutes appear nearly identical to those with CPR times >35 minutes (17.8% versus 15.9%).[126] In the pediatric ICU setting, Berg et al. observed that though survival was lower with extended CPR times >30 minutes, the rate of survival with favorable neurological outcomes (89%, n=8/9) did not differ from survivors with only 1-3 minutes of CPR (90%, n=26/29).[119] This is evidence that, while in the pursuit of ROSC, high-quality CPR has the potential to provide life-sustaining perfusion that is also adequate for neurological protection in pediatric survivors of cardiac arrest. This is the foundation of the work presented in **Chapter 4** and central to our vision of improving upon existing physiologic indicators of high-quality CPR.

C.2. Pediatric CPR Guidelines and Quality Monitoring

With varied levels of emergency response training and interventions ranging from the lay-graduate student performing hands-only CPR to the critical care attending physician initiating extracorporeal life support (ECLS), we are compelled to inquire, what defines “high-quality” CPR? How does one know if ongoing CPR is “high-quality”? And critically, with persisting rates of >50% mortality in the hospital setting where trained professionals administer CPR, what is the future of “high-quality” CPR? Every 5 years the International Liaison Committee on Resuscitation (ILCOR), which includes representative organizations from the US, Canada, Europe, Latin America, South Africa, Asia, Australia and New Zealand, reviews previous guidelines and new literature and consolidates evidence into a report detailing the Consensus on Science with Treatment Recommendations (CoSTR). This is the core component of updated guidelines published by the American Heart Association (AHA) for Pediatric Basic and Advanced Life Support[127,138] and Cardiopulmonary Resuscitation Quality.[139] The current guidelines are described in relation to recent advances in CPR quality monitoring.

What defines “high-quality” CPR?

High-quality CPR, summarized by the AHA catch phrase, “PUSH HARD and PUSH FAST,” is explicitly defined as 1) ensuring chest compressions of adequate rate, 2) ensuring chest compressions of adequate depth, 3) allowing full chest recoil between compressions, 4) minimizing interruptions in chest compressions, and 5) avoiding excessive ventilation.[139] Many aspects of the guidelines for basic life support (BLS) CPR (*see* **Table 1.1**) in infants and children are consistent with those of adult CPR to permit minimized teaching complexity and improved skill retention. These include initial scene safety checks, pulse and breathing checks for a maximum of 10 seconds, identical chest compression rate recommendations of 100-120 compressions per minute, and the 2010 adoption of the C-A-B (“Circulation”-“Airway”-“Breathing”) sequence of initiating CPR over the historic A-B-C (“Airway”-“Breathing”-“Circulation”) sequence to minimize time to first compression, a well-established risk factor in adult OHCA,[140] but, as of yet, has had no demonstrated impact on survival in pediatric populations compared to the A-B-C sequence. Recommendations specific to children (defined as before puberty) include, in the event of an unwitnessed collapse, immediate initiation of 2-minutes of CPR with a chest compression depth at least 1/3 of the anterior-posterior diameter of the chest (*i.e.*, front-back distance of upper torso), which is approximately 4 cm in infants and 5 cm in children, and an emphasis on using rescue breathing, either in a 30 compression-to-2 breath (30:2) ratio with a single rescuer or 15:2 with two rescuers; following 2-minutes of CPR, the emergency response system should be activated and an automated external defibrillator (AED) should be sought and used.

In comparison, for witnessed collapses, or in adolescents and adults where the predominant arrest etiology is cardiac in origin,[141] with a single rescuer, the emergency response system should be activated and AED sought and applied immediately before beginning, or with two-rescuers, concurrently to beginning CPR; CPR should be provided until the AED is ready to use.[141,142] In adolescents and adults, compression depths should be at least 5 cm, but not exceeding 6 cm. Notably, while a trained rescuer should initiate C-A-B CPR with rescue breathing in a 30:2 ratio, a new version of chest compression-only CPR with no rescue breathing (*i.e.*, “hands-only” CPR) was introduced in the 2010 guidelines for the lay-bystander to improve low-rates of bystander intervention (43.8% in adults[143]; 37.4% in children[122]). It has shown significant improvements in adult survival when dispatcher-assisted, and no significant difference from conventional C-A-B CPR when un-assisted.[144] However, these findings have not translated to children where survival following the use of compression-only CPR (12%), while better than survival with no CPR (9%), is significantly lower than conventional CPR (17%).[131,145,146] This resulted in a 2017 update of the 2015 AHA Guidelines[147] to emphasize, "against the convenience of aligning with adult recommendations for chest compression-only CPR," the necessity of rescue breathing in infants and children. These findings and recommendations underscore that the majority of pediatric cardiac arrest events with known etiology, either out-of-hospital (27%)[130] or in-hospital (57%)[129,132], are asphyxial in nature and, in instances of unwitnessed collapse (>70% of pOHCA[122,125,148]), should be treated distinctly from cardiac arrest in adults. To align the generalizability of our work with these findings, the presented methodology utilizes a model of asphyxia-induced cardiac arrest.

How does one know if ongoing CPR is "high-quality"?

Adherence to the 2010 AHA CPR guidelines for over 60% of the duration when chest compressions were performed by a trained professional during pediatric IHCA conveyed a 10.3-fold increase in 24-hour survival over individuals where compressions did not adhere.[149] However, outside of the healthcare profession, it is often difficult to imagine witnessing the cardiac arrest of a child and being able to perform CPR with an innate sense of a 4 or 5 cm compression depth or 100 to 120 compressions-per-minute. The advent of "feedback technology" in the last 15 years has, via force transducers and accelerometers, begun to provide quantitative measures and both auditory and visual feedback of CPR quality in real-time.[121,150,151] This data has defined the guideline range of chest compression rates[152,153] and, in trained professionals, has helped identify and correct methodological errors (*e.g.*, leaning during the conduct of CPR[154,155]) as well as improved guideline adherence in pediatric IHCA through the use of active feedback during resuscitation.[156]

However, the impact of active feedback on patient outcomes, either pediatric or adult or during IHCA or OHCA, remains unclear[121,157] and an ongoing area of investigation. In the meantime, the positive impact on conduct of CPR by non-healthcare providers is worthy of highlight. While previous studies identified a CPR quality discrepancy between non-health care provider, lay-bystander CPR and trained professional CPR during OHCA arrests,[158] excitingly, two recent studies in the last year have demonstrated that the activation of audio feedback on public AEDs has enabled lay-bystanders to perform a comparable quality of CPR to trained EMS rescuers.[159,160] Given that a bystander response incorporating both CPR and public AED use compared to CPR-only has already shown a 3 to 5-fold improvement in survival with favorable neurological outcomes in pediatric OHCA *without* active feedback,[148,161] these findings give promise that even further improvements in pediatric OHCA outcomes are possible through the continued proliferation of public AED devices *with* feedback and overall awareness of their benefit. In relation to the presented work, it is encouraging that real-time CPR monitoring of risk factors has helped define “high-quality” care[142,152,153] and holds the potential to significantly improve future outcomes for children.

Table 1.1. 2015 Summary of High-Quality CPR Components for BLS Providers

Component	Adults and Adolescents	Children (Age 1 Year to Puberty)	Infants (Age < 1 Year, Excluding Newborns)
Scene Safety	Make sure the environment is safe for rescuers and victim		
Recognition of cardiac arrest	Check for responsiveness No breathing or only gasping (i.e., no normal breathing) No definite pulse felt within 10 seconds (Breathing and pulse check can be performed simultaneously in less than 10 seconds)		
Activation of emergency response systems	**Alone with no mobile phone**: Leave the victim to activate the emergency response system and get the AED before beginning CPR **Otherwise**: Send someone and begin CPR immediately; use the AED as soon as it is available	**Witnessed collapse:** Follow steps for adults and adolescents on the left **Unwitnessed collapse:** Give 2 minutes of CPR Leave the victim to activate the emergency response system and get the AED Return to the child or infant and resume CPR; use the AED as soon as it is available	
Compression-ventilation ratio *without advanced airway*	**1 or 2 rescuers** 30:2	**1 rescuer,** 30:2 **2 or more rescuers,** 15:2	
Compression-ventilation ratio *with advanced airway*	Continuous compressions at a rate of 100-120/min. Give 1 breath every 6 seconds (10 breaths/min)		
Compression rate	100-120/min		
Compression depth	At least 2 inches (5 cm); No more than 2.4 inches (6cm)	At least 1/3 AP diameter of chest; About 2 inches (5 cm)	At least one third AP diameter of chest; About 1.5 inches (4 cm)
Hand placement	2 hands on the lower half of the breastbone (sternum)	2 hands *or* 1 hand (optional for very small child) on the lower half of the breastbone (sternum)	**1 rescuer** 2 fingers in the center of the chest, just below the nipple line **2 or more rescuers** 2 thumb–encircling hands in the center of the chest, just below the nipple line
Chest recoil	Allow full recoil of chest after each compression; do not lean on the chest after each compression		
Minimizing interruptions	Limit interruptions in chest compressions to less than 10 seconds		

Abbreviations: AED, automated external defibrillator; AP, anteroposterior; BLS, basic life support; CPR, cardiopulmonary resuscitation. Reproduced with permission from the AHA.[162]

C.3. Future of "High-Quality" CPR: Physiologic Monitoring

In the continual pursuit of improved survival and neurological outcomes, novel interventions and risk factors with greater specificity for outcomes are continually being explored, identified and validated. Despite the demonstrated improvements in care, the current application of force and depth sensors still suffer from inaccuracies dependent on the surface of compression;[163] without the use of a rigid backboard, sensors placed on the body are unable to account for surface compression and inaccurately report deeper compressions than truly applied. In an evolutionary path reminiscent of the application of force transducers and accelerometers for compression depth and rate, institutional-level advances in high-resolution physiological monitoring and data recording at the bedside in the in-hospital setting have permitted unprecedented understanding of the physiology underlying high-quality CPR, achievement of ROSC, and neurologically intact survival.[164,165] Real-time vitals data collection are a major component of Pediatric Early Warning Scores (PEWS)[166–168] and pivotal to a potential methodological transition from "rescuer-centric" resuscitation guidance using exogenous setpoints (*e.g.*, compressions characteristics) to "patient-centric" resuscitation guidance using *the individual's physiologic response*.[137] Given demonstrated improvements in achievement of ROSC using physiologic-directed CPR during adult IHCA[169] and updates to the Pediatric Advanced Life Support (PALS) recommendations supporting the use of invasive hemodynamic targets, when available, to guide pIHCA resuscitation,[127] this transition is underway and reflects *the future of "high-quality" CPR*.[137]

Hemodynamic Monitoring

In a landmark study by Paradis et al. in 1990, coronary perfusion pressure (CoPP), defined as the difference between aortic arterial blood pressure and right atrial (central venous) blood pressure during diastole, was shown to be a highly specific predictor of ROSC in adults, with no achievement of ROSC in subjects with maximal CoPP $\leq$15mmHg.[170] CoPP is a measure of the pressure gradient driving blood flow and oxygenation to the myocardium and has been shown to be highly predictive of successful defibrillation.[171] However, due to the difficulty of inserting both invasive arterial and central venous blood pressure monitors during an ongoing arrest, and the lack of mathematical subtraction on vitals display devices, implementation of CoPP guidance is often prohibitive; data regarding CoPP during CPR remains limited to subjects where such monitoring is clinically necessary.[172] To address this challenge, arterial blood pressure (ABP) monitoring alone as well as monitoring of end-tidal carbon dioxide ($ETCO_2$) have been explored as surrogate measures of CoPP and were identified as pertinent physiologic signals during CPR in a 2013 AHA Consensus Statement[137] as well as recent reviews of physiology-directed CPR[173] and CPR practices in pediatric and cardiac ICUs.[174]

The latest pediatric-related evidence regarding ABP monitoring during CPR comes from a prospective study examining promising diastolic ABP (DBP) targets from animal studies[175–177] in 164 children (60% infants, <1 year old) where invasive ABP monitoring was in place prior to IHCA. A mean DBP $\geq$25 mmHg in infants and mean DBP $\geq$30 mmHg in children over 1 year old, during CPR, was associated with a 1.7-fold (95% CI: 1.2, 2.6) improvement in survival to discharge with favorable neurological outcomes. This study defines important thresholds for guidance that will now move towards independent validation in a future cohort.

End-Tidal Carbon Dioxide (ETCO2)

A similar pediatric investigation was performed examining an $ETCO_2 \geq$20 mmHg target extrapolated from recommendations[137] and studies in adults.[178–182] In contrast to diastolic ABP thresholds, mean $ETCO_2 \geq 20$ mmHg over the first 10 minutes of CPR in 43 children with quantitative capnography in place prior to arrest, either in a pediatric ICU or cardiac ICU, did *not* demonstrate improved rates of ROSC or survival to hospital discharge. A recent review of studies in adults and children[173] highlights the high variability in measured $ETCO_2$ across studies depending on the etiology of the arrest (*e.g.*, cardiac, respiratory, out-of-hospital) and ventilation rates. In addition, a few-minute delay in prognostic value during the conduct of CPR during IHCA further limits the use of $ETCO_2$ for real-time guidance.[183] However, there was significant support for alternative recommended uses of $ETCO_2$ monitoring as a marker of CPR futility, when $ETCO_2$ remains <10 mmHg for over 20 minutes,[179] or as an identifier of ROSC.[184] The independent identification of ROSC could potentially remove compression pauses for cardiac rhythm checks and permit the ideal scenario of minimally interrupted chest compressions.[185,186] Reported data regarding $ETCO_2$ during pediatric CPR remains limited and deserves further examination as, in contrast to invasive ABP monitoring, measurements of $ETCO_2$ have been readily studied during IHCA *and* OHCA.[179,187] While still requiring an advanced life support EMS responder to place an advanced airway, $ETCO_2$ monitoring is relatively non-invasive compared to hemodynamic monitoring and may potentially be applicable to a broader population of children outside of the hospital setting.

C.4. Diffuse Optical Neuromonitoring: An Emerging Diagnostic of CPR Quality

Diffuse optical neuromonitoring, our modality of focus and more commonly known as near-infrared spectroscopy (NIRS) in clinical CPR contexts, is a promising emerging technology for monitoring CPR quality which, as repeatedly highlighted in this work, provides truly *non-invasive* measurement of *cerebral* hemodynamics.[173,188] Diffuse optical neuromonitoring may be performed with the simple application of a rubber probe pad on the forehead and may be initiated with significantly reduced procedural barriers compared to either ABP or $ETCO_2$ monitoring. Magnetic resonance imaging,[189–191] transcranial Doppler ultrasound,[192,193] and electroencephalography (EEG)[194–196] have also been explored for neuromonitoring,[197] but currently face prohibitive limitations for out-of-hospital use; their discussion here is limited, but they remain interesting adjunct modalities for further investigation.

Neuroprotection is Critical

The importance of cerebral physiology is innately emphasized during cardiac arrest; in a pediatric animal model (6-12 kg, young mongrel dogs) of cardiac arrest by ventricular fibrillation, evaluation of the regional distribution of blood flow by radioactive microsphere injection, preceded by 30 seconds of CPR and followed by 2.5 minutes of CPR and a single defibrillation, albeit a now outdated version of CPR (chest compression fraction of 50%, chest compression rate of 62 compressions per minute, and simultaneous compression to ventilation ratio of 5:1), demonstrated that, compared to normal controls with sinus rhythm, 90% of cerebral blood flow was sustained versus 35% for the heart and 15% for the kidneys.[198] This dynamic distribution reflects the central role of brain and heart function to survival as well as identifies tradeoffs in perfusion during resuscitation. Maintained perfusion to the heart versus the brain has been more highly associated with ROSC following defibrillation,[171] however neurological injury accounts for 81% of subsequent deaths in resuscitated children following OHCA.[199] These compounded risk factors necessitate a multifactorial approach that incorporates real-time assessment of both cardiac and cerebral status during CPR to optimize survival with favorable neurological outcomes.

Diffuse Optical Neuromonitoring: Current Progress

Prior to the presented work, the clinical application of diffuse optical neuromonitoring of active resuscitation efforts have been limited to the use of continuous-wave NIRS techniques. In 1995, Mullner et al. first reported on the diagnostic potential of NIRS in the peri-arrest period in humans.[200] Immediately after emergency department arrival, a NIRS sensor was placed and cerebral oxygen saturation (rSO_2) was measured in adults following OHCA where 6 of 18 subjects had failed to achieve ROSC prior to arrival. A significant difference was observed between subjects with 1-week survival (rSO_2 = 63%, 95% CI: 60%-68%) and non-survivors (rSO_2 = 46%, 95% CI: 17%-51%; p=0.003); a similar examination of pulse oximetry did not demonstrate group differences. This represented a promising new application for non-invasive neuromonitoring which has since been reinforced in a 27-month-long, nationwide study in Japan published by Nishiyama et al. in 2015. Patients (n=1921) who were unresponsive (Glasgow Coma Score <9) upon hospital admission following OHCA, both with (n=148) and without ROSC (n=1773), were measured by bilateral cerebral NIRS for a minimum of 1 minute. The lowest NIRS value during measurement was found to have significant correlation with incidence of favorable neurological outcomes (p<0.01). Interestingly, a decorrelation in right-left NIRS rSO_2 was observed in subjects without ROSC (Pearson's R=0.66) compared to those with ROSC (Pearson's R=0.94). These results confirmed the prognostic potential for neuromonitoring to inform long-term neurological outcomes.

Recent reviews[188,201–203] have documented the dramatic increase in the utilization of NIRS *during* adult CPR over the last 10 years, in both the in-hospital and out-of-hospital setting. This, firstly, is a testament to the accessibility and ease-of-use of current NIRS systems, and, secondly, holds promise for *rapid translation of advances in diffuse* *optical neuromonitoring to healthcare providers*. Three recent studies (reported in 2016 and after) represent the largest, prospective evaluations of the association of rSO_2 measurements during CPR with outcomes, and are subsequently examined here.[204–206]

In the in-hospital setting, NIRS measurements of 183 adults by Parnia et al. demonstrated a significant difference in mean rSO_2 during CPR between individuals who achieved ROSC versus those who did not (mean (SD): 51.8% (11.2) vs. 40.9% (12.3)). Median and mean rSO_2 in the last 5 minutes of CPR, as well as median and mean rSO_2 over all CPR, and percentage of time with rSO_2 above 50% in the last 5 minutes of CPR and over all CPR were assessed as predictors of ROSC and neurologically intact survival to discharge. Mean rSO_2 in the last 5 minutes demonstrated highest predictive value for ROSC with a receiver-operating-characteristic (ROC) area under the curve (AUC) value of 0.76 (95% CI: 0.69, 0.83). Percentage time with rSO_2 >50% best predicted favorable neurological outcomes (AUC = 0.79, 95% CI: 0.70-0.88). Furthermore, critical decision thresholds for ROSC prediction were identified as mean $rSO_2 \geq 25\%$ (sensitivity = 100%) and mean $rSO_2 \geq 65\%$ (specificity = 100%). This study provided critical assessments of potential diagnostic parameters that informed predictor selection in a subsequent study in the out-of-hospital setting.

From the same authorship group, Singer et al. examined adults (n=100) with out-of-hospital cardiac arrest upon hospital admission with both $ETCO_2$ and rSO_2 monitoring.[205] The predictive value of mean $ETCO_2$ and mean rSO_2 values during subsequent CPR were assessed and compared. Both mean $ETCO_2$ and mean rSO_2 were significantly higher in patients who achieved ROSC (mean (SD), $ETCO_2$ = 41.1 mmHg (18.1), rSO_2 = 45.8% (12.2)) versus those who did not ($ETCO_2$ = 23.8 mmHg (15.0), $p<0.001$; rSO_2 = 36.4% (13.4), $p=0.001$). But while the AUCs were similar ($ETCO_2$: 0.77, rSO_2: 0.69), the two measures were not significantly correlated.

Furthermore, optimal prediction thresholds determined by maximal Youden index (ETCO $\geq$19mmHg, rSO_2 $\geq$50%) had greater sensitivity with respect to $ETCO_2$ (sensitivity = 100%, specificity 45%) but greater specificity with respect to rSO_2 (specificity = 85%, sensitivity = 48%). These findings confirm that the physiology reflected by each measure are distinct but potentially complimentary and warrant further multivariate optimization.

The most recent report, by Genbrugge et al., also addressed OHCA following hospital admission and represents the largest prospective multicenter study to-date with continuous neuromonitoring during CPR.[206] In 329 patients, both initial rSO_2 values and change in rSO_2 during CPR were significantly higher in individuals who achieved sustained ROSC (>20 minutes) versus those who did not (mean (SD) initial rSO_2: 41% (13) vs. 33% (13), p<0.001; median [IQR] change in rSO_2: 9% [2,24] vs. 2% [-2.7], p<0.001). A linear mixed-effects model was used to analyze the trajectory of rSO_2 during CPR as a function of time and found significant differences between ROSC and no-ROSC subjects (p<0.001). Change in rSO_2 >15% during CPR was a highly promising predictor identified during analysis; adjusting for sex, age, witnessed arrest, bystander CPR, pre-hospital defibrillation, initial rhythm, EMS response time, *and* arrest etiology, achieving a change in rSO_2 >15% conveyed a 4.9-fold increase in chances of ROSC. Given the study sample size, this result is noteworthy and highly relevant to the methodology and findings of the presented work where both absolute and change in cerebral hemodynamics are examined during CPR.

These studies provide substantial evidence *that non-invasive monitoring of cerebral hemodynamics during CPR may be prognostic of both ROSC and neurological outcome*. However, diffuse optical neuromonitoring during *pediatric* CPR has been limited to animals studies[207–215] and three descriptive case reports in children.[216–218] Most recently, Çağlar et al. reported on the largest group of children (n=10) who were monitoring by NIRS during CPR following OHCA. Three of ten children achieved sustained ROSC (>20 minutes) with abrupt increases in measured cerebral oxygenation at ROSC. With cautious interpretation due to sample size, minimum rSO_2 values were found to be significantly lower in children who did not achieve ROSC compared to those who did (mean (SD), 20.7% (5.7) vs. 30.0% (1.0); p=0.02). Despite these limited reports, the future holds promise for growth; the 2018 AHA Scientific Statement on CPR in Infants and Children with Cardiac Disease has incorporated new recommendations for NIRS neuromonitoring during pre- and post-arrest care[219] following an expert consensus assessment determining NIRS safe and effective for use in the pediatric critical care setting.[220] To further improve the diagnostic potential of diffuse optical neuromonitoring during pediatric CPR, the presented work explores the use of more sophisticated diffuse optical techniques[8] to address existing limitations of continuous-wave NIRS in the context of CPR.[202]

C.5. Significance and Innovation

Maintaining perfusion to the heart and the brain during pediatric cardiac arrest is vital to resuscitation and neurologically intact survival. As the presented evidence has shown, these outcomes are highly dependent on the administration of high-quality CPR. Transitioning away from “rescuer-centric” guidance parameters, physiologic-directed CPR is a novel frontier that permits optimization of high-quality CPR for the *individual*. Non-invasive diffuse optical neuromonitoring techniques have demonstrated the potential to extend the current bounds of physiologic-directed cardiopulmonary resuscitation to include *neurological* resuscitation. However, the application of these techniques to CPR are currently limited to continuous-wave (CW) NIRS measurements of cerebral tissue oxygenation which suffer from high inter-subject variability and the lack of precision.[221–223] At baseline in healthy volunteers, this has been attributed to tissue heterogeneity[224] and extracerebral contributions.[225,226] Even greater variability is introduced in the context of extreme values and dynamic changes seen during resuscitation when the optical assumptions which underlie CW NIRS quantification are violated (**Chapter 1, Section A.5**) and physiologic conditions deviate from the rSO_2 = 50-90% range where commercial oximeters are validated in healthy individuals for FDA approval.[29,227] The use of continuous-wave light sources effectively limit CW NIRS quantification to spectral and spatial changes in optical intensity which are equated exclusively to changes in absorption; assumed optical scattering properties are used to calculate these changes in absorption. These scattering properties have been shown to have significant inter-subject variability in healthy infants [5] as well as significant changes following cardiac arrest.[26] The use of more sophisticated, *quantitative* diffuse optical techniques provides the ability to limit this variability through absolute quantification of dynamic absorption *and* scattering properties,[8] resulting in greater *individual* physiologic accuracy.

In **Chapter 4**, entitled “Prediction of Return of Spontaneous Circulation During Cardiopulmonary Resuscitation using Non-Invasive Frequency-Domain Diffuse Optical Spectroscopy”, we apply the quantitative diffuse optical technique of frequency-domain (FD) diffuse optical spectroscopy (DOS) to provide physiologically accurate measurements of cerebral hemodynamics during asphyxia, cardiac arrest by ventricular fibrillation, and subsequent CPR. As described in **Chapter 1, Section A.1-4**, the addition of sinusoidally amplitude modulated laser sources and high-sensitivity detectors permits additional phase discrimination resulting in the resolution of tissue optical scattering properties. These methods are applied in a high-fidelity pediatric swine model of asphyxial cardiac arrest which has been incorporated in expert consensus statements[127] and widely regarded as an accurate model of physiologic response during high-quality CPR in children approximately 1 year of age.[228–230] With respect to the overall incidence rates by age group presented, this reflects the approximate median age of a pediatric cardiac arrest victim.[120,128]

In addition to cerebral tissue oxygen saturation, which we will abbreviate as StO_2 when measured by FD-DOS and rSO_2 when measured by CW NIRS, the accurate resolution of variability in scattering by FD-DOS permits quantitative measurements of *absolute* concentrations of oxy-, deoxy- and total hemoglobin in tissue ($[HbO_2]$. [Hb] and THC, respectively). This provides novel diagnostic measures of physiology related to oxygen availability, via $[HbO_2]$, and blood volume, via THC,[231] whose associations with ROSC are reported. Secondly, the most comprehensive report of CW NIRS during CPR to-date by Genbrugge et al. highlights the importance of additionally examining the change in physiology during CPR; these trends and associations are also examined. In total, these quantitative diagnostics reveal exciting new insights regarding the necessary evolution of cerebral hemodynamic conditions for achievement of ROSC. Finally, to address the time-sensitive nature of neuroprotection and successful achievement of ROSC,[135] the predictive power of significant cerebral hemodynamic parameters are examined with respect to time within the first 10 minutes CPR. Using the novel application of time-stability analysis to these parameters, the optimal ROSC predictor is selected, considering both predictive power as well as predictive stability throughout early CPR.

The predominant cause of death due to neurological injury in short-term survivors of pediatric cardiac arrest[199] warrants focused development of real-time physiologic neuromonitoring to ensure high-quality CPR also addresses the needs of the vulnerable pediatric brain. As evidenced by the neurological resilience of survivors after extended periods of CPR,[119,126] high-quality CPR has the potential to provide adequate perfusion for neurological protection. By elucidating the cerebral physiology necessary for ROSC and providing promising, non-invasively measured, decision thresholds for guidance, the presented work makes important strides towards the realization of high-quality cardio-, pulmonary- and neurological resuscitation for all children both in and out of the hospital setting.

CHAPTER 2: NON-INVASIVE OPTICAL NEUROMONITORING OF THE TEMPERATURE- DEPENDENCE OF CEREBRAL OXYGEN METABOLISM DURING DEEP HYPOTHERMIC CARDIOPULMONARY BYPASS IN NEONATAL SWINE

A. Abstract

Management of deep hypothermic (DH) cardiopulmonary bypass (CPB), a critical neuroprotective strategy, currently relies on non-invasive temperature to guide cerebral metabolic suppression during complex cardiac surgery in neonates. Considerable inter-subject variability in temperature response and residual metabolism may contribute to the persisting risk for postoperative neurological injury. To characterize and mitigate this variability, we assess the sufficiency of conventional nasopharyngeal temperature (NPT) guidance, and in the process, validate combined non-invasive frequency-domain diffuse optical spectroscopy (FD-DOS) and diffuse correlation spectroscopy (DCS) for direct measurement of cerebral metabolic rate of oxygen ($CMRO_2$). During CPB, n=8 neonatal swine underwent cooling from normothermia to 18°C, sustained DH perfusion for 40 minutes, and then rewarming to simulate cardiac surgery. Continuous non-invasive and invasive measurements of intracranial temperature (ICT) and $CMRO_2$ were acquired. Significant hysteresis ($p<0.001$) between cooling and rewarming periods in the NPT versus ICT and NPT versus $CMRO_2$ relationships were found. Resolution of this hysteresis in the ICT versus $CMRO_2$ relationship identified a crucial insufficiency of conventional NPT guidance. Non-invasive $CMRO_2$ temperature coefficients with respect to NPT ($Q_{10} = 2.0$) and ICT ($Q_{10} = 2.5$) are consistent with previous reports and provide

further validation of FD-DOS/DCS CMRO$_2$ monitoring during DH CPB to optimize management.

B. Introduction

Deep hypothermia (DH) is an important neuroprotective therapy used during cardiopulmonary bypass (CPB) in an attempt to mitigate hypoxic-ischemic brain injury by suppressing cellular metabolic demand in neonates with congenital heart disease during complex cardiac repairs.[74] Over the last two decades, survival rates for these children have substantially improved;[232] however, the incidence of neurological injury has remained constant and, in some cases, has resulted in developmental delays and lifelong neurological deficits.[47] Despite widespread use of DH CPB, uncertainty predominates regarding optimal temperature management due to hitherto poorly defined individual cerebral metabolic responses to hypothermia.

Real-time neuromonitoring is needed to address a key challenge for DH protocols by confirming, on a patient-by-patient basis, that the suppression of metabolism is sufficient to prevent adverse neurological sequelae during procedural cerebral ischemia.[73,74,91,233] Decreased cerebral blood flow, oxygen extraction, and metabolism in response to deep hypothermia has been widely demonstrated, but significant inter-subject variability in temperature-response has also been observed.[234] Specifically, the use and value of conventional core temperature guidance for assessment of the adequacy of metabolic suppression during DH has been questioned.[79,81,235–237] Systematic study of core temperature, brain temperature, and residual cerebral metabolism as neurological risk factors are needed. Such studies are hindered by a lack of noninvasive, cerebral metabolic monitoring tools suitable for the operative environment. If this limitation can be ameliorated, then assessment of current neuroprotection strategies, and development of new personalized strategies to optimize neurological outcomes, should be possible for these at-risk children.

Multimodal neuromonitoring, including clinical continuous-wave near-infrared spectroscopy (CW NIRS) for cerebral oxygen saturation and transcranial Doppler ultrasound (TCD) for cerebral blood flow-velocity, has shown evidence of improving post-operative neurological complications.[97] The quantitative uncertainty of CW NIRS and the logistical difficulty of employing and interpreting TCD in the operating room has prevented their combined use for routine metabolic monitoring and likely impacted efficacy of goal-directed therapy.[238] By contrast, the combination of frequency- or time-domain diffuse optical spectroscopy (FD-DOS, TD-DOS), to measure *absolute* cerebral tissue oxygen saturation (StO_2, %), with diffuse correlation spectroscopy (DCS) to measure cerebral blood flow (CBF), enables a compact, all-optical method for continuous non-invasive monitoring of cerebral metabolism. This approach has been demonstrated in vulnerable pediatric populations outside the operating room.[24,39,40,105,109,110,112,239–245] Although recent work has established intraoperative feasibility for some of this technology [37,112], *non-invasive* diffuse optical measurements of CBF and metabolism have never been validated against *invasive* monitoring during the profound physiologic and temperature changes induced by DH CPB and subsequent rewarming.

Here we carry out an observational study of concurrent conventional monitoring of nasopharyngeal temperature alongside invasive intracranial temperature and invasive and non-invasive (*i.e.*, diffuse optical) measurements of cerebral oxygen metabolism during a simulated cardiac surgical procedure using DH CPB with subsequent rewarming in neonatal swine. The sufficiency of nasopharyngeal temperature guidance is examined with respect to intracranial temperature, and the temperature-dependence of cerebral oxygen metabolism is assessed with respect to both modalities using high temporal resolution *in vivo* sampling methods. Non-invasive diffuse optical measurements are compared directly with invasive measurements, and similarities and differences of measured parameters are identified and understood.

C. Methods

Neonatal, female Yorkshire swine (n=8, 6-10 days old, 3-5kg) were continuously monitored during cardiopulmonary bypass (CPB) from induction of deep hypothermia (DH) through recovery to normothermia. All procedures were approved by the CHOP Institutional Animal Care and Use Committee, performed in strict accordance with the NIH Guide for the Care and Use of Laboratory Animals, and reported according to the ARRIVE guidelines (https://www.nc3rs.org.uk/arrive-guidelines).

C.1. Selection of Animal Model

Pediatric large-animal model studies describing $CMRO_2$ temperature-dependence during DH CPB have been reported in dogs[246] and pigs using sparse sampling methods.[237,247–252] The neonatal swine model offers comparable anatomical size and cortical maturation with the human neonate, as well as excellent intersection of DH CPB and diffuse optical neuromonitoring literature.[32,40,253,254]

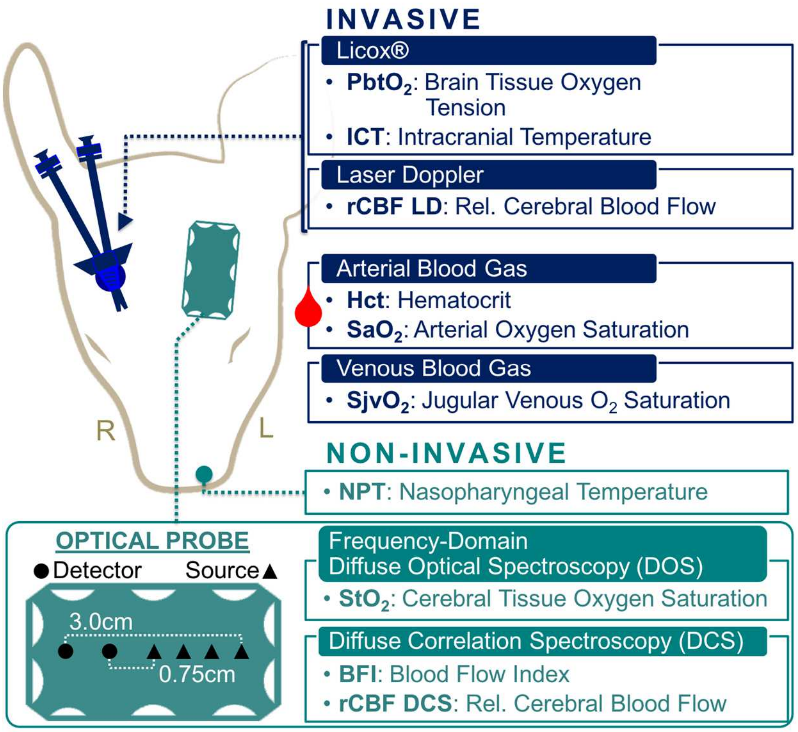

Figure 2.1. Neuromonitoring: Head placement of non-invasive (*green*; left hemisphere) and invasive (*blue*; right hemisphere) neuromonitoring technologies. A diagram showing details about the FD-DOS/DCS optical probe is given on the lower left (source positions, *triangles*; detector positions, *circles*).

C.2. Neuromonitoring

Non-invasive and invasive neuromonitoring were placed and secured following anesthetic induction and intubation as detailed in the Appendix (**Section F.1**).[255] Continuous *non-invasive* measurements comprised nasopharyngeal temperature (NPT, °C), for guidance of hypothermic therapy, and frequency-domain diffuse optical spectroscopy (FD-DOS) and diffuse correlation spectroscopy (DCS), which are detailed below. FD-DOS/DCS measurements were acquired in the left frontal cortex via an optical probe sutured to the left forehead (**Figure 2.1**). Continuous *invasive* neuromonitoring was performed symmetrically on the contralateral hemisphere through small burr holes made over the right frontal cortex (10mm paramedian; **Figure 2.1**). Subcortical intracranial oxygen tension ($PbtO_2$, mmHg) and cortical intracranial

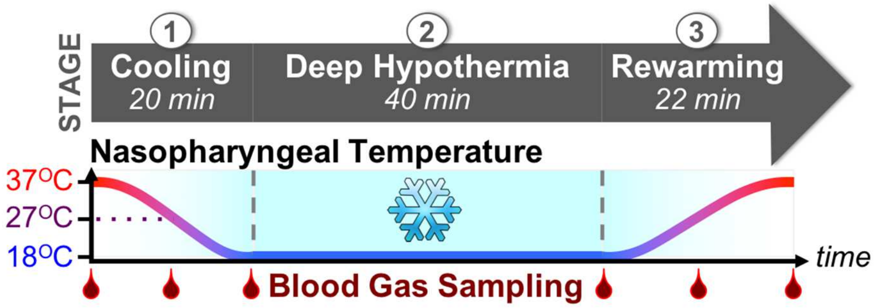

Figure 2.2. Temperature and Blood Gas Sampling Protocol: Each subject underwent three stages of treatment: 1) Induction of deep hypothermia ("Cooling"); 2) Forty minutes of continuous cold perfusion ("Deep Hypothermia"); 3) Recovery from deep hypothermia ("Rewarming"). Arterial and jugular venous blood gas sampling was performed at multiple time-points indicated by red droplets along the time-axis.

temperature (ICT, °C) were measured ~15 mm and ~5 mm, respectively, below the cortical surface (Licox CC1-P1, Integra LifeSciences), and relative cortical cerebral blood flow (rCBF LD, %) was measured with a laser Doppler probe (PeriFlux 5000, Perimed Inc.) secured to the dura matter. A double lumen, 4Fr central venous catheter was placed in the superior vena cava and advanced into the internal jugular bulb for invasive discontinuous sampling of cerebral venous drainage.

C.3. Deep Hypothermia Protocol

Protocols for institution of DH CPB are detailed in the Appendix (**Section F.1**) and closely mirrored clinical practice at our institution (**Figure 2.2**). Subjects were stabilized on CPB at normothermia (NPT=37°C) and baseline measurements acquired for five minutes. Guided by nasopharyngeal temperature, subjects were then cooled at a target rate of 1°C per minute. Once 18°C was attained, subjects were maintained on continuous DH perfusion for 40 minutes. Though continuous CPB with more mild hypothermia is used at the surgeon's discretion, here we aimed to characterize cerebral metabolism across the full range of temperatures currently used in neonates (*i.e.,* from normothermia to a low NPT of 18°C).[83,85] Rewarming to normothermia occurred at a target rate of 1°C per minute. Invasive arterial and venous blood gas sampling (0.3 cc of blood per draw from the bypass arterial outflow and jugular bulb, respectively) occurred at the start of cooling (*i.e.,* baseline, 37°C), midpoint of cooling (27°C), end of cooling (18°C), start of rewarming (18°C), midpoint of rewarming (27°C) and end of rewarming (37°C; **Figure 2.2**). Immediate analysis was facilitated through a point-of-care blood gas analyzer (GEM 3000, Instrumentation Laboratory). Blood pH was optimized by pH-stat management during cooling. During rewarming and while normothermic, blood pH was optimized by alpha-stat.

C.4. Diffuse Optical Techniques

Frequency-Domain Diffuse Optical Spectroscopy (FD-DOS)

Multi-distance FD-DOS was used to continuously measure cerebral tissue oxygen saturation (StO_2, %) and oxygen extraction fraction (OEF). FD-DOS employs radio-frequency intensity-modulated near-infrared light to quantify wavelength-dependent absorption and scattering properties of tissue.[9,10,256]

A customized, commercial instrument (Imagent, ISS Inc.), equipped with four 690, 725, 785, and 830 nm intensity-modulated (110 MHz) diode laser sources and two photomultiplier tube detectors, was coupled to the fiberoptic probe; source-detector separations ranged from 0.75 cm to 3 cm (**Figure 2.1**, *lower left*). For each subject, the source- and detector-fiber coupling coefficients to the tissue were estimated using a phantom-calibration approach[19] and used to correct continuous (10Hz) AC intensity and phase data. Using a multi-distance linear fitting method, absolute absorption and scattering coefficients were calculated for each wavelength from this data. Coefficients were excluded if the linear fit Pearson correlation coefficient was <0.95, and the data-point excluded if more than one of the four scattering or absorption coefficients were excluded. Assuming a cerebral water volume fraction of 75%,[257] the absolute cerebral tissue concentration of oxy-hemoglobin ($[HbO_2]$, μmol/L) and deoxy-hemoglobin ($[Hb]$, μmol/L) was quantified from the absorption coefficient[9] and StO_2 calculated as:

$$StO_2(\%) = \frac{[HbO_2]}{[Hb] + [HbO_2]}. \tag{2.1}$$

Importantly, the FD-DOS technique directly measures the tissue scattering coefficient and eliminates optical absorption measurement errors introduced by physiologic shifts in optical scattering,[11,26] a parameter which cannot be determined by commercial CW NIRS.

Diffuse Correlation Spectroscopy (DCS)

DCS is a photon correlation technique that derives a cerebral blood flow index (BFI, cm^2/s) from quantification of the rapid speckle intensity fluctuations of multiply scattered coherent near-infrared light induced by red blood cell motion.[30–32] DCS measurements were made using a source-detector separation of 2.5 cm, wherein the detected light fields were sensitive to blood flow at an average depth of ~1 cm below the scalp surface.[258]

The DCS light source was a continuous-wave, long-coherence length (>10 m), 785 nm laser (RCL-080-785S, CrystaLaser, Inc). A bundle of eight single-mode detection fibers coupled diffuse light emerging from the head onto two detection arrays of four single-photon-counting avalanche photodiodes (SPCM-AQ4C, Excelitas Technologies, Corp.). Calculation of the intensity autocorrelation curve for each detector was accomplished using a commercial eight-channel correlator board (FLEX03OEM-8CH, Correlator.com) with a fixed integration time of 3 seconds per measurement. The tissue absorption and scattering coefficients, measured concurrently over the same tissue volume by FD-DOS, were used as inputs for the calculation of BFI from the intensity autocorrelation curve, averaged across all co-located detection fibers; the calculation was based on the semi-infinite homogeneous medium approximation of the diffusion correlation equation.[33] Individual measurements were rejected when the average detected photon count rate (light intensity) was <5kHz, when the intensity autocorrelation curve failed to decay below 1.01, or when the fit of the intensity autocorrelation curve had greater than 10% error from the sampled curve.

For validation of DCS against invasive laser Doppler, relative CBF from DCS (rCBF DCS, %) was computed from BFI normalized to the mean baseline BFI value.

C.5. Calculation of Cerebral Metabolic Rate of Oxygen ($CMRO_2$)

Cerebral metabolic rate of oxygen ($CMRO_2$) was calculated using the Fick principle:[259]

$$CMRO_2 = CaO_2 \times OEF \times CBF, \tag{2.2}$$

where CaO_2 is the arterial blood concentration of oxygen and OEF is the cerebral oxygen extraction fraction.

<u>Invasive Calculation of $CMRO_2$</u>

Systemic arterial hematocrit (Hct, %), arterial oxygen saturation (SaO_2, %) and jugular venous oxygen saturation ($SjvO_2$, %) were determined at each blood gas sampling time-point and assumed to estimate cerebral arteriole and venule oxygen content, respectively.[260] Using the piglet-specific mean corpuscular hemoglobin concentration (MCHC) of 32.2g/mL[261] and a mammalian hemoglobin oxygen binding capacity of 1.36mL O_2/g Hgb,[262] OEF and CaO_2 were computed as:

$$OEF = \frac{SaO_2 - SjvO_2}{SaO_2}; \tag{2.3}$$

$$CaO_2 = \frac{1.36\, mL\ O_2}{1g\ Hgb} \times Hct\ (\%) \times MCHC \left(\frac{g\ Hgb}{mL\ blood}\right) \times SaO_2(\%). \tag{2.4}$$

Continuous laser Doppler measurements of relative CBF (rCBF LD, %) were calculated with respect to the mean baseline value such that the baseline blood gas draw at the start of cooling corresponded to an rCBF LD of 100%. For each subsequent blood gas sample, the mean rCBF LD value in the 30 seconds preceding the time of blood gas draw was used. CaO_2 and OEF were also normalized to baseline and combined into an invasive measure of relative $CMRO_2$ (invasive $rCMRO_2$, %):

$$Invasive\ rCMRO_2 = \frac{CaO_2}{CaO_{2,baseline}} \times \frac{OEF}{OEF_{baseline}} \times \frac{rCBF\ LD}{rCBF\ LD_{baseline}}. \tag{2.5}$$

Non-Invasive FD-DOS/DCS Calculation of $CMRO_2$

Non-invasive $CMRO_2$ calculation utilized the baseline arterial blood gas oxygen concentration ($CaO_{2,\ baseline}$, %); this was assumed to remain constant. OEF was derived from FD-DOS-measured cerebral tissue oxygen saturation (StO_2, %), baseline arterial oxygen saturation ($SaO_{2,\ baseline}$, %), and an assumed cerebral arterio-venous mixing fraction (γ) of 0.75:[23,43,263]

$$OEF = \frac{SaO_{2,baseline} - StO_2}{\gamma \times SaO_{2,baseline}}. \tag{2.6}$$

The DCS-measured BFI was used as a surrogate for CBF. As previously described in Roche-Labarbe, et al., baseline CaO_2, OEF, and BFI, were combined into an absolute index of non-invasive $CMRO_2$ ($CMRO_{2,i}$), calculated continuously as:[39,105,264]

$$CMRO_{2,i} = CaO_{2,baseline} \times OEF \times BFI. \tag{2.7}$$

For comparison with invasive quantification, a relative non-invasive $CMRO_2$ (non-invasive $rCMRO_2$, %) was also calculated for each blood gas sample. Corresponding non-invasive OEF and BFI values were calculated as the mean value measured in the 30 seconds prior to blood gas draw. These values were then normalized to their respective baseline blood gas values and, assuming constant CaO_2 and γ, were combined to calculate non-invasive $rCMRO_2$:

$$Noninvasive\ rCMRO_2 = \frac{OEF}{OEF_{baseline}} \times \frac{BFI}{BFI_{baseline}}. \tag{2.8}$$

C.6. Modeling $CMRO_2$ Temperature-Dependence

The van't Hoff Equation has been widely applied in human and animal studies to describe the relationship between temperature and cerebral metabolism.[114,234] Here, the van't Hoff Equation, either reformulated as the empirical Arrhenius equation[113,115] (**Equation 2.9**) or as the Q_{10} temperature coefficient (**Equation 2.11**), is employed as a means to understand and quantify the temperature-dependence of cerebral oxygen metabolism.

Arrhenius Equation Approach

In the Arrhenius relationship (**Equation 2.9**), a rate of reaction (k) depends on temperature (T), the universal gas constant (R), an activation free energy barrier (E_a), and a pre-exponential factor (A) which is related to the reaction attempt frequency:

$$k = Ae^{-\frac{E_a}{RT}}. \tag{2.9}$$

Here we assume this rate of reaction (k) to be the metabolic rate, $CMRO_2$. Rearrangement and substitution yields a linear expression ($y = ax + b$) that models the relationship between $CMRO_2$ and temperature:

$$\ln(CMRO_2) = \frac{E_a}{R}\left(\frac{1}{T}\right) + \ln(A). \tag{2.10}$$

Model parameters, $a = \frac{E_a}{R}, b = \ln(A)$, are obtained from data using linear regression.

Assessment of Model Accuracy

Arrhenius-type approaches such as the version we utilize represent an oversimplification of the physiology, since cerebral metabolism is known to depend on many chemical reactions and other factors.[234] The model selection we have made might be valid, for example, if a single rate-limiting reaction exists for the metabolic process, or if multiple important reactions had roughly the same Free Energy Barrier height. Dense temperature sampling *in vitro* has shown good agreement,[265] however, multiple reports of *in vivo* characterization using sparse sampling methods have found non-Arrhenius or multiphasic behavior, depending on temperature range.[116,235,266] Thus, using continuous quantification of non-invasive $CMRO_{2,i}$ and temperature, we evaluated model robustness *in vivo* by goodness-of-fit of the linear regression (**Equation 2.10**).

Temperature Coefficient, Q_{10}

Most commonly, the temperature-dependence of metabolism has been assessed using the *temperature coefficient,* Q_{10}. This metric is a reduction of the van't Hoff Equation for use under physiologic conditions (*see* **Appendix, Section F.2**). Q_{10} is defined as the relative change in cerebral metabolic rate per 10°C change in temperature. It can be calculated using an initial and subsequent measurement of temperature and $CMRO_2$:

$$Q_{10} = \left(\frac{CMRO_{2,1}}{CMRO_{2,2}}\right)^{\frac{10}{T_1 - T_2}}. \tag{2.11}$$

The Q_{10} for both invasive and non-invasive $rCMRO_2$ measurements were quantified with respect to nasopharyngeal and intracranial temperatures.

C.7. Statistical Analysis

All statistical analyses were carried out using MATLAB 2014a. Summary statistics were reported as mean and standard deviation, unless otherwise noted. Continuous time-series data were synchronized using 15 second epoch averages.

The sufficiency of nasopharyngeal temperature guidance was assessed via the relationship between *non-invasive* nasopharyngeal temperature and *invasive* intracranial temperature, and especially via the functional relationship between non-invasive $CMRO_{2,i}$ and each temperature source during cooling and rewarming (*i.e.,* using the linear form of the Arrhenius equation; **Equation 2.10**). These relationships were individually examined using linear mixed-effects models that incorporated subject-specific random intercept and slope effects to allow for variation in the intercept and slope among individuals. To quantify the potential hysteresis between cooling and rewarming periods, each model included period-specific (*e.g.*, cooling, rewarming) fixed slope, ($\boldsymbol{a}$, $\Delta\boldsymbol{a}$), and intercept, ($\boldsymbol{b}$, $\Delta\boldsymbol{b}$), effects reported as mean and standard error. The modeled relationship during *cooling* is expressed as

$$y = \boldsymbol{a}x + \boldsymbol{b}, \tag{2.12}$$

and the modeled relationship during *rewarming* expressed as

$$y = (\boldsymbol{a} + \Delta\boldsymbol{a})x + (\boldsymbol{b} + \Delta\boldsymbol{b}). \tag{2.13}$$

Parameters $\Delta\boldsymbol{a}$ and $\Delta\boldsymbol{b}$ should be interpreted as the incremental effects of rewarming on the slope ($\boldsymbol{a}$) and intercept ($\boldsymbol{b}$), respectively, of cooling. The goodness-of-fit of these models were evaluated using the coefficient of determination (R^2) of a separate generalized linear regression model with slope and intercept interaction terms for each subject and period.

Validation of non-invasive against invasive $CMRO_2$ measures at discontinuous blood gas sampling time-points was conducted by paired t-test, assuming equal variances and evaluated at a pooled significance level of $\alpha=0.05$ with Bonferroni correction for multiple comparisons. Consequently, the five individual time-point t-tests were evaluated at an adjusted significance level of $\alpha=0.01$. Given a type II error rate of $\beta=0.2$ and an assumed within-subject correlation of 0.875, the analysis was powered to detect a 10% difference in paired observations. Secondarily, to assess the *continuous* relationship between *invasive* rCBF LD versus *non-invasive* rCBF DCS and *invasive* $rCMRO_2$ versus *non-invasive* $rCMRO_2$, linear mixed-effects models with random slope effects were used to quantify the slope relating the change from baseline (ΔrCBF, %; $\Delta rCMRO_2$, %; respectively) between modalities; slope are reported as mean and standard error. To balance continuous rCBF data across the full range of temperatures from normothermia to deep hypothermia, the synchronized time-series data was bin-averaged by corresponding temperature in 1°C intervals from 18°C to 37°C. Linearity was evaluated by the goodness-of-fit, as described above. Finally, agreement between non-invasive measures versus invasive measures of rCBF and $rCMRO_2$ was evaluated by the bias and precision from repeated-measures Bland-Altman analysis.[267,268]

Calculated $CMRO_2$ Q_{10} coefficients for both nasopharyngeal and intracranial temperature-dependence were compared between modalities and to values reported in the literature. Due to their non-normal sample distributions, these results were reported as median and interquartile range (IQR), and intra-subject Q_{10} comparisons were made using the Wilcoxon signed-rank test.

Table 2.1. Summary Statistics

	Start of Cooling	End of Cooling	Start of Rewarming	End of Rewarming
Arterial Blood Gas*				
pH	7.4 (0.1)	7.1 (0.1)	7.1 (0.1)	7.4 (0.1)
pCO2 (mmHg)	45.8 (17.2)	86.5 (16.9)	83.3 (20.5)	39.8 (8.4)
pO2 (mmHg)	278.6 (92.7)	327.3 (58.5)	286.6 (34.8)	181.7 (80.5)
Glu (umol/L)	163.9 (56.1)	156.1 (45.7)	162.9 (37.7)	142.1 (36.7)
Lac (mmol/L)	3.5 (1.2)	3.8 (1.2)	4.1 (1.4)	6.0 (4.9)
Hct (%)	29.9 (2.8)	29.3 (6.4)	33.2 (7.5)	35.6 (7.0)
HCO3 (mmol/L)	29.5 (3.1)	29.6 (3.2)	27.2 (5.0)	24.8 (2.9)
SaO$_2$ (%)	99.2 (2.5)	100.0 (0.0)	99.9 (0.2)	98.8 (2.3)
Invasive Neuromonitoring				
ICT (°C)	34.5 (2.4)	22.6 (2.1)	18.8 (1.1)	30.2 (3.1)
PbtO$_2$ (mmHg)	8.0 (2.7)	8.6 (4.9)	11.1 (8.7)	6.2 (4.9)
SjvO$_2$ (%)*	76.6 (13.2)	95.3 (5.3)	97.3 (2.2)	84.2 (7.3)
OEF	0.23 (0.13)	0.047 (0.053)	0.026 (0.022)	0.15 (0.06)
rCBF LD (%)	100.0 (-)	45.9 (18.1)	41.9 (21.2)	49.4 (9.9)
rCMRO$_2$ (%)	100.0 (-)	9.3 (9.9)	3.4 (3.2)	32.3 (7.9)
Non-Invasive Neuromonitoring				
NPT (°C)	37.3 (0.5)	17.8 (0.3)	18.2 (0.5)	37.3 (0.5)
μ_a (1/cm)				
λ = 690nm	0.17 (0.02)	0.14 (0.02)	0.15 (0.02)	0.19 (0.03)
λ = 725nm	0.14 (0.02)	0.13 (0.02)	0.14 (0.01)	0.16 (0.02)
λ = 785nm	0.14 (0.02)	0.15 (0.03)	0.15 (0.03)	0.16 (0.03)
λ = 830nm	0.15 (0.02)	0.16 (0.03)	0.17 (0.03)	0.17 (0.02)
μ_s' (1/cm)				
λ = 690nm	12.2 (1.7)	11.6 (1.6)	11.7 (1.3)	12.4 (1.6)
λ = 725nm	10.2 (1.5)	10.0 (1.4)	10.1 (1.2)	10.6 (1.6)
λ = 785nm	9.9 (1.5)	10.0 (1.5)	10.0 (1.4)	10.3 (1.7)
λ = 830nm	9.4 (2.0)	10.1 (2.1)	9.9 (1.8)	9.9 (1.7)
THC (μmol/L)	75.3 (9.3)	81.0 (14.0)	85.1 (14.9)	86.1 (12.6)
StO$_2$ (%)	57.2 (5.3)	68.6 (8.7)	69.9 (11.4)	58.6 (6.7)
OEF	0.56 (0.07)	0.41 (0.10)	0.39 (0.14)	0.54 (0.08)
BFI (10^{-8} cm^2/s)	1.2 (1.2)	0.57 (0.55)	0.49 (0.51)	0.69 (0.73)
rCBF DCS (%)	100.0 (-)	50.1 (17.5)	45.9 (28.9)	64.5 (31.6)
rCMRO$_2$ (%)	100.0 (-)	35.8 (8.7)	27.8 (11.4)	63.2 (35.5)

*Values are corrected to 37°C

Abbreviations: Glu – Glucose; Lac – Lactate; Hct – Hematocrit; SjvO$_2$ – internal jugular venous oxygen saturation; rCBF LD – relative cerebral blood flow measured using laser Doppler; ICT – intracranial temperature; PbtO$_2$ – partial pressure of oxygen in brain tissue; StO$_2$ – cerebral tissue oxygen saturation from FD-DOS; BFI – blood flow index measured using DCS; rCBF DCS – relative cerebral blood flow measured using DCS; NPT – nasopharyngeal temperature; THC – total hemoglobin concentration measured using FD-DOS.

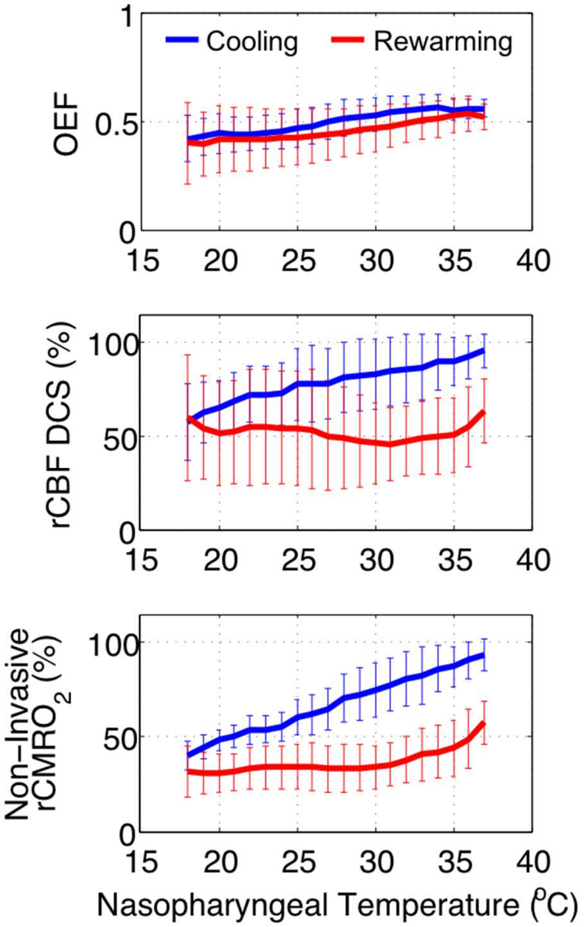

Figure 2.3. Temperature-dependence of non-invasive optical measures of cerebral oxygen extraction fraction, flow, and metabolism during cooling (*blue*) from normothermia to deep hypothermia, and during rewarming (*red*) from deep hypothermia back to normothermia. Mean values across subjects (n=8) are plotted along with standard deviation. Abbreviations: OEF, oxygen extraction fraction; rCBF DCS, DCS measure of relative cerebral blood flow; rCMRO$_2$, relative cerebral metabolic rate of oxygen.

D. Results

Neonatal swine (n=8), with a mean (SD) weight of 4.1 (0.5) kg, were cooled to deep hypothermia in 25.7 (5.3) minutes, maintained at deep hypothermia for 42.6 (1.1) minutes, and subsequently rewarmed to normothermia in 27.2 (7.0) minutes. Summary statistics of experimental parameters are listed in **Table 2.1**.

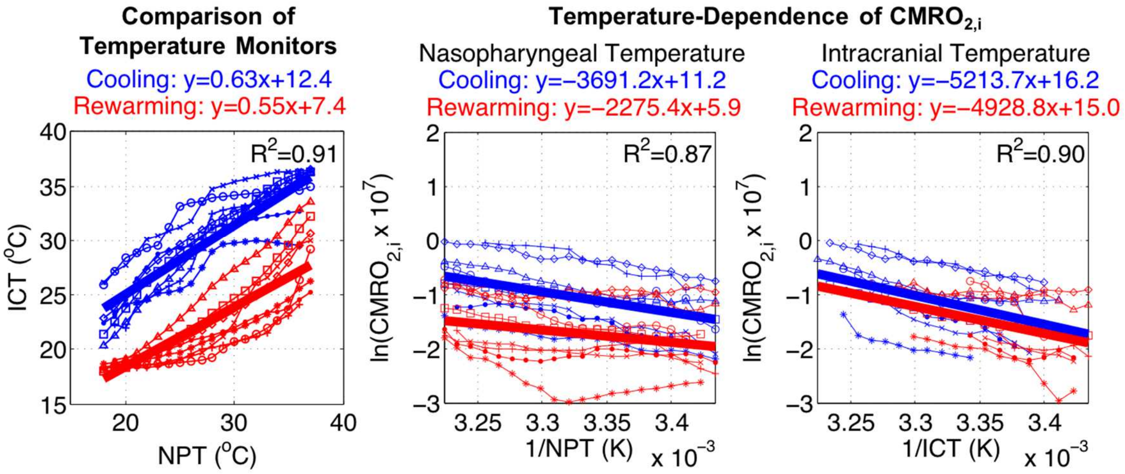

Figure 2.4. (*Left*) Intracranial Temperature Hysteresis: Significant hysteresis of intracranial temperature (ICT) with respect to nasopharyngeal temperature (NPT) during rewarming (*red*) versus cooling (*blue*); rewarming slope $p<0.001$, intercept $p<0.001$. **Non-invasive CMRO$_{2,i}$ Temperature-Dependence**: (*Center*) CMRO$_{2,i}$, with respect to (NPT)$^{-1}$, also demonstrates significant hysteresis in rewarming slope ($p=0.001$) and intercept ($p<0.001$). (*Right*) CMRO$_{2,i}$, with respect to (ICT)$^{-1}$, has improved concordance between rewarming versus cooling; rewarming slope $p=0.647$, intercept $p=0.585$. Thick lines represent fitted linear mixed-effects models; unique symbols connected by thin lines represent individual subject data (n=8).

D.1. Temperature-Dependence of Cerebral Oxygen Metabolism: Comparison of Nasopharyngeal and Intracranial Temperature

Here we examine the impact of nasopharyngeal temperature (NPT) guidance on cerebral metabolic parameters. An example of non-invasive optical time-series data is available in the Appendix (**Section F.3**). The mean and standard deviation of the non-invasive optical measurements of OEF, rCBF DCS, and rCMRO$_2$ with respect to NPT during cooling and rewarming periods are plotted in **Figure 2.3**. Cooling to deep hypothermia caused a decrease in all parameters. During rewarming, OEF values agree with cooling, but a hysteresis in rCBF and rCMRO$_2$ is apparent.

Characterization of the relationship of NPT and intracranial temperature (ICT) provided additional insights regarding the hysteresis (**Figure 2.4**, *left*). A significant slope effect ($\boldsymbol{a}$ = 0.63 [0.06], $p<0.001$) confirmed an association between the two temperature monitors with the effect size < 1 indicating a lag of ICT behind NPT (**Figure 2.4, left)**. Significant rewarming slope ($\Delta\boldsymbol{a}$ = -0.08 [0.01], $p<0.001$) and intercept ($\Delta\boldsymbol{b}$ = -5.0 [0.3], $p<0.001$) effects demonstrated a hysteresis between the two temperature monitors with an increased lag and offset in ICT. The mismatch in ICT between the end of cooling and the beginning of rewarming indicated that, despite NPT indicating attainment of deep hypothermia, the brain had not reached thermal equilibrium.

The NPT-dependence of non-invasive $CMRO_{2,i}$ exhibited a significant slope effect ($\boldsymbol{a}$ = -3.7 [0.4] x10^3, $p<0.001$) which verified an association between metabolism and temperature (**Figure 2.4**, *center*). Confirming the observed hysteresis, rewarming had a significant and dampening effect on slope ($\Delta\boldsymbol{a}$ = +1.4 [0.4] x10^3, $p=0.001$), which suggests metabolism had diminished sensitivity to NPT. Linear regression resulted in a strong coefficient of determination (R^2 = 0.87) and affirms use of Arrhenius-type models for examining cerebral metabolic temperature-dependence at physiologic temperatures. The ICT-dependence of non-invasive $CMRO_{2,i}$ also demonstrated a strong coefficient of determination with linear regression (R^2 = 0.90) and had a significant slope effect ($\boldsymbol{a}$ = -5.2 [1.0] x10^3, $p<0.001$; **Figure 2.4**, *right*). Surprisingly, rewarming did not have a significant effect on slope ($\Delta\boldsymbol{a}$ = +0.3 [0.6] x10^3, $p=0.647$) or intercept ($\Delta\boldsymbol{b}$ = -1.1 [2.1], $p=0.585$).

These results highlight critical insufficiencies of NPT guidance to accurately reflect ICT or metabolic status during DH CPB. Furthermore, they suggest that the presence of cerebral metabolic hysteresis with respect to temperature may be an artifact resulting from use of NPT to approximate ICT.

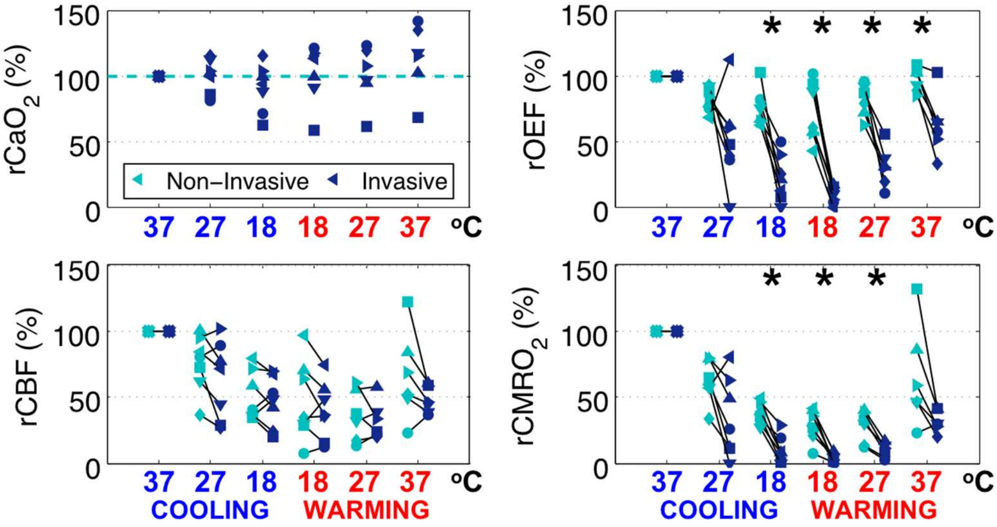

Figure 2.5. Comparison of invasive versus non-invasive tissue sampling at each blood gas time-point demonstrate validity of optical assumptions of arterial concentration of oxygen (CaO_2), agreement of relative cerebral blood flow (rCBF) measurements, but a discrepancy in relative oxygen extraction fraction (rOEF) and relative metabolic rate of oxygen ($rCMRO_2$). Paired data at each time-point are displayed with a unique symbol for each subject (n=7) colored by modality (*i.e.*, non-invasive, *green*; invasive, *blue*), and the x-axis labeled by respective nasopharyngeal temperature with stage designated by color (*i.e.*, cooling, *blue*; rewarming, *red*). Asterisks (*) denote significant differences ($p<0.01$) in paired t-tests between invasive and non-invasive sampling.

D.2. Validation of Non-Invasive Quantification of Cerebral Oxygen Metabolism

The results of models examining discontinuous and continuous repeated measures of $CMRO_2$ parameters to assess differences between invasive and non-invasive modalities are reported. Blood gas analysis was hampered by a machine malfunction in a single animal, resulting in the inclusion of 7 of 8 animals.

Arterial Concentration of Oxygen (CaO_2)

CaO_2 quantified discontinuously from invasive blood gas samples, were used to examine the non-invasive assumption that CaO_2 remained constant through deep hypothermia and recovery to normothermia. Importantly, no significant differences from baseline were observed in relative CaO_2 ($rCaO_2$; **Figure 2.5**, *top left*). From these results, we conclude that the assumption of constant CaO_2 for non-invasive quantification during deep hypothermia was reasonable.

Oxygen Extraction Fraction (OEF)

Significant differences between non-invasive versus discontinuous invasive measures of relative OEF (rOEF; **Figure 2.5**, *top right*) were found at the end of cooling (difference = +53.9% (24.3), p=0.001), start of rewarming (difference = +62.4% (22.6), p<0.001), midpoint of rewarming (difference = +50.8% (20.4), p=0.002), and end of rewarming (difference = +34.2% (17.2), p=0.005). Non-invasive sampling demonstrated consistently greater rOEF across all time-points.

The non-invasive calculation of OEF is derived from baseline blood gas SaO_2 and from continuous non-invasive measurement of cerebral tissue oxygen saturation (StO_2; **Equation 2.6**). Given the limited range in SaO_2 (98.0-100.0%) during cooling and rewarming, significant differences in non-invasive and invasive OEF must be attributed to a disagreement between non-invasive StO_2 and invasive sampling of jugular venous oxygen saturation ($SjvO_2$). Additional analysis of the relationship of StO_2 and $SjvO_2$ is included in the Appendix (**Section F.4**).

Cerebral Blood Flow (CBF)

Non-invasive, continuous rCBF DCS measurement demonstrated good agreement with invasive, continuous rCBF LD. Significant differences were not found at all discontinuous blood gas sampling time-points (**Figure 2.5**, *bottom left*). Examination of the *continuous* relationship between modalities demonstrated that the change from baseline (ΔrCBF, %) of non-invasive DCS significantly predicted (**Figure 2.6**, *left*) invasive laser Doppler with a slope effect of 1.26 [0.15] (p<0.001). Linear regression with subject-specific slope interactions resulted in a good coefficient of determination (R^2 = 0.73), suggesting a strong linear relationship between modalities. Using Bland-Altman

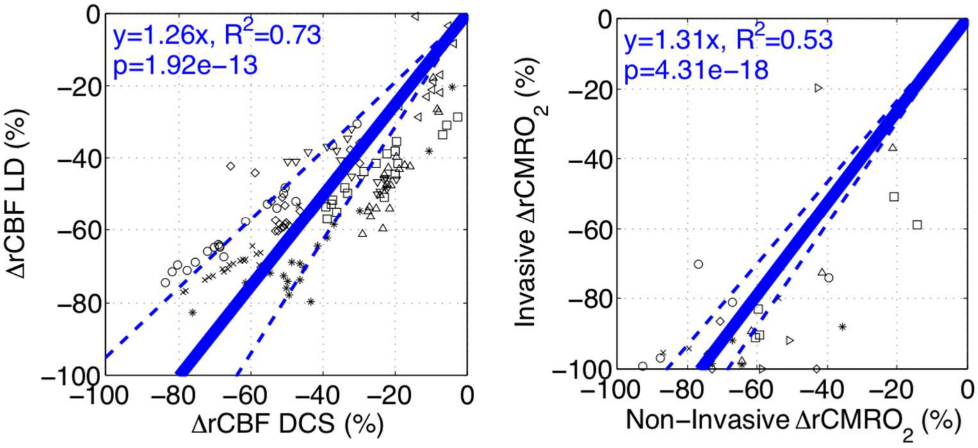

Figure 2.6. Validation of Non-Invasive Diffuse Correlation Spectroscopy (DCS, *left*) and CMRO$_2$ (*right*): Data from individual subjects are indicated by a unique symbol. Measurements of change in relative cerebral blood flow using laser Doppler (rCBF LD, %) and DCS (rCBF DCS, %) are compared using a linear mixed-effects model (n=8; *left*). DCS measurements demonstrate a good linear correlation (fixed slope effect $p<0.001$; $R^2=0.73$) against laser Doppler measurements. Similarly, invasive and non-invasive measurements of rCMRO$_2$ (%) are compared using a linear mixed-effects model (n=7; *right*). Non-invasive rCMRO$_2$ quantification demonstrates a significant association but limited linearity (fixed slope effect $p<0.001$; $R^2=0.53$) against invasive sampling. Fitted linear relationships (*solid line*) with 95% confidence intervals (*dotted line*) are plotted in blue.

analysis, the comparison of mean rCBF (%) between modalities was found to have a bias of -10.0% and precision of 13.1% (**Appendix, Section F.5**). These findings support the use of DCS for non-invasive measurement of rCBF during DH CPB.

Cerebral Metabolic Rate of Oxygen (CMRO$_2$)

Non-invasive versus invasive relative CMRO$_2$ measured discontinuously exhibited significant differences at the end of cooling (difference = +26.9% (9.7), p<0.001), start of rewarming (difference = +25.1% (11.7), p=0.001), and midpoint of rewarming (difference = +18.3% (8.1), p=0.003; **Figure 2.5**, *bottom right*). Due to the dependence of CMRO$_2$ on OEF, significant differences in rOEF directly contributed to differences in rCMRO$_2$ whereby non-invasive sampling reflected higher levels of metabolism versus invasive sampling.

Examination of the continuous relationship between modalities by linear mixed-effects model analysis demonstrated that non-invasive $\Delta rCMRO_2$ (%) significantly predicted (**Figure 2.6**, *right*) invasive $\Delta rCMRO_2$ (%) with a slope effect of 1.31 [0.07] ($p<0.001$); however linear regression resulted in only a fair coefficient of determination ($R^2=0.53$) suggesting underlying non-linearity. Using Bland-Altman analysis, agreement of $rCMRO_2$ between modalities was found to have a bias of -25.8% and precision of 12.5% (**Appendix, Section F.4**). Despite modest quantitative agreement, these findings show a highly significant association between non-invasive and invasive $rCMRO_2$ measurements; this association, in turn, supports use of non-invasive measurements as an indicator of cerebral status.

CMRO$_2$ Temperature Coefficient (Q$_{10}$)

Computed $CMRO_2$ temperature coefficient Q_{10} derived from invasive sampling differed significantly from that of non-invasive sampling, whether assessed with respect to nasopharyngeal temperature (non-invasive versus invasive median [IQR]: 2.0 [1.6, 2.3] versus 4.9 [3.6, 6.3], $p=0.016$) or intracranial temperature (non-invasive versus invasive median [IQR]: 2.5 [2.0, 3.5] versus 9.0 [6.9, 11.0], $p=0.016$). This finding further affirms our discrepant findings at individual blood gas sampling time-points. As may be expected from the presence of significant temperature hysteresis, Q_{10} based on intracranial temperature was significantly different from Q_{10} based on nasopharyngeal temperature, *i.e.,* whether measured non-invasively (NPT versus ICT median [IQR]: 2.0 [1.6, 2.3] versus 2.5 [2.0, 3.5], $p=0.016$) or invasively (NPT versus ICT median [IQR]: 4.9 [3.6, 6.3] versus 9.0 [6.9, 11.0], $p=0.016$). Regardless of metabolic sampling method, sensitivity to nasopharyngeal temperature was lower than to intracranial temperature.

E. Discussion

Continuous, non-invasive optical metabolic neuromonitoring using FD-DOS combined with DCS permits understanding of the physiologic alterations of cerebral metabolism that occur during therapeutic hypothermia. This approach has the potential to address critical shortfalls in conventional temperature guidance of hypothermia, as well as to enable individualized neuroprotective strategies. The present study takes important steps towards this goal.

E.1. Temperature-Dependence of Cerebral Oxygen Metabolism: Comparison of Nasopharyngeal and Intracranial Temperature

Nasopharyngeal temperature is an established source of guidance for DH CPB management[74] and has been found, among other non-invasive sites of core temperature measurement, to best approximate cerebral temperature.[87] However, our data adds to mounting evidence that nasopharyngeal temperature does not adequately reflect intracranial temperature, nor the metabolic state of the brain.[269,270] This finding is evident from the metabolic hysteresis with respect to nasopharyngeal temperature between cooling and rewarming periods, and in the significantly different temperature coefficients exhibited by nasopharyngeal versus intracranial temperature. The finding that intracranial temperature has more concordant metabolic temperature-dependence between cooling and rewarming periods is supported by prior *in vitro* observations of the reversibility of hypothermic metabolic inhibition.[265] The continued decline of intracranial temperature following cooling indicates the clinical cooling interval used was insufficient for thermal equilibrium and underscores the importance of directly measuring the metabolic state of the brain in lieu of using nasopharyngeal temperature as a surrogate.

By coupling continuous FD-DOS/DCS measurements of cerebral oxygen metabolism with continuous temperature measurements during deep hypothermia, we were additionally able to examine the validity of temperature-dependent models for the metabolic rate based on the Arrhenius equation. These models were consistent with our data, whether using nasopharyngeal temperature (R^2=0.87) or intracranial temperature (R^2 = 0.90). Our results support the continued use of Q_{10} to characterize the temperature-dependence of cerebral oxygen metabolism.

E.2. Validation of Non-Invasive Quantification of Cerebral Oxygen Metabolism

Non-invasive $rCMRO_2$ significantly predicted *invasive* $rCMRO_2$ ($p<0.001$). However, we found significant discrepancies in measured values with a bias of -25.8% and precision of 12.5%. This mismatch is discussed, and rationalized, with respect to each component of the $CMRO_2$ calculation below.

Arterial Concentration of Oxygen (CaO_2)

A critical assumption of non-invasive $CMRO_2$ quantification is that CaO_2 remains constant from baseline. While increases in CaO_2 are expected during hypothermia,[271] avoidance of hyperoxia during cardiopulmonary bypass has been established.[272] Fortuitously, oxygen administration is intentionally adjusted during hypothermia to maintain constant arterial blood oxygen tension. In-line with these recommendations, we found that only the last sampling time-point after recovery to normothermia demonstrated a significant difference from baseline. Thus, the assumption of constant CaO_2 for non-invasive quantification during deep hypothermic cardiopulmonary bypass seems reasonable and is concordant with invasive sampling.

Oxygen Extraction Fraction (OEF)

Absolute oxygen extraction fraction (OEF) was found to differ significantly between invasive and non-invasive sampling methods at all time-points. We determined that this effect resulted from a disagreement between optically-measured cerebral tissue oxygen saturation (StO_2), and the compartment model computation of StO_2 via $StO_2 = (1-\gamma)SaO_2 + \gamma SjvO_2$, wherein an arterio-venous mixing fraction of $\gamma = 0.75$ was assumed.[43,263] In fact, StO_2 was consistently lower than $SjvO_2$, thus violating a necessarily positive γ. This phenomenon has been reported in the context of CW NIRS instruments and FD-DOS measurements in animals models[19,273] and human subjects,[23,239] and remains to be further explored in future studies. Our findings support the reproducibility of this phenomenon and sheds further light on the issue.

The use of jugular venous sampling in this study was based on its wide utilization in pediatric cardiac surgery for this purpose[79,274] and for comparison with non-invasive cerebral oximetry.[23,275–277] Prior reports of jugular venous sampling in swine models of cardiopulmonary bypass agree with our observations. In Sasaki et al., $SjvO_2$ were calculated from reported OEF as 74.5±7.1% at normothermia and 89.5±4.2% at 18°C in comparably-aged neonatal piglets.[273] In slightly older (3-4 wk) and larger piglets (9.4±0.8kg), Walther et al. reported $SjvO_2$ of 86-88% at normothermia, 91% at a body temperature of 25°C, and 93% at a body temperature of 18°C.[252] While these values are in the range of our $SjvO_2$ measurements at normothermia (76.6±13.2%) and at deep hypothermia (95.3±5.3%), further comparison with sagittal sinus sampling suggests these measurements may have been affected by reported limitations of jugular venous sampling to access cerebral venous saturation.[278]

Animal studies wherein sagittal sinus oxygen saturation ($SssO_2$) was directly sampled during hypothermic cardiopulmonary bypass show consistently lower values than reported $SjvO_2$. Two observations in moderately larger piglets (5-13 kg) reported an $SssO_2$ of 75±10% at normothermia and 85±5% at deep hypothermia (18-20°C).[237,251] While normothermic values are comparable to our observations, hypothermic saturations are markedly lower . These comparisons indicate that internal jugular venous sampling overestimates sagittal sinus saturations, resulting in an underestimation of true cerebral OEF in pediatric swine models. We believe this to be the primary source of error in our invasively quantified OEF and, subsequently, $CMRO_2$.

Probable physiologic mechanisms that could elevate $SjvO_2$ with respect to $SssO_2$ include systemic venous contamination of jugular venous sampling due, in-part, to the logistical difficulty of advancing a catheter into small neonatal vessels. Contributions from the external jugular vein or superior vena cava would reflect higher saturations due to lower somatic oxygen utilization rates compared to the brain. This hypothesis is corroborated by central venous saturations of ~75% at normothermia and 98±2% at 18°C in Cavus et al.;[251] our $SjvO_2$ agrees at baseline and is only ~3% lower at deep hypothermia. Future studies conducted in neonatal swine should be wary of systemic contributions with this sampling method that may inaccurately diminish cerebral OEF.

Cerebral Blood Flow (CBF)

Significant agreement was observed between invasive laser Doppler (LD) and non-invasive DCS measurement of cerebral blood flow throughout deep hypothermia. Our invasive data, in particular, advances recent cross-validation of DCS with transcranial Doppler ultrasound.[37] In principle, quantitative variation between LD and DCS can be attributed to regional variability in metabolic and cerebrovascular response to hypothermia, which has been previously reported,[279–281] and can also result from extracerebral contributions to the optical signal.[282–284] Measuring tissue thickness post-mortem, we found ~0.5 cm of superficial tissue (*e.g.*, skull, scalp) above the brain. The potential contribution from this tissue should be explored in future studies using advanced multi-layered optical extraction.

Cerebral Metabolic Rate of Oxygen ($CMRO_2$)

Taken in total, non-invasive optical measurement of $CMRO_2$ demonstrated lower temperature-sensitivity and higher residual metabolic rates at deep hypothermia than invasively sampled $CMRO_2$. As discussed above, we believe this to be a direct result of systemic contributions to invasive jugular venous sampling. For further validation, calculated Q_{10} temperature coefficients were compared to those reported in the literature.

In studies utilizing non-invasive temperature methods and jugular venous sampling, Greeley et al. reported an average Q_{10} of 3.65 in neonates and children, and McCullough et al. reported a Q_{10} of 2.3 in adults.[79,81] While these measurements are potentially confounded by pathologic conditions necessitating the use of hypothermic cardiopulmonary bypass, plausibility is provided for our non-invasive (Q_{10} = 2.0) versus invasive (Q_{10} = 4.9) measurements with respect to nasopharyngeal temperature.

In healthy animal models with invasive intracranial temperature and sagittal sinus sampling, Michenfelder, et al. saw a Q_{10} of 2.23 for mild hypothermia (ICT between 37°C and 27°C) and 4.53 for deep hypothermia (27 to 14°C) in canines; CBF was measured using a flow-through electromagnetic flow probe placed in the sagittal sinus.[235] Using both radioactive and fluorescent microspheres for CBF determination, Erlich et al. observed a Q_{10} of 2.46 with a 95% CI of 2.1 to 2.9 (38°C to 8°C) in piglets ranging in weight from 7-13kg.[237] These values support the validity of our non-invasive metabolic measurements, which exhibited a Q_{10} of 2.5 with respect to intracranial temperature, versus our invasive measurements (Q_{10} = 9.0) which incorporated jugular venous sampling. In sum, despite significant differences between our non-invasive and invasive sampling methods, we are confident that our non-invasive metabolic measurements are in agreement with prior studies of cerebral metabolic temperature-response and hold tremendous clinical promise to measure an individual patient's $CMRO_2$.

E.3. Limitations of Animal Model

Several considerations affect the interpretation of our animal model results for application to neonatal cardiac patients. First, we utilized only female animals; in light of reported sexual dimorphisms with respect to brain development[285] and tolerance to neurological injury,[286,287] further study is required to understand potential sex differences in metabolic temperature-dependence. Additionally, piglet resting core temperatures are slightly higher than human neonates (38.5°C vs. 36.5°C).[280,288] The impact of relative hypothermia in the animal model may have resulted in lower metabolic values than an animal at natural baseline. Variation in anesthetic management, rate and duration of temperature derangement, and the use of circulatory arrest among pediatric cardiac surgical practices may also impact generalizability.[248,289,290] Notably, the oxygen binding affinity of swine hemoglobin has been shown to be significantly lower than that of human hemoglobin.[291] This effect could account for the lower baseline cerebral oxygen tissue saturations measured versus baseline values in human subjects. Furthermore, there is less impact of cooling on oxygen binding affinity.[292] Therefore, greater changes in cerebral metabolism (*i.e.,* larger temperature coefficients) may be observed in humans than those measured here.

E.4. Clinical Applications of Cerebral Metabolic Monitoring during Therapeutic Hypothermia

Clinical imaging modalities that permit access to cerebral metabolism include stand-alone PET, which typically requires the injection or inhalation of radioactive tracers such as $^{15}O\text{-}H_2O$ and ^{18}F-FDG for glucose metabolism[293] or $^{15}O_2$ gas for oxygen metabolism,[294] and stand-alone MRI,[295] which uses a combination of arterial spin labeling or phase-contrast mapping for CBF and calibrated blood-oxygen-level-dependent T2* signal mapping for oxygenation. More recently, integrated PET/MRI paradigms that decrease the invasive vascular access requirements of stand-alone PET have been demonstrated.[296] These modalities have profoundly impacted clinical care, as well as our understanding of developmental and pathologic alterations in cerebral metabolism; however, extensive patient transport and operating room requirements, the incremental ionizing radiation exposure of PET, and the prolonged durations and limited throughput associated with MRI data acquisition prohibit real-time, intraoperative monitoring, particularly in neonates.

FD-DOS/DCS sacrifices spatial resolution and sensitivity for temporal resolution and portability that, as specifically demonstrated in the present work, permit real-time guidance during procedural hypothermia. Frequently, neonatal surgical protocols utilize deep hypothermia for neuroprotection during subsequent circulatory arrest. Temperature of initiation and what duration of circulatory arrest is safe remain controversial.[74,91,95] Precise determination of residual cerebral metabolism using diffuse optics could be used to individually guide cooling to adequate levels of cerebral metabolic suppression as well as provide a subject-specific estimate of safe arrest duration based on rate of $[HbO_2]$ depletion in cerebral tissue. Alternatively, mild hypothermia has also demonstrated therapeutic potential to improve mortality[297,298] and neurological[299] and neurodevelopmental outcomes[300] in infants with hypoxic-ischemic encephalopathy. Non-invasive optical CW NIRS and FD-DOS/DCS have already been used at the bedside in these infants to examine alterations in cerebral autoregulation[301] and metabolism.[302] We anticipate that our findings will enable and motivate closer examination of the magnitude and rate of hypothermia-induced cerebral metabolic suppression and neurological outcomes in these patients.

E.5. Conclusions

This study identifies critical limitations in conventional nasopharyngeal temperature guidance during deep hypothermic cardiopulmonary bypass in neonates, and it provides strong evidence for the validity and utility of non-invasive diffuse optical measurements of cerebral oxygen metabolism to address these limitations. Continuous measurements throughout cooling and rewarming enabled novel high-fidelity determination of metabolic temperature-dependence *in vivo* and validation of Arrhenius-type models (*i.e.,* the van't Hoff Law and Q_{10}). The relationship between non-invasive $CMRO_2$ and nasopharyngeal temperature demonstrated a problematic hysteresis between cooling and rewarming periods. The finding that intracranial temperature-dependence improved concordance suggests that nasopharyngeal temperature inadequately reflects cerebral metabolic state and may be a significant source of uncertainty in the clinical guidance of hypothermia for brain protection. The application of non-invasive FD-DOS/DCS for direct quantification of cerebral oxygen metabolism thus offers promise for improved guidance of therapeutic hypothermia and for mitigation of neurological injury in vulnerable pediatric populations.

F. Appendix

F.1. Neonatal Swine Model

One-week-old, healthy female Yorkshire piglets (n=8; Meck Farms, Lancaster, PA) were included in this study. Animals were housed in the Abramson Research Center Large Animal Facility for a maximum of 7 days prior to study with daily care monitoring by a trained Division of Veterinary Resources technician. All animals underwent identical care and study procedures as described.

Anesthesia

On the morning of study, animals were fasted a minimum of 2 hours prior to receiving a pre-medicated intramuscular injection of ketamine (20 mg/kg) for comfort followed by weighing and transport to operating room within the same facility. Prior to intubation, piglets were administered 4% inhaled isoflurane in 100% FiO2 via snout mask until abolishment of response to reflexive pinch stimulus. Animals were then intubated with a 3mm endotracheal tube with in-line capnometer; placement was confirmed by normative end-tidal CO_2 tracings. Subsequently, a maximum of 1.5% inhaled isoflurane was used for maintenance of anesthesia with depth of anesthesia confirmed by heart rate, blood pressure, mandibular jaw tone, and absence of withdrawal response to toe pinch. Ventilator settings were maintained within a peak expiratory pressure of 6cm H2O, and tidal volumes (8-12 ml/kg) and respiratory rate titrated to maintain end-tidal CO2 between 38-42 mmHg.

Surgical Preparation

Piglets were initially positioned prone. Then neuromonitoring and rectal and nasopharyngeal temperature probes for guidance of hypothermic therapy were placed and secured. A heating pad and blanket were placed along the dorsum and ventral aspects and were used as needed to maintain normothermia.

Piglets were then positioned supine, neuromonitoring probe placements optimized, and limbs secured. The right femoral artery and vein were exposed and cannulated to permit pressure transduction and vascular access, respectively. Intravenous fentanyl (25-200 μg/kg/min) and dexmetetomidine (0.5-2.0 μg/kg/min) were initiated and titrated as needed for depth of anesthesia. A standard median sternotomy incision was performed, along with thymectomy, pericardiotomy, and exposure of the great vessels for cannulation. Systemic heparin 200 IU/kg was then administered directly into the right atrium. Additional heparin was used as needed to ensure an activated clotting time (ACT) greater than 400 seconds prior to establishment of cardiopulmonary bypass.

Cardiopulmonary Bypass (CPB)

The cardiopulmonary bypass circuit was primed with 200 ml of Plasmalyte and 300 ml of donor swine whole blood added to establish a hematocrit level of 30%. The prime volume was treated with 500 units of heparin, 1 mEq + 5 mEq/kg of sodium bicarbonate, 1mg/kg of Lasix, and 450 mg of calcium gluconate and swept at 0.5L/min for 2 minutes. Circuit lines were connected via two 3/16” x ¼” connectors and de-aired. The ascending aorta and right atrial appendage were cannulated with a 10-Fr arterial cannula and a 20-Fr single stage venous cannula, respectively. Cardiopulmonary bypass flows were steadily increased to target baseline flows of 150 ml/kg/min and continuously monitored via an ultrasonic flow probe affixed to the arterial outflow. The cardiopulmonary bypass heater/cooler unit was used as necessary to stabilize nasopharyngeal temperature at normothermic baseline (37°C) and for all subsequent periods of cooling and warming as described in the following protocol for deep hypothermia.

Deep Hypothermia (DH) Protocol

Therapeutic deep hypothermia (DH) protocol closely mirrored clinical practice at our institution (*see* **Methods**; **Figure 2.2**). DH was directed using nasopharyngeal temperature. Following stable normothermia for a minimum of 5 minutes, subjects were cooled to 18°C at an approximate rate of 1°C per minute by maintaining an 8-10°C gradient between the cooling bath and venous return temperature. Subjects remained under DH with continuous perfusion for a total of 40 minutes, at which point rewarming to normothermia occurred at an approximate rate of 1°C per minute.

Arterial and jugular venous blood sampling (0.3 cc of blood per draw), as described (*see* **Methods**; **Figure 2.2**), were analyzed for pH, pCO_2 (mmHg), pO_2 (mmHg), Na+ (mmol/L), K+ (mmol/L), Ca++ (mmol/L), glucose (mg/dL), lactate (mmol/L), and hematocrit (%) and derivation of HCO_3- (mmol/L), base excess (mmol/L), and SO_2 (%) using the point-of-care blood gas analyzer (GEM 3000, Instrumentation Laboratory, Blauvelt, NY, USA). Per clinical protocol at the Children's Hospital of Philadelphia (CHOP), blood pH was optimized by pH-stat management during cooling, whereby increased concentrations of carbon dioxide were added to the oxygenator as necessary to maintain a temperature-corrected pCO_2 of 40 mmHg resulting in a blood pH of 7.4; during rewarming and while normothermic, the blood pH was optimized by alpha-stat (*i.e.,* maintenance of pCO_2 at 40 mmHg without temperature correction).

Mean arterial pressure was maintained between 40-70 mmHg with titration of intravenous nitroglycerin (0.25-20 μg/kg/min), milrinone (50 μg/kg bolus, 0.25-0.75 μg/kg/min infusion), or nicardipine (0.5-3.0 μg/kg/min) as necessary for hypertension. Significant changes in blood pressure, blood gas analytes, hyperglycemic status and any evidence of subject discomfort were treated immediately. At the conclusion of the study, animals were euthanized using 20 mEq/kg of potassium chloride.

F.2. Derivation and Interpretation of Q_{10}

The *temperature coefficient,* Q_{10}, can be expressed as:

$$Q_{10} = \left(\frac{CMRO_{2,1}}{CMRO_{2,2}}\right)^{\frac{10}{T_1 - T_2}}. \tag{2.A1}$$

Calculation of Q_{10} requires only two measurement points (*i.e.,* knowledge of a temperature change and corresponding relative change in $CMRO_2$), and intuitively it describes the relative impact of temperature change on metabolism. This scalar coefficient formulation can be directly derived from the definite integral of the van't Hoff Equation or from simple substitution per the Arrhenius Equation. By the Arrhenius Equation,

$$k = Ae^{-\frac{E_a}{RT}}, \tag{2.A2}$$

a rate of reaction (k) depends on temperature (T), the universal gas constant (R), an activation free energy barrier (E_a), and a pre-exponential factor (A) which is related to the frequency (*i.e.*, incidence) of reaction. Using $CMRO_2$ as the rate of reaction (k), the relationship between the measured $CMRO_2$ at two different temperatures, T_1 and T_2, is easily shown to be exponentially related to the product of a scalar constant (E_a/R) and the difference of the inverse of the two temperatures:

$$\frac{CMRO_{2,1}}{CMRO_{2,2}} = e^{-\frac{E_a}{R}\left(\frac{1}{T_1} - \frac{1}{T_2}\right)}. \tag{2.A3}$$

Simple algebraic rearrangement yields the following expression incorporating the constants E_a, R, and the temperatures, T_1 and T_2:

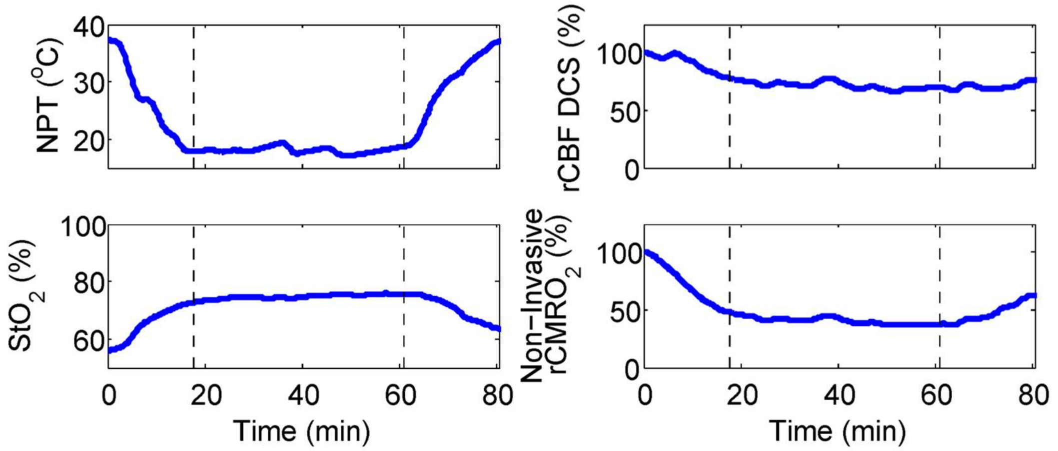

Figure 2.A1: Continuous Cerebral Hemodynamics During Deep Hypothermia: Continuous measurements of cerebral tissue oxygen saturation (StO_2, %) measured using FD DOS, relative cerebral blood flow (rCBF) measured using DCS, and the combined measure of relative cerebral metabolic rate of oxygen ($rCMRO_2$) during cooling, forty minutes of continuous deep hypothermic perfusion, and rewarming. Decrease in temperature causes an increase in StO_2, decrease in rCBF, and decrease in $rCMRO_2$.

$$Q_{10} = e^{\frac{E_a}{R}\left(\frac{10}{T_1 T_2}\right)}. \tag{2.A4}$$

Assuming a metabolic system is accurately modeled by the Arrhenius equation, this result implies that Q_{10} may be interpreted as a scalar constant, as long as the temperature difference between T_1 and T_2 is relatively small compared to the absolute baseline temperature, T_1, in Kelvin (*i.e.,* $|T_1 - T_2| \ll T_1$ such that $\frac{1}{T_1 T_2} \approx \frac{1}{T_1^2}$). These are reasonable assumptions for studies of cerebral metabolism given the narrow range of normative baseline body temperatures [288]. As a result, even without measurement of absolute metabolism, comparison of the Q_{10} between such studies provides direct insight regarding differences in activation energy E_a of each respective metabolic system.

F.3. Example Cerebral Hemodynamic Time-Series Data

Table 2.A1. Oxygen Saturation Sampling and Calculated OEF

	Cooling Start	Cooling Mid	Cooling End	Rewarm Start	Rewarm Mid	Rewarm End
SaO_2, %	98.9 (3.0)	100.0 (0.0)	100.0 (0.0)	99.9 (0.2)	99.8 (0.4)	98.3 (2.7)
$SjvO_2$, %	74.1 (14.8)	88.3 (6.6)	93.7 (5.7)	97.2 (2.6)	92.0 (4.8)	82.5 (8.5)
StO_2, %	55.7 (4.2)	63.3 (5.5)	66.1 (8.0)	67.9 (12.3)	62.9 (7.6)	56.4 (6.1)
$eqSbtO_2$, %	11.0 (9.0)	10.8 (3.9)	20.0 (11.3)	37.6 (28.8)	23.9 (29.5)	12.4 (14.3)
$OEF_{optical}$	0.58 (0.06)	0.48 (0.07)	0.44 (0.09)	0.42 (0.16)	0.48 (0.10)	0.57 (0.08)
$OEF_{blood\ gas}$	0.25 (0.15)	0.12 (0.07)	0.06 (0.06)	0.03 (0.03)	0.08 (0.04)	0.16 (0.07)
p-value*	<0.001	<0.001	<0.001	<0.001	<0.001	<0.001

*p-value of two-sample t-test between $OEF_{optical}$ and $OEF_{blood\text{-}gas}$

Non-invasive frequency-domain diffuse optical spectroscopy (FD DOS) and diffuse correlation spectroscopy (DCS) enables concurrent and continuous measurement of cerebral hemodynamics and metabolism. A case example of these measurements in shown in **Figure 2.A1** with corresponding nasopharyngeal temperature (NPT) during induction of deep hypothermia, continuous deep hypothermic perfusion, and rewarming back to normothermia.

F.4. Examination of Cerebral Oxygenation

Cerebral tissue oxygen saturation (StO_2) is expected to be higher than cerebral venous oxygen saturation. However, at all blood gas sampling time-points, $SjvO_2$, our invasive surrogate measure of cerebral venous saturation, was consistently higher than non-invasively measured StO_2 **(Table 2.A1)**.

A linear mixed-effects model (**Figure 2.A2, *left***) was used to quantify the relationship between the repeated measures of $SjvO_2$ and StO_2. A significant ($p<0.001$) and positive slope effect illustrates a strong positive association between the two values; however, the mean +27.4% bias between the two modalities from Bland-Altman analysis (**Figure 2.A2, *right***) with the zero-difference line outside the 95% limits of agreement

([+10.5%, +44.4%]) are evidence of a discrepancy from the theoretical compartment model computation of StO_2.[43,263]

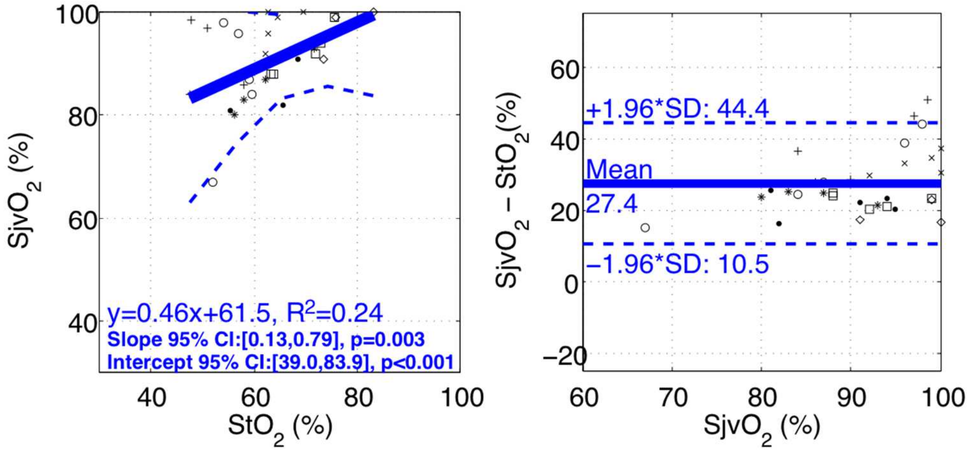

Figure 2.A2: Linear Mixed-Effects Model (*left*) and Bland-Altman Analysis (*right*) of Invasive versus Non-Invasive Oxygen Saturation Measurements – Invasive oxygen saturation derived from jugular venous blood gas sampling ($SjvO_2$) and non-invasive tissue oxygen saturation derived from FD-DOS sampling (StO_2) in n=7 subjects demonstrates a significant (p=0.003) and positive (slope [95% CI] = 0.46 [0.13, 0.79]) association and a bias and precision of +27.4% and 8.7%, respectively.

To further elucidate cerebral oxygen status, our secondary invasive measure of oxygen, $PbtO_2$, was used in combination with invasive intracranial temperature, pH, HCO_3, and base excess, analyzed from corresponding blood gas sampling, to estimate equilibrated vascular saturation of brain tissue ($eqSbtO_2$, %).[303,304] This data is listed in **Table 2.A1** and mean and standard deviation plotted alongside non-invasive and invasive saturation data in **Figure 2.A3**). Interestingly, the response to hypothermia and the absolute value of StO_2 during hypothermia is more comparable to $eqSbtO_2$ than the response and absolute value of $SjvO_2$. This observation suggests that non-invasive StO_2 measurements may reflect brain oxygen content better than blood gas sampling from the jugular vein.

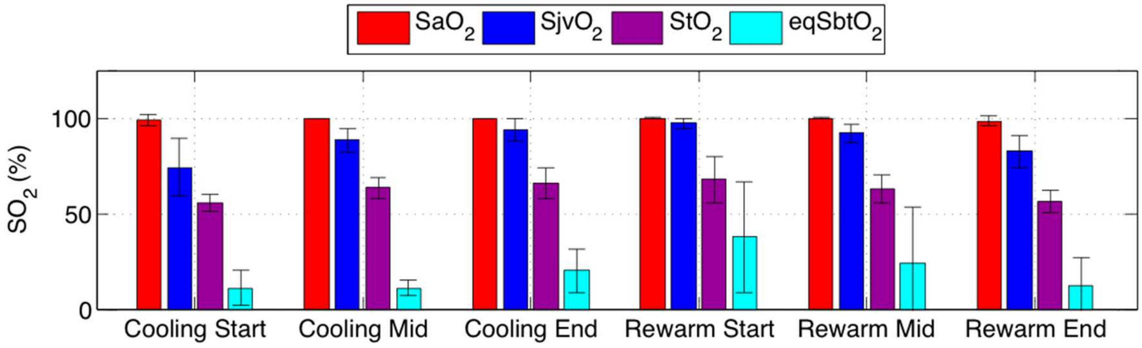

Figure 2.A3: Comparison of Invasive and Non-Invasive Oxygen Saturation Measurements: Mean and standard deviation across subjects (n=7) of oxygen saturation measurements derived from arterial (*red*) and jugular venous (*blue*) blood gas sampling (SaO_2 and $SjvO_2$, respectively), FD-DOS sampling (StO_2; *purple*), and invasive $PbtO_2$ measurements ($eqSbtO_2$; *cyan*), are presented for each blood gas sampling time-point.

F.5. Bland-Altman Repeated-Measures Analysis

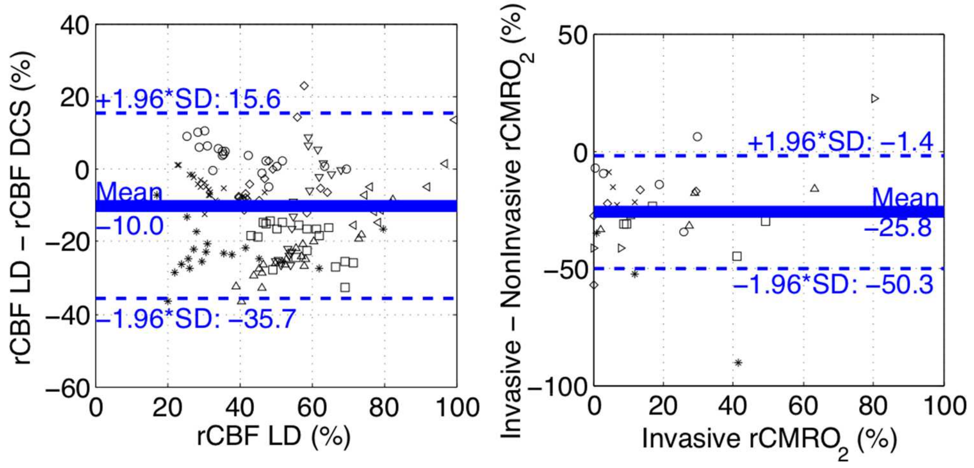

Figure 2.A4: Bland-Altman Analysis of Non-Invasive Diffuse Correlation Spectroscopy (DCS; *left*) and $rCMRO_2$ (*right*): Data from individual subjects is indicated by a unique symbol. DCS measurements of relative cerebral blood flow (rCBF DCS) demonstrated a mean bias of -10.0% and precision of 13.1% (95% limits of agreement = [-35.7%, 15.6%]) against laser Doppler (rCBF LD; n=8). Non-invasive $rCMRO_2$ quantification demonstrated a mean bias of -25.8% and precision of 12.5% (95% limits of agreement = [-50.3%, -1.4%]) against invasive $rCMRO_2$ measurements (n=7).

CHAPTER 3: IMPACT OF DEEP HYPOTHERMIC CIRCULATORY ARREST ON NON-INVASIVE DIFFUSE OPTICAL MEASUREMENT OF CEREBRAL OXYGEN METABOLISM IN NEONATAL SWINE

A. Abstract

Extended durations of deep hypothermic circulatory arrest (DHCA) during complex surgical repair of congenital heart defects in neonates is used to improve tolerance to hypoxic-ischemic injury. However, ~50% of infants still exhibit post-operative neurological injury. Using real-time non-invasive diffuse optical monitoring techniques, we aimed to perform novel quantification of the impact of DHCA on cerebral oxygen metabolism, and the persisting effects following reperfusion in healthy neonatal swine. Twenty-four piglets (3-5 kg) were placed on cardiopulmonary bypass and were randomized to undergo deep hypothermia with continuous perfusion (DHCP; n=10) or with circulatory arrest (DHCA; n=10) for 40 minutes; in addition four piglets comprised a normothermic control group (n=4). Oxygen extraction fraction (OEF) and an index of cerebral metabolic rate of oxygen ($CMRO_{2,i}$) were derived from the optical measurements continuously. During DHCA, we determined that OEF reached a maximum at a mean (SD) time of 19.6 (6.7) minutes, indicating complete oxygen utilization. After 40 minutes of deep hypothermia, the arrested DHCA group demonstrated significantly increased OEF over the DHCP group ($p<0.001$). During rewarming following reperfusion, the DHCA group also demonstrated a significant hysteresis in the $CMRO_{2,i}$ temperature-dependence; *i.e.,* metabolism exhibited diminished temperature sensitivity compared to cooling ($p<0.001$). The findings present novel continuous quantification of cerebral metabolic status both during and after DHCA

that demonstrates the diagnostic potential of non-invasive diffuse optical monitoring; moreover, this information may offer a prognostic indicator of neurological injury.

B. Introduction

The optimal cerebral perfusion strategy for infants requiring aortic arch reconstruction remains a contentious topic across pediatric cardiac centers. Specifically, the ability of the infant brain to tolerate deep hypothermic (DH) cardiopulmonary bypass (CPB) and circulatory arrest during the course of aortic arch repair is not well understood.[78,94] Deep hypothermic circulatory arrest (DHCA) is a strategy characterized by an extended period of circulatory arrest following venous vacuum-assisted exsanguination and perfusion-supporting CPB cannula removal. This approach facilitates a bloodless surgical field and thus improved visualization, factors which can potentially lead to decreased surgical times and overall CPB support times. Prior to circulatory arrest, deep hypothermia (DH) is induced, wherein core body temperature is commonly decreased to 18°C to decrease metabolic demand and permit extended cerebral tolerance to circulatory arrest. Optimization of strategies and neurological outcomes in neonates and infants must thereby address a complex interplay of compounded risk. The use of extracorporeal CPB support is associated with incremental release of inflammatory mediators.[66,305,306] Deep hypothermia causes a loss of cerebral autoregulation,[237,307] and extended durations of deep hypothermia have been associated with transient post-operative choreoathetosis;[308] moreover, duration of circulatory arrest >40 minutes conveys an increased risk of seizures[95] and adverse neurodevelopmental outcomes at school-age.[91] Currently, none of the routinely employed intraoperative neuromonitoring methods characterize the evolution of these compounding risks in real-time. Thus, a knowledge gap for development and implementation of neuroprotective strategies persists.

To date, one intraoperative intervention strategy, based on combined non-invasive neuromonitoring of cerebral tissue oxygen saturation (StO_2) via continuous-wave (CW) near-infrared spectroscopy (NIRS) and cerebral blood flow velocity via transcranial Doppler (TCD) ultrasound, has shown that individualized intraoperative feedback about cerebral oxygen metabolism can facilitate improved neurological outcomes in children following their cardiac operation.[97] Specifically, interpretation of concurrent CW NIRS and TCD trends in cerebral oxygen utilization and cerebral perfusion, respectively, permitted estimation of cerebral metabolic rate of oxygen ($CMRO_2$) and identification of vulnerable periods of cerebral hypoxia and ischemia. In another recent prospective study, wherein DHCA was performed in 65 (87%) patients, a lower cerebral tissue oxygenation index (<58%) measured by CW NIRS in combination with blood lactate levels > 7.4mmol/L at 24 hours post-operation; this study showed a sensitivity of 95% to poor outcome defined as death, or a BSID < 70 (Bayley Scales of Infant Development, II).[309] Together, these findings contribute to the limited evidence that alterations in perioperative cerebral metabolism are prognostic of neonatal brain injury.

Unfortunately, few clinical modalities are suitable for continuous intraoperative neuromonitoring in neonates, and even fewer permit direct quantification of cerebral metabolism. Following Austin et al.'s landmark study with CW NIRS and TCD, the only other neuromonitoring modality for pediatric congenital heart surgery that has persisted in the last two decades[25,101,310–314] is electroencephalography (EEG). EEG is recommended for postoperative seizure monitoring,[315] but it has not been found to be an accurate indicator of cerebral metabolism.[316,317] Thus the combination of CW NIRS and

TCD remains the only modality based on “conventional” methods that has proven feasible for intraoperative metabolic monitoring.[37,97,318,319] Yet, this multimodal strategy has thus far seen limited clinical use.[312,320] This limited use could be due to the continuing susceptibility of TCD to motion artifacts and cautery interference, difficulties maintaining TCD probe positioning on the small neonatal head, and small blood flow velocities during low-flow cardiopulmonary bypass.[25,34,101,215]

Per optical techniques, intraoperative stand-alone CW NIRS has experienced growing clinical adoption,[321–323] in part because the instruments are FDA approved. However, CW NIRS represents a class of diffuse optical spectroscopy (DOS) with comparatively limited information.[9,324] It does not quantify oxy- and deoxy-concentration absolutely, and it fails to quantify cerebral blood flow or metabolism; thus its benefits remain controversial.[103,313] Ultimately, quantification of oxygenation relies on accurate separation and assignment of tissue absorption and scattering properties (see “Methods”), and even the most advanced, spatially resolved, multi-wavelength CW NIRS systems rely upon baseline assumptions about the subject’s tissue optical scattering properties. Furthermore, in CW NIRS, the changes in light intensity are equated to changes in tissue optical absorption properties, without considering potential changes in scattering. Consequently, the accuracy of CW NIRS suffers during perioperative monitoring and, specifically, during DHCA, *i.e.,* it suffers whenever tissue optical properties can be significantly impacted by the profound physiological changes[325], by ATP depletion[326], and by changes in tissue composition[11] that result from deep hypothermia, exsanguination via venous cannula vacuum, or extended hypoxia-ischemia. These issues, along with the lack of cerebral perfusion monitoring, lead to challenges for defining specific quantitative targets based on CW NIRS as part of goal-directed therapy. Thus, CW NIRS has failed to show a clear benefit on overall outcomes in pediatric critical care.[238]

On the other hand, more sophisticated diffuse optical techniques exist that permit all-optical, continuous non-invasive quantification of cerebral oxygen metabolism by combining absolute measures of cerebral oxygenation, via time-domain (TD) or frequency-domain (FD) diffuse optical spectroscopy (DOS), and via direct measurement of blood flow by diffuse correlation spectroscopy (DCS).[30–32] Recent proof-of-principle demonstrations of intraoperative metabolic monitoring feasibility in infants[37,112] have been carried out. In these studies, the all-optical techniques show promise to address the shortfalls of conventional clinical imaging modalities (including CW NIRS). Indeed, in a subset of neonatal swine of the present study, invasive validation data based on these techniques during DH CPB through cooling and rewarming have been reported (**Chapter 2**); these data provide reason for improved confidence per the use of these novel tools to inform clinical care during congenital heart surgery.

In this work, we employ these sophisticated non-invasive all-optical hemodynamic methods to better understand the factors that contribute to cerebral metabolic vulnerability. Specifically, the present study reports on characterization of the incremental impact of circulatory arrest on cerebral oxygen metabolism with respect to time during DHCA, and with respect to temperature following DHCA. The data are derived using continuous non-invasive FD-DOS/DCS measurements in a neonatal swine model of cardiac surgery.

C. Methods

The results in the present paper utilize unreported data from a prospective, observational cohort study whose methods have been previously described.[255] Briefly, in this work, twenty neonatal, female Yorkshire swine (6-10 days old, 3-5kg) were continuously monitored through cardiopulmonary bypass (CPB) and were randomized, following induction of deep hypothermia, to receive either continuous perfusion (DHCP; n=10) or circulatory arrest (DHCA; n=10) for 40 minutes; these management scenarios were followed by reperfusion of the DHCA group and rewarming to normothermia in both groups. An additional control cohort (n=4) underwent CPB for a duration matching the timing of the DHCP and DHCA cohorts, but without deep hypothermia or circulatory arrest. All procedures were approved by the CHOP Institutional Animal Care and Use Committee, performed in strict accordance with the NIH Guide for the Care and Use of Laboratory Animals, and reported according to the ARRIVE guidelines (https://www.nc3rs.org.uk/arrive-guidelines).

C.1. Selection of Animal Model

Neonatal swine models have provided foundational data contributions to our understanding of the impact of circulatory arrest on the brain.[250,255,327–330] This statement is also true for the clinical translation of diffuse optical techniques for pediatric neuromonitoring,[19,22,26,41,324] due to comparability in the anatomical thickness of superficial tissue (*i.e.*, scalp, skull). The animal model used here was developed based on surgical practices at our institution. The investigation builds upon and connects with these two bodies of literature.

C.2. Neurological Monitoring

The methods for neurological monitoring have been previously detailed (**Chapter 2, Section C.2 and C.4**)[331,332] but will be briefly summarized herein. Following, anesthetic induction and intubation, and prior to initiation of cardiopulmonary bypass support, neurological monitoring modalities were placed. These monitoring modalities included nasopharyngeal temperature (NPT, °C) for guidance of hypothermic therapy, intracranial brain temperature (ICT, °C; CC1-P1, Integra LifeSciences; Plainsboro, NJ, USA), and non-invasive frequency-domain diffuse optical spectroscopy (FD-DOS) and diffuse correlation spectroscopy (DCS). Invasive measures of ICT were acquired in the right frontal cortex, symmetrically contralateral to non-invasive FD-DOS/DCS measurements over the left frontal cortex. Following placement, measurements from all instruments were recorded continuously for the duration of the protocol.

Diffuse Optical Monitoring of Cerebral Oxygen Metabolism

Optical indices of cerebral metabolic rate of oxygen ($CMRO_{2,i}$, mL O_2/dL*cm^2/s) and relative $CMRO_2$ ($rCMRO_2$, %) were continuously quantified according to models based on Fick's Law [259]. The resulting model, which is given below, uses the combination of tissue oxygen extraction fraction (OEF) from FD-DOS, cerebral blood flow index (BFI; cm^2/s) from DCS, and baseline arterial blood gas sampling for the arterial concentration of oxygen (CaO_2, mL O_2/dL):[9,31,43,44,240,333]

$$CMRO_{2,i} = CaO_2 \times OEF \times BFI \ . \tag{3.1}$$

CaO_2 was assumed to remain constant throughout deep hypothermia. Validation data regarding this assumption is reported in **Chapter 2, Section D.2**.[331,332] Relative cerebral metabolic rate of oxygen, $rCMRO_2$, at a given time-point, t, was computed as:

$$rCMRO_2(t) = \frac{CMRO_{2,i}(t)}{CMRO_{2,i,baseline}} \times 100\% \, , \tag{3.2}$$

where the baseline value of $CMRO_{2,i}$ was calculated as the mean $CMRO_{2,i}$ measured during the baseline period prior to cooling.

Using a customized commercial FD-DOS instrument (Imagent, ISS Inc., Champaign, IL, USA) with radio-frequency (110MHz) intensity-modulated near-infrared light sources and two photomultiplier tube detectors, the AC intensity and phase were measured as a function source-detector separation. These data were then used to derive absolute tissue absorption and scattering properties (μ_a and $\mu_s{}'$, respectively) at four wavelengths (λ = 690, 725, 785, and 830 nm). Assuming constant cerebral tissue water content [257], these measured absorption coefficients were used to quantify cerebral tissue concentration of oxy- and deoxyhemoglobin ([HbO_2] and [Hb], respectively; μmol/L) [9,10,256]. Subsequently, total hemoglobin concentration (THC, μmol/L), and tissue oxygen saturation (StO_2, %) were computed as:

$$THC = [Hb] + [HbO_2]\,; \tag{3.3}$$

$$StO_2(\%) = \frac{[HbO_2]}{[Hb] + [HbO_2]} \times 100\%\,. \tag{3.4}$$

Assuming an optical venous fraction of γ = 0.75 and using the arterial oxygen saturation (SaO_2) obtained from baseline blood gas sampling, OEF was determined as:

$$OEF = \frac{SaO_2 - StO_2}{\gamma \times SaO_2}\,. \tag{3.5}$$

DCS measurements were performed using custom instrumentation with a continuous-wave, long-coherence length (>10 m), λ =785 nm laser source (RCL-080-785S; CrystaLaser, Inc, Reno, NV, USA), and two detection arrays of four single-photon-counting avalanche photodiode detectors (SPCM-AQ4C; Excelitas Technologies, Corp., Waltham, MA, USA). The DCS calculations of blood flow index (BFI) incorporated the concurrent measurements of tissue absorption and scattering properties from FD-DOS. BFI was derived from fitting the average (*i.e.*, across all detectors) hardware-calculated (FLEX03OEM-8CH; Correlator.com, NJ, USA) intensity temporal autocorrelation function with the homogenous solution for the semi-infinite diffusion correlation equation [33]. Measures of relative cerebral blood flow (rCBF; %) at a given time-point (t) were computed as:

$$rCBF(t) = \frac{BFI(t)}{BFI_{baseline}} \times 100\%\,, \tag{3.6}$$

where the baseline BFI value was calculated as the mean BFI measured during the baseline period prior to cooling.

$CMRO_2$ Temperature-Dependence

The Arrhenius Equation (**Equation 2.7**)[113,115] was used to quantify the temperature-dependence of cerebral metabolism during cooling and rewarming in DHCP and DHCA groups. For example, the model for $CMRO_{2,i}$ (*i.e.*, a rate of reaction) is dependent on intracranial temperature (ICT), the universal gas constant (R), an activation free energy barrier (E_a), and a pre-exponential factor (A) which is related to the attempt frequency associated with the reaction:

$$CMRO_{2,i} = Ae^{-\frac{E_a}{R \cdot ICT}}\,. \tag{3.7}$$

This equation may be rearranged into a linear form ($y = ax + b$) such that model parameters, $a = \frac{E_a}{R}$ and $b = \ln(A)$, may be derived from linear regression of the data:

$$ln(CMRO_2) = \frac{E_a}{R}\left(\frac{1}{T}\right) + ln(A)\,. \tag{3.8}$$

C.3. Cardiopulmonary Bypass and Deep Hypothermia

The procedure and timing for institution of cardiopulmonary bypass, deep hypothermia and circulatory arrest are illustrated in **Figure 3.1** and have been described in Mavroudis et al.[255] All subjects (n=24) were stabilized on CPB (flow rate = 150 ml/kg/min) at normothermia (NPT = 37°C), and baseline measurements were acquired for five minutes. Subsequently, DHCP and DHCA animals were cooled to deep hypothermia (NPT = 18°C) at a target rate of 1°C per minute. After attainment of 18°C, the subjects were randomized to either DHCA (n=10) or DHCP (n=10) for a duration of

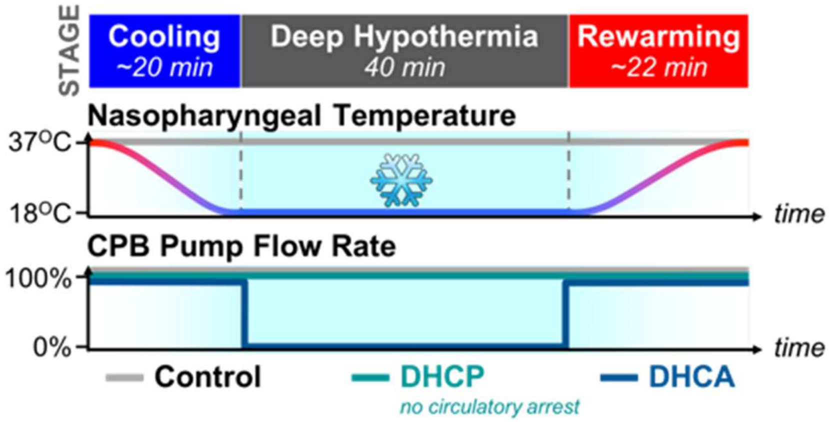

Figure 3.1. DHCA versus DHCP Experimental Protocol: Study subjects (n=24) were randomized to three treatments. The control group (*grey*; n=4) received continuous normothermic perfusion. Remaining animals were cooled to deep hypothermia (nasopharyngeal temperature = 18°C) and received either continuous perfusion (DHCP, n=10; *green*) or circulatory arrest (DHCA, n=10; *blue*).

40 minutes. To initiate DHCA, the CPB arterial outlet flow was turned off and clamped, with venous drainage remaining open for patient exsanguination (*i.e.*, removal of blood from the body). Once the lack of venous return became apparent, the venous drainage was also clamped. Donor blood was added as needed to ensure a minimum hematocrit of 30%; similarly, 2 meq/kg of sodium bicarbonate and 0.5 g/kg mannitol were added immediately prior to reinitiating CPB. Following reperfusion of DHCA animals, DHCA and DHCP groups were rewarmed to normothermia (NPT = 37°C) at a target rate of 1°C per minute. The normothermic control group (n=4) were maintained on CPB for a total of 70 minutes, *i.e.,* 15 minutes for simulated cooling, 40 minutes for simulated deep hypothermia, and 15 minutes for simulated rewarming.

C.4. Statistical Analysis

All statistical analyses were carried out using MATLAB 2014a. Summary statistics are reported as mean and standard deviation (SD), unless otherwise noted. Primary analyses comprised examination of the timing of oxygen utilization during

DHCA, differences in cerebral metabolic parameters at 40 minutes of DHCA versus DHCP. Additionally, we carried out a comparison of $CMRO_{2,i}$ temperature-dependence during rewarming, following DHCA, versus during cooling. The latter analysis has been described in DHCP animals in **Chapter 2. Section D.1**.

Timing of oxygen utilization during DHCA was characterized by a time-to-maximal oxygen extraction ($t_{OEF,MAX}$), and a time-to-minimal [HbO_2] depletion ($t_{HbO_2,MIN}$). Continuous time-series data were synchronized using 15 s epoch averages. $t_{OEF,MAX}$ and $t_{HbO_2,MIN}$ were determined as the earliest time-point at which the absolute change in the subsequent five-minutes became less than 0.5% of baseline OEF and [HbO_2], respectively. To examine the temporal characteristics of the change, discrete differential time-series were also calculated from the continuous data as a function of time by computing the difference in values recorded between adjacent 15 s epochs.

Cerebral metabolic parameters were compared between DHCA versus DHCP groups at 40 minutes of deep hypothermia. Secondary comparisons were conducted at baseline and end of cooling, as well as comparisons of changes (Δ) from baseline at end of cooling and at 40 minutes of deep hypothermia. All single-parameter comparisons between groups were made using a two-sample t-test, assuming equal variances, and evaluated at a pooled significance level of α=0.05. A Bonferroni correction was applied to adjust the significance level for the five multiple comparisons to α=0.01. Assuming a type II error rate of β=0.2, the two-sample t-test comparisons between DHCP and DHCA groups were powered to identify a minimum effect size of 1.67*SD of each parameter at a two-tailed significance level of α=0.01.

In the control group, within-group paired t-test comparisons between baseline and end values were conducted to examine the presence of significant changes as a result of 70 minutes of normothermic CPB support. Assuming a type II error rate of β=0.2, and a within-subject correlation of 0.875, this test was powered to identify a minimum effect size of 0.67 times the SD of each parameter at a two-tailed significance level of α=0.05.

Linear mixed-effects models were used to quantify differences in the relationship between $CMRO_{2,i}$ and intracranial temperature (**Equation 3.6**). *i.e.,* during cooling versus rewarming in DHCA animals. The model included fixed and random slope and intercept effects, with a period-specific (*i.e.*, cooling or rewarming) interaction term. Random effects were included to allow for subject-specific slope and intercept variations. The goodness-of-fit of these models were evaluated using the coefficient of determination (R^2) of a generalized linear regression model, including subject interactions and excluding random effects.

D. Results

Twenty-four neonatal swine (mean weight = 3.6 kg) underwent CPB with neurological monitoring. Successful diffuse optical monitoring was achieved in 8 of 10 DHCP animals, 8 of 10 DHCA animals, and 3 of 4 control animals with fallout of remaining animals due to incidental obstruction of optical signal by cutaneous bleeding. Following adjustments in sample size, two-sample t-test comparisons between DHCP and DHCA groups were powered to identify a minimum effect size of 2*SD and paired t-test within-subject comparisons in the control group were subsequently powered to identify an effect size of 0.75*SD in each parameter.

Table 3.2. Summary of Temperature and Cerebral Metabolic Parameters in the Control Group (n=3)

Parameter	Baseline	70 Minutes	p-value
NPT	37.2 (0.3)	37.2 (0.3)	1.000
ICT	36.0 (1.4)	36.0 (1.8)	0.954
$[HbO_2]$	53.7 (10.8)	58.8 (21.4)	0.505
[Hb]	42.2 (6.0)	44.3 (10.5)	0.592
THC	95.9 (14.4)	103.1 (30.0)	0.529
StO_2	55.9 (4.6)	56.4 (6.5)	0.685
OEF	0.59 (0.06)	0.58 (0.09)	0.685
$BFI*10^8$	1.42 (0.67)	1.35 (0.54)	0.468
$CMRO_{2,i}*10^8$	12.6 (6.3)	12.0 (5.6)	0.285
rCBF, %	100.0 (-)	98.1 (9.2)	0.757
$rCMRO_2$, %	100.0 (-)	96.3 (5.6)	0.375

Abbreviations: See Table 1.

The mean baseline arterial concentration of oxygen (CaO_2) across all animals (n=19), measured by blood gas sampling, was 14.3 (1.8) mL O_2/dL blood. On average, DHCP (n=8) and DHCA (n=8) animals were cooled to deep hypothermia in 26.5 (4.9) minutes. DHCP animals were maintained with continuous deep hypothermic perfusion for 42.6 (1.6) minutes while DHCA animals underwent circulatory arrest for 41.0 (1.4) minutes. These animals were subsequently rewarmed to normothermia in 27.5 (5.8) minutes. No differences in timing, temperature, or other cerebral metabolic parameters were found between groups at baseline or at the end of cooling (**Table 3.1**). We examined the impact of prolonged cardiopulmonary bypass support alone within the control group animals (n=3), who underwent normo-thermic CPB support for 72.6 (1.5) minutes; they exhibited no differences in cerebral metabolic parameters from baseline after this time (**Table 3.2**).

D.1. Timing of Cerebral Oxygen Utilization During DHCA

Mean oxygen extraction fraction (OEF) as a function of time from start of DHCP or DHCA is depicted in **Figure 3.2** for each group. In the control group, OEF remains

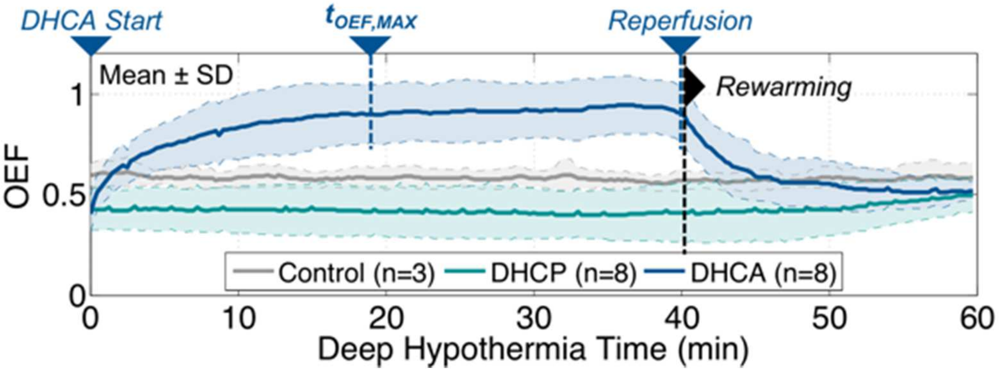

Figure 3.2. Oxygen Extraction Fraction (OEF) during Deep Hypothermia: The mean and standard deviation of OEF within each group is shown with respect to time from the start of deep hypothermia, in DHCP animals (*green*), or from the start of circulatory arrest, in DHCA animals (*blue*). For comparison, data is also shown from normothermic control animals (*gray*) following 15 minutes of cardiopulmonary bypass support. DHCA induces an increasing OEF over time; the mean (SD) time-to-maximal OEF ($\mathrm{t_{OEF,MAX}}$) was 19.6 (6.7) minutes after the start of DHCA. Notice, OEF recovers following reperfusion and aligns with values of the DHCP group within 20 minutes.

stable for the entire period. The DHCP group also exhibits a stable, but depressed OEF throughout the 40-minute period; this is followed by recovery during rewarming with values trending towards the control group. The DHCA and DHCP group both begin at lower OEF in comparison to the normothermic group (note, this is a qualitative observation; no statistical testing was performed), but in both cases there is an immediate and rapid increase in OEF with time. Mean time-to-maximal OEF ($t_{OEF,MAX}$) in DHCA animals was determined to be 19.6 (6.7) minutes after the start of DHCA.

Further examination of absolute [HbO_2], [Hb], THC (**Figure 3.3**, *left*), and StO_2 (**Figure 3.3**, *right*) and their change from baseline (ΔBaseline) during DHCA shows expectedly similar timing trends. Decreasing [HbO_2] and increasing [Hb], resulted in decreased StO_2 and demonstrates rapidly increasing oxygen utilization. The mean time-to-minimal [HbO_2] ($t_{HbO_2,MIN}$) was determined to be 18.4 (6.8) minutes after start of DHCA.

Table 3.1. Summary of Temperature and Cerebral Metabolic Parameters in DHCP and DHCA Groups

ABSOLUTE VALUES				CHANGE FROM BASELINE			
	DHCP, n=8	DHCA, n=8	p-value		DHCP, n=8	DHCA, n=8	p-value
Cooling Time	25.7 (5.3)	27.3 (4.7)	0.538				
Rewarm Time	27.2 (7.0)	27.7 (4.7)	0.878				
Baseline							
NPT	37.2 (0.6)	37.4 (0.8)	0.593				
ICT	34.1 (2.4)	36.5 (0.9)	0.068				
[HbO$_2$]	42.3 (7.7)	47.1 (15.7)	0.480				
[Hb]	33.3 (4.3)	37.7 (6.7)	0.174				
THC	75.6 (10.7)	84.8 (21.8)	0.339				
StO$_2$	55.7 (4.2)	54.8 (4.4)	0.719				
OEF	0.58 (0.06)	0.60 (0.06)	0.529				
BFI*10^8	0.75 (0.30)	1.04 (0.44)	0.192				
CMRO$_{2,i}$*10^8	5.6 (2.7)	9.7 (5.0)	0.084				
End of Cooling							
NPT	17.7 (0.4)	18.6 (1.7)	0.206	ΔNPT	-19.5 (0.7)	-19.0 (1.9)	0.509
ICT	22.7 (2.3)	23.2 (1.7)	0.724	ΔICT	-11.4 (3.2)	-13.3 (2.7)	0.360
[HbO$_2$]	52.0 (13.4)	64.2 (23.2)	0.261	Δ[HbO$_2$]	+9.7 (8.9)	+16.6 (8.5)	0.184
[Hb]	26.0 (5.6)	26.7 (7.1)	0.852	Δ[Hb]	-7.3 (3.5)	-10.8 (4.0)	0.122
THC	78.0 (14.1)	90.9 (28.5)	0.313	ΔTHC	+2.4 (7.9)	+5.8 (6.3)	0.408
StO$_2$	66.1 (8.0)	70.1 (5.7)	0.325	ΔStO$_2$	+10.4 (5.5)	+15.0 (6.0)	0.175
OEF	0.44 (0.09)	0.40 (0.08)	0.365	ΔOEF	-0.14 (0.07)	-0.20 (0.08)	0.175
BFI*10^8	0.39 (0.24)	0.63 (0.45)	0.258	ΔrCBF, %	-48.9 (18.7)	-40.4 (23.4)	0.500
CMRO$_{2,i}$*10^8	2.1 (1.1)	3.5 (2.2)	0.163	ΔrCMRO$_2$, %	-62.8 (8.4)	-61.2 (16.3)	0.823
End of DH							
NPT	18.1 (0.5)	18.9 (0.5)	0.007*	ΔNPT	-19.1 (0.8)	-18.4 (0.8)	0.131
ICT	18.8 (1.1)	19.4 (1.3)	0.369	ΔICT	-15.2 (2.7)	-16.4 (1.2)	0.358
[HbO$_2$]	58.0 (18.4)	21.8 (15.3)	<0.001**	Δ[HbO$_2$]	15.2 (15.0)	-27.0 (7.1)	<0.001**
[Hb]	24.8 (6.0)	45.6 (10.0)	<0.001**	Δ[Hb]	-8.1 (7.2)	7.4 (4.7)	<0.001**
THC	82.8 (15.0)	67.4 (24.9)	0.155	ΔTHC	7.0 (11.5)	-19.5 (7.7)	<0.001**
StO$_2$	68.6 (11.1)	29.4 (10.6)	<0.001**	ΔStO$_2$	12.3 (9.4)	-27.0 (9.9)	<0.001**
OEF	0.41 (0.15)	0.94 (0.14)	<0.001**	ΔOEF	-0.16 (0.14)	0.36 (0.13)	<0.001**
BFI*10^8	0.43 (0.38)	0.01 (0.01)	0.008*	ΔrCBF, %	-49.9 (32.7)	-98.8 (0.5)	0.004*
CMRO$_{2,i}$*10^8	1.9 (1.3)	0.2 (0.2)	0.003*	ΔrCMRO$_2$, %	-70.2 (12.1)	-98.1 (1.0)	<0.001**

*p<0.01; **p<0.001.

Abbreviations (Units): Δ, change from baseline; Cooling Time (min); Rewarm Time (min); NPT, nasopharyngeal temperature (°C); ICT, intracranial temperature (°C); [HbO2], concentration of oxy-hemoglobin (μmol/L); [Hb], concentration of deoxyhemoglobin (μmol/L); THC, total hemoglobin concentration (μmol/L); StO2, tissue oxygen saturation (%); OEF, oxygen extraction fraction; BFI, blood flow index (cm2/s); CMRO2,i, optical index of cerebral metabolic rate of oxygen (mL O2/dL * cm2/s); rCBF, relative cerebral blood flow (% baseline); rCMRO2, relative cerebral metabolic rate of oxygen (% baseline).

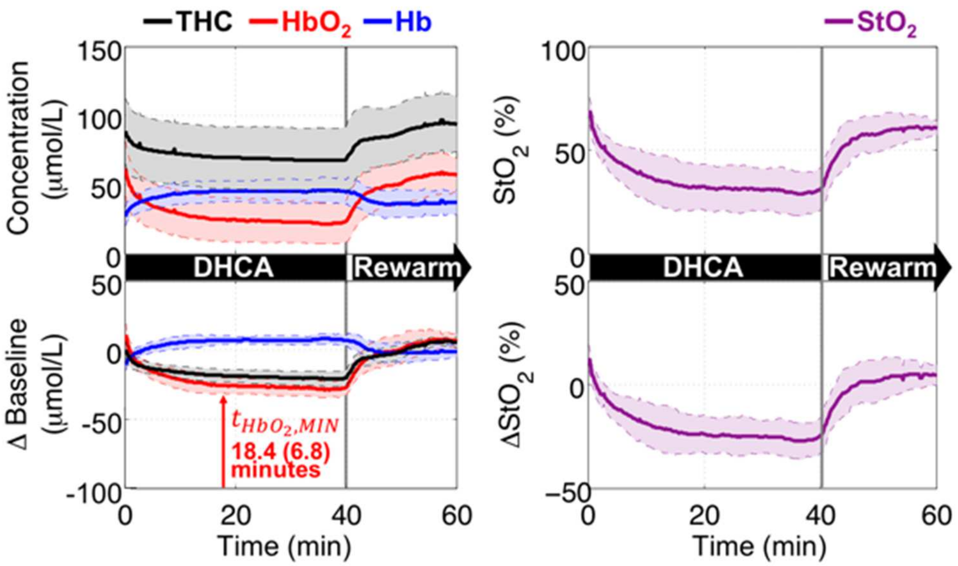

Figure 3.3. Effect of DHCA on Cerebral Hemoglobin Concentration and Tissue Oxygenation: The mean (*solid line*) and standard deviation (*shaded region*) of absolute values of oxy- and deoxy- hemoglobin concentration ([HbO_2], *red*; and [Hb], *blue*; respectively), total hemoglobin concentration (THC; *black*), and cerebral tissue oxygen saturation (StO_2, *purple*) are shown as a function of time from the start of deep hypothermic circulatory arrest through the first 20 minutes following reperfusion (DHCA; n=8). Absolute values are displayed in the adjacent top panels alongside changes-from-baseline (Δ) values in the adjacent bottom panels. Rapid depletion and recovery of oxygenation and total hemoglobin are seen at the onset of DHCA and upon reperfusion, respectively. Mean (SD) time-to-minimal [HbO_2] ($t_{HbO_2,MIN}$) was after 18.4 (6.8) minutes of DHCA.

Supplemental analyses of the first and second discrete differentials of the OEF and [HbO_2] time-series identified a distinct initial period of rapid rate change in the first six minutes (**Figure 3.4**) of DHCA. Subsequently, the first differential continued to decline for the remainder of circulatory arrest, but it declined at a stable rate, as indicated by the zero-value of the second differential. Given that changes in oxygen utilization are often indications of changes in the magnitude of underlying cellular metabolism, these distinct periods are suggestive of underlying alterations in cellular metabolism.

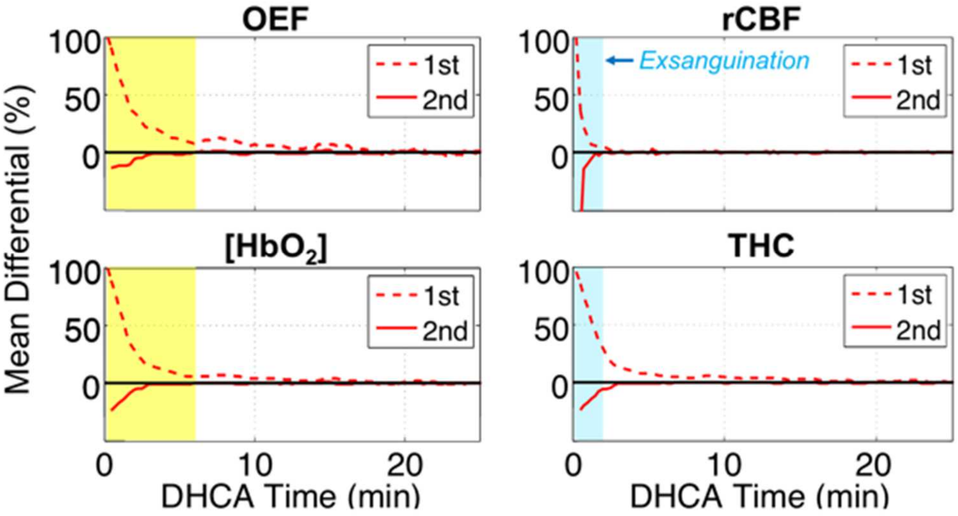

Figure 3.4. Timing of differential changes in OEF, [HbO$_2$], rCBF and THC: The mean first (1st, *dotted line*) and second (2nd, *solid line*) differential time-series is plotted for oxygen extraction fraction (OEF, *top left*) and oxyhemoglobin concentration ([HbO$_2$], *bottom left*) in DHCA subjects. The first differential is normalized to the change in the first 15 seconds of DHCA. The second differential identifies an initial 6-minute period (*yellow*) of rapid change, which subsequently stabilizes as the second differential goes to zero. This analysis identifies distinct periods with differential rates of change which may reflect changes in cellular metabolism during onset of hypoxia. The agreement of timing between OEF and [HbO$_2$] confirms that depletion of available oxygen is tightly linked to oxygen utilization. In the differential times series of relative cerebra blood flow (rCBF; *top right*) and total hemoglobin concentration (THC; *bottom right*), rapid declines are likely the result of exsanguination during the first two minutes (*blue*) of DHCA.

Interestingly, THC also demonstrated progressive depletion with an average loss of 19.5 (7.7) μmol/L at the end of DHCA. In addition to progressive hypoxia as a result of oxygen metabolism, this observation identifies a compound effect of progressive ischemia which further diminishes tolerance to DHCA. Another notable observation was made regarding the change from baseline in [Hb], [HbO$_2$] and THC; these tissue properties exhibited substantially smaller inter-subject variability (*i.e.*, standard deviation) compared to their absolute values. This adjustment in inter-subject variability is not observed between absolute values of StO$_2$ and its difference from baseline. This effect potentially indicates that, regardless of the varying amounts of blood volume in the region of optical light penetration, the absolute value of oxygen that is either utilized or accessible for extraction is relatively homogenous across subjects. This finding also holds true during reperfusion and subsequent rewarming, which suggests that differences from baseline should be taken into consideration to provide a more discriminating measure of oxygen utilization.

D.2. Impact of Prolonged DHCA on Cerebral Oxygen Metabolism

Following 40 minutes of DHCA versus DHCP, significant differences ($p<0.01$) were detected in all cerebral metabolic parameters except intracranial temperature (**Table 3.1,** "*End of DH*"). Nasopharyngeal temperature was significantly greater in DHCA animals (18.9 (1.7)°C) than in DHCP animals (18.1 (0.5)°C). Given the lack of cold perfusion to maintain stable deep hypothermia in DHCA animals, mild rewarming is plausible due to equilibration with room temperature and due to residual cellular metabolism.

Additional significant differences between DHCA and DHCP groups were seen in [HbO_2], [Hb], THC, StO_2, OEF, BFI, and $CMRO_{2,i}$. Inter-subject variability observed in the time-series analysis of THC affected comparability of absolute values between DHCP and DHCA groups ($p=0.155$). However, examination of differences in THC changes from baseline (ΔTHC) between groups revealed a highly significant difference (DHCP ΔTHC = +7.0 (11.5) μmol/L, DHCA ΔTHC = -19.5 (7.7) μmol/L; $p<0.001$). Significant differences in all other variables were confirmed in comparisons of changes from baseline. As expected from earlier examination of the OEF, [HbO_2], and [Hb] time-series, in DHCA animals, OEF was significantly higher (DHCA: 0.94 (0.14), DHCP: 0.41 (0.15); $p<0.001$), [HbO_2] was significantly lower (DHCA: 21.8 (15.3) μmol/L, DHCP: 58.0 (18.4) μmol/L; $p<0.001$), [Hb] was significantly higher (DHCA: 45.6 (10.0) μmol/L, DHCP: 24.8 (6.0);

p<0.001), and StO_2 was significantly lower (DHCA: 29.4% (10.6), DHCP: 68.6% (11.1); p<0.001) than in DHCP animals.

While both DHCA and DHCP groups saw similar depression of CBF (DHCA ΔrCBF = -40.4% (23.4), DHCP ΔrCBF = -48.9% (18.7); p=0.500) and $CMRO_2$ (DHCA $\Delta rCMRO_2$ = -61.2% (16.3), DHCP $\Delta rCMRO_2$ = -62.8% (8.4); p=0.500) following cooling, the overall changes from baseline at the end of deep hypothermia reflected a significant difference resulting from lack of perfusion in DHCA animals (DHCA ΔrCBF = -98.8% (0.5), $\Delta rCMRO_2$ = -98.1% (1.0)) as compared to continuous perfusion in DHCP animals (DHCP ΔrCBF = -49.9% (32.7), $\Delta rCMRO_2$ = -70.2% (12.1)) on rCBF (p=0.004) and $rCMRO_2$ (p<0.001). This observation provides clear evidence that non-invasive FD-DOS/DCS monitoring enables quantification of the impact of DHCA on cerebral oxygen metabolism; the corresponding variation of hemodynamic parameters reflects the hypoxic and ischemic conditions of the brain.

D.3. $CMRO_{2,i}$ Temperature-Dependence Following DHCA

A comparison of $CMRO_{2,i}$ temperature-dependence during cooling and rewarming in DHCP animals (**Figure 3.5**, *left*) has been previously reported in **Chapter 2, Section D.1**.[331,332] A primary objective of the previous study was to characterize the adequacy of current non-invasive nasopharyngeal temperature guidance of deep hypothermia through comparisons to true brain temperature and to cerebral metabolism. A significant finding was that the use of nasopharyngeal temperature introduced discrepancies in $CMRO_{2,i}$ temperature dependence due to mismatch with brain temperature. As a result, in the present study, we exclusively examined intracranial brain temperature-dependence, and we compared our previous findings in DHCP animals to the results of an identical analysis conducted in *DHCA animals*.

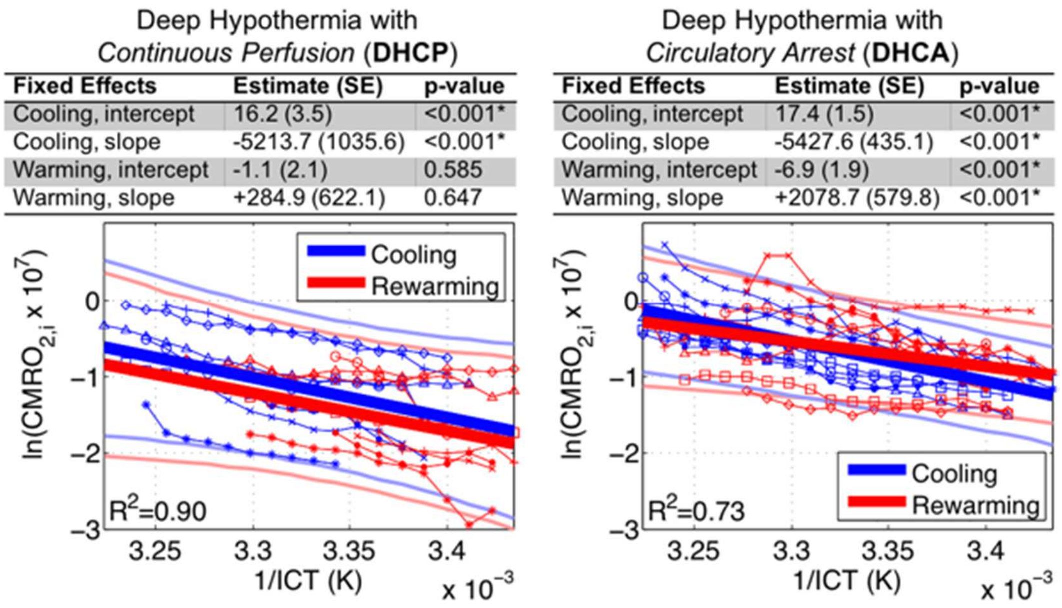
Deep Hypothermia with *Continuous Perfusion* (**DHCP**)

Fixed Effects	Estimate (SE)	p-value
Cooling, intercept	16.2 (3.5)	<0.001*
Cooling, slope	-5213.7 (1035.6)	<0.001*
Warming, intercept	-1.1 (2.1)	0.585
Warming, slope	+284.9 (622.1)	0.647

Deep Hypothermia with *Circulatory Arrest* (**DHCA**)

Fixed Effects	Estimate (SE)	p-value
Cooling, intercept	17.4 (1.5)	<0.001*
Cooling, slope	-5427.6 (435.1)	<0.001*
Warming, intercept	-6.9 (1.9)	<0.001*
Warming, slope	+2078.7 (579.8)	<0.001*

Figure 3.5. Temperature-Dependence of CMRO$_{2,i}$, Cooling versus Rewarming: The fitted slope and intercept effects during cooling and rewarming are reported in tabular form above the plotted individual data (unique symbols for each subject) and modeled relationships (*solid lines*). The fitted model (*thick solid line*) is depicted with 95% confidence intervals (*thin solid lines*) for cooling (*blue*) and for rewarming (*red*). Concordance of the temperature-dependence of the optical index of cerebral metabolic rate of oxygen (CMRO$_{2,i}$) between cooling and rewarming, with respect to intracranial temperature (ICT), in DHCP animals has been previously reported in **Chapter 2, Section D.1** (*left*).[331,332] In contrast to DHCP animals, the DHCA animals (*right*) exhibit a significant hysteresis between cooling, prior to circulatory arrest, and rewarming, following circulatory arrest, whereby the effect of rewarming adjusts the slope of the temperature-dependence relationship towards zero; this indicates diminished sensitivity of metabolism to temperature.

In a linear mixed-effects model of the CMRO$_{2,i}$ temperature-dependence with respect to intracranial temperature (ICT) during cooling and rewarming in DHCA animals (**Figure 3.5**, *right*), a significant slope (Mean [SE] = -5427.6 [435.1], p<0.001) effect during cooling was found. This confirms a strong association between temperature and CMRO$_{2,i}$ in DHCA animals. Moreover, while rewarming did not exhibit a significant effect on slope or intercept in *DHCP animals*, *in DHCA animals,* both a significant rewarming slope (Mean [SE] = +2078.7 [579.8], p<0.001) and intercept (Mean [SE] = -6.9 [1.9], p<0.001) were found. This observation indicates that circulatory arrest significantly impacted the relationship of temperature and metabolism, and in this case, metabolism exhibited diminished temperature sensitivity. Examination of individual subject data suggests that, immediately following circulatory arrest, $CMRO_{2,I}$ appears heightened with respect to pre-arrest $CMRO_{2,i}$ at deep hypothermia. This effect is likely secondary to prolonged hypoxia, such that once oxygen availability is restored, oxygen metabolism rapidly increases to replenish hypoxic tissue. Furthermore, the R^2 of the temperature-dependence in DHCA animals is markedly lower ($R^2 = 0.73$) than that seen in DHCP animals ($R^2 = 0.90$). The latter finding indicates that the variability in cerebral oxygen metabolism explained by temperature has decreased, which may be plausibly explained by the added variability of hypoxia. In sum, these findings demonstrate the novel continuous characterization of $CMRO_{2,I}$ temperature-dependence by non-invasive FD-DOS/DCS which may eventually be used to more accurately quantify and compare alterations in cerebral metabolism following DHCA in alternative study populations.

E. Discussion

We have quantified the impact of deep hypothermic circulatory arrest (DHCA) on cerebral oxygen metabolism during and following DHCA in a neonatal swine model. The measurements employed continuous, non-invasive diffuse optical techniques which advance substantially beyond conventional continuous-wave NIRS. Continuous sampling methods permitted new quantification of the magnitude and the timing of hemodynamic and metabolic variations during circulatory arrest, as well as cerebral metabolic temperature-dependence following reperfusion. These findings complement other reports of intraoperative monitoring in human neonates undergoing complex cardiac repair[37,112] by providing reference data in healthy neonatal animals of comparable size and development. Moreover, our comparison with animals who received deep hypothermia continuous perfusion (DHCP) enabled the independent effects of circulatory arrest to be separated from those of deep hypothermia. Generalization of this work to intraoperative guidance of DHCA in children appears feasible.

E.1. Timing of Cerebral Oxygen Utilization During DHCA

During DHCA, non-invasive optical measurements of oxygen extraction fraction (OEF) from oxy-hemoglobin concentration ([HbO_2]) permitted decoupling of oxygen utilization (OEF) from oxygen availability ([HbO_2]). The average (standard deviation) of the time-of-minimal [HbO_2], 18.4 (6.8) minutes, was comparable to time-of-maximal OEF, 19.6 (6.7) minutes. These delays are shorter than the mean (SD) nadir time for [HbO_2] reported in a study by Sakamoto, et al. of 51.3 (12.3) minutes in moderately older animals (mean weight = 9.36kg) who were similarly maintained at a hematocrit of 30%.[328] The differences may be attributed to a longer cooling protocol (40 minutes) and to a lower target temperature (esophageal, 13-14°C) in Sakamoto, et al., which could lead to more homogenous brain cooling and lower residual metabolism with slower oxygen utilization. Our average rate-of-change in StO_2 was mean [range] = 1.0% [0.7, 1.7] per minute; it is calculated as the total StO_2 change during DHCA divided by total DHCA time. This number overlaps well with the range of 0.5-1.6% reported by Tobias et al. in eight children, aged 2 weeks to 6 months, which showed a mean (SD) DHCA time of 43.4 (8) minutes.[334] Importantly, our findings confirm the wide inter-subject variability in timing of oxygen depletion observed. From our data the mean absolute change in StO_2 during DHCA was 40.0%. Assuming an, albeit crude, constant consumption rate ranging from 1.6% to 0.5% per minute, the time to deplete StO_2 by 40% ranges from 25-80 minutes; inadequate cooling would lower initial saturations and further decrease timing of depletion. These uncertainties (or range of variation) underscore the importance of neuromonitoring *during DHCA* to individually characterize the timing of oxygen depletion and prevent extended periods of hypoxia.

Examination of the differential OEF and [HbO_2] time-series uncovered a matching time period of rapid rate-change at the start of DHCA. A similar observation of [HbO_2] variation was made by Abdul-Khaliq, et al. and was attributed to blood loss due to exsanguination following DHCA.[335] From review of our operative notes, the period of exsanguination, between clamping of the arterial outflow and venous inflow lines, was always less than 2 minutes and was typically 30-40 seconds. In the first 2 minutes of DHCA, we observed a rapid decline in both the THC (-8% to -17%) and the BFI (-2% to -12%) time-series which corroborates contribution from the exsanguination effect. By combining the first differential THC time-series (**Figure 3.4**) with the StO_2 time-series, we find that this loss of THC in the first two minutes of DHCA results in a loss of 14-21% of the total [HbO_2] loss during the 40 minutes of DHCA. Mitigating strategies to maintain or limit this loss could potentially result in extended tolerance to DHCA.

Exsanguination, however, is unable to account for the period of rapid rate change extending beyond two minutes. Thus, the changes in rate of oxygen utilization we have observed, without rapid volume loss, suggest that alterations in cellular metabolism might also be occurring. Cerebral metabolic response and tolerance to hypoxia in developing mammals has been observed to be markedly different than in more mature individuals.[336,337] From studies performed in developing mammals, two promising metabolic mechanisms potentially underlie the observed effect are: 1) a shift in energy substrate usage from oxygen to glucose, and/or 2) a hypometabolic neuroprotective response during hypoxia whereby total energy utilization decreases during periods of extended hypoxia.

In Pigula et al., children with a median age of 5 months demonstrated a decrease in the ratio of oxygen-to-glucose utilization during deep hypothermia.[338] Two additional studies, using invasive cerebral microdialysis sampling in piglets, also support the presence of this substrate shift because lactate/pyruvate ratios were significantly elevated during DHCA.[251,255] However, their use of discontinuous sampling methods prevented further insights regarding the timing of this shift. A critical clue was found in fetal sheep wherein Hunter et al. observed an exponential increase in the cerebral glucose/oxygen utilization ratio when oxygen availability dropped below 50% of baseline during severe hypoxia induced by cord occlusion.[339] The timing of this metabolic shift aligns well with depletion of [HbO_2] in our experiments; across all DHCA subjects, [HbO_2] decreased to the midway point between baseline [HbO_2] and end-of-DHCA [HbO_2] in 5.2 (2.8) minutes. The second differential [HbO_2] time-series (**Figure 3.4**) rapidly decays to zero after this time, which corresponds to stabilization of the slope of the first differential until complete depletion of [HbO_2]. In the future, the association between the timing and magnitude of decreased [HbO_2] utilization should be examined for its potential as surrogate measure of anaerobic metabolism.

Hypometabolic response in newborns, which have been reviewed in detail by Rogalska et al., offers another explanation for the decreasing rate of oxygen utilization during hypoxia.[337] A compelling example of hypometabolism was the significant decrease in oxygen utilization seen by Cross et al. in infants ventilated by air with 15% oxygen as opposed to the customary 21% oxygen in room air.[340] Furthermore, neonatal rat neurons have exhibited significantly lower energy utilization during prolonged hypoxia compared to adult rat neurons.[341] Methods of diminished energy utilization include suppression of non-essential cellular processes such as pathways for thermogenesis, repair and growth.[342] Supporting the potentially concurrent and complimentary action of both identified mechanisms, Cavus et al. reported significantly lower cerebral pyruvate *and* lactate production (measured invasively by cerebral microdialysis) which, in combination, demonstrated an increased lactate-pyruvate ratio in 5-11 kg piglets during DHCA compared to those who received continuous cerebral perfusion.[251] Therefore, an approach based on examination of the timing of cerebral oxygen utilization during DHCA by continuous diffuse optical methods together with quantification of key cerebral tissue metabolites offers a new route to elucidate these mechanisms.

In the setting of complex neonatal cardiac repair, varying degrees of cerebral metabolic derangement may be observed due to persisting pre-operative hypoxia[109,110] and diminished cerebral perfusion.[343] Thus, improved understanding of the correlation between temporal characteristics of oxygen availability and utilization, and about the underlying mechanisms facilitating hypoxic tolerance, should enable continuous intraoperative monitoring to provide precise, subject-specific estimates of the rate of metabolic substrate depletion to inform neuroprotective care strategies.

E.2. Impact of Prolonged DHCA on Cerebral Oxygen Metabolism

The reported effects of 40-minutes of DHCA on all cerebral metabolic parameters represent novel data which could not have been obtained simultaneously without application of advanced, quantitative diffuse optical techniques. The effects of cooling to deep hypothermia in DHCA animals showed no significant differences from DHCP animals. These findings are consistent with the summary results reported in **Chapter 2, Section D.1**,[331,332] as well as with prior studies in comparable neonatal swine models.[249,273] Following 40 minutes of deep hypothermia, however, significant differences in all measured cerebral metabolic parameters were observed. Herein, our results are interpreted in the context of the physiology and are compared to measurements by CW NIRS, and FD-DOS/DCS measurements in related hypoxic-ischemic conditions.

Trends in StO_2, THC, [HbO_2], and [Hb] during DHCA were consistent with reported changes measured by CW NIRS in piglet models[328,335,344] and infants.[37,57,61,317,323,334,338,345,346] This data corroborates well-known effects of severe hypoxia in the brain resulting from DHCA. However, the absolute values of CW NIRS parameters (when reported) vary across the different studies. This is likely due, at least in part, to variability in physiologic baseline assumptions across CW NIRS systems, to the changes in scattering during deep hypothermia and circulatory arrest that occur and are not accounted for, and to general intra-subject variability.[27,276]

To examine the variability of scattering we reviewed the measured optical scattering coefficients through cooling, DHCA, and rewarming. Depending on wavelength, the scattering coefficients showed a 2.5 to 5-fold increase in the coefficient of variation (COV) with respect to baseline measurements. This COV finding indicates that there are substantial shifts in scattering associated with temperature changes and circulatory arrest.

In related physiologic contexts, our FD-DOS StO_2 quantification at baseline (54.8% (4.4)) and during DHCA (29.4% (10.6)) agree well with previous FD-DOS measurements at baseline (56.5 ± 0.5%), post-sacrifice (~32%),[26] and during severe hypoxia as indicated by a sagittal sinus oxygen saturation < 5% (StO_2 ranged from 20-40%)[22] in neonatal piglet models. Thus, our results demonstrate that the addition of deep hypothermia and ischemia do not to dramatically impact the physiologic values of StO_2 found in severe hypoxia.

The physiology underlying the significant decreases of THC in DHCA animals compared to DHCP animals remains unclear. THC has been used as a surrogate measure of cerebral blood volume.[109,112,231] The significant rCBF changes we observed, in the early period of rapid change during DHCA, provides plausibility for blood volume (THC) changes during exsanguination; however, THC continues to decline rapidly for another few minutes with a more gradual but persistent decline till the end of DHCA. Similar drops in THC have been reported following animal sacrifice, however, these declines appear to reach a minimum by 12 minutes. A persistent decline could be caused by continued blood vessel leakage and vascular collapse secondary to exsanguination, as well as by cellular swelling secondary to ATP depletion resulting in increased tissue water content and decreased tissue hemoglobin concentration.[337] DCS measurements of BFI would provide an indication of the former, and clearly combined BFI and THC measurements should be explored in the future in conjunction with measures of brain water to elucidate changes in tissue composition. This information would be complementary to the present diagnostics of oxygen availability and utilization.

E.3. $CMRO_{2,i}$ Temperature-Dependence Following DHCA

Significant hysteresis was found between the metabolic temperature-dependence during cooling and during rewarming with respect to intracranial temperature in DHCA animals. Specifically, $CMRO_{2,i}$ exhibited an early increase at low temperatures following reperfusion, and it had diminished temperature sensitivity during rewarming. The identical analysis in DHCP animals did not demonstrate hysteresis (**Chapter 2, Section D.1**).[332] Additionally, previous assessment of the adequacy of nasopharyngeal temperature guidance in the DHCP group showed limited agreement with cerebral metabolism; here, metabolism was assessed with respect to intracranial temperature to mitigate this uncertainty. Given decreased variability with use of invasive intracranial temperature, the clinical use of non-invasive temperature measurements to approximate cerebral metabolic status during rewarming should be increasingly interpreted with caution following DHCA. Further, to mitigate the hysteresis, alternative strategies, such as a period of continuous cold re-perfusion following DHCA, could be explored to allow recovery of tissue oxygen content before metabolic demand is increased during rewarming.

E.4. Limitations of Animal Model

The limitations of our measurements should be carefully considered in the extrapolation of our neonatal swine model results to human neonates. RF modulation affords the FD-DOS technique additional information over CW NIRS; however, other assumptions in our calculations of $CMRO_{2,i}$ could deviate during DHCA and should be explored.

The concentration of arterial oxygen is assumed to remain constant and also to be a good approximation of arteriolar oxygen concentration. While the former assumption has been validated during DHCP (**Chapter 2, Section D.2)**,[331,332] it is impossible to draw a representative blood gas sample from the brain during DHCA following exsanguination without significantly perturbing metabolic substrate availability. This is a limitation. Additional invasive studies combining microscopy for vessel identification[347] with fluorescence or phosphorescent oxygen content imaging[348,349] could potentially clarify these temporal changes.

The tissue water volume fraction is also assumed to remain constant. Brain water is believed to change in response to CPB and during cellular injury. Thus additional/alternative techniques which permit continuous quantification of brain water concentration should be explored, *e.g.,* wideband optical spectroscopy.[11,350]

Finally, Fick's Law applied to $CMRO_2$ assumes a steady state between the vascular compartment and the tissue compartment. This is often a good approximation which has led to extensive use in cerebral metabolic literature. However, a reformulation of this model to incorporate the effects of dynamic blood volume changes which may perturb both the concentration and volume of these compartments is possible and should be explored.[241,351–353]

Per comparison to human neonates undergoing cardiac repair, we consider a recent feasibility study by Ferradal et al. that employed discontinuous FD-DOS/DCS monitoring in nine neonates undergoing DH CPB during cardiac surgery.[112] This study measured identical cerebral hemodynamic parameters as in the current study during DH CPB; they are reported here as an estimated mean and standard deviation from plotted data. In comparison to our measurements at 18°C, a higher StO_2 (~80% (6) vs. 68% (7)), lower THC (~40 (-) vs. 68 (7) μmol/L), lower OEF (~0.25 (-) vs. 0.42 (0.09)), comparable BFI (~0.9 (0.6) vs. 0.5 (0.4) $*10^{-8}$ cm^2/s), and comparable $CMRO_{2,i}$ (~3.5 (3.0) vs. 2.7 (1.7) $*10^{-8}$ mL $O_2/dL*cm^2/s$) were observed in human neonates at a nasopharyngeal temperature of 20.5°C (2.4). The differences in StO_2 and OEF may be attributed to the lower impact of cooling on oxygen binding affinity in swine compared to humans.[292] Another consideration is that our flow rates were maintained at 150 mL/min/kg. Clinically, the CPB flow rates ranged between subjects from 111 to 173 mL/kg/min during deep hypothermia. Pump flow modulation is often a technique used to expedite cooling to deep hypothermia. Its impact on cerebral metabolism and recovery following DHCA should be explored further.

E.5. Conclusions

In this study we perform novel, continuous quantification of the effects of 40 minutes of deep hypothermic continuous perfusion (DHCP) and deep hypothermic circulatory arrest (DHCA) on cerebral oxygen metabolism in healthy neonatal piglets who underwent simulated cardiac surgery. The advanced diffuse optical imaging techniques represent a significant improvement over CW NIRS, which is more commonly employed. This permitted continuous characterization of the absolute value and changes in critical physiologic parameters during circulatory arrest as a function of time. Specifically, timing to maximal oxygen extraction and minimal concentration of oxy-hemoglobin in tissue were reported. The comparison between DHCA and DHCP groups provided quantification of differences in cerebral metabolic parameters specific to the effects of circulatory arrest which may be used as references values for related measurements in human neonates. Following re-perfusion in DHCA animals, a significant hysteresis in metabolic temperature-dependence during rewarming compared to cooling identified a period of increased neurological risk whereby oxygen metabolism demonstrated diminished sensitivity to temperature. These results demonstrate the utility of non-invasive optical monitoring to individually quantify the effects of DHCA on cerebral oxygen metabolism. These parameters, in turn, may now be explored as potential diagnostics of neurological outcomes for human neonates undergoing DHCA.

CHAPTER 4: PREDICTION OF RETURN OF SPONTANEOUS CIRCULATION DURING CARDIOPULMONARY RESUSCITATION USING NON-INVASIVE FREQUENCY-DOMAIN DIFFUSE OPTICAL SPECTROSCOPY

A. Abstract

Standardized non-invasive neuromonitoring tools with prognostic value during cardiopulmonary resuscitation (CPR) are desirable to help optimize resuscitation strategies for improved neurological outcomes, especially in pediatric cardiac arrest which has very high rates of mortality (>50%) and neurological morbidity. Here, we take steps towards this goal by examining the association between return of spontaneous circulation (ROSC) and cerebral hemodynamics measured non-invasively using frequency-domain diffuse optical spectroscopy (FD-DOS).

One-month old swine (n=31) underwent asphyxia for seven minutes followed by ventricular fibrillation. Resuscitation was conducted for a maximum of 20 minutes, or until ROSC, with pauses for cardiac rhythm check every two minutes and with eligibility for external defibrillation after 10 minutes. FD-DOS measurements of cerebral oxy- and deoxy-hemoglobin concentration ([HbO_2], [Hb], respectively), tissue oxygen saturation (StO_2) and total hemoglobin concentration (THC) were acquired continuously beginning 10 minutes prior to asphyxiation. Associations between FD-DOS measurements and ROSC were determined at 10-minutes of CPR. These parameters, measured from 1-minute into CPR, were assessed for optimal prediction of ROSC and for possible sensitivity and specificity thresholds throughout early CPR (*i.e.,* 2-10 minutes of CPR) using univariate ROC curve analysis at 1-minute intervals.

ROSC was achieved in 74% of the subjects (23/31). At 10 minutes of CPR, absolute and relative values of [HbO_2], StO_2, and THC, with respect to baseline and with respect to the value after 1-minute of CPR, showed significant differences ($p<0.05$) between subjects who attained ROSC compared to those who did not. Absolute change in [HbO_2] from 1-minute of CPR demonstrated the highest mean (SD) AUC of 0.91 (0.07), as well as a stable sensitivity and specificity threshold across 1-minute intervals from 2-10 minutes of CPR. No significant associations between [Hb] and ROSC were found.

Our results demonstrate an early association between non-invasive optical measurement of cerebral hemodynamics during the conduct of CPR and subsequent achievement of ROSC. The work provides proof of concept data for the definition of treatment thresholds for real-time optimization of resuscitation strategies and demonstrates a novel tool for rapid assessment of cerebral health in the event of pediatric cardiac arrest.

B. **Introduction**

Children who suffer cardiac arrest, both in and out of the hospital, face a mortality rate of over 55%[117,123,129] and, among survivors, many do not achieve favorable neurological outcomes.[125,126,354] Current pediatric guidance for cardiopulmonary resuscitation (CPR) incorporates a basic life support strategy comprising chest compressions combined with rescue breathing;[138,355,356] additionally, high-quality CPR includes monitoring of chest compression rate, chest compression depth based on age, and permitting full recoil of the chest between subsequent compressions. This approach, however, neglects individual physiologic response to resuscitative efforts. Indeed, individualized optimization of resuscitation strategies for improved neurological outcomes has been hindered by a lack of standardized neuromonitoring with demonstrated prognostic value. Recent work along these lines has identified the potential of non-invasive cerebral near-infrared spectroscopy (NIRS) to improve guidance of resuscitation for cardiac arrest in adult populations.[201,204–206] Moreover, although only a few case studies of use in pediatric populations have been reported,[216–218] recently published recommendations by the French Group for Pediatric Intensive Care and Emergencies[357] recommends the use of the continuous-wave (CW) NIRS probes, despite no clear evidence of efficacy and limited physiologic accuracy.

Unfortunately, physiologic interpretation of CW NIRS regional cerebral tissue oxygen saturation (rSO_2) has limitations. Calculations of rSO_2 from CW techniques, for example, require assumptions about baseline status (*i.e.,* tissue optical scattering, oxygen saturation, total hemoglobin concentration).[358] These assumptions are problematic because age, physiologic condition, and degree of hypoxic insult can be highly variable from patient-to-patient at the time of CPR initiation.[359] In contrast to CW NIRS, frequency-domain diffuse optical spectroscopy (FD-DOS) is a diffuse optical, near-infrared technique wherein radio frequency modulation of laser sources provides additional phase information that permits quantification of tissue scattering, and thereby ameliorates the need for the baseline assumptions. FD-DOS provides improved quantitative accuracy,[9] and has been used in pediatric populations as a clinical research tool to quantify absolute values of cerebral oxy- and deoxy-hemoglobin concentrations ($[HbO_2]$ and $[Hb]$, respectively), total hemoglobin concentration (THC) and cerebral tissue oxygen saturation (StO_2, %).[24,39,242–245,40,105,109,110,112,239–241] However, FD-DOS has not yet been applied during CPR.

In this work, we endeavored to demonstrate the feasibility of FD-DOS for continuous, absolute quantification of cerebral hemodynamics during asphyxia, ventricular fibrillation, cardiac arrest, cardiopulmonary resuscitation (CPR), and, if achieved, after return of spontaneous circulation (ROSC). The feasibility study was carried out in a pediatric swine model of asphyxia-induced cardiac arrest. Our primary objective was to examine the association between non-invasive, FD-DOS-measured cerebral hemodynamics during CPR and successful ROSC. A second aim was to identify those parameters of FD-DOS that offer significantly associated predictors for ROSC, and a third goal was to explore the feasibility for stable critical decision thresholds during the first 10 minutes of CPR based on FD-DOS parameters. In total the research aims to assess and facilitate potential applications of FD-DOS for non-invasive CPR optimization.

C. Methods

Cerebral hemodynamics were continuously monitored by non-invasive frequency-domain diffuse optical spectroscopy (FD-DOS) in one-month-old, female Yorkshire swine (8-10kg) during asphyxia, ventricular fibrillation (VF) to induce cardiac arrest, and subsequent cardiopulmonary resuscitation. All animal procedures were approved by the Institutional Animal Care and Use Committee at the Children’s Hospital of Philadelphia and conducted in strict accordance with the NIH Guide for the Care and Use of Laboratory Animals.

C.1. Frequency-Domain Diffuse Optical Spectroscopy

FD-DOS is a clinically validated technique for quantification of tissue oxy- and deoxy-hemoglobin concentrations ([Hb] and [HbO_2], respectively. FD-DOS benefits from the simultaneous measurement of optical absorption and scattering properties (μ_a and μ_s’, respectively).[23,109,360] This approach is superior to conventional clinical continuous-wave (CW) near-infrared spectroscopy (NIRS) systems, because it employs radio-frequency amplitude modulation to generate diffusive waves in tissue, permitting measurement of both phase and amplitude information from detected light. Together the changes in amplitude and phase enable unique determination of μ_a and μ_s' at each source wavelength (λ). Given the known wavelength-specific extinction coefficients (ε) of oxy- and deoxy-hemoglobin, the absorption coefficient of water (μ_{a,H_2O}),[20] and an assumed 75% water volume fraction,[257] the cerebral [Hb] and [HbO_2] can derived by solving a system of equations for $\mu_a(\lambda)$ at multiple wavelengths via the relationship:

$$\mu_a(\lambda) = \varepsilon_{HbO_2}(\lambda)[HbO2] + \varepsilon_{Hb}(\lambda)[Hb] + 0.75\mu_{a,H_2O}(\lambda). \quad (4.1)$$

Compared to CW NIRS systems, which assume normative scattering properties to resolve absorption properties, FD-DOS permits more accurate, individualized quantification that takes into account alterations in optical scattering that may result from profound changes in oxygen saturation,[325] metabolic remodeling of cellular membranes due to ATP depletion,[326] changes in red blood cell morphology,[361] and variation in tissue composition.[11]

C.2. Selection of Animal Model

An asphyxia model was selected to best approximate pediatric in-hospital arrests, which are predominantly respiratory mediated.[126,164] This model also permitted a clinical scenario wherein the application of a neuromonitoring device early in the resuscitation period is feasible. Preclinical piglet models have played a critical role in both the optimization of resuscitation strategies[228,362,363] and in the development and validation of FD-DOS techniques.[19,26] One month-old piglets correspond anatomically and neuro-developmentally with toddler-aged humans,[364] which approximates the median age of pediatric victims of cardiac arrest.[119,128]

C.3. Animal Preparation

Animals were initially sedated with ketamine (20 mg/kg IM) followed by 4% inhaled isoflurane via snout mask until intubation by endotracheal tube was achieved with confirmation by end-tidal CO_2 ($EtCO_2$) capnometry. Subsequently, animals were mechanically ventilated (Modulus SE, DatexOhmeda; Madison, WI) on room air using a tidal volume of 10mL/kg, a positive end-expiratory pressure of 6cm H_2O, and titration of respiratory rate to maintain $EtCO_2$ within 38-42mmHg. Anesthesia was maintained using 1-2% inhaled isoflurane with depth of anesthesia monitored via heart rate and blood pressure and confirmed by toe-pinch reflex at 5-minute intervals. Morphological measurements of animal weight, length, and anterior-posterior chest diameter were recorded.

C.4. Physiologic Monitoring

FD-DOS cerebral monitoring was performed using an optical probe with source-detector separations ranging from 0.75 - 3 cm (**Figure 4.1**). The probe was calibrated using tissue phantoms before each animal measurement.[19] Following secure placement of the probe over the left frontal cortex, absolute absorption and scattering coefficients (μ_a and μ_s', respectively) at λ=690, 725, 785, and 830nm were continuously quantified from measurements of amplitude and phase collected at a rate of 10Hz by a commercial FD-DOS instrument operating at a modulation frequency of 110MHz (Imagent, ISS Inc., Champaign, IL). Recorded measures of absorption were used to derive cerebral oxy- and deoxy-hemoglobin concentrations ([HbO_2] and [Hb], respectively), from which cerebral tissue oxygen saturation (StO_2, %) and total hemoglobin concentration (THC, μmol/L) were calculated as:

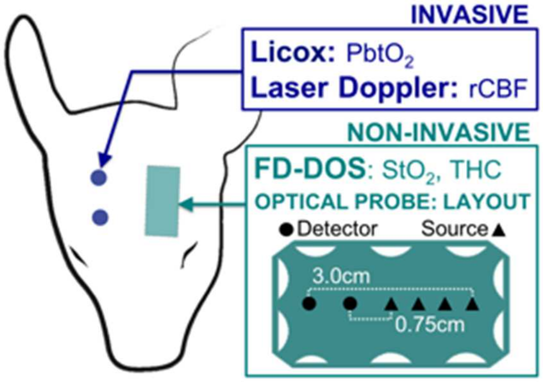

Figure 4.1. CPR Neuromonitoring Placement: Non-invasive frequency-domain diffuse optical (FD-DOS) probe was placed over the left frontal cortex. Source-detector separations ranged from 0.75cm to 3cm. Invasive measurement of $PbtO_2$ and relative cerebral blood flow were conducted through two burrs holes over the right cortex.

$$StO_2\ (\%) = \frac{[HbO_2]}{[HbO_2]+[Hb]}; \tag{4.2}$$

$$THC\ \left(\frac{\mu mol}{L}\right) = [HbO_2]+[Hb]. \tag{4.3}$$

Aortic and right atrial pressures were transduced via solid-state, micromanometer-tipped catheters (4.5-6Fr; Millar Instruments, Houston, TX) inserted through the right femoral artery and vein, respectively, using ultrasound-guided Seldinger technique. A balloon-tipped, thermodilution Swan-Ganz catheter (Edwards Lifesciences; Irvine, CA) was similarly introduced via the left femoral vein and was fluoroscopically directed into the main pulmonary artery. To prevent subsequent clot formation, 200 units/kg of unfractionated heparin was administered following cannula placement.

Additional invasive cerebral monitoring was achieved through two burr holes on the right side of head. This facilitated measurement of relative cerebral blood flow (rCBF, %) in the cortex via a laser Doppler probe (PeriFlux, PeriMed Inc.; Ardmore, PA) affixed to the dura matter and measurement of subcortical brain tissue oxygen content ($PbtO_2$, mmHg) ~1 cm below the cortical surface (Licox CC1-P1, Integra LifeSciences; Plainsboro, NJ).

Systemic physiologic and hemodynamic monitoring comprised electrocardiogram (ECG), aortic pressure (AoP), right atrial pressure (RaP), peripheral saturation (SpO_2) via pulse oximetry, $EtCO_2$, and rectal temperature data. All of these monitoring devices were sampled at rate of 256Hz and displayed using PowerLab software and interfacing hardware (ADI Instruments; Colorado Springs, CO). Chest compression depth and compression rate were captured using a CPR quality monitoring defibrillator (Zoll R Series Plus, Zoll Medical Corp.; Chelmsford, MA).

Following placement of physiologic monitors, a 20 mL/kg bolus of 0.9% sodium chloride solution was administered for post-fasting fluid repletion. Continuous recording of physiologic monitors was initiated 10 minutes prior to asphyxia to establish baseline values and was discontinued either at the end of CPR for non-survivors, or at 4 hours following return of spontaneous circulation (ROSC).

C.5. Experimental Protocol

The experimental protocol is summarized in **Figure 4.2**. Five minutes prior to asphyxia, analgesia was initiated using continuous syringe-pump infusion of intravenous fentanyl (1–10 mcg/kg/h); this was sustained through the asphyxial period. Immediately following confirmation of absence of toe-pinch reflex, asphyxia was induced by clamping of the endotracheal tube following exhalation and was confirmed by the absence of $EtCO_2$. After 7 minutes of sustained asphyxia, ventricular fibrillation (VF) was induced using transcutaneous ventricular pacing. Once VF was confirmed by ECG, the endotracheal tube was unclamped and mechanical ventilation was restarted with a tidal volume of 10 mL/kg, a positive end-expiratory pressure of 6cm H_2O, 100% fraction inspired oxygen, and a respiratory rate of 6 breaths per minute. Manual CPR was immediately initiated with chest compressions administered at a rate of 100

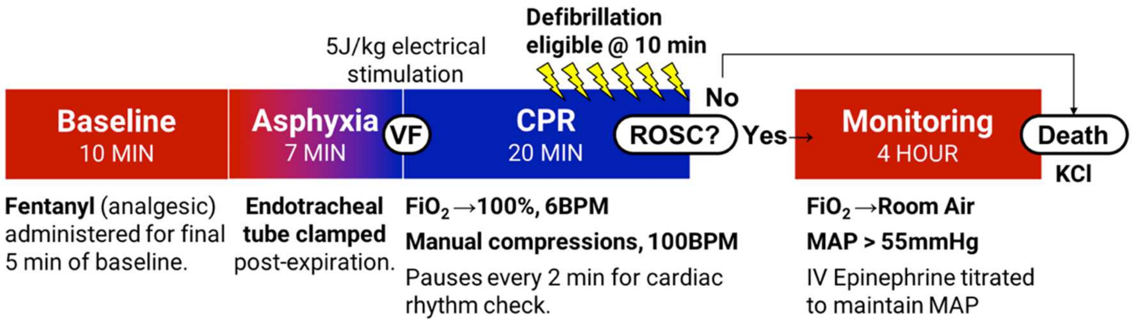

Figure 4.2. Asphyxia-Induced Cardiac Arrest and CPR Experimental Protocol: Continuous non-invasive frequency-domain diffuse optical spectroscopy (FD-DOS) measurements of cerebral hemodynamics were continuously acquired from start of Baseline, through Asphyxia, CPR, and four-hours post-Return of Spontaneous Circulation (ROSC).

compressions per minute. Auditory guidance was provided by metronome and visual feedback provided from the CPR quality monitoring defibrillator. Chest compression depth and vasopressor dosing was determined according to animal allocation into one of three treatment groups:

I. **Depth-guided CPR** (DG-CPR; n = 14): Chest compressions were delivered at the guideline-recommended depth of 1/3 of the anterior-posterior chest diameter, and epinephrine (0.02 mg/kg IV) was administered every four minutes.

II. **Hemodynamic-directed CPR (HD-CPR):** Chest compression depth was actively titrated to maintain an a priori aortic systolic pressure goal of either 90 mmHg (n = 2) or 110 mmHg (n = 2). Vasopressors were administered only when coronary perfusion pressure (CoPP) was less than 20 mmHg; this parameter was automatically calculated and displayed as the difference between the mid-diastolic aortic pressure and right atrial pressure. Vasopressor dosing followed a three-stage cycle starting with 0.02 mg/kg of epinephrine, a repeated 0.02 mg/kg of epinephrine, followed by a switch to

0.4 units/kg of vasopressin, as indicated by CoPP. Administration continued cyclically with a minimum interval of one minute after epinephrine doses and two minutes after a vasopressin dose.

III. **DG-CPR with inhaled nitric oxide** (iNO; n = 10): iNO (20 ppm) was administered beginning one minute into CPR and was continued through the end of the resuscitation period.

In all animals, chest compressions were paused for cardiac rhythm check (every two minutes) for a duration of four seconds. Following ten minutes of chest compressions, animals were externally defibrillated with 5 J/kg, a dose that has had demonstrated efficacy in this animal model.[365] If ROSC was not achieved following defibrillation, CPR was resumed and defibrillation was re-attempted as indicated during cardiac rhythm checks at two-minute intervals. CPR concluded immediately, upon attainment of ROSC, or after the final unsuccessful external defibrillation at 20 minutes of CPR. Following ROSC, FiO_2 was gradually down-titrated from 100% to room air within 10 minutes while maintaining an SpO_2 between 94-99%. Inhaled isoflurane was titrated to absence of toe-pinch reflex. Intravenous epinephrine (0.1 -1 mcg/kg/minute) was titrated as necessary to maintain a minimum mean aortic pressure of > 45 mmHg. Animals were euthanized at four hours post-ROSC using intravenous potassium chloride.

C.6. Statistical Analysis

Our primary analysis examined the association of non-invasive cerebral hemodynamic measurement values at 10 minutes of CPR and the attainment of ROSC. Cerebral hemodynamics incorporated absolute values of $[HbO_2]$, [Hb], StO_2, and THC, absolute and relative changes of $[HbO_2]$, [Hb], StO_2, and THC from baseline, and absolute and relative changes of [HbO_2], [Hb], StO_2, and THC from 1 minute into CPR. The 1-minute time-point was selected for two reasons. First, this corresponds to the clinical period allotted for chest molding (*i.e.*, conformational adaptation of the chest wall to the force of compressions), which impacts the efficacy of early chest compressions. Second, this is a feasible timing window for when non-invasive monitoring could be placed on the patient after arrest recognition and the initiation of CPR. Non-parametric Wilcoxon Rank-Sum tests ($\alpha = 0.05$) were performed to compare values between ROSC and no-ROSC groups, due to the presence of non-parametric variable distributions within each group. Supplementary analysis summarizing post-ROSC absolute and relative changes from baseline at 1-hour intervals was also performed.

Baseline values for each physiologic measure were determined as the mean value acquired during the 2-minute interval prior to asphyxia. Asphyxia-end values were calculated as the mean value acquired in the 15-seconds prior to the end (*i.e.,* 7-minutes) of asphyxia. In order to allow a full 1 minute of chest molding and time for FD-DOS placement, 1-minute CPR values were calculated as the mean of values measured in the 15 seconds immediately following 1 minute of CPR. The 10-minute CPR values were calculated as the mean of values measured in the 15 seconds immediately preceding the 9.5-minute mark of CPR to ensure all subjects were included due to experimental variability in timing of confirmation of ventricular fibrillation.

Selection of Optimal Predictor and Critical Decision Thresholds

Following identification of the FD-DOS parameters significantly associated with ROSC, a secondary analysis was performed to identify which parameter was the optimal predictor for ROSC and to examine the feasibility of stable critical decision thresholds over time during the first 10 minutes of CPR. Only parameters that could be feasibly measured after the start of CPR were included in this analysis. These data were comprised of absolute values, and absolute and relative changes from 1-minute into CPR. In our selection of critical thresholds, we chose to separately maximize specificity (*i.e.,* inverse of false positive rate) or sensitivity (*i.e.,* inverse of false negative rate) to minimize incidence of false outcomes. Our reasoning is that if it is to be a novel diagnostic for CPR optimization, then FD-DOS guidance should only impact care if the prediction is accurate.

For each significant parameter, a ROC curve and two critical thresholds, maximizing specificity (=1) or sensitivity (=1), were determined at 1-minute intervals from 2-10 minutes of CPR using univariate logistic regression for the outcome of ROSC. The average value measured within each 1-minute interval was used to determine the ROC curve, the corresponding AUC, and the critical thresholds whereby the "specificity threshold" corresponded to the parameter value with highest sensitivity for ROSC while maintaining a specificity for ROSC equal to 1, and, similarly, the "sensitivity threshold" corresponded to the parameter value with highest specificity while maintaining sensitivity equal to 1.

The optimal FD-DOS predictor and overall predictor, including systemic hemodynamics, was selected based on the highest mean AUC. A stable specificity or sensitivity threshold was determined to be feasible if the mean threshold had a specificity or sensitivity >0.9 over all intervals, respectively.

D. Results

ROSC was achieved in 74.2% of subjects (n = 23/31) which included n = 9/14 in the DG-CPR group who underwent standard-of-care AHA guideline resuscitation, n = 10/10 who received inhaled nitric oxide (iNO) during AHA guideline resuscitation, and n

= 4/7 who underwent HD-CPR. All animals received a minimum of 10 minutes of CPR, with resumed resuscitation immediately following unsuccessful defibrillation attempts.

D.1. Association of Cerebral Hemodynamics and ROSC

A summary of pairwise comparisons between cerebral and systemic hemodynamic measures, presented as median [IQR], in ROSC and no-ROSC groups at baseline, at the end of asphyxia, and at 10 minutes of CPR, is given in **Table 4.1**. While no significant differences are seen between groups at baseline or during asphyxia (**Figure 4.3**), significant differences in the absolute values of [HbO_2], StO_2, and THC, and significant differences in absolute and relative changes from baseline and 1-minute of CPR, are seen at 10-minutes of CPR. The most highly significant differences ($p<0.001$) were seen in in the absolute and relative change from 1-minute of CPR in these three parameters (**Figure 4.4**). No difference between groups was observed in relative or absolute [Hb] values. This finding suggests that attainment of ROSC and subsequent survival is largely determined by performing high-quality CPR, which in turn provides both adequate oxygen and adequate blood volume (clinical analogue of THC) to the brain.

Table 4.1. Parameters at Baseline, End-of-Asphyxia and 10-minutes of CPR

	ROSC, n=23	No-ROSC, n=8	p-value
Baseline			
$[HbO_2]$§, μmol/L	33.7 (30.3, 37.3)	36.3 (34.4, 43.1)	0.130
[Hb], μmol/L	30.4 (26.8, 35.5)	30.4 (28.1, 34.4)	0.769
StO_2, %	52.2 (46.2, 58.0)	54.8 (53.0, 56.3)	0.484
THC, μmol/L	66.1 (58.9, 68.9)	69.6 (62.3, 74.5)	0.250
Asphyxia, End			
$[HbO_2]$, μmol/L	18.3 (11.3, 24.7)	23.0 (18.7, 24.7)	0.269
[Hb], μmol/L	-15.4 (-22.3, -11.3)	-18.2 (-25.0, -13.1)	0.668
StO_2, %	50.9 (40.4, 66.3)	57.7 (44.4, 62.8)	0.542
THC, μmol/L	48.5 (45.0, 58.8)	56.5 (50.3, 58.5)	0.379
CPR, 10 minutes			
$[HbO_2]$, μmol/L	29.3 (22.1, 34.6)	18.4 (12.5, 21.8)	0.006†
$\Delta[HbO_2]$ from Baseline	-5.5 (-11.7, -1.6)	-22.9 (-29.6, -13.0)	<0.001‡
$r[HbO_2]$ to Baseline, %	84.7 (62.2, 94.3)	39.5 (31.8, 64.0)	0.002†
$\Delta[HbO_2]$ from 1min-CPR	8.3 (4.2, 10.5)	-5.6 (-11.1, -0.2)	<0.001‡
$r[HbO_2]$ to 1min-CPR, %	135.7 (115.8, 148.1)	79.2 (57.6, 99.2)	<0.001‡
[Hb], μmol/L	41.0 (37.3, 47.0)	43.8 (38.2, 49.0)	0.542
Δ[Hb] from Baseline	11.3 (5.6, 14.6)	10.0 (6.4, 17.2)	0.839
r[Hb] to Baseline, %	135.5 (118.8, 152.2)	125.5 (122.2, 156.5)	0.982
Δ[Hb] from 1min-CPR	-4.4 (-9.3, -1.7)	-4.3 (-8.4, -2.5)	0.804
r[Hb] to 1min-CPR, %	89.5 (81.3, 96.2)	90.6 (83.1, 94.0)	1.000
StO_2, %	41.9 (33.3, 48.1)	27.6 (22.1, 35.1)	0.006†
ΔStO_2 from Baseline	-12.4 (-18.7, -6.2)	-25.7 (-34.2, -19.1)	0.006†
$rStO_2$ to Baseline, %	76.2 (62.9, 88.2)	51.0 (40.6, 64.7)	0.005†
ΔStO_2 from 1min-CPR	8.7 (4.9, 14.8)	-1.6 (-7.9, 0.6)	<0.001‡
$rStO_2$ to 1min-CPR, %	126.4 (114.3, 147.6)	96.2 (77.7, 103.8)	<0.001‡
THC, μmol/L	68.8 (62.7, 78.0)	56.4 (55.9, 66.3)	0.020*
ΔTHC from Baseline	6.0 (2.3, 9.6)	-11.1 (-18.6, -2.2)	<0.001‡
rTHC to Baseline, %	109.5 (103.3, 114.5)	84.5 (77.5, 96.2)	<0.001‡
ΔTHC from 1min-CPR	1.0 (0.1, 5.0)	-12.7 (-19.9, -3.2)	<0.001‡
rTHC to 1min-CPR, %	101.6 (100.1, 108.1)	82.6 (75.2, 95.5)	<0.001‡

Reported as median (IQR).

*p<0.05; †p<0.01; ‡p<0.001; § Abbreviations: $[HbO_2]$, oxy-hemoglobin concentration; [Hb], deoxy-hemoglobin concentration; StO_2, tissue oxygen saturation; THC, total hemoglobin concentration; Δ-prefix, absolute change; r-prefix, relative value compared to 100% at baseline.

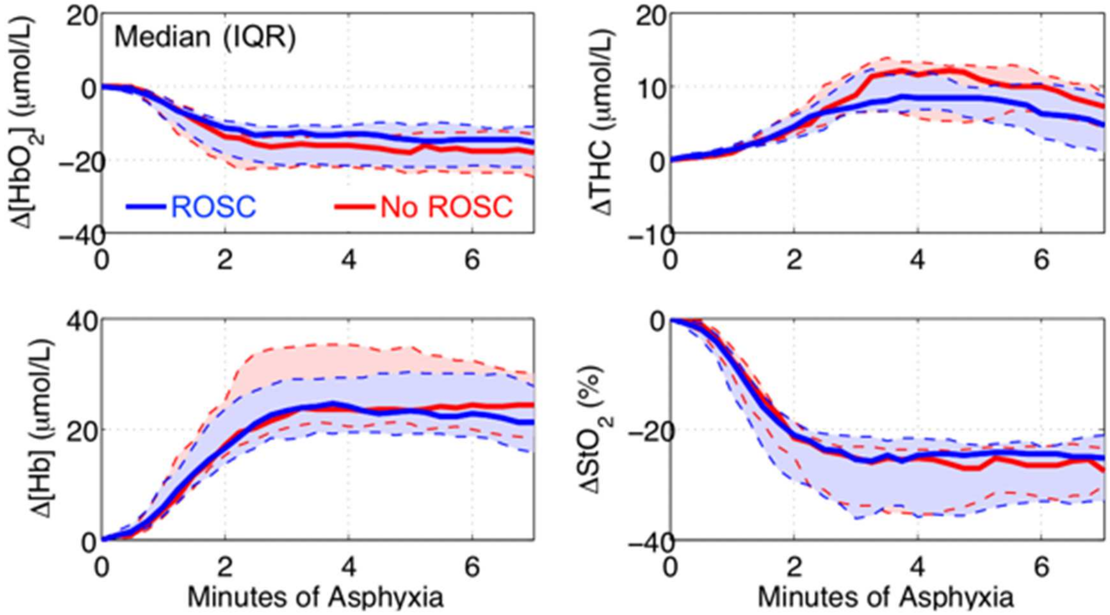

Figure 4.3. Changes in Cerebral Hemodynamics during Asphyxia, ROSC versus No-ROSC: During the 7-minute asphyxial period, all subjects experienced a decreased in concentration of oxy-hemoglobin ([HbO$_2$]) and tissue oxygen saturation (StO$_2$) and an increase in deoxy-hemoglobin concentration ([Hb]) and total hemoglobin concentration (THC). Data is depicted as median (*solid line*) and IQR (shaded region between dotted lines) and colored with respect to outcome group (ROSC, *blue*; No-ROSC, *red*). No significant differences in cerebral hemodynamics distinguish ROSC from No-ROSC subjects prior to start of CPR.

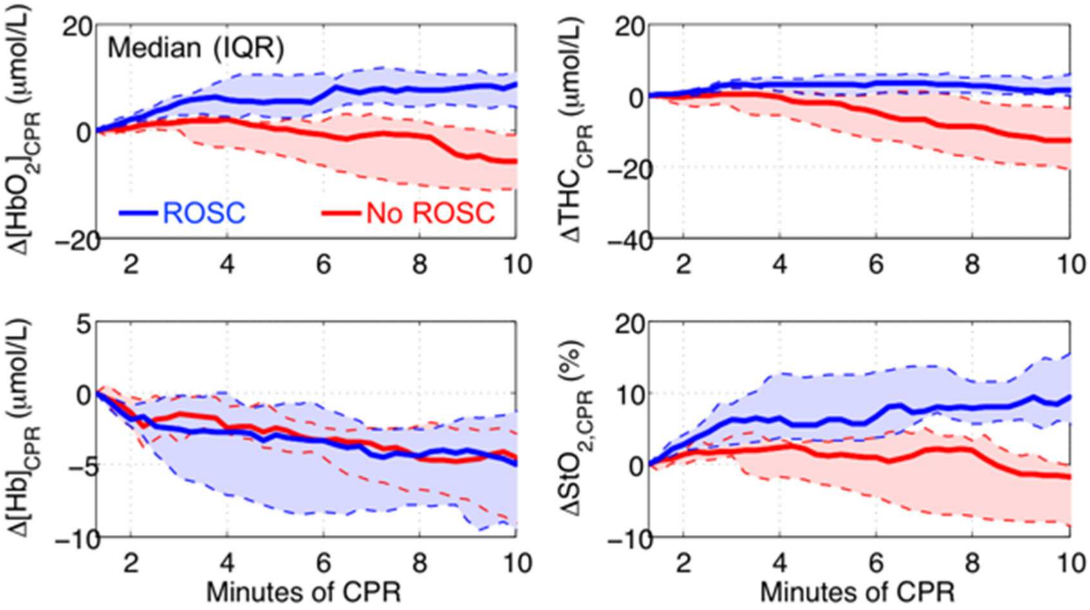

Figure 4.4. Changes in Cerebral Hemodynamics during Early CPR, ROSC versus No-ROSC: For each CPR outcome (i.e., ROSC, in *blue*, or No ROSC, in *red*), the median (*solid line*) and IQR (shaded region between dotted lines) of the change in cerebral oxy-hemoglobin concentration (Δ[HbO$_2$]; *top left*), deoxy-hemoglobin concentration (Δ[Hb]; *bottom left*), total hemoglobin concentration (ΔTHC; top right) and tissue oxygen saturation (ΔStO$_2$; *bottom right*) from 1-minute into CPR are plotted over the first 10-minutes of CPR. Early separation between outcome groups is seen in Δ[HbO$_2$], ΔTHC, and ΔStO$_2$.

D.2. Selection of Optimal Predictor and Critical Decision Thresholds

Table 4.2. Mean AUC and Critical Thresholds Over 1-Minute CPR Intervals for Significant Predictors at 10-Minutes of CPR

Significant Predictors	AUC	Sensitivity Threshold	Specificity Threshold
$[HbO_2]$, µmol/L*	0.72 (0.10)	10.1 (1.7)	30.2 (3.5)
$\Delta[HbO_2]$ from 1min-CPR	0.91 (0.07)	+0.3 (0.8)	+4.6 (1.8)
$r[HbO_2]$ to 1min-CPR, %	0.89 (0.06)	101.2 (3.0)	126.9 (10.1)
StO_2, %	0.71 (0.09)	12.6 (2.0)	46.5 (4.2)
ΔStO_2 from 1min-CPR	0.90 (0.07)	+1.4 (1.6)	+5.1 (0.9)
$rStO_2$ to 1min-CPR, %	0.87 (0.08)	103.8 (4.7)	124.2 (10.3)
THC, µmol/L	0.64 (0.12)	65.3 (19.8)	83.7 (19.0)
ΔTHC from 1min-CPR	0.85 (0.06)	-5.3 (1.6)	+3.3 (1.3)
rTHC to 1min-CPR, %	0.83 (0.07)	94.0 (1.7)	104.7 (1.4)

Reported as mean (standard deviation).

*Abbreviations: $[HbO_2]$, oxy-hemoglobin concentration; StO_2, tissue oxygen saturation.; THC, total hemoglobin concentration; Δ-prefix, absolute change; r-prefix, relative value compared to 100% at baseline.

In **Table 4.2** we list the mean AUC, as well as the mean of the critical specificity and sensitivity thresholds, across all 1-minute intervals from 2-10 minutes of CPR for each significant parameter ($p<0.05$) at 10-minutes of CPR. Examination of the mean AUC values demonstrates a similarity with our comparisons at 10-minutes of CPR, wherein the best predictors of each hemodynamic parameter (*e.g.*, absolute value, relative value) were the absolute and relative change from 1-minute of CPR. Overall, the hemodynamic parameter with the highest mean (SD) AUC of 0.91 (0.07) was absolute change in $[HbO_2]$ from 1min-CPR: ($\Delta[HbO_2]_{CPR}$; **Figure 4.5**). The corresponding mean (SD) sensitivity threshold (*i.e.,* the mean of all thresholds which achieved a specificity of 1 in each 1-min interval) was $\Delta[HbO_2]_{CPR}$ = +0.3 (0.8) μmol/L. Applying this threshold across all 1-min intervals achieved an overall sensitivity of 0.98. Similarly, the mean (SD) specificity threshold was $\Delta[HbO_2]_{CPR}$ = +4.6 (1.8) μmol/L; it achieved an overall specificity of 0.94. Attaining high (>0.9) overall sensitivity or specificity indicates that these mean threshold values may be suitable for sensitive or specific prediction applications at any time-point from 2-10 minutes of CPR.

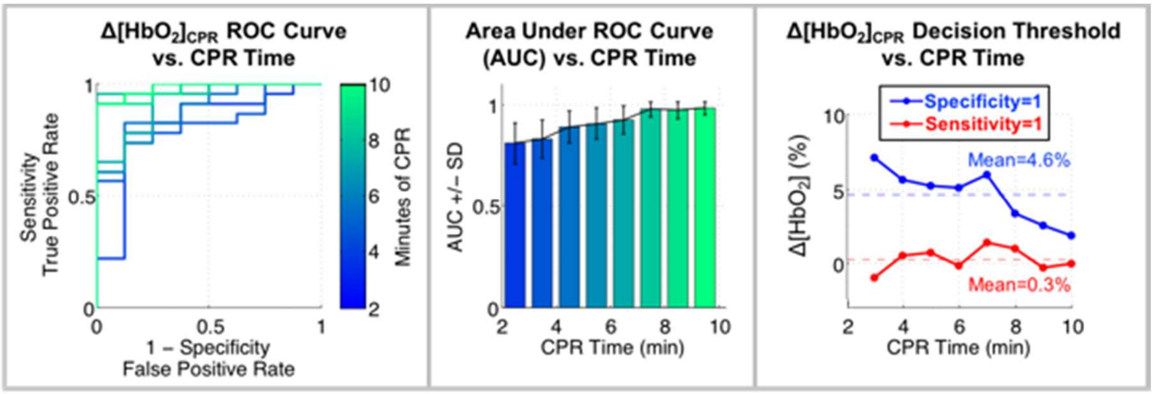

Figure 4.5. Optimal Predictor $\Delta[HbO_2]_{CPR}$ Receiver Operating Characteristic (ROC) Curve Analysis during Early CPR: (*left*) Computed ROC curves, (*center*) corresponding AUCs, and (*right*) critical sensitivity and specificity thresholds for change in absolute cerebral tissue oxy-hemoglobin concentration from 1-minute of CPR ($\Delta[HbO_2]_{CPR}$) are shown. The AUC demonstrated a monotonic increase over early CPR beginning at 0.81 (0.10) after 3 minutes and reaching a maximum value of 0.98 (0.03) after 10 minutes of CPR. The stability of the maximum sensitivity threshold at $\Delta[HbO_2]_{CPR} \sim 0$ indicates animals where no increased in $[HbO_2]$ occurred during CPR did not survive.

D.3. Assessment of Scattering Error Effects on Continuous-Wave (CW) NIRS

The variance in optical scattering (*i.e.*, the reduced scattering coefficient, μ_s') at baseline and changes in optical scattering during asphyxia and CPR were examined in a supplementary analysis (see **Section F. Appendix, Figure 4.A4** and **4.A5**) to characterize the potential errors of CW NIRS physiologic quantification *instead* of FD-DOS. Changes in scattering from baseline and difference between ROSC and no-ROSC groups were examined by Wilcoxon signed-rank test and by Wilcoxon rank sum test, respectively, at the end of asphyxia (7th minute) and in the 10th minute of CPR.

At the end of asphyxia, a significant increase in scattering was observed at 785nm with a median [IQR] = +0.11cm^{-1} [0.01, 0.43] increase from baseline (p = 0.013);

but no differences were found at 690, 725, and 830nm or between ROSC and no-ROSC groups. Red blood cells are known to predominate the near-infrared reduced scattering spectra of whole blood and the reduced scatting spectrum exhibits a monotonic decrease with wavelength > 600nm; however spectral features are present between 750 and 800nm in the reduced scattering coefficient of plasma.[366] The finding of differential changes in scattering with wavelength may correspond to dynamic changes in composition of the blood volume probed by near-infrared photons.

At 10-minutes of CPR, no significant changes in scattering from baseline were observed in subjects who achieved ROSC. However, in the no-ROSC group, we found significant increases in scattering from baseline at 690nm (median [IQR] = +0.87 cm^{-1} [0.26, 1.05], p = 0.039), 785nm (median [IQR] = +0.58 cm^{-1} [0.27, 0.96], p = 0.016) and 830nm (median [IQR] = +0.27 cm^{-1} [0.03, 0.61], p = 0.016). This represents a pronounced 7.8-10.4% change in scattering consistent with observed changes in scattering 17 minutes following euthanasia by pentobarbital in neonatal pigs[324] and during extreme hypoxia (sagittal sinus oxygen saturation < 10%) in piglets.[19] Note, 17 minutes was selected for comparison to the combined period of 7-minutes of asphyxia and 10-minutes of CPR.

Thus, we carried out a simulated assessment of “typical” spatially-resolved CW NIRS measurement errors using simulated infant and pediatric probes from recent publications regarding commercial CW NIRS systems. The infant probe contains two source-detector separations of 0.9 and 2.5cm,[227] and, similarly, the pediatric probe, separations of 1.2 and 4.0cm.[29] to assess the effects of varying scattering from the CW NIRS assumptions of constant scattering from baseline. Using the ‘dc slope’ method of the spatially-resolved CW NIRS technique,[26] the absolute value of optical absorption (μ_a) is calculated from a fitted slope (S) and an assumed optical scattering coefficient ($\mu_s{}'$) as:

$$\mu_a = \frac{S^2}{3\mu_s'}. \tag{4.4}$$

Errors in the CW NIRS calculation of μ_a are equated to 1) errors in the assumption of a linear "dc slope" relationship (explained below), 2) the assumption of constant scattering coefficients over time, and 3) the assumptions of a constant scattering power, a parameter which determines the wavelength-dependence of the assumed scattering coefficients. The impact of these errors on μ_a and the calculation of [HbO_2], [Hb], THC, and StO_2 are examined. As the assumptions underlying the first error incorporate the second error, these will be examined in unison. Due to normality of baseline scattering across subjects by Shapiro-Wilk test, the methodology and results of our scattering error analysis is reported using means, standard deviations, and 95% CIs.

Assumption of Constant Scattering and Source-Detector Separation Linearity

The linear "dc slope" relationship underlying the spatially-resolved CW NIRS technique can be derived from the CW solution for the detected diffuse reflectance (R, W cm^{-2}) at a source-detector separation r (cm) with underlying tissue modeled as a semi-infinite homogeneous medium (**Equation 1.24**):[26]

$$\mathrm{R_{CW}}(r) = C\left[\left(\sqrt{3\mu_a\mu_s'} + \frac{1}{r}\right)\frac{e^{-\sqrt{3\mu_a\mu_s'}r}}{r^2}\right]. \tag{4.5}$$

The variable $C \cong 5I_0/6\pi\mu_s'$ when $\mu_s' \gg \mu_a$ and the index of refraction of the medium is matched with the index of refraction outside the medium at the semi-infinite boundary. I_0 is the intensity of the source (measured in W). Given these assumptions, C may be assumed to remain constant with respect to r. **Equation 4.5** may be rearranged into the following expression

$$\ln\left(\frac{\mathrm{R_{CW}}(r)\cdot r^2}{I_0}\right) = -r\sqrt{3\mu_a\mu_s'} + \left[\ln\left(\frac{r\sqrt{3\mu_a\mu_s'}+1}{r}\right) + constant\right], \tag{4.6}$$

which becomes linear with respect to r on the right-hand side when $r\sqrt{3\mu_a\mu_s'} \gg 1$. The measured diffuse reflectance ($\mathrm{R_{CW}}(r)$) may be fitted by linear regression with respect to source-detector separations (r) to derive the slope ($S = -\sqrt{3\mu_a\mu_s'}$). This brings us to the result of **Equation 4.4** which is used to calculate μ_a.

The assumption of linearity and the accuracy of the relationship between the fitted slope and tissue optical properties (**Equation 4.4**) requires that $r\sqrt{3\mu_a\mu_s'} \gg 1$. While this is generally true, for small source-detector separations or absorption or scattering coefficients, the accuracy of this assumption becomes diminished. Without assuming $r\sqrt{3\mu_a\mu_s'} \gg 1$, for a typical commercial SRS probe geometry with two separations (r_1, r_2), the expression for the fitted slope (S) becomes

$$-\sqrt{3\mu_a\mu_s'} + \ln\left[\frac{r_1}{r_2}\left(\frac{r_2\sqrt{3\mu_a\mu_s'}+1}{r_1\sqrt{3\mu_a\mu_s'}+1}\right)\right](r_2 - r_1)^{-1}. \tag{4.8}$$

The error of the SRS-approximated slope is readily given by the second additive term in the expression. Because r_1 and r_2 are necessarily positive, this error term always results in an increase in the absolute value of the slope. This translates into a fitted S^2 that is always more positive than an S^2 calculated from **Equation 4.4** using accurate optical properties. The error becomes smaller as $|r_2 - r_1| \gg 0$, i.e., the difference in the selected source-detector separations is large. Also, as observed earlier, when μ_a and μ_s' increase and $r_1\sqrt{3\mu_a\mu_s'}$ and $r_2\sqrt{3\mu_a\mu_s'}$ both become $\gg 1$, the logarithmic error expression reduces to 0.

However, errors are introduced in the calculation of μ_a (**Equation 4.4**) by both errors in the slope (S) in the numerator, and errors in the assumption of μ_s' in the denominator. Errors in μ_a may be expressed as:

$$\frac{\mu_{a,CW}}{\mu_a} = \left(\frac{S_{CW}}{S}\right)^2 \frac{\mu_s'}{\mu_{s,CW}'}. \tag{4.9}$$

Thus, as scattering is over-estimated, absorption becomes under-estimated.

To best quantify potential μ_a errors attributed to the use of a fixed "population-average" scattering assumption for all subjects, we examine our experimental measurements of inter-subject variation at baseline and at 10-minutes of CPR. At baseline, our absolute scattering coefficient at $\lambda = 690nm$ exhibits a coefficient of variation of 17.3% across 31 subjects. This is in agreement with optical property variability in human neonates[5] and neonatal pigs.[19] At 10-minutes of CPR, the no-ROSC group demonstrated a +10.8% (SD=8.8%) change in scattering from baseline. Using the mean $\mu_s'(\lambda = 690nm)$ at baseline (11.0 cm^{-1}) as an informed scattering assumption for CW NIRS, the error in the CW NIRS measurements of $\mu_a(690nm)$ at 10-minutes of CPR is plotted in **Figure 4.6** with respect to the error in assumed scattering.

Due to the SRS linearity assumption, even with no error in scattering, estimations of μ_a exhibit a 5.2% (95% CI: 3.9-7.6) error using the pediatric probe and a 10.5% (95% CI: 8.1-15.34) error using the infant probe. Given that the 95% CI of FD-DOS measured scattering values at 10-minutes of CPR ranged from 7.9 to 15.0 cm^{-1}, our analysis assessed a realistic range of scattering errors (from -26% to +40%) that would be observed during this critical time-period. This range of error in $\mu_s'(690nm)$ resulted in a $\mu_a(690nm)$ error ranging from +47% to -18% in the infant probe, and from +41 to -24% in the pediatric probe. We next observe how these errors in μ_a quantification propagate into errors in physiologic measurements.

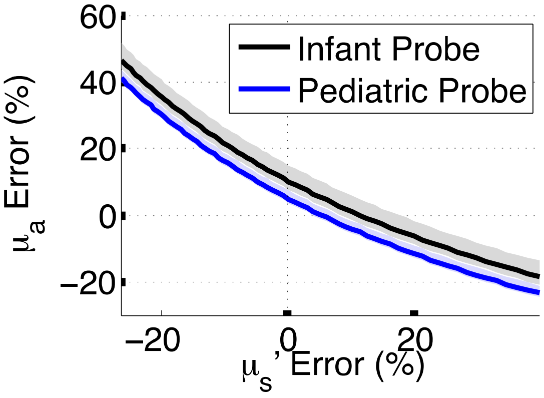

Figure 4.6. Spatially-Resolved CW NIRS μ_a Measurement Error at 10-Minutes of CPR is plotted for a typical infant probe (SDS = 0.9 and 2.5cm) and a pediatric probe (SDS = 1.2 and 4.0cm) with respect to the error of an assumed scattering coefficient (μ_s') over the 95% CI of measured μ_s'(690nm) at 10-minutes of CPR.

Assumption of Constant Scattering Power

In order to translate measurements of μ_a into physiologic properties, measurements at additional wavelengths are necessary. As a result, CW NIRS systems also require assumptions regarding the dependence of scattering on wavelength, which has been shown to be well approximated by Mie scattering using the expression[11]

$$a\left(\frac{\lambda}{500nm}\right)^{-b} = \mu_s'(\lambda). \qquad (4.10)$$

From the mean of reported scattering coefficient values in neonatal piglets of comparable size to our population,[26] we are able to solve for the normalization factor a = $\mu_s'(500nm)$ = 15.3 cm^{-1} and the scattering power b = 1.22. Notably, the scattering power varied widely, from 0.49 to 1.60, across subjects in this prior report; this identifies yet another source of error that cannot be determined by CW NIRS methods. Using these literature-derived parameters, we calculate reasonable CW NIRS assumptions for $\mu_s'(\lambda)$ at 690, 725, 785, and 830nm as 10.4, 9.7, 8.8, and 8.3 cm^{-1}, respectively. For comparison, the scattering power was also determined from measured scattering properties across all subjects in the present work, at baseline and in the no-ROSC group at 10-minutes of CPR, by linear regression of the linear rearrangement of **Equation 4.10** with respect to $\ln(\lambda)$:

$$\ln\left(\mu_s'(\lambda)\right) = -b(\ln(\lambda)) + \text{constant}. \tag{4.11}$$

With similar variation to the referenced scattering power, the mean (SD) scattering power at baseline was 1.15 (0.63), and at 10-minutes of CPR, 1.49 (0.79). Scattering power has been shown to vary greatly both with-in similar tissues as well as across different types of tissue.[11] A shift in scattering power in the no-ROSC group may be diagnostic of a deleterious change in tissue composition and should be examined in future investigations.

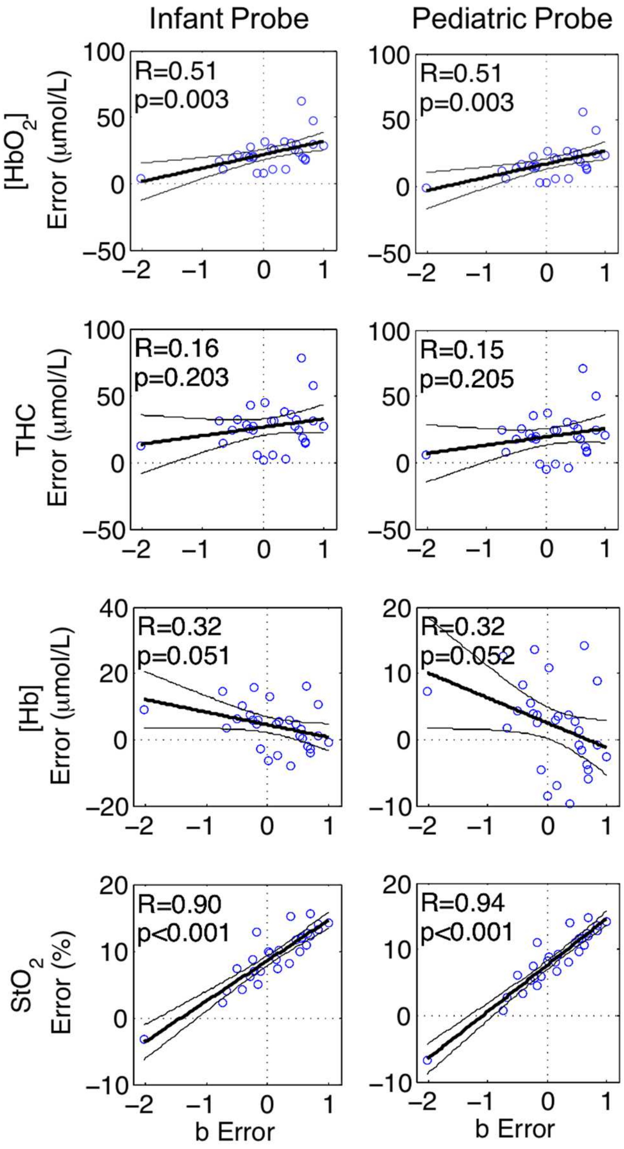

Figure 4.7. Physiologic Error Dependency on Scattering Power: The absolute error in [HbO$_2$], [Hb], THC, and StO$_2$ are plotted for the infant probe (*left*) and the pediatric probe (*right*) with respect to the absolute error in assumed scattering power (b) at baseline. The error in b is significantly and positively correlated with error in [HbO$_2$] ($p=0.003$) and StO$_2$ ($p<0.001$).

Using calculated scattering assumptions from literature, we computed the error in CW NIRS quantification of StO$_2$ (analogous to rSO$_2$ for CW NIRS), [Hb], [HbO$_2$], and THC with respect to the error in scattering power at baseline. Note that this error results from both errors in scattering power as well as the errors in the scattering coefficients.

To quantify the specific dependency of error on scattering power, we examined the Pearson's correlation coefficient (R) between absolute error in measured physiologic values and error in scattering power (**Figure 4.7**).

When there is no error in scattering power (b Error = 0), we observe that the linearity assumption and scattering assumptions (discussed in the previous section) have predominantly resulted in an overestimation of all physiologic parameters for both the infant and pediatric probe. The error in scattering power demonstrates a significant correlation with error in [HbO_2] (R=0.51, p=0.003) and error in StO_2 (R=0.90-0.94, p<0.001). When the scattering power is over-estimated (b Error > 0), even greater over-estimation of StO_2 and [HbO_2] result. Notably, the Pearson's correlation coefficient for StO_2 corresponds to a high coefficient of determination (R^2) ranging from 0.81-0.88. From this finding we conclude that the majority of CW NIRS StO_2 quantification error at baseline in our data is explained by error in the assumed scattering power.

CW NIRS Quantification Error during Asphyxia and CPR

To conclude our error analysis, we examine the physiologic error during asphyxia and CPR resulting from the assumptions of linearity and constant scattering and scattering power discussed in the previous two sections. Using the simulated CW NIRS data, we re-evaluate the significant effects observed in our FD-DOS data to determine if similar results would have been achieved using CW NIRS techniques.

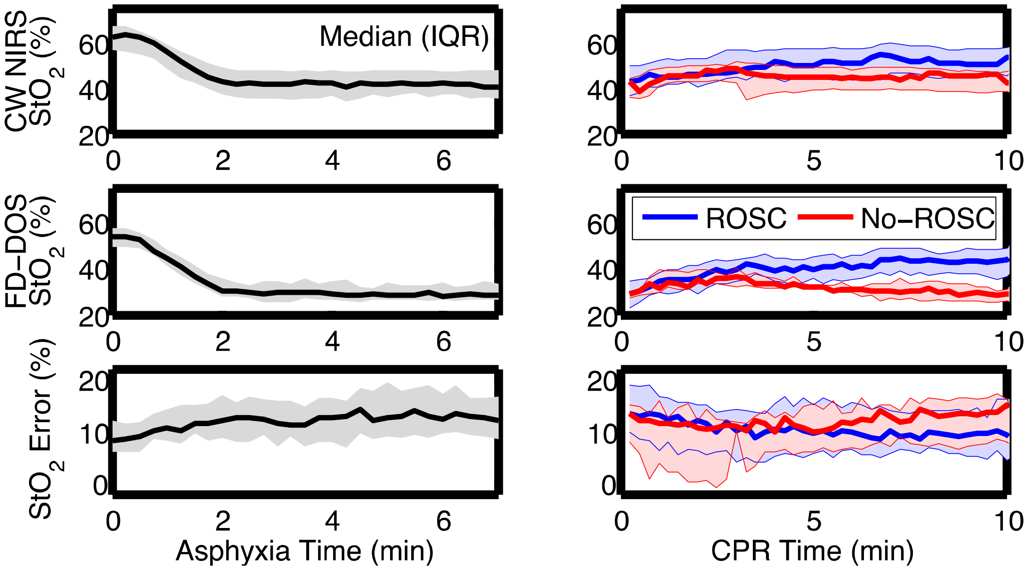

Figure 4.8. Error in CW-NIRS Measurement of StO_2 during Asphyxia (*left*) and CPR (*right*): The error (*bottom*) in the CW NIRS quantification of StO_2 (*top*), compared to FD-DOS quantification of StO_2 (*middle*), is plotted with respect to time. The CW NIRS StO_2 measurements exhibit greater inter-subject variability and diminished contrast during asphyxia and CPR. Limited separability between ROSC and No-ROSC groups is observed using the CW NIRS technique.

The median and IQR of errors in CW NIRS quantification of StO_2 and the change in StO_2 (ΔStO_2; from baseline during asphyxia, from 1-minute of CPR during CPR) are plotted in **Figure 4.8** and **Figure 4.9**, respectively. In the absolute value data, during asphyxia, CW NIRS data exhibits greater variability and over-estimates FD-DOS data at all time points with a median absolute error ranging from +8.2 to +16%. During CPR, separate analyses of ROSC and no-ROSC groups reveal a reduction in separability resulting from a decreasing trend error in the ROSC group with time but increasing trend in error in the no-ROSC group with time. A comparison of the CW NIRS StO_2 and its change at 10-minutes of CPR, between ROSC and no-ROSC groups (**Table 4.3**), demonstrates significant ($p<0.05$) for absolute StO_2, but not ΔStO_2 or $rStO_2$. Neither CW NIRS quantification of THC or $[HbO_2]$ was found to significantly differ ($p<0.05$) between groups.

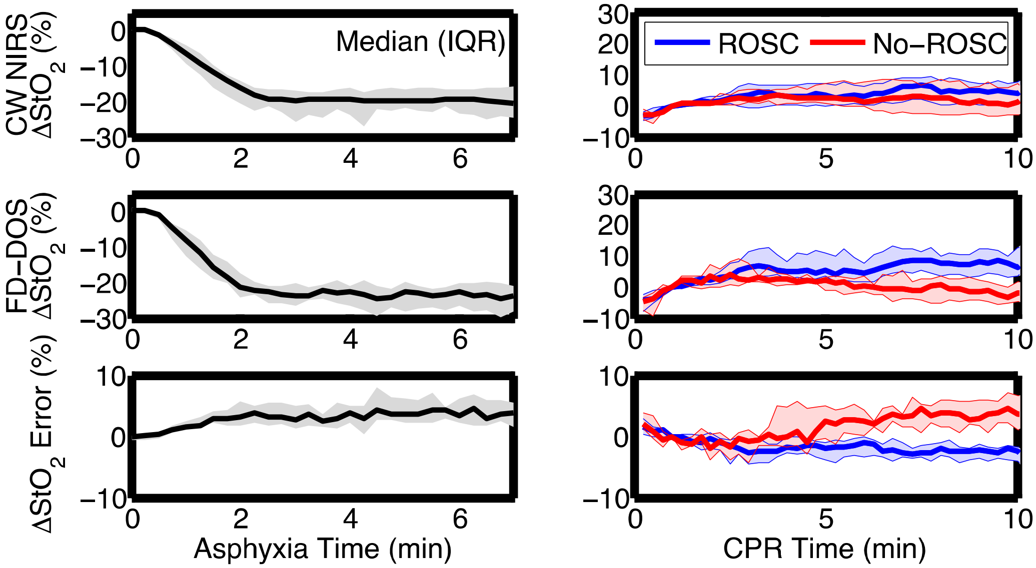

Figure 4.8. Error in CW-NIRS Measurement of Change in StO₂ (ΔStO_2) during Asphyxia (*left*) and CPR (*right*): The error (*bottom*) in the CW NIRS quantification of ΔStO_2 (*top*), compared to FD-DOS quantification of ΔStO_2 (*middle*), is plotted with respect to time. The CW NIRS ΔStO_2 measurements exhibits less error compared to absolute measurements of StO_2, however, contrast during asphyxia and CPR remains diminished compared to FD-DOS measurements. Limited separability between ROSC and No-ROSC groups is observed using the CW NIRS technique.

Identical assessment of the predictive power of CW NIRS StO_2 over time (as described in Section C.6, “Selection of Optimal Predictor and Critical Decision Thresholds”) resulted in a mean (SD) AUC of 0.70 (0.09). This is comparable in predictive power and predictive stability to the FD-DOS StO_2 AUC result of 0.71 (0.09). More modest agreement of predictive power and stability is also achieved by CW NIRS quantification of [HbO_2] which exhibits a mean (SD) AUC of 0.64 (0.11) compared to 0.72 (0.10) using FD-DOS. Examination of the identical tabulation of the AUC of the remaining CW NIRS variables (**Table 4.3**), as reported in **Table 4.2** for FD-DOS variables, show diminished predictive power by greater than one standard deviation. These results reveal the limited ability of the CW NIRS technique to accurately quantify absolute concentrations of [HbO_2], [Hb], and THC in tissue; this, in turn, limits the predictive utility of CW NIRS measurements of these parameters to guide CPR.

Table 4.3. Simulated CW NIRS Predictors, ROSC Association and Mean AUC from 2 to 10-Minutes of CPR

CW NIRS Predictors	ROSC	No-ROSC	p	Mean AUC
$[HbO_2]$, μmol/L*	43.9 (38.5, 54.0)	32.1 (29.9, 38.9)	0.079	0.64 (0.11)
$\Delta[HbO_2]$ from 1min-CPR	5.2 (0.8, 8.7)	-4.7 (-15.3, 3.7)	0.038	0.70 (0.07)
$r[HbO_2]$ to 1min-CPR, %	111.8 (101.9, 126.6)	92.7 (72.1, 110.5)	0.109	0.65 (0.05)
StO_2, %	50.3 (45.0, 57.0)	45.7 (38.0, 46.9)	0.023	0.70 (0.09)
ΔStO_2 from 1min-CPR	4.4 (0.7, 7.6)	-0.4 (-4.2, 3.6)	0.097	0.64 (0.06)
$rStO_2$ to 1min-CPR, %	106.9 (101.6, 116.9)	99.3 (90.0, 107.9)	0.153	0.62 (0.06)
THC, μmol/L	87.7 (72.8, 100.8)	82.8 (77.5, 83.4)	0.593	0.49 (0.11)
ΔTHC from 1min-CPR	1.2 (-1.3, 6.3)	-10.3 (-21.3, -0.1)	0.033	0.72 (0.07)
rTHC to 1min-CPR, %	101.5 (98.4, 109.2)	90.9 (80.2, 99.8)	0.033	0.72 (0.05)

Reported as mean (standard deviation).

*Abbreviations: $[HbO_2]$, oxy-hemoglobin concentration; StO_2, tissue oxygen saturation.; THC, total hemoglobin concentration; Δ-prefix, absolute change; r-prefix, relative value compared to 100% at baseline.

In summary, the CW NIRS quantification of absolute StO_2 demonstrates the potential to achieve similar results to more quantitative diffuse optical techniques during CPR; however, it fails to comparably quantify the change in StO_2 or underlying physiologic parameters of $[HbO_2]$, [Hb], and THC and their changes during CPR. These parameters yield greater predictive power for ROSC and cannot be accurately assessed by CW NIRS.

E. Discussion

In this work, the novel application of quantitative, non-invasive frequency-domain diffuse optical (FD-DOS) monitoring during CPR uncovered significant associations between measured cerebral hemodynamic parameters and the outcome of ROSC, a critical step towards survival following cardiac arrest. Further analysis of the predictive value and stability of prediction for these parameters during the first 10 minutes of CPR demonstrated the potential utility of non-invasive optical monitoring during CPR for real-time optimization of resuscitation outcomes. Specifically, cerebral tissue oxygen saturation (StO_2), oxy-hemoglobin and total hemoglobin concentration ($[HbO_2]$ and THC, respectively), measured using FD-DOS at 10-minutes of CPR, were each significantly associated with ROSC at 10-minutes of CPR. Across these first 10 minutes, absolute change in $[HbO_2]$ from 1-minute of CPR ($\Delta[HbO_2]_{CPR}$) was found to be the best predictor of subsequent ROSC, and stable, high-sensitivity and high-specificity thresholds were determined. This application of FD-DOS to CPR represents an important advancement in physiologic quantification over previous clinical applications of CW-NIRS to CPR. By providing improved physiologic accuracy and ROSC prediction, real-time FD-DOS guidance of CPR holds tremendous promise to improve neurological outcomes following pediatric cardiac arrest.

Prior adult and pediatric literature, as well as animal models, describing the use of non-invasive cerebral optical monitoring during CPR have been limited to reporting of CW-NIRS measurements of rSO_2 (*i.e.*, an analogue of StO_2) and either trends or estimated values of [Hb], $[HbO_2]$, and THC. By quantifying absolute scattering and its change, the present application of FD-DOS permitted the critical examination of absolute $[HbO_2]$, [Hb], and THC during CPR; it also permitted their association with outcome. The study thus uncovered new insights into the necessary and sufficient requirements for ROSC in the brain. Measured values of [Hb], or its changes during CPR, did not have an association with resuscitation outcome. This suggests that the level of extraction of oxygen and, potentially, the level of persisting metabolic activity of the brain, is not a key factor for resuscitation. Levels of $[HbO_2]$ and THC, and their ratio, StO_2, were significantly associated with ROSC. However, the most significant parameters were not absolute values, but rather the change from start of CPR. This supports the notion that significant inter-subject variability exists in the absolute value of these parameters.

Importantly, a positive increase in [HbO_2] and THC in the ROSC group underscores that the ability of CPR to deliver oxygen and maintain blood volume in the brain is critical to resuscitation. By the 5th minute of CPR, $\Delta[HbO_2]_{CPR}$ demonstrated an AUC > 0.90 suggesting neuromonitoring may be used to quickly identify whether or not ongoing CPR is a viable strategy for the patient or if alternative or supplementary interventions are necessary.

Existing clinical reports of CW NIRS monitoring were examined for comparability of trends to explore whether our model mirrored the effects of cardiac arrest and CPR seen clinically. The absolute value of StO_2 after 10-minutes of CPR in the ROSC (median [IQR] = 41.9% [33.3, 48.1]) versus no-ROSC groups (median [IQR] = 27.6% [22.1, 35.1]), as well as the difference between group medians (14.3%), is within the range of mean rSO_2 values reported in a recent meta-analysis by Cournoyer et al. of CW-NIRS monitoring during cardiac arrest and resuscitation in human subjects.[201] The mean values during CPR in individuals who achieved ROSC ranged from 35% to 47.2%, and in individuals who did not achieve ROSC ranged from 17% to 35.4%, with standard deviations of both groups ranging from 1.26% to 17.9%. The difference in means between groups ranged from 6.3% to 23.3%. Another finding corroborated by our results, is that while minimal differences were seen at initiation of CPR between patients who would go on to ROSC and those who would not, the administration of CPR had significant intra-subject variability causing a differentiation in ROSC outcome and associated changes in cerebral oxygenation. This finding emphasizes that current CPR administration guidelines are not an effective strategy for everyone, and that non-invasive neuromonitoring of cerebral hemodynamics could provide more individualized guidance.

The quantitative agreement with Cournoyer et al. reflects that the assumptions used for clinical CW-NIRS rSO_2 monitors are a reasonable representation of average physiologic properties. However, in the setting of profound ischemia, changes in scattering have been shown to become significant.[26,324] The Fahraeus effect is a potential mechanism behind these changes whereby decreased axial alignment at lower red blood cell flow velocities causes dynamic hemoconcentration within the vessel and, as a result, an increase in scattering.[367] Because the scattering spectra of red blood cells and tissue slope down with increasing wavelength,[11,367] changes in scattering differentially impact the concentration of deoxy-hemoglobin compared to oxy-hemoglobin.

Supplementary analysis was performed to quantify these potential errors in CW NIRS physiologic measurements resulting from methodologic assumptions. These errors were calculated with respect to our quantitative FD-DOS measurements of baseline absorption and scattering properties and their change during asphyxia and resuscitation. This analysis clearly demonstrated limitations of CW NIRS monitoring. Using a typical pediatric-sized optical probe, errors in the assumed constant scattering coefficient, ranging from -26% to +40% at 10-minutes of CPR, resulted in CW NIRS absorption property errors ranging from +41% to -24%. Notably, nearly 90% of the variation in StO_2 error at baseline was explained by the error of the assumed scattering power (i.e., the wavelength-dependence of scattering assumptions). During asphyxia and CPR, CW NIRS quantification of StO_2 (or, analogously, rSO_2) consistently over-estimated the true StO_2 value. While a comparison of CW NIRS StO_2 between ROSC and no-ROSC groups at 10-minutes of CPR remained significant, all other hemodynamic parameters and their changes no longer discriminated outcome. This evidence reinforces that absolute hemoglobin concentration measures from CW NIRS instruments should be interpreted cautiously. While absolute errors are substantially diminished when examining changes in hemodynamic parameters, the physiologic impact of hypoxic-ischemia on scattering causes differential trends in error that confound the interpretation of CW NIRS measures. Ultimately, CW NIRS was unable to access the predictive power of changes in hemodynamic parameters. However, the CW NIRS measurement of StO_2 had comparable predictive power to the FD-DOS StO_2 measurement. Given the widespread adoption of CW NIRS systems, we are optimistic that this parity may reduce barriers for clinical translation of non-invasive optical neuromonitoring.

Both Asim et al. and a recent study by Parnia et al. have made significant strides in demonstrating the clinical feasibility of non-invasive optical neuromonitoring during the conduct of in-hospital resuscitation in adults.[204,368] However, the identified predictors in both studies were assessed as averages over several minutes and stability throughout the resuscitation period was not assessed; these issues present prohibitive challenges for real-time guidance. Using improved FD-DOS quantification of cerebral hemoglobin concentrations, we have identified $\Delta[HbO_2]_{CPR}$ as a promising predictor to address these shortfalls. The advanced application of FD-DOS quantification to the CPR domain offers improved predictive power and real-time sensitivity by correcting for errors in assumptions of scattering and linearity (*see above*, **Section D.3**) inherent to CW-NIRS methods. Note, from the perspective of exercising caution when deploying a novel diagnostic for guidance, we determined critical thresholds with maximized sensitivity and specificity to minimize false-negatives and false-positives, respectively, with the intent of minimizing impact to standard-of-care. As such, reported sensitivity thresholds may be used to identify subjects who would not ROSC and for whom an alternative intervention should be considered. Similarly, specificity thresholds may be used to identify individuals where the standard-of-care is sufficient and should not be considered for alternative intervention. Ultimately, these thresholds should be evaluated more broadly by including respective healthcare and patient costs for the given decision outcome.

E.1. Study Limitations

This observational study has determined important associations between cerebral hemodynamics and ROSC and has established a model for optimal predictor selection that should be further optimized, as discussed, depending on clinical application. Furthermore, independent prospective validation is necessary to confirm our observational findings. Open questions remain regarding appropriate interventions in-response to deficits in $\Delta[HbO_2]_{CPR}$. A multifactorial response using other significant parameters is likely necessary to determine the most effective strategy. For example, if both $\Delta[HbO_2]_{CPR}$ and ΔTHC_{CPR} are diminished, this is indicative of limited oxygen supply as well as oxygen availability. Efforts should be made to both increase brain perfusion (*e.g.*, increased depth of compressions) as well as oxygenation (*e.g.,* increased rescue breathing, use of supplemental oxygen); however, if only $\Delta[HbO_2]_{CPR}$ is diminished and THC levels are stable or rising, this is indicative of sufficient cerebral preload pressure (*i.e.*, compressions are getting blood to the brain) but delayed transit through the brain resulting in critical levels of oxygen depletion that may be ameliorated by drug administration to decrease central venous pressure (*i.e.*, the “afterload”). The exciting prospect of non-invasively directing optimized CPR still requires improved understanding of the impact of such interventions on cerebral hemodynamic parameters such that an optimal management strategy may be devised and subsequently optimized.
Furthermore, while this large-animal model is a high-fidelity replication of pediatric resuscitation procedures following respiratory-mediated arrest, generalizability of

determined thresholds to alternative pediatric populations where the arrest is cardiac in origin requires additional study.

E.2. Conclusions

Advanced, quantitative diffuse optical neuromonitoring was applied during CPR, for the first time, to determine significant associations between measured cerebral hemodynamics and ROSC following asphyxia and cardiac arrest in a pediatric swine model. Our findings have provided novel insights regarding the cerebral physiology of resuscitation as well as provided promising predictors of ROSC that may be applied within the first few minutes of CPR. Rigorous characterization of quantification error due to assumptions underlying clinical spatially-resolved CW NIRS systems demonstrate the limited potential of this technique to access our novel diagnostics. Further use of non-invasive hemodynamic neuromonitoring during investigations of cardiac arrest and resuscitation is needed to improve our understanding of the impact of existing CPR strategies on cerebral physiology and its association with successful resuscitation outcomes. It is our earnest hope that the development of novel strategies incorporating non-invasive, *quantitative* optical neuromonitoring guidance will facilitate reduction of mortality and neurological morbidity in children following cardiac arrest.

F. Appendix

F.1. Supplemental Methods

Comparison of Invasive and Non-Invasive Neuromonitoring

Comparisons between invasive and non-invasive neuromonitoring offer improved confidence that non-invasive measurements accurately reflect the dynamic physiology of the brain. Separate linear mixed-effects models including random slope and intercept effects were used to examine the relationship between relative values (%) of non-invasive and invasive measurements of cerebral oxygenation (i.e., tissue oxygen saturation, StO_2, and brain tissue oxygen content, $PbtO_2$, respectively) and cerebral blood flow (i.e., diffuse correlation spectroscopy blood flow index, rCBF DCS, and laser Doppler blood flow, rCBF LD, respectively) during asphyxia and CPR. Results are shown and discussed in **Figure 4.A1** and **Figure 4.A2** (see **Section F.3**).

Recovery of Cerebral Hemodynamics following ROSC

Non-parametric Wilcoxon signed rank tests ($\alpha = 0.05$) were performed to compare post-ROSC values to pre-asphyxia baseline values due to the presence of non-parametric distributions of the difference within each parameter. The 1, 2, 3 and 4-hour post-ROSC values were calculated as the mean of values measured in the 1 minute immediately preceding each time-point. Results are summarized in **Table 4.A1** (see **Section F.2**) and plotted in **Figure 4.A3** (see **Section F.3**).

F.2. Supplemental Tables

Table 4.A1. Cerebral Hemodynamic Recovery following ROSC

	Post-ROSC 1 hour	Post-ROSC 2 hour	Post-ROSC 3 hour	Post-ROSC 4 hour
$[HbO_2]$, µmol/L	32.3 (28.8, 37.1)	34.0 (28.3, 36.9)	35.2 (30.7, 41.4)	37.5 (32.8, 43.1)†
r$[HbO_2]$ to Baseline, %	92.5 (90.0, 105.3)	101.1 (85.9, 112.8)	101.1 (95.0, 125.8)	112.8 (98.5, 133.8)
$\Delta[HbO_2]$ from Baseline	-1.7 (-3.6, 1.6)	0.4 (-3.6, 3.5)	0.5 (-1.7, 6.2)	4.2 (-0.5, 10.9)
[Hb], µmol/L	32.4 (29.8, 37.6)†	32.8 (29.5, 36.9)†	30.6 (28.9, 34.9)*	29.5 (27.7, 32.6)
r[Hb] to Baseline, %	110.5 (101.8, 120.6)	110.9 (104.0, 116.7)	106.1 (98.8, 113.5)	106.3 (90.4, 113.9)
Δ[Hb] from Baseline	2.5 (0.6, 6.0)	3.2 (1.3, 4.6)	1.6 (-0.4, 3.9)	1.9 (-3.1, 4.0)
THC, µmol/L	63.5 (60.4, 71.6)	66.3 (61.0, 69.0)	65.2 (63.1, 70.8)*	67.5 (64.6, 76.4)†
rTHC to Baseline, %	102.8 (95.8, 106.9)	103.5 (97.2, 108.1)	105.9 (97.3, 110.7)	107.5 (100.8, 115.5)
ΔTHC from Baseline	1.7 (-3.1, 4.8)	2.1 (-1.9, 4.7)	3.9 (-1.4, 6.5)	5.3 (0.5, 9.0)
StO_2, %	48.7 (44.3, 52.3)†	49.0 (43.3, 53.8)*	52.8 (47.0, 56.1)	56.5 (49.3, 59.6)
rStO_2 to Baseline, %	94.6 (85.3, 98.7)	95.5 (88.6, 103.3)	99.6 (94.0, 110.5)	103.1 (97.6, 115.8)
ΔStO_2 from Baseline	-3.0 (-7.0, -0.6)	-2.5 (-5.3, 1.7)	-0.2 (-3.5, 5.1)	1.7 (-1.2, 7.5)

Reported as Median (IQR)

*p<0.05; †p<0.01; ‡p<0.001; § Abbreviations: $[HbO_2]$, oxy-hemoglobin concentration; [Hb], deoxy-hemoglobin concentration; StO_2, tissue oxygen saturation; THC, total hemoglobin concentration; Δ-prefix, absolute change; r-prefix, relative value compared to 100% at baseline.

F.3. Supplemental Figures

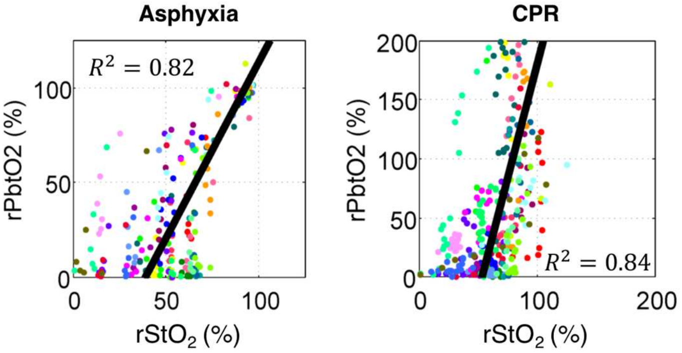

Figure 4.A1. Comparison of Invasive and Non-Invasive Measures of Cerebral Oxygenation: During asphyxia (*left*) and CPR (*right*), relative StO_2 demonstrates a strong correlation with relative $PbtO_2$. During asphyxia, the modeled linear relationship exhibited a significant slope (mean [95% CI] = 1.9 [1.6, 2.1]; $p<0.001$) with a high coefficient of determination ($R^2 = 0.82$). Similarly, the relationship during CPR also exhibited a significant slope (mean [95% CI] = 3.9 [2.3, 5.5]; $p<0.001$) with a high coefficient of determination ($R^2 = 0.84$). These results provide substantial confidence that changes in non-invasive measurements of StO_2 reflect true changes in cerebral oxygen content.

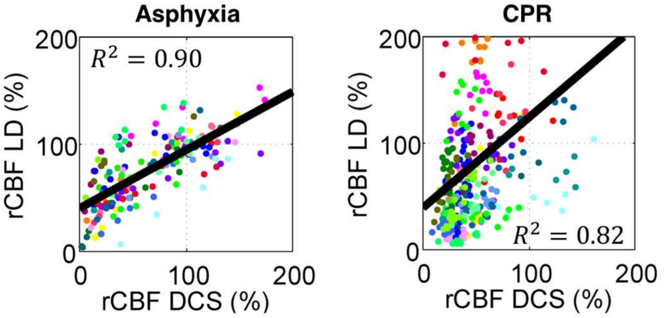

Figure 4.A2. Comparison of Invasive and Non-Invasive Measures of Cerebral Blood Flow: During asphyxia (*left*) and CPR (*right*), relative cerebral blood flow measured by non-invasive diffuse correlation spectroscopy (rCBF DCS, %) demonstrates a strong correlation with invasive intracranial measures by laser Doppler (rCBF LD, %). During asphyxia, the modeled linear relationship exhibited a significant slope (mean [95% CI] = 0.5 [0.5, 0.6]; $p<0.001$) with a strong coefficient of determination ($R^2 = 0.90$). Similarly, the relationship during CPR also exhibited a significant slope (mean [95% CI] = 0.9 [0.4, 1.3]; $p<0.001$) with a high coefficient of determination ($R^2 = 0.82$). These results highlight that motion during CPR substantially increases variance in the quantitative relationship between non-invasive and invasive measurements of cerebral blood flow compared to measurements during asphyxia. Despite this variation, the high coefficient of determination supports that changes in non-invasive rCBF DCS value continue to reflect changes in invasive rCBF LD. Further study is needed to understand and remove the contribution of motion during CPR from both measurement modalities.

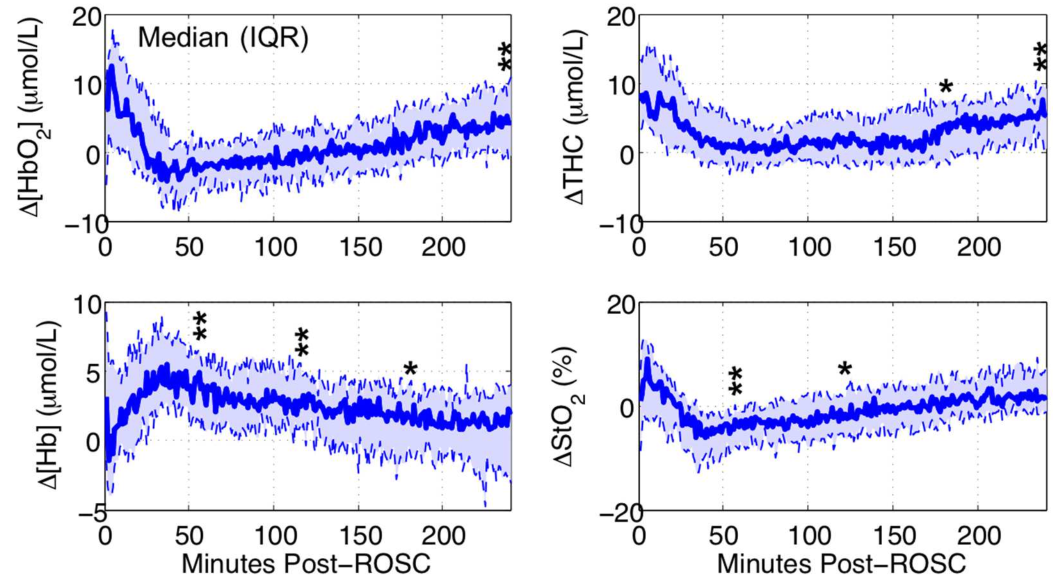

Figure 4.A3. Changes from Baseline in Cerebral Hemodynamics during 4 Hour Post-ROSC Recovery: For subjects who achieved return of spontaneous circulation (ROSC; n=23), the median (*solid line*) and IQR (*shaded region* between dotted lines) of the absolute change in cerebral oxy-hemoglobin concentration (Δ[HbO_2]; *top left*), deoxy-hemoglobin concentration (Δ[Hb]; *bottom left*), total hemoglobin concentration (ΔTHC; *top right*) and tissue oxygen saturation (ΔStO_2; *bottom right*) from pre-asphyxia baseline values for the 4 hours following ROSC are plotted. Three points of inflection qualitatively define different stages of cerebral hemodynamic recovery comprising an acute (0 - 10 minutes), subacute (10 – 45 minutes), intermediate (45 – 170 minutes) and extended (>170 minutes) stage. Significant differences from baseline at 1, 2, 3, and 4 hours post-ROSC are indicated by asterisks (*, p<0.05; **, p<0.01).

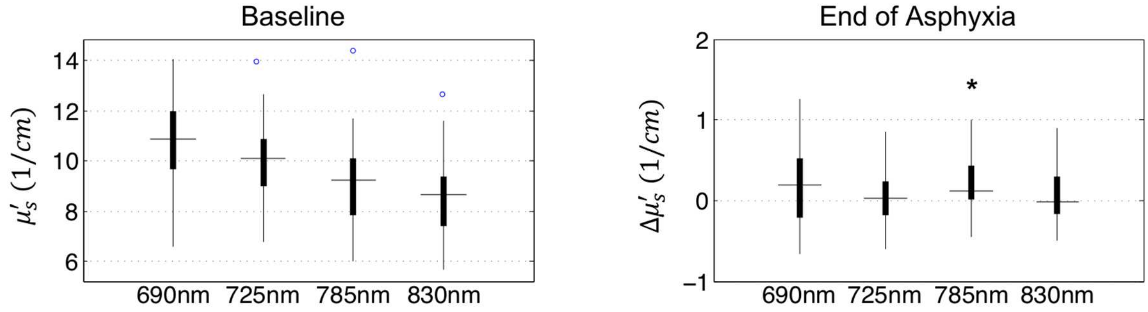

Figure 4.A4. Baseline Optical Reduced Scattering Coefficient (μ_s') and Changes at End-Asphyxia: The median, IQR and range, excluding outliers (*blue circles*), of the μ_s' at baseline, and end of asphyxia change from baseline ($\Delta\mu_s'$), are plotted for each measured wavelength (*horizontal axis*) across all subjects (n=31). The asterisk (*) denotes a significant change from baseline (p=0.013) at the 785nm wavelength at the end of asphyxia.

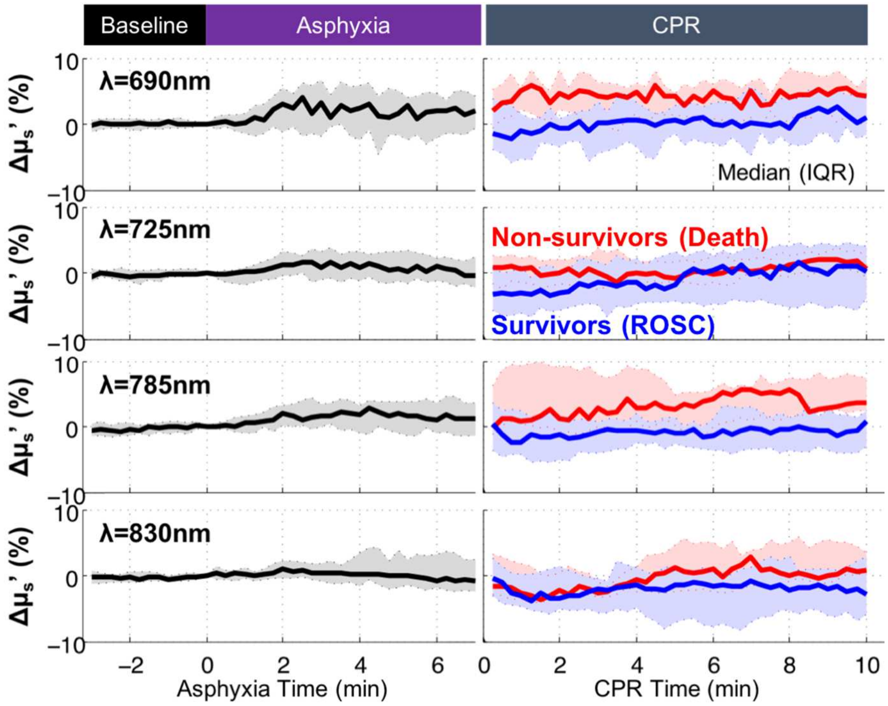

Figure 4.A5. Percentage Change in Optical Reduced Scattering Coefficient ($\Delta\mu_s'$) during Asphyxia and CPR: The median and IQR (*shaded*), of the "percentage of baseline" change in μ_s' are plotted across asphyxia (7 minutes) and the first 10 minutes of CPR. During CPR, the changes for survivors who achieved ROSC are plotted in *red*, and non-survivors plotted in *blue*.

CHAPTER 5: CONCLUSIONS AND FUTURE OUTLOOK

In the presented work, non-invasive, *quantitative* diffuse optical neuromonitoring has demonstrated the potential to substantially improve the individualization of care in children who are at risk for hypoxic-ischemic neurological injury. Using this novel clinical tool, in **Chapter 2** and **Chapter 3**, we quantified the *continuous* effects of cardiopulmonary bypass, deep hypothermia, and circulatory arrest (each distinct intraoperative neurological risk factors) on cerebral oxygen metabolism in a neonatal swine model of surgical cardiac repair for newborns with severe congenital heart defects. And in **Chapter 4**, we determined highly predictive associations of non-invasively measured cerebral hemodynamics with return of spontaneous circulation (ROSC) in a pediatric model of respiratory-mediated cardiac arrest. In this concluding chapter, our findings and our future outlook for this innovative clinical modality are summarized.

A. Mitigating Pediatric Brain Injury During Hypothermic Cardiopulmonary Bypass

Newborns with complex congenital heart defects (CHD) who must undergo open heart surgery within the first weeks of life to repair the aortic arch suffer a disproportionate burden of new or worsened post-operative neurological injury.[54] Neurological injury has been associated with the use of extended cardiopulmonary bypass (CPB), rapid cooling to and rewarming from deep hypothermia (DH), and the use of deep hypothermic circulatory arrest (DHCA). In our first study, which spanned **Chapter 2** and **Chapter 3**, we critically examined these risk factors using non-invasive diffuse optical measurements of cerebral tissue oxy- and deoxy-hemoglobin concentration ([HbO_2] and [Hb], respectively), total hemoglobin concentration (THC), oxygen saturation (StO_2), blood flow index (BFI), and cerebral rate of oxygen metabolism ($CMRO_2$). Importantly, our findings identified specific limitations of conventional temperature guidance of deep hypothermic cardiopulmonary bypass in CHD neonates. Furthermore, these findings also provide strong evidence for the validity and utility of non-invasive diffuse optical measurements to address these limitations and lays the framework for unique diagnostic parameters of cerebral status.

Using unprecedented *continuous* determination of the temperature-dependence of cerebral oxygen metabolism *in vivo* in a neonatal swine model of DH CPB, we found that the relationship, with respect to non-invasive nasopharyngeal temperature, demonstrated a significant hysteresis between cooling and rewarming periods. In contrast, the relationship with respect to invasive intracranial temperature did *not* demonstrate hysteresis. This result (**Chapter 2**) underscores that not only is nasopharyngeal temperature an inaccurate reflection of intracranial temperature, *non-invasive diffuse optical measurement of cerebral oxygen metabolism is better*. Second, we performed an identical analysis of the hysteresis of metabolic temperature-dependence between cooling and rewarming periods in neonatal swine who underwent deep hypothermia *with circulatory arrest* (DHCA). In these animals, even when metabolic temperature-dependence was assessed with respect to intracranial temperature, a significant hysteresis was found. From this effect, we concluded that *DHCA has a significant impact on cerebral oxygen metabolism that persists beyond the end of the DHCA into the rewarming period*. Furthermore, because this impact cannot be adequately explained by variability in temperature, it must be independently measured (**Chapter 3**); diffuse optics provides this capability.

Furthermore, continuous measurement of cerebral metabolic parameters during DHCA provided new physiologic insights and identified novel diagnostic parameters. First, procedural exsanguination in the first two minutes following DHCA was found to deplete a disproportionate amount of [HbO_2] from cerebral tissue. These *two minutes* accounted for 14-21% of the total [HbO_2] loss over *40 minutes* of DHCA. Strategies to mitigate this loss should be explored and may permit extended cerebral tolerance to DHCA. Next, the timing of the stabilization of the [HbO_2] depletion rate was found to agree well with the transition from aerobic to anaerobic metabolism (*i.e.*, substrate transition from oxygen to glucose). Because this transition rapidly escalates after 50% depletion of baseline oxygen content, the timing of this transition may prove to be a useful diagnostic of remaining oxygen availability in cerebral tissue as well as the rate of depletion. Finally, depletion of THC during DHCA should be examined in combination with DCS measures of cerebral blood flow as a surrogate for changes in tissue composition which impact the concentration of tissue hemoglobin; these measurements may provide additional markers of vascular and cellular injury.

In sum, these findings form a substantial basis for the future investigation of non-invasive diffuse optical *guidance* of therapeutic hypothermia and deep hypothermic circulatory arrest. Associations of these parameters with outcomes assessing neurological injury will permit the development of optimal neuroprotective strategies for CHD neonates and other similarly vulnerable pediatric populations.

B. Neurological Predictors of CPR Outcome following Respiratory-Mediated Cardiac Arrest

Physiological monitoring in the context of resuscitation represents a recent and ongoing paradigm shift from “rescuer”-centric guidance, which focuses on chest compression parameters, to “patient”-centric optimization, where each individual’s real-time physiologic-response to resuscitation is emphasized. Neurological morbidity remains the primary cause of death in resuscitated children. This stresses the need for physiologic monitoring of the brain during resuscitation. In **Chapter 4**, a high-fidelity pediatric swine model of asphyxial cardiac arrest provided the opportunity to associate cerebral hemodynamics during cardiopulmonary resuscitation (CPR), measured non-invasively for the first time by *quantitative* frequency-domain diffuse optical spectroscopy (FD-DOS), with the critical outcome of return of spontaneous circulation (ROSC).

At 10-minutes of CPR, immediately prior to the first defibrillation attempt, *non-invasive FD-DOS measures of* [HbO_2]*, THC, and* StO_2*, as well as their change from baseline and the first minute of CPR, were significantly associated with subsequent ROSC*. FD-DOS measurement of elevated [HbO_2] and StO_2 in subjects who achieved ROSC (versus those who did not achieve ROSC) provides improved physiologic quantification of the oxygenation difference over prior applications of continuous-wave NIRS techniques in this context. Furthermore, the finding that changes in [HbO_2] and THC from baseline were more significantly associated with ROSC than changes in StO_2 from baseline revealed that maintenance of elevated cerebral blood volume is critical. Thus, *monitoring of oxygen saturation alone (i.e., the fraction of oxygenated blood) may not be sufficient for guidance of resuscitation*. Underscoring this limitation, we found that among associated parameters, the change in [HbO_2] during CPR demonstrated the highest predictive power and stability (mean AUC = 0.91) in the first 10 minutes of CPR. Importantly, through critical examination of assumptions underlying spatially-resolved continuous-wave (CW) NIRS, a technique commonly used in clinical cerebral oximeters, we determined that *CW NIRS is unable to sufficiently quantify this diagnostic parameter for ROSC prediction*. The use of more advanced, quantitative diffuse optical techniques is necessary to improve accuracy, minimize inter-subject variability, and maximize predictive power.

This work has determined significant associations between cerebral hemodynamics and ROSC and identified change in [HbO_2] as a promising *non-invasive* predictor which may be utilized for guidance *in the first few minutes of CPR*. Further optimization is necessary for application in multimodal monitoring schema (*e.g.*, with arterial blood pressure and/or end-tidal CO_2 monitoring), in alternative clinical populations (*e.g.*, cardiac etiologies) and for specific use scenarios (*e.g.*, to guide use of pressor interventions, or to determine futility). While independent prospective validation is also needed to confirm these observational findings, it is our earnest belief that the use of non-invasive, *quantitative* diffuse optical neuromonitoring will facilitate the development of novel CPR optimization strategies that will reduce the devastating burden of neurological morbidity in children following cardiac arrest.

In Closing

The body of evidence presented in this thesis represents a significant step towards the clinical realization of diffuse optical neuromonitoring and guidance using *quantitative* diffuse optical spectroscopy and diffuse correlation spectroscopy. These modalities and their application to medicine are borne from a diverse community of visionary scientists, engineers and healthcare providers who have come together, across continents and with decades of determination, to improve survival, neurological outcomes, and subsequent quality of life in these at-risk children. In turn, the unique simplicity and non-invasive nature of this technology, like the pulse oximeter or a simple thermometer, has demonstrated ease of use and holds the potential for widespread accessibility by diverse patient populations and by individual users with or without medical training. With this powerful vision in mind, we continue forward.

BIBLIOGRAPHY

1. Wyatt JS, Cope M, Delpy DT, et al. Measurement of Optical Path Length for Cerebral Near-Infrared Spectroscopy in Newborn Infants. *Dev Neurosci* 1990; 12: 140–144.
2. Benaron DA, Gwiazdowski S, Kurth CD, et al. Optical path length of 754nm and 816nm light emitted into the head of infants. In: *Proceedings of the Twelfth Annual International Conference of the IEEE Engineering in Medicine and Biology Society*. IEEE, 1990, pp. 1117–1119.
3. Duncan A, Meek JH, Clemence M, et al. Optical pathlength measurements on adult head, calf and forearm and the head of the newborn infant using phase resolved optical spectroscopy. *Phys Med Biol* 1995; 40: 295–304.
4. Zhao J, Ding HS, Hou XL, et al. In vivo determination of the optical properties of infant brain using frequency-domain near-infrared spectroscopy. *J Biomed Opt* 2005; 10: 024028.
5. Ijichi S, Kusaka T, Isobe K, et al. Developmental changes of optical properties in neonates determined by near-infrared time-resolved spectroscopy. *Pediatr Res* 2005; 58: 568–573.
6. Patterson MS, Chance B, Wilson BC. Time resolved reflectance and transmittance for the non- invasive measurement of tissue optical properties. *Appl Opt* 1989; 28: 2331–2336.
7. Farrell TJ, Patterson MS, Wilson B. A diffusion theory model of spatially resolved, steady-state diffuse reflectance for the noninvasive determination of tissue optical properties in vivo. *Medical Physics* 1992; 19: 879–88.
8. Arridge SR, Cope M, Delpy DT. The theoretical basis for the determination of

optical pathlengths in tissue : temporal and frequency analysis The theoretical basis for the determination of optical. *Phys Med Biol* 1992; 37: 1531–1560.

9. Durduran T, Choe R, Baker WB, et al. Diffuse optics for tissue monitoring and tomography. *Reports Prog Phys* 2010; 73: 076701.
10. Bigio IJ, Fantini S. *Quantitative Biomedical Optics: Theory, Methods, and Applications*. 2016.
11. Jacques SL. Optical properties of biological tissues: A review. *Phys Med Biol* 2013; 58: R37.
12. Steinke JM, Shepherd AP. Diffuse Reflectance of Whole Blood: Model for a Diverging Light Beam. *IEEE Trans Biomed Eng* 1987; BME-34: 826–834.
13. Chance B, Nioka S, Kent J, et al. Time-resolved spectroscopy of hemoglobin and myoglobin in resting and ischemic muscle. *Anal Biochem* 1988; 174: 698–707.
14. Delpy DT, Cope M. Quantification in tissue near − infrared spectroscopy. *Philos Trans R Soc London* 1997; 352: 649–659.
15. Boas DA, Dale AM, Franceschini MA. Diffuse optical imaging of brain activation: Approaches to optimizing image sensitivity, resolution, and accuracy. *Neuroimage*; 23. Epub ahead of print 2004. DOI: 10.1016/j.neuroimage.2004.07.011.
16. Lloyd-Fox S, Blasi A, Elwell CE. Illuminating the developing brain: The past, present and future of functional near infrared spectroscopy. *Neurosci Biobehav Rev* 2010; 34: 269–284.
17. Haskell RC, Svaasand LO, Tsay TT, et al. Boundary conditions for the diffusion equation in radiative transfer. *J Opt Soc Am A Opt Image Sci Vis* 1994; 11: 2727–41.
18. Groenhuis RAJ, Ferwerda HA, Bosch JJ Ten. Scattering and absorption of turbid

materials determined from reflection measurements. 1: Theory. *Appl Opt* 1983; 22: 2456–2462.

19. Hueber DM, Franceschini MA, Ma HY, et al. Non-invasive and quantitative near-infrared haemoglobin spectrometry in the piglet brain during hypoxic stress, using a frequency-domain multidistance instrument. *Phys Med Biol* 2001; 46: 41–62.
20. Prahl SA. Tabulated molar extinction coefficient for hemoglobin in water. *http://omlc.ogi.edu/spectra/hemoglobin/summary.html*.
21. Jobsis F. Noninvasive, infrared monitoring of cerebral and myocardial oxygen sufficiency and circulatory parameters. *Science (80-)* 1977; 198: 1264–1267.
22. Kurth CD, Levy WJ, McCann J. Near-Infrared Spectroscopy Cerebral Oxygen Saturation Thresholds for Hypoxia–Ischemia in Piglets. *J Cereb Blood Flow Metab* 2002; 22: 335–341.
23. Watzman HM, Kurth CD, Montenegro LM, et al. Arterial and venous contributions to near-infrared cerebral oximetry. *Anesthesiology* 2000; 93: 947–953.
24. Buckley EM. *Cerebral Hemodynamics in High-Risk Neonates Probed by Diffuse Optical Spectroscopies*. University of Pennsylvania, 2011.
25. Andropoulos DB, Stayer SA, Diaz LK, et al. Neurological monitoring for congenital heart surgery. *Anesth Analg* 2004; 99: 1365–1375.
26. Fantini S, Hueber D, Franceschini MA, et al. Non-invasive optical monitoring of the newborn piglet brain using continuous-wave and frequency-domain spectroscopy. *Phys Med Biol* 1999; 44: 1543–1563.
27. Kurth CD, Uher B. Cerebral hemoglobin and optical pathlength influence near-infrared spectroscopy measurement of cerebral oxygen saturation. *Anesth Analg* 1997; 84: 1297–1305.
28. Liu H, Boas DA, Zhang Y, et al. Determination of optical properties and blood

oxygenation in tissue using continuous NIR light. *Phys Med Biol* 1995; 40: 1983–1993.

29. Benni PB, MacLeod D, Ikeda K, et al. A validation method for near-infrared spectroscopy based tissue oximeters for cerebral and somatic tissue oxygen saturation measurements. *J Clin Monit Comput* 2018; 32: 269–284.
30. Boas DA, Yodh AG. Spatially varying dynamical properties of turbid media probed with diffusing temporal light correlation. *J Opt Soc Am A* 1997; 14: 192.
31. Mesquita RC, Durduran T, Yu G, et al. Direct measurement of tissue blood flow and metabolism with diffuse optics. *Philos Trans R Soc A Math Phys Eng Sci* 2011; 369: 4390–4406.
32. Durduran T, Yodh AG. Diffuse correlation spectroscopy for non-invasive, micro-vascular cerebral blood flow measurement. *Neuroimage* 2014; 85: 5163.
33. Irwin D, Dong L, Shang Y, et al. Influences of tissue absorption and scattering on diffuse correlation spectroscopy blood flow measurements. *Biomed Opt Express* 2011; 2: 1969.
34. Zimmerman AA, Burrows FA, Jonas RA, et al. The limits of detectable cerebral perfusion by transcranial Doppler sonography in neonates undergoing deep hypothermic low-flow cardiopulmonary bypass. *J Thorac Cardiovasc Surg* 1997; 114: 594–600.
35. Kim MN, Durduran T, Frangos S, et al. Noninvasive measurement of cerebral blood flow and blood oxygenation using near-infrared and diffuse correlation spectroscopies in critically brain-injured adults. *Neurocrit Care* 2010; 12: 173–180.
36. Buckley EM, Cook NM, Durduran T, et al. Cerebral hemodynamics in preterm infants during positional intervention measured with diffuse correlation spectroscopy and transcranial Doppler ultrasound. *Opt Express* 2009; 17: 12571–

12581.

37. Busch DR, Rusin CG, Miller-Hance W, et al. Continuous cerebral hemodynamic measurement during deep hypothermic circulatory arrest. *Biomed Opt Express* 2016; 7: 3461–3470.

38. Buckley EM, Hance D, Pawlowski T, et al. Validation of diffuse correlation spectroscopic measurement of cerebral blood flow using phase-encoded velocity mapping magnetic resonance imaging. *J Biomed Opt* 2012; 17: 037007.

39. Jain V, Buckley EM, Licht DJ, et al. Cerebral oxygen metabolism in neonates with congenital heart disease quantified by MRI and optics. *J Cereb Blood Flow Metab* 2014; 34: 380–388.

40. Durduran T, Zhou C, Buckley EM, et al. Optical measurement of cerebral hemodynamics and oxygen metabolism in neonates with congenital heart defects. *J Biomed Opt* 2010; 15: 037004.

41. Zhou C, Eucker S a., Durduran T, et al. Diffuse optical monitoring of hemodynamic changes in piglet brain with closed head injury. *J Biomed Opt* 2009; 14: 034015.

42. Culver JP, Durduran T, Cheung C, et al. Diffuse optical measurement of hemoglobin and cerebral blood flow in rat brain during hypercapnia, hypoxia and cardiac arrest. *Adv Exp Med Biol* 2003; 510: 293–297.

43. Culver JP, Durduran T, Furuya D, et al. Diffuse Optical Tomography of Cerebral Blood Flow, Oxygenation, and Metabolism in Rat during Focal Ischemia. *J Cereb Blood Flow Metab* 2003; 23: 911–924.

44. Durduran T, Yu G, Burnett MG, et al. Diffuse optical measurement of blood flow, blood oxygenation, and metabolism in a human brain during sensorimotor cortex activation. *Opt Lett* 2004; 29: 1766.

45. Franceschini MA, Thaker S, Themelis G, et al. Assessment of infant brain development with frequency-domain near-infrared spectroscopy. *Pediatr Res* 2007; 61: 546–551.

46. Bernier PL, Stefanescu A, Samoukovic G, et al. The challenge of congenital heart disease worldwide: Epidemiologic and demographic facts. *Semin Thorac Cardiovasc Surg Pediatr Card Surg Annu* 2010; 13: 26–34.

47. Marino BS, Lipkin PH, Newburger JW, et al. Neurodevelopmental Outcomes in Children With Congenital Heart Disease: Evaluation and Management: A Scientific Statement From the American Heart Association. *Circulation* 2012; 126: 1143–1172.

48. Khalil A, Suff N, Thilaganathan B, et al. Brain abnormalities and neurodevelopmental delay in congenital heart disease: Systematic review and meta-analysis. *Ultrasound Obstet Gynecol* 2014; 43: 14–24.

49. Gaynor JW, Stopp C, Wypij D, et al. Neurodevelopmental Outcomes After Cardiac Surgery in Infancy. *Pediatrics* 2015; 135: 816–825.

50. Hövels-Gürich HH. Factors Influencing Neurodevelopment after Cardiac Surgery during Infancy. *Front Pediatr* 2016; 4: 1–6.

51. Rollins CK, Asaro LA, Akhondi-Asl A, et al. White Matter Volume Predicts Language Development in Congenital Heart Disease. *J Pediatr* 2017; 181: 42–48.

52. Mussatto KA, Hoffmann RG, Hoffman GM, et al. Risk and Prevalence of Developmental Delay in Young Children With Congenital Heart Disease. *Pediatrics* 2014; 133: e570–e577.

53. Uzark K, Jones K, Slusher J, et al. Quality of Life in Children With Heart Disease as Perceived by Children and Parents. *Pediatrics* 2008; 121: e1060–e1067.

54. Beca J, Gunn JK, Coleman L, et al. New White matter brain injury after infant

heart surgery is associated with diagnostic group and the use of circulatory arrest. *Circulation* 2013; 127: 971–979.

55. Newburger JW, Sleeper LA, Bellinger DC, et al. Early developmental outcome in children with hypoplastic left heart syndrome and related anomalies: The single ventricle reconstruction trial. *Circulation* 2012; 125: 2081–2091.
56. Kurth CD, Steven JM, Nicolson SC, et al. Cerebral oxygenation during cardiopulmonary bypass in children. *J Thorac Cardiovasc Surg* 1997; 113: 71–79.
57. Plessis AJD, Newburger J, Jonas RA, et al. Cerebral oxygen supply and utilization during infant cardiac surgery. *Ann Neurol* 1995; 37: 488–497.
58. Scallan MJH. Cerebral injury during paediatric heart surgery: perfusion issues. *Perfusion* 2004; 19: 221–228.
59. Marino BS. New concepts in predicting, evaluating, and managing neurodevelopmental outcomes in children with congenital heart disease. *Curr Opin Pediatr* 2013; 25: 574–584.
60. McQuillen PS, Barkovich AJ, Hamrick SEG, et al. Temporal and anatomic risk profile of brain injury with neonatal repair of congenital heart defects. *Stroke* 2007; 38: 736–741.
61. Kussman BD, Wypij D, Laussen PC, et al. Relationship of Intraoperative Cerebral Oxygen Saturation to Neurodevelopmental Outcome and Brain MRI at One Year of Age in Infants Undergoing Biventricular Repair. *Circulation* 2010; 122: 245–254.
62. Von Rhein M, Buchmann A, Hagmann C, et al. Brain volumes predict neurodevelopment in adolescents after surgery for congenital heart disease. *Brain* 2014; 137: 268–276.
63. Markowitz SD, Ichord RN, Wernovsky G, et al. Surrogate Markers for Neurological

Outcome in Children After Deep Hypothermic Circulatory Arrest. *Semin Cardiothorac Vasc Anesth* 2007; 11: 59–65.

64. Dönmez A, Yurdakök O. Cardiopulmonary bypass in infants. *J Cardiothorac Vasc Anesth* 2014; 28: 778–788.

65. Jonas RA. The effect of extracorporeal life support on the brain: Cardiopulmonary bypass. *Semin Perinatol* 2005; 29: 51–57.

66. Wan S, Leclerc JL, Vincent JL. Inflammatory response to cardiopulmonary bypass: Mechanisms involved and possible therapeutic strategies. *Chest* 1997; 112: 676–692.

67. Hickey E, Karamlou T, You J, et al. Effects of Circuit Miniaturization in Reducing Inflammatory Response to Infant Cardiopulmonary Bypass by Elimination of Allogeneic Blood Products. *Ann Thorac Surg*; 81. Epub ahead of print 2006. DOI: 10.1016/j.athoracsur.2006.02.071.

68. Laursen H, Waaben J, Gefke K, et al. Brain histology, blood-brain barrier and brain water after normothermic and hypothermic cardiopulmonary bypass in pigs. *Eur J Cardio-thoracic Surg* 1989; 3: 539–543.

69. Salameh A, Kühne L, Grassl M, et al. Protective effects of pulsatile flow during cardiopulmonary bypass. *Ann Thorac Surg* 2015; 99: 192–199.

70. Bissonnette B, Holtby HM, Davis a J, et al. Cerebral hyperthermia in children after cardiopulmonary bypass. *Anesthesiology* 2000; 93: 611–618.

71. Kaukuntla H, Harrington D, Bilkoo I, et al. Temperature monitoring during cardiopulmonary bypass - Do we undercool or overheat the brain? *Eur J Cardio-thoracic Surg* 2004; 26: 580–585.

72. Serraf A, Robotin M, Bonnet N, et al. Alteration of the neonatal pulmonary physiology after total cardiopulmonary bypass. *J Thorac Cardiovasc Surg* 1997;

114: 1061–1069.

73. Kirkham FJ. Recognition and prevention of neurological complications in pediatric cardiac surgery. *Pediatr Cardiol* 1998; 19: 331–345.

74. Kouchoukos N, Blackstone E, Hanley F, et al. Hypothermia, Circulatory Arrest, and Cardiopulmonary Bypass. *Kirklin/Barratt-Boyes Card Surg*.

75. Barratt-Boyes BG, Simpson M, Neutze JM. Intracardiac surgery in neonates and infants using deep hypothermia with surface cooling and limited cardiopulmonary bypass. *Circulation* 1971; 43: I25-30.

76. Saleh M, Barr TMFA. The impact of slow rewarming on inotropy, tissue metabolism, and 'after drop' of body temperature in pediatric patients. *J Extra Corpor Technol* 2005; 37: 173–179.

77. Maxton F, Justin L, Gillies D. Estimating core temperature in infants and children after cardiac surgery: a comparison of six methods. *J Adv Nurs*.

78. Kornilov IA, Sinelnikov YS, Soinov IA, et al. Outcomes after aortic arch reconstruction for infants: Deep hypothermic circulatory arrest versus moderate hypothermia with selective antegrade cerebral perfusion. *Eur J Cardio-thoracic Surg* 2015; 48: e45–e50.

79. Greeley WJ, Kern FH, Ungerleider RM, et al. The effect of hypothermic cardiopulmonary bypass and total circulatory arrest on cerebral metabolism in neonates, infants, and children. *J Thorac Cardiovasc Surg* 1991; 101: 783–94.

80. Croughwell N, Smith LR, Quill T, et al. The effect of temperature on cerebral metabolism and blood flow in adults during cardiopulmonary bypass. *The Journal of Thoracic and Cardiovascular Surgery* 1992; 103: 549–54.

81. McCullough JN, Zhang N, Reich DL, et al. Cerebral metabolic suppression during hypothermic circulatory arrest in humans. *Ann Thorac Surg* 1999; 67: 1895–1899.

82. Mavroudis C, Backer C, Idriss RF (eds). *Pediatric Cardiac Surgery*. 4th ed. Blackwell Publishing Ltd., 2013.

83. Fuller S, Rajagopalan R, Jarvik GP, et al. J. Maxwell Chamberlain Memorial Paper for congenital heart surgery. Deep hypothermic circulatory arrest does not impair neurodevelopmental outcome in school-age children after infant cardiac surgery. *Ann Thorac Surg* 2010; 90: 1985-94; discussion 1994–5.

84. Hori D, Everett AD, Lee JK, et al. Rewarming rate during cardiopulmonary bypass is associated with release of glial fibrillary acidic protein. *Ann Thorac Surg* 2015; 100: 1353–1358.

85. Gaynor JW, Stopp C, Wypij D, et al. Impact of Operative and Postoperative Factors on Neurodevelopmental Outcomes After Cardiac Operations. *Ann Thorac Surg* 2016; 102: 843–849.

86. Coselli JS, Crawford ES, Beall AC, et al. Determination of Brain Temperatures for Safe Circulatory Arrest during Cardiovascular Operation. *Ann Thorac Surg* 1988; 45: 638–642.

87. Stone JG, Young WL, Smith CR, et al. Do standard monitoring sites reflect true brain temperature when profound hypothermia is rapidly induced and reversed? *Anesthesiology* 1995; 82: 344–351.

88. Ko HK, Flemmer A, Haberl C, et al. Methodological investigation of measuring nasopharyngeal temperature as noninvasive brain temperature analogue in the neonate. *Intensive Care Med* 2001; 27: 736–742.

89. Akata T, Setoguchi H, Shirozu K, et al. Reliability of temperatures measured at standard monitoring sites as an index of brain temperature during deep hypothermic cardiopulmonary bypass conducted for thoracic aortic reconstruction. *J Thorac Cardiovasc Surg*; 133. Epub ahead of print 2007. DOI:

10.1016/j.jtcvs.2006.11.031.

90. Busto R, Dietrich WD, Globus MY-T, et al. Small Differences in Intraischemic Brain Temperature Critically Determine the Extent of Ischemic Neuronal Injury. *J Cereb Blood Flow Metab* 1987; 7: 729–738.

91. Wypij D, Newburger JW, Rappaport LA, et al. The effect of duration of deep hypothermic circulatory arrest in infant heart surgery on late neurodevelopment: The Boston Circulatory Arrest Trial. *J Thorac Cardiovasc Surg* 2003; 126: 1397–1403.

92. Pigula FA, Nemoto EM, Griffith BP, et al. Regional low-flow perfusion provides cerebral circula tory support during neona tal aortic arch reconstruction. *J Thorac Cardiovasc SurgeryThoracic Car* 2000; 119: 331–339.

93. Fraser CD, Andropoulos DB. Principles of Antegrade Cerebral Perfusion During Arch Reconstruction in Newborns/Infants. *Pediatr Card Surg Annu* 2008; 11: 61–68.

94. Hanley FL. Religion, politics…deep hypothermic circulatory arrest. *J Thorac Cardiovasc Surg* 2005; 130: 1236.e1-1236.e8.

95. Gaynor JW, Nicolson SC, Jarvik GP, et al. Increasing duration of deep hypothermic circulatory arrest is associated with an increased incidence of postoperative electroencephalographic seizures. *J Thorac Cardiovasc Surg* 2005; 130: 1278–1286.

96. Algra SO, Jansen NJG, Van Der Tweel I, et al. *Neurological injury after neonatal cardiac surgery: A randomized, controlled trial of 2 perfusion techniques*. 2014. Epub ahead of print 2014. DOI: 10.1161/CIRCULATIONAHA.113.003312.

97. Austin EH, Edmonds HL, Auden SM, et al. Benefit of neurophysiologic monitoring for pediatric cardiac surgery. *J Thorac Cardiovasc Surg* 1997; 114: 707–717.

98. Zanatta P, Benvenuti SM, Bosco E, et al. Multimodal Brain Monitoring Reduces Major Neurologic Complications in Cardiac Surgery. *J Cardiothorac Vasc Anesth* 2011; 25: 1076–1085.

99. Sakamoto T, Duebener LF, Laussen PC, et al. Cerebral ischemia caused by obstructed superior vena cava cannula is detected by near-infrared spectroscopy. *J Cardiothorac Vasc Anesth* 2004; 18: 293–303.

100. Dent CL, Spaeth JP, Jones B V., et al. Brain magnetic resonance imaging abnormalities after the Norwood procedure using regional cerebral perfusion. *J Thorac Cardiovasc Surg* 2006; 131: 190–197.

101. Williams GD, Ramamoorthy C. Brain Monitoring and Protection During Pediatric Cardiac Surgery. *Semin Cardiothorac Vasc Anesth* 2007; 11: 23–33.

102. Liu H, Chance B, Hielscher a H, et al. Influence of blood vessels on the measurement of hemoglobin oxygenation as determined by time-resolved reflectance spectroscopy. *Med Phys* 1995; 22: 1209–1217.

103. Hirsch JC, Charpie JR, Ohye RG, et al. Near-infrared spectroscopy: What we know and what we need to know-A systematic review of the congenital heart disease literature. *J Thorac Cardiovasc Surg* 2009; 137: 154–159.e12.

104. Smith M, Elwell C. Near-infrared spectroscopy: Shedding light on the injured brain. *Anesth Analg* 2009; 108: 1055–1057.

105. Roche-Labarbe N, Carp SA, Surova A, et al. Noninvasive Optical Measures of CBV, StO2, CBF Index, and rCMRO2 in Human Premature Neonates' Brains in the First Six Weeks of Life. *Hum Brain Mapp* 2010; 31: 341–352.

106. Lipton P. Effects of membrane depolarization on light scattering by cerebral cortical slices. *J Physiol* 1973; 231: 365–83.

107. Laufer J, Simpson R, Kohl M, et al. Effect of temperature on the optical properties

of ex vivo human dermis and subdermis. *Phys Med Biol* 1998; 43: 2479–2489.

108. Gottlieb EA, Mossad EB. Limitations of cerebral oxygenation monitoring by near-infrared spectroscopy in children with cyanotic congenital heart disease and profound polycythemia. *J Cardiothorac Vasc Anesth* 2014; 28: 347–349.

109. Lynch JM, Buckley EM, Schwab PJ, et al. Time to surgery and preoperative cerebral hemodynamics predict postoperative white matter injury in neonates with hypoplastic left heart syndrome. *J Thorac Cardiovasc Surg* 2014; 148: 2181–2188.

110. Lynch JM, Ko T, Busch DR, et al. Preoperative cerebral hemodynamics from birth to surgery in neonates with critical congenital heart disease. *J Thorac Cardiovasc Surg*. Epub ahead of print 2018. DOI: 10.1016/j.jtcvs.2018.04.098.

111. Dean Kurth C, Thayer WS. A multiwavelength frequency-domain near-infrared cerebral oximeter. *Phys Med Biol* 1999; 44: 727–740.

112. Ferradal SL, Yuki K, Vyas R, et al. Non-invasive assessment of cerebral blood flow and oxygen metabolism in neonates during hypothermic cardiopulmonary bypass: Feasibility and clinical implications. *Sci Rep* 2017; 7: 1–9.

113. Arrhenius S. *Über die Dissociationswärme und den Einfluss der Temperatur auf den Dissociationsgrad der Elektrolyte*. Leipzig: Wilhelm Engelmann, 1889.

114. van’t Hoff MJH. *Etudes de dynamique chimique*. WILEY‐VCH Verlag, 2010.

115. Laidler KJ. The development of the Arrhenius equation. *J Chem Educ* 1984; 61: 494.

116. Chapman AG. Temperature response of oxygen uptake in brain mitochondria from normal and ischemic rats. *Neurochemistry International* 1982; 4: 39–47.

117. Girotra S, Spertus JA, Li Y, et al. Survival trends in pediatric in-hospital cardiac arrests an analysis from get with the guidelines-resuscitation. *Circ Cardiovasc*

Qual Outcomes 2013; 6: 42–49.

118. Chan PS, Spertus JA, Krumholz HM, et al. A validated prediction tool for initial survivors of in-hospital cardiac arrest. *Arch Intern Med* 2012; 172: 947–53.

119. Berg RA, Nadkarni VM, Clark AE, et al. Incidence and Outcomes of Cardiopulmonary Resuscitation in PICUs. *Crit Care Med* 2016; 44: 798–808.

120. Martinez PA, Totapally BR. The epidemiology and outcomes of pediatric in-hospital cardiopulmonary arrest in the United States during 1997 to 2012. *Resuscitation* 2016; 105: 177–181.

121. Sutton RM, Case E, Brown SP, et al. A quantitative analysis of out-of-hospital pediatric and adolescent resuscitation quality - A report from the ROC epistry-cardiac arrest. *Resuscitation* 2015; 93: 150–157.

122. Tijssen JA, Prince DK, Morrison LJ, et al. Time on the scene and interventions are associated with improved survival in pediatric out-of-hospital cardiac arrest. *Resuscitation* 2015; 94: 1–7.

123. Jayaram N, McNally B, Tang F, et al. Survival after out-of-hospital cardiac arrest in children. *J Am Heart Assoc* 2015; 4: 1–9.

124. Donoghue AJ, Nadkarni V, Berg RA, et al. Out-of-hospital pediatric cardiac arrest: An epidemiologic review and assessment of current knowledge. *Ann Emerg Med* 2005; 46: 512–522.

125. Atkins DL, Everson-Stewart S, Sears GK, et al. Epidemiology and outcomes from out-of-hospital cardiac arrest in children: The resuscitation outcomes consortium epistry-cardiac arrest. *Circulation* 2009; 119: 1484–1491.

126. Matos RI, Watson RS, Nadkarni VM, et al. Duration of cardiopulmonary resuscitation and illness category impact survival and neurologic outcomes for in-hospital pediatric cardiac arrests. *Circulation* 2013; 127: 442–451.

127. De Caen AR, Berg MD, Chameides L, et al. Part 12: Pediatric advanced life support: 2015 American Heart Association guidelines update for cardiopulmonary resuscitation and emergency cardiovascular care. *Circulation* 2015; 132: S526–S542.

128. Fink EL, Prince DK, Kaltman JR, et al. Unchanged pediatric out-of-hospital cardiac arrest incidence and survival rates with regional variation in North America. *Resuscitation* 2016; 107: 121–8.

129. Nadkarni VM, Larkin GL, Peberdy MA, et al. First documented rhythm and clinical outcome from in-hospital cardiac arrest among children and adults. *J Am Med Assoc* 2006; 295: 50–57.

130. Michiels EA, Dumas F, Quan L, et al. Long-term outcomes following pediatric out-of-hospital cardiac arrest. *Pediatr Crit Care Med* 2013; 14: 755–760.

131. Naim MY, Burke R V., McNally BF, et al. Association of bystander cardiopulmonary resuscitation with overall and neurologically favorable survival after pediatric out-of-hospital cardiac arrest in the United States a report from the cardiac arrest registry to enhance survival surveillance regist. *JAMA Pediatr* 2017; 171: 133–141.

132. Knudson JD, Neish SR, Cabrera AG, et al. Prevalence and outcomes of pediatric in-hospital cardiopulmonary resuscitation in the United States: An analysis of the Kids' Inpatient Database. *Crit Care Med* 2012; 40: 2940–2944.

133. Sasson C, Magid DJ, Chan P, et al. Association of Neighborhood Characteristics with Bystander-Initiated CPR. *N Engl J Med* 2012; 367: 1607–1615.

134. Case R, Cartledge S, Siedenburg J, et al. Identifying barriers to the provision of bystander cardiopulmonary resuscitation (CPR) in high-risk regions: A qualitative review of emergency calls. *Resuscitation* 2018; 129: 43–47.

135. Weisfeldt M, Becker L. Resuscitation after cardiac arrest. *JAMA J Am …* 2002; 288: 3035–3038.

136. Berg RA, Sutton RM, Holubkov R, et al. Ratio of PICU versus ward cardiopulmonary resuscitation events is increasing. *Crit Care Med* 2013; 41: 2292–2297.

137. Meaney PA, Bobrow BJ, Mancini ME, et al. Cardiopulmonary resuscitation quality: Improving cardiac resuscitation outcomes both inside and outside the hospital: A consensus statement from the American heart association. *Circulation* 2013; 128: 417–435.

138. De Caen AR, Maconochie IK, Aickin R, et al. Part 6: pediatric basic life support and pediatric advanced life support: 2015 International Consensus on Cardiopulmonary Resuscitation and Emergency Cardiovascular Care Science With Treatment Recommendations. *Circulation* 2015; 132: S177–S203.

139. Atkins DL, Berger S, Duff JP, et al. Part 11: Pediatric basic life support and cardiopulmonary resuscitation quality: 2015 American Heart Association guidelines update for cardiopulmonary resuscitation and emergency cardiovascular care. *Circulation* 2015; 132: S519–S525.

140. Van Vleet LM, Hubble MW. Time to first compression using medical priority dispatch system compression-first dispatcher-assisted cardiopulmonary resuscitation protocols. *Prehospital Emerg Care* 2012; 16: 242–250.

141. Kleinman ME, Brennan EE, Goldberger ZD, et al. Part 5: Adult basic life support and cardiopulmonary resuscitation quality: 2015 American Heart Association guidelines update for cardiopulmonary resuscitation and emergency cardiovascular care. *Circulation* 2015; 132: S414–S435.

142. Hellevuo H, Sainio M, Nevalainen R, et al. Deeper chest compression - More

complications for cardiac arrest patients? *Resuscitation* 2013; 84: 760–765.

143. McNally B, Robb R, Mehta M, et al. Out-of-hospital cardiac arrest surveillance. Cardiac Arrest Registry to Enhance Survival (CARES), United States, October 1, 2005 - December 31, 2010. *Morb Mortal Wkly Rep Surveill Summ* 2011; 60: 1–19.

144. Hupfl M, Selig H, Nagele P. Chest Compression-Only CPR: A Meta-Analysis. *Lancet* 2010; 376: 1552–1557.

145. Fukuda T, Ohashi-Fukuda N, Kobayashi H, et al. Conventional Versus Compression-Only Versus No-Bystander Cardiopulmonary Resuscitation for Pediatric Out-of-Hospital Cardiac Arrest. *Circulation* 2016; 134: 2060–2070.

146. Goto Y, Funada A, Goto Y. Conventional versus chest-compression-only cardiopulmonary resuscitation by bystanders for children with out-of-hospital cardiac arrest. *Resuscitation* 2018; 122: 126–134.

147. Atkins DL, de Caen AR, Berger S, et al. 2017 American Heart Association Focused Update on Pediatric Basic Life Support and Cardiopulmonary Resuscitation Quality: An Update to the American Heart Association Guidelines for Cardio pulmonary Resuscitation and Emergency Cardiovascular Care. *Circulation* 2017; CIR.0000000000000540.

148. Akahane M, Tanabe S, Ogawa T, et al. Characteristics and outcomes of pediatric out-of-hospital cardiac arrest by scholastic age category. *Pediatr Crit Care Med* 2013; 14: 130–136.

149. Sutton RM, French B, Niles DE, et al. 2010 American Heart Association recommended compression depths during pediatric in-hospital resuscitations are associated with survival. *Resuscitation* 2014; 85: 1179–1184.

150. Aase SO, Myklebust H. Compression depth estimation for CPR quality assessment using DSP on accelerometer signals. *IEEE Trans Biomed Eng* 2002;

49: 263–268.

151. Abella BS, Alvarado JP, Myklebust H, et al. Quality of Cardiopulmonary Resuscitation During In-Hospital Cardiac Arrest. *JAMA* 2005; 293: 305–310.

152. Idris AH, Guffey D, Aufderheide TP, et al. Relationship between chest compression rates and outcomes from cardiac arrest. *Circulation* 2012; 125: 3004–3012.

153. Idris AH, Guffey D, Pepe PE, et al. Chest compression rates and survival following out-of-hospital cardiac arrest. *Crit Care Med* 2015; 43: 840–848.

154. Niles D, Nysaether J, Sutton R, et al. Leaning is common during in-hospital pediatric CPR, and decreased with automated corrective feedback. *Resuscitation* 2009; 80: 553–557.

155. Fried DA, Leary M, Smith DA, et al. The prevalence of chest compression leaning during in-hospital cardiopulmonary resuscitation. *Resuscitation* 2011; 82: 1019–1024.

156. Sutton RM, Niles D, French B, et al. First quantitative analysis of cardiopulmonary resuscitation quality during in-hospital cardiac arrests of young children. *Resuscitation* 2014; 85: 70–74.

157. Yeung J, Meeks R, Edelson D, et al. The use of CPR feedback/prompt devices during training and CPR performance: A systematic review. *Resuscitation* 2009; 80: 743–751.

158. Nishi T, Takei Y, Kamikura T, et al. Improper bystander-performed basic life support in cardiac arrests managed with public automated external defibrillators. *Am J Emerg Med* 2015; 33: 43–49.

159. Gyllenborg T, Granfeldt A, Lippert F, et al. Quality of bystander cardiopulmonary resuscitation during real-life out-of-hospital cardiac arrest. *Resuscitation* 2017;

120: 63–70.

160. Fernando SM, Vaillancourt C, Morrow S, et al. Analysis of bystander CPR quality during out-of-hospital cardiac arrest using data derived from automated external defibrillators. *Resuscitation* 2018; 128: 138–143.

161. Fukuda T, Ohashi-Fukuda N, Kobayashi H, et al. Public access defibrillation and outcomes after pediatric out-of-hospital cardiac arrest. *Resuscitation* 2017; 111: 1–7.

162. Hazinski M, Shuster M, Donnino M, et al. Highlights of the 2015 American Heart Association - Guidelines Update for CPR and ECG. *Am Hear Assoc* 2015; 1–36.

163. Nishisaki A, Nysaether J, Sutton R, et al. Effect of mattress deflection on CPR quality assessment for older children and adolescents. *Resuscitation* 2009; 80: 540–545.

164. Meert KL, Donaldson A, Nadkarni V, et al. Multicenter Cohort Study of In-Hospital Pediatric Cardiac Arrest. *Pediatr Crit Care Med* 2009; 10: 544–553.

165. Sutton RM, French B, Nishisaki A, et al. American Heart Association cardiopulmonary resuscitation quality targets are associated with improved arterial blood pressure during pediatric cardiac arrest. *Resuscitation* 2013; 84: 168–172.

166. Duncan H, Hutchison J, Parshuram CS. The pediatric early warning system score: A severity of illness score to predict urgent medical need in hospitalized children. *J Crit Care* 2006; 21: 271–278.

167. Gold DL, Mihalov LK, Cohen DM. Evaluating the pediatric early warning score (PEWS) system for admitted patients in the pediatric emergency department. *Acad Emerg Med* 2014; 21: 1249–1256.

168. Sivarajan V Ben, Bohn D. Monitoring of standard hemodynamic parameters: Heart rate, systemic blood pressure, atrial pressure, pulse oximetry, and end-tidal

CO2. *Pediatr Crit Care Med*; 12. Epub ahead of print 2011. DOI: 10.1097/PCC.0b013e318220e7ea.

169. Sutton RM, French B, Meaney PA, et al. Physiologic monitoring of CPR quality during adult cardiac arrest: A propensity-matched cohort study. *Resuscitation* 2016; 106: 76–82.

170. Paradis NA, Martin G, Rivers E. Coronary Perfusion Pressure and the Return of Spontaneous Circulation in Human Cardiopulmonary Resuscitation. *JAMA J Am Med Assoc* 1990; 263: 1106.

171. Ralston SH, Voorhees WD, Babbs CF. Intrapulmonary epinephrine during prolonged cardiopulmonary resuscitation: Improved regional blood flow and resuscitation in dogs. *Ann Emerg Med* 1984; 13: 79–86.

172. Kern KB. Coronary perfusion pressure during cardiopulmonary resuscitation. *Bailliere's Best Pract Res Clin Anaesthesiol* 2000; 14: 591–609.

173. Marquez AM, Morgan RW, Ross CE, et al. Physiology-directed cardiopulmonary resuscitation: Advances in precision monitoring during cardiac arrest. *Curr Opin Crit Care* 2018; 24: 143–150.

174. Sutton RM, Morgan RW, Kilbaugh TJ, et al. Cardiopulmonary Resuscitation in Pediatric and Cardiac Intensive Care Units. *Pediatr Clin North Am* 2017; 64: 961–972.

175. Pearson JW, Redding JS. Peripheral vascular tone on cardiac resuscitation. *Anesth Analg* 1965; 44: 746–52.

176. Sanders AB, Ewy GA, Taft T V. Prognostic and therapeutic importance of the aortic diastolic pressure in resuscitation from cardiac arrest. *Crit Care Med* 1984; 12: 871–873.

177. Kern KB, Ewy GA, Voorhees WD, et al. Myocardial perfusion pressure: A

predictor of 24-hour survival during prolonged cardiac arrest in dogs. *Resuscitation* 1988; 16: 241–250.

178. Sanders AB, Kern KB, Otto CW, et al. End-Tidal Carbon Dioxide Monitoring During Cardiopulmonary Resuscitation: A Prognostic Indicator for Survival. *JAMA J Am Med Assoc* 1989; 262: 1347–1351.

179. Grmec, Klemen P. Does the end-tidal carbon dioxide (EtCO2) concentration have prognostic value during out-of-hospital cardiac arrest? *Eur J Emerg Med* 2001; 8: 263–269.

180. Paiva EF, Paxton JH, O'Neil BJ. The use of end-tidal carbon dioxide (ETCO2) measurement to guide management of cardiac arrest: A systematic review. *Resuscitation* 2018; 123: 1–7.

181. Hartmann SM, Farris RWD, Di Gennaro JL, et al. Systematic Review and Meta-Analysis of End-Tidal Carbon Dioxide Values Associated With Return of Spontaneous Circulation During Cardiopulmonary Resuscitation. *J Intensive Care Med* 2015; 30: 426–35.

182. Touma O, Davies M. The prognostic value of end tidal carbon dioxide during cardiac arrest: A systematic review. *Resuscitation* 2013; 84: 1470–1479.

183. Heradstveit BE, Sunde K, Sunde GA, et al. Factors complicating interpretation of capnography during advanced life support in cardiac arrest-A clinical retrospective study in 575 patients. *Resuscitation* 2012; 83: 813–818.

184. Link MS, Berkow LC, Kudenchuk PJ, et al. Part 7: Adult advanced cardiovascular life support: 2015 American Heart Association guidelines update for cardiopulmonary resuscitation and emergency cardiovascular care. *Circulation* 2015; 132: S444–S464.

185. Cunningham LM, Mattu A, O'Connor RE, et al. Cardiopulmonary resuscitation for

cardiac arrest: The importance of uninterrupted chest compressions in cardiac arrest resuscitation. *Am J Emerg Med* 2012; 30: 1630–1638.

186. Berg RA, Sanders AB, Kern KB, et al. Adverse hemodynamic effects of interrupting chest compressions for rescue breathing during cardiopulmonary resuscitation for ventricular fibrillation cardiac arrest. *Circulation* 2001; 104: 2465–2470.

187. Sheak KR, Wiebe DJ, Leary M, et al. Quantitative relationship between end-tidal carbon dioxide and CPR quality during both in-hospital and out-of-hospital cardiac arrest. *Resuscitation* 2015; 89: 149–154.

188. Schnaubelt S, Sulzgruber P, Menger J, et al. Regional cerebral oxygen saturation during cardiopulmonary resuscitation as a predictor of return of spontaneous circulation and favourable neurological outcome – A review of the current literature. *Resuscitation* 2018; 125: 39–47.

189. Järnum H, Knutsson L, Rundgren M, et al. Diffusion and perfusion MRI of the brain in comatose patients treated with mild hypothermia after cardiac arrest: A prospective observational study. *Resuscitation* 2009; 80: 425–430.

190. Youn CS, Park KN, Kim JY, et al. Repeated diffusion weighted imaging in comatose cardiac arrest patients with therapeutic hypothermia. *Resuscitation* 2015; 96: 1–8.

191. Krep H, Böttiger BW, Bock C, et al. Time course of circulatory and metabolic recovery of cat brain after cardiac arrest assessed by perfusion- and diffusion-weighted imaging and MR-spectroscopy. *Resuscitation* 2003; 58: 337–348.

192. Hoedemaekers CW, Ainslie PN, Hinssen S, et al. Low cerebral blood flow after cardiac arrest is not associated with anaerobic cerebral metabolism. *Resuscitation* 2017; 120: 45–50.

193. Lewis LM, Gomez CR, Ruoff BE, et al. Transcranial Doppler determination of cerebral perfusion in patients undergoing CPR: methodology and preliminary findings. *Ann Emerg Med* 1990; 19: 1148–51.

194. Nishisaki A, Sullivan J, Steger B, et al. Retrospective analysis of the prognostic value of electroencephalography patterns obtained in pediatric in-hospital cardiac arrest survivors during three years. *Pediatr Crit Care Med* 2007; 8: 10–17.

195. Reagan EM, Nguyen RT, Ravishankar ST, et al. Monitoring the Relationship Between Changes in Cerebral Oxygenation and Electroencephalography Patterns During Cardiopulmonary Resuscitation. *Crit Care Med* 2018; 1.

196. Pilkington SN, Hett D a, Pierce JM, et al. Auditory evoked responses and near infrared spectroscopy during cardiac arrest. *Br J Anaesth* 1995; 74: 717–719.

197. Wijdicks EFM, Hijdra A, Young GB, et al. Practice Parameter: Prediction of outcome in comatose survivors after cardiopulmonary resuscitation (an evidence-based review): Report of the Quality Standards Subcommittee of the American Academy of Neurology. *Neurology* 2006; 67: 203–210.

198. Voorhees WD, Babbs CF, Tacker WA. Regional blood flow during cardiopulmonary resuscitation in dogs. *Critical care medicine* 1980; 8: 134–136.

199. Du Pont-Thibodeau G, Fry M, Kirschen M, et al. Timing and Modes of Death after Pediatric Out-of-Hospital Cardiac Arrest Resuscitation. *Resuscitation*. Epub ahead of print 2018. DOI: 10.1016/j.resuscitation.2018.08.014.

200. Müllner M, Sterz F, Binder M, et al. Near infrared spectroscopy during and after cardiac arrest--preliminary results. *Clin Intensive Care* 1995; 6: 107–11.

201. Cournoyer A, Iseppon M, Chauny J-M, et al. Near-infrared Spectroscopy Monitoring During Cardiac Arrest: A Systematic Review and Meta-analysis. *Acad Emerg Med* 2016; 23: 851–862.

202. Genbrugge C, Dens J, Meex I, et al. Regional Cerebral Oximetry during Cardiopulmonary Resuscitation: Useful or Useless? *J Emerg Med* 2016; 50: 198–207.

203. Sanfilippo F, Serena G, Corredor C, et al. Cerebral oximetry and return of spontaneous circulation after cardiac arrest: A systematic review and meta-analysis. *Resuscitation* 2015; 94: 67–72.

204. Parnia S, Yang J, Nguyen R, et al. Cerebral Oximetry During Cardiac Arrest. *Crit Care Med* 2016; 44: 1663–1674.

205. Singer AJ, Nguyen RT, Ravishankar ST, et al. Cerebral oximetry versus end tidal CO2 in predicting ROSC after cardiac arrest. *Am J Emerg Med* 2018; 36: 403–407.

206. Genbrugge C, De Deyne C, Eertmans W, et al. Cerebral saturation in cardiac arrest patients measured with near-infrared technology during pre-hospital advanced life support. Results from Copernicus I cohort study. *Resuscitation* 2018; 129: 107–113.

207. López-Herce J, Fernández B, Urbano J, et al. Correlations between hemodynamic, oxygenation and tissue perfusion parameters during asphyxial cardiac arrest and resuscitation in a pediatric animal model. *Resuscitation* 2011; 82: 755–759.

208. Solevåg AL, Dannevig I, Wyckoff M, et al. Return of spontaneous circulation with a compression:ventilation ratio of 15:2 versus 3:1 in newborn pigs with cardiac arrest due to asphyxia. *Arch Dis Child Fetal Neonatal Ed* 2011; 96: 1–7.

209. Chien JC, Jeng MJ, Chang HL, et al. Cerebral oxygenation during hypoxia and resuscitation by using near-infrared spectroscopy in newborn piglets. *J Chinese Med Assoc* 2007; 70: 47–55.

210. Nosrati R, Lin S, Ramadeen A, et al. Cerebral Hemodynamics and Metabolism During Cardiac Arrest and Cardiopulmonary Resuscitation Using Hyperspectral Near Infrared Spectroscopy. *Circ J* 2017; 81: 879–887.

211. López-Herce J, Fernández B, Urbano J, et al. Hemodynamic, respiratory, and perfusion parameters during asphyxia, resuscitation, and post-resuscitation in a pediatric model of cardiac arrest. *Intensive Care Med* 2011; 37: 147–155.

212. Koudouna E, Xanthos T, Bassiakou E, et al. Levosimendan improves the initial outcome of cardiopulmonary resuscitation in a swine model of cardiac arrest. *Acta Anaesthesiol Scand* 2007; 51: 1123–1129.

213. Solevåg AL, Dannevig I, Nakstad B, et al. Resuscitation of severely asphyctic newborn pigs with cardiac arrest by using 21% or 100% oxygen. *Neonatology* 2010; 98: 64–72.

214. Lee JK, Brady KM, Mytar JO, et al. Cerebral blood flow and cerebrovascular autoregulation in a swine model of pediatric cardiac arrest and hypothermia. *Crit Care Med* 2011; 39: 2337–45.

215. Polito A, Ricci Z, Di Chiara L, et al. Cerebral blood flow during cardiopulmonary bypass in pediatric cardiac surgery: the role of transcranial Doppler – a systematic review of the literature. *Cardiovasc Ultrasound* 2006; 4: 47.

216. Abramo T, Aggarwal N, Kane I, et al. Cerebral oximetry and cerebral blood flow monitoring in 2 pediatric survivors with out-of-hospital cardiac arrest. *Am J Emerg Med* 2014; 32: 394.e5-394.e10.

217. Nagdyman N, Fleck TPK, Ewert P, et al. Cerebral oxygenation measured by near-infrared spectroscopy during circulatory arrest and cardiopulmonary resuscitation. *Br J Anaesth* 2003; 91: 438–442.

218. Çağlar A, Er A, Ulusoy E, et al. Cerebral oxygen saturation monitoring in pediatric

cardiopulmonary resuscitation patients in the emergency settings: a small descriptive study. *Turk J Pediatr* 2017; 59: 642.

219. Marino BS, Tabbutt S, MacLaren G, et al. *Cardiopulmonary Resuscitation in Infants and Children With Cardiac Disease*. 2018. Epub ahead of print 2018. DOI: 10.1161/CIR.0000000000000524.

220. Ghanayem NS, Wernovsky G, Hoffman GM. Near infrared spectroscopy as a hemodynamic monitor in critical illness. *Pediatr Crit Care Med* 2011; 23: S27–S32.

221. Sorensen LC, Greisen G. Precision of measurement of cerebral tissue oxygenation index using near-infrared spectroscopy in preterm neonates. *J Biomed Opt* 2006; 11: 054005.

222. Jenny C, Biallas M, Trajkovic I, et al. Reproducibility of cerebral tissue oxygen saturation measurements by near-infrared spectroscopy in newborn infants. *J Biomed Opt* 2011; 16: 097004.

223. Wolf M, Naulaers G, Bel F Van, et al. Review: A review of near infrared spectroscopy for term and preterm newborns. *J Near Infrared Spectrosc* 2012; 20: 43–55.

224. Arri SJ, Muehlemann T, Biallas M, et al. Precision of cerebral oxygenation and hemoglobin concentration measurements in neonates measured by near-infrared spectroscopy. *J Biomed Opt* 2011; 16: 047005.

225. Davie SN, Grocott HP. Impact of extracranial contamination on regional cerebral oxygen saturation: A comparison of three cerebral oximetry technologies. *Anesthesiology* 2012; 116: 834–840.

226. Ohmae E, Ouchi Y, Oda M, et al. Cerebral hemodynamics evaluation by near-infrared time-resolved spectroscopy: Correlation with simultaneous positron

emission tomography measurements. *Neuroimage* 2006; 29: 697–705.

227. CAS Medical Systems I. *Pediatric Validation of the FORE-SIGHT ELITE ® Tissue Oximeter*. 2018.

228. Morgan RW, Kilbaugh TJ, Shoap W, et al. A hemodynamic-directed approach to pediatric cardiopulmonary resuscitation (HD-CPR) improves survival. *Resuscitation* 2017; 111: 41–47.

229. Sutton RM, Friess SH, Bhalala U, et al. Hemodynamic directed CPR improves short-term survival from asphyxia-associated cardiac arrest. *Resuscitation* 2013; 84: 696–701.

230. Friess SH, Sutton RM, French B, et al. Hemodynamic directed CPR improves cerebral perfusion pressure and brain tissue oxygenation. *Resuscitation* 2014; 85: 1298–1303.

231. Wyatt JS, Cope M, Delpy DT, et al. Quantitation of cerebral blood volume in human infants by near-infrared spectroscopy. *J Appl Physiol* 1990; 68: 1086–1091.

232. Mahle WT, Clancy RR, Moss EM, et al. Neurodevelopmental Outcome and Lifestyle Assessment in School-Aged and Adolescent Children With Hypoplastic Left Heart Syndrome. *Pediatrics* 2000; 105: 1082–1089.

233. Bellinger DC, Wypij D, Du Plessis AJ, et al. Developmental and neurologic effects of alpha-stat versus pH-stat strategies for deep hypothermic cardiopulmonary bypass in infants. *J Thorac Cardiovasc Surg* 2001; 121: 374–383.

234. Erecinska M, Thoresen M, Silver IA. Effects of Hypothermia on Energy Metabolism in Mammalian Central Nervous System. *J Cereb Blood Flow Metab* 2003; 23: 513–530.

235. Michenfelder JD, Milde JH. The Relationship among Canine Brain Temperature,

Metabolism, and Function during Hypothermia. *Anesthesiology* 1991; 75: 130–136.

236. Croughwell ND, Frasco P, Blumenthal JA, et al. Warming during cardiopulmonary bypass is associated with jugular bulb desaturation. *Ann Thorac Surg* 1992; 53: 827–832.
237. Ehrlich MP, McCullough JN, Zhang N, et al. Effect of hypothermia on cerebral blood flow and metabolism in the pig. *Ann Thorac Surg* 2002; 73: 191–197.
238. Neshat Vahid S, Panisello JM. The state of affairs of neurologic monitoring by near-infrared spectroscopy in pediatric cardiac critical care. *Curr Opin Pediatr* 2014; 26: 299–303.
239. Lynch JM, Buckley EM, Schwab PJ, et al. Noninvasive Optical Quantification of Cerebral Venous Oxygen Saturation in Humans. *Acad Radiol* 2014; 21: 162–167.
240. Lin P-Y, Roche-Labarbe N, Dehaes M, et al. Non-invasive Optical Measurement of Cerebral Metabolism and Hemodynamics in Infants. *J Vis Exp* 2013; e4379.
241. Roche-Labarbe N, Fenoglio A, Radhakrishnan H, et al. Somatosensory evoked changes in cerebral oxygen consumption measured non-invasively in premature neonates. *Neuroimage* 2014; 85: 279–286.
242. Lynch JM. *Investigations of Cerebral Hemodynamics in Infants With Critical Congenital Heart Disease Using Diffuse Optics*. University of Pennsylvania, 2014.
243. Buckley EM, Lynch JM, Goff DA, et al. Early postoperative changes in cerebral oxygen metabolism following neonatal cardiac surgery: Effects of surgical duration. *J Thorac Cardiovasc Surg* 2013; 145: 196–205.e1.
244. Busch DR, Lynch JM, Winters ME, et al. Cerebral blood flow response to hypercapnia in children with obstructive sleep apnea syndrome. *Sleep* 2016; 39: 209–216.

245. Dehaes M, Cheng HH, Buckley EM, et al. Perioperative cerebral hemodynamics and oxygen metabolism in neonates with single-ventricle physiology. *Biomed Opt Express* 2015; 6: 4749.

246. Mezrow CK, Midulla PS, Sadeghi AM, et al. Evaluation of cerebral metabolism and quantitative electroencephalography after hypothermic circulatory, arrest and low-flow cardiopulmonary bypass at different temperatures. *J Thorac Cardiovasc Surg* 1994; 107: 1006–1019.

247. Busija DW, Leffler CW. Hypothermia reduces cerebral metabolic rate and cerebral blood flow in newborn pigs. *Am J Physiol* 1987; 253: H869–H873.

248. Mault JR, Ohtake S, Klingensmith ME, et al. Cerebral metabolism and circulatory arrest: Effects of duration and strategies for protection. *Ann Thorac Surg* 1993; 55: 57–64.

249. Skaryak LA, Chai PJ, Kern FH, et al. Blood gas management and degree of cooling: Effects on cerebral metabolism before and after circulatory arrest. *J Thorac Cardiovasc Surg* 1995; 110: 1649–1657.

250. Langley SM, Chai PJ, Miller SE, et al. Intermittent perfusion protects the brain during deep hypothermic circulatory arrest. *Ann Thorac Surg* 1999; 68: 4–12.

251. Cavus E, Hoffmann G, Bein B, et al. Cerebral metabolism during deep hypothermic circulatory arrest vs moderate hypothermic selective cerebral perfusion in a piglet model: A microdialysis study. *Paediatr Anaesth* 2009; 19: 770–778.

252. Walther T, Dhein S, Ullmann C, et al. Cerebral protection during controlled hypoperfusion in a piglet model: comparison of moderate (25 degrees C) versus deep (18 degrees C) hypothermia at various flow rates using intraoperative measurements and ex vivo investigation. *Thorac Cardiovasc Surg* 2013; 61: 546–

552.

253. Torricelli A, Contini D, Mora AD, et al. Neurophotonics: Non-invasive optical techniques for monitoring brain functions. *Funct Neurol* 2014; 29: 223–230.

254. Bale G, Elwell CE, Tachtsidis I. From Jöbsis to the present day: a review of clinical near-infrared spectroscopy measurements of cerebral cytochrome-c-oxidase. *J Biomed Opt* 2016; 21: 091307.

255. Mavroudis CD, Karlsson M, Ko T, et al. Cerebral mitochondrial dysfunction associated with deep hypothermic circulatory arrest in neonatal swine†. *Eur J Cardio-Thoracic Surg* 2018; 0: 1–7.

256. Wang L V., Hsin-I Wu. *Biomedical Optics: Principles and Imaging*. Hoboken, NJ, USA: John Wiley & Sons, Inc., 2012.

257. Kreis R, Ernst T, Ross BD. Development of the human brain: in vivo quantification of metabolite and water content with proton magnetic resonance spectroscopy. *Magn Reson Med* 1993; 30: 424–37.

258. Patterson MS, Andersson-Engels S, Wilson BC, et al. Absorption spectroscopy in tissue-simulating materials: a theoretical and experimental study of photon paths. *Appl Opt* 1995; 34: 22.

259. Kety SS, Schmidt CF. The nitrous oxide method for the quantitative determination of cerebral blood flow in man: theory, procedure and normal values. *J Clin Invest* 1948; 27: 476–483.

260. Schell RM, Cole DJ. Cerebral Monitoring: Jugular Venous Oximetry. *Anesth Analg* 2000; 90: 559–566.

261. Kabalin AE, Balenović T, Valpotić I, et al. The influence of birth mass and age of suckling piglets on erythrocyte parameters. *Vet Arch* 2008; 78: 307–319.

262. Larimer JL. Hemoglobin concentration and oxygen capacity of mammalian blood.

1959.

263. Ito H, Kanno I, Iida H, et al. Arterial fraction of cerebral blood volume in humans measured by positron emission tomography. *Ann Nucl Med* 2001; 15: 111–116.

264. Liu P, Chalak LF, Lu H. Non-invasive assessment of neonatal brain oxygen metabolism: A review of newly available techniques. *Early Hum Dev* 2014; 90: 695–701.

265. Field J, Fuhrman FA, Martin AW. Effect of temperature on the oxygen consumption of brain tissue. *J Neurophysiol* 1944; 7: 117–126.

266. Michenfelder JD, Milde JH. The Effect of Profound Levels of Hypothermia (Below 14°C) on Canine Cerebral Metabolism. *J Cereb Blood Flow Metab* 1992; 12: 877–880.

267. Bland JM, Altman DG. Agreement Between Methods of Measurement with Multiple Observations Per Individual. *J Biopharm Stat* 2007; 17: 571–582.

268. Krouwer JS. Why Bland-Altman plots should use X, not (Y + X)/2 when X is a reference method. *Stat Med* 2008; 27: 778–780.

269. Johnson RI, Fox MA, Grayson A, et al. Should we rely on nasopharyngeal temperature during cardiopulmonary bypass? *Perfusion* 2002; 17: 145–151.

270. Engelman R, Baker RA, Likosky DS, et al. The Society of Thoracic Surgeons, The Society of Cardiovascular Anesthesiologists, and The American Society of ExtraCorporeal Technology: Clinical Practice Guidelines for Cardiopulmonary Bypass—Temperature Management During Cardiopulmonary Bypass. *J Cardiothorac Vasc Anesth* 2015; 29: 1104–1113.

271. Bacher A. Effects of body temperature on blood gases. *Intensive Care Med* 2005; 31: 24–27.

272. Toraman F, Evrenkaya S, Senay S, et al. Adjusting oxygen fraction to avoid

hyperoxemia during cardiopulmonary bypass. *Asian Cardiovasc Thorac Ann* 2007; 15: 303–6.

273. Sasaki T, Boni L, Riemer RK, et al. Cerebral oxygen metabolism during total body flow and antegrade cerebral perfusion at deep and moderate hypothermia. *Artif Organs* 2010; 34: 980–986.
274. Kern FH, Schell RM, Greeley WJ. Cerebral monitoring during cardiopulmonary bypass in children. *J Neurosurg Anesthesiol* 1993; 5: 213–217.
275. Abdul-Khaliq H, Troitsch D, Berger F, et al. Regional transcranial oximetry with near infrared spectroscopy (NIRS) in comparison with measuring oxygen saturation in the jugular bulb in infants and children for monitoring cerebral oxygenation. *Biomed Tech Eng* 2000; 45: 328–332.
276. Daubeney PEF, Pilkington SN, Janke E, et al. Cerebral oxygenation measured by near-infrared spectroscopy: Comparison with jugular bulb oximetry. *Ann Thorac Surg* 1996; 61: 930–934.
277. Nagdyman N, Fleck T, Schubert S, et al. Comparison between cerebral tissue oxygenation index measured by near-infrared spectroscopy and venous jugular bulb saturation in children. *Intensive Care Med* 2005; 31: 846–850.
278. Rudinsky BF, Meadow WL. Internal Jugular Venous Oxygen Saturation Does Not Reflect Sagittal Sinus Oxygen Saturation in Piglets. *Neonatology* 1991; 59: 322–328.
279. Hansen NB, Brubakk A-M, Bratlid D, et al. The Effects of Variations in Paco2 on Brain Blood Flow and Cardiac Output in the Newborn Piglet. *Pediatr Res* 1984; 18: 1132–1136.
280. Laptook AR, Shalak L, Corbett RJT. Differences in Brain Temperature and Cerebral Blood Flow During Selective Head Versus Whole-Body Cooling. 2001.

281. Schears G, Zaitseva T, Schultz S, et al. Brain oxygenation and metabolism during selective cerebral perfusion in neonates. *Eur J Cardio-Thoracic Surg* 2006; 29: 168–174.

282. Gagnon L, Desjardins M, Jehanne-Lacasse J, et al. Investigation of diffuse correlation spectroscopy in multi-layered media including the human head. *Opt Express* 2008; 16: 15514–15530.

283. Mesquita RC, Schenkel SS, Minkoff DL, et al. Influence of probe pressure on the diffuse correlation spectroscopy blood flow signal: extra-cerebral contributions. *Biomed Opt Express* 2013; 4: 978.

284. Baker WB, Parthasarathy AB, Ko TS, et al. Pressure modulation algorithm to separate cerebral hemodynamic signals from extracerebral artifacts. *Neurophotonics* 2015; 2: 035004.

285. Conrad MS, Dilger RN, Johnson RW. Brain growth of the domestic pig (Sus scrofa) from 2 to 24 weeks of age: A longitudinal MRI study. *Dev Neurosci* 2012; 34: 291–298.

286. Semenas E, Nozari A, Wiklund L. Sex differences in cardiac injury after severe haemorrhage and ventricular fibrillation in pigs. *Resuscitation* 2010; 81: 1718–1722.

287. Armstead WM, Kiessling JW, Kofke WA, et al. Impaired cerebral blood flow autoregulation during posttraumatic arterial hypotension after fluid percussion brain injury is prevented by phenylephrine in female but exacerbated in male piglets by extracellular signal-related kinase mitogen-activated prot. *Crit Care Med* 2010; 38: 1868–1874.

288. Takayama JI, Teng W, Uyemoto J, et al. Body temperature of newborns: What is normal? *Clin Pediatr (Phila)* 2000; 39: 503–510.

289. Anand KJS, Hickey PR. Halothane–Morphine Compared with High-Dose Sufentanil for Anesthesia and Postoperative Analgesia in Neonatal Cardiac Surgery. *N Engl J Med* 1992; 326: 1–9.

290. Enomoto S, Hindman BJ, Dexter F, et al. Rapid rewarming causes an increase in the cerebral metabolic rate for oxygen that is temporarily unmatched by cerebral blood flow. A study during cardiopulmonary bypass in rabbits. *Anesthesiology* 1996; 84: 1392–400.

291. Condò SG, Corda M, Sanna MT, et al. Molecular basis of low-temperature sensitivity in pig hemoglobins. *Eur J Biochem* 1992; 209: 773–776.

292. Willford DC, Hill EP. Modest effect of temperature on the porcine oxygen dissociation curve. *Respir Physiol* 1986; 64: 113–123.

293. Henriksen OM, Vestergaard MB, Lindberg U, et al. Interindividual and regional relationship between cerebral blood flow and glucose metabolism in the resting brain. *J Appl Physiol* 2018; japplphysiol.00276.2018.

294. Ito H, Ibaraki M, Kanno I, et al. Changes in cerebral blood flow and cerebral oxygen metabolism during neural activation measured by positron emission tomography: Comparison with blood oxygenation level-dependent contrast measured by functional magnetic resonance imaging. *J Cereb Blood Flow Metab* 2005; 25: 371–377.

295. Rodgers ZB, Detre JA, Wehrli FW. MRI-based methods for quantification of the cerebral metabolic rate of oxygen. *J Cereb Blood Flow Metab* 2016; 36: 1165–1185.

296. Sundar LK, Muzik O, Rischka L, et al. Towards quantitative [18F]FDG-PET/MRI of the brain: Automated MR-driven calculation of an image-derived input function for the non-invasive determination of cerebral glucose metabolic rates. *J Cereb Blood*

Flow Metab. Epub ahead of print 23 May 2018. DOI: 10.1177/0271678X18776820.

297. Shankaran S, Laptook AR, Ehrenkranz RA, et al. Whole-body hypothermia for neonates with hypoxic-ischemic encephalopathy. *N Engl J Med* 2005; 353: 1574–1584.

298. Laptook AR, Shankaran S, Tyson JE, et al. Effect of therapeutic hypothermia initiated after 6 hours of age on death or disability among newborns with hypoxic-ischemic encephalopathy a randomized clinical trial. *JAMA - J Am Med Assoc* 2017; 318: 1550–1560.

299. Rutherford M, Ramenghi LA, Edwards AD, et al. Assessment of brain tissue injury after moderate hypothermia in neonates with hypoxic-ischaemic encephalopathy: a nested substudy of a randomised controlled trial. *Lancet Neurol* 2010; 9: 39–45.

300. Edwards AD, Brocklehurst P, Gunn AJ, et al. Neurological outcomes at 18 months of age after moderate hypothermia for perinatal hypoxic ischaemic encephalopathy: Synthesis and meta-analysis of trial data. *BMJ* 2010; 340: 409.

301. Massaro AN, Govindan RB, Vezina G, et al. Impaired cerebral autoregulation and brain injury in newborns with hypoxic-ischemic encephalopathy treated with hypothermia. *J Neurophysiol* 2015; 114: 818–824.

302. Dehaes M, Aggarwal A, Lin P-Y, et al. Cerebral Oxygen Metabolism in Neonatal Hypoxic Ischemic Encephalopathy during and after Therapeutic Hypothermia. *J Cereb Blood Flow Metab* 2014; 34: 87–94.

303. Gabel RA. Algorithms for calculating and correcting blood-gas and acid-base variables. *Respir Physiol* 1980; 42: 211–232.

304. Abbott Point of Care. *pO2 and Calculated Oxygen Saturated (sO2)*. 2011.

305. Millar AB, Armstrong L, van der Linden J, et al. Cytokine production and

hemofiltration in children undergoing cardiopulmonary bypass. *AnnThorac Surg* 1993; 56: 1499–1502.

306. Liguori GR, Kanas AF, Moreira LFP. Managing the inflammatory response after cardiopulmonary bypass: review of the studies in animal models. *Rev Bras Cir Cardiovasc* 2014; 29: 93–102.

307. Hsia TY, Gruber PJ. Factors Influencing Neurologic Outcome After Neonatal Cardiopulmonary Bypass: What We Can and Cannot Control. *Ann Thorac Surg*; 81. Epub ahead of print 2006. DOI: 10.1016/j.athoracsur.2006.02.074.

308. Wong PC, Barlow CF, Hickey PR, et al. Factors associated with choreoathetosis after cardiopulmonary bypass in children with congenital heart disease. *Circulation* 1992; 86: II-118-II-126.

309. Aly SA, Zurakowski D, Glass P, et al. Cerebral tissue oxygenation index and lactate at 24 hours postoperative predict survival and neurodevelopmental outcome after neonatal cardiac surgery. *Congenit Heart Dis* 2017; 12: 188–195.

310. Lee JK, Easley RB, Brady KM. Neurocognitive Monitoring and Care During Pediatric Cardiopulmonary Bypass—Current and Future Directions. *Curr Cardiol Rev* 2008; 4: 123–139.

311. Su XW, Ündar A. Brain protection during pediatric cardiopulmonary bypass. *Artif Organs*; 34. Epub ahead of print 2010. DOI: 10.1111/j.1525-1594.2009.00963.x.

312. Clark JB, Barnes ML, Undar A, et al. Multimodality Neuromonitoring for Pediatric Cardiac Surgery. *World J Pediatr Congenit Hear Surg* 2012; 3: 87–95.

313. Hirsch JC, Jacobs ML, Andropoulos D, et al. Protecting the infant brain during cardiac surgery: A systematic review. *Ann Thorac Surg* 2012; 94: 1365–1373.

314. Mittnacht AJC, Rodriguez-Diaz C. Multimodal neuromonitoring in pediatric cardiac anesthesia. *Ann Card Anaesth* 2014; 17: 25–32.

315. Naim MY, Gaynor JW, Chen J, et al. Subclinical seizures identified by postoperative electroencephalographic monitoring are common after neonatal cardiac surgery. *J Thorac Cardiovasc Surg* 2015; 150: 169–180.

316. Griepp RB, Ergin MA, McCullough JN, et al. Use of hypothermic circulatory arrest for cerebral protection during aortic surgery. *J Card Surg* 1997; 12: 312–321.

317. Toet MC, Flinterman A, Van De Laar I, et al. Cerebral oxygen saturation and electrical brain activity before, during, and up to 36 hours after arterial switch procedure in neonates without pre-existing brain damage: Its relationship to neurodevelopmental outcome. *Exp Brain Res* 2005; 165: 343–350.

318. Kwak JG, Kim WH, Oh AY, et al. Is unilateral brain regional perfusion neurologically safe during congenital aortic arch surgery? *Eur J Cardio-thoracic Surg* 2007; 32: 751–755.

319. Su XW, Guan Y, Barnes M, et al. Improved Cerebral Oxygen Saturation and Blood Flow Pulsatility With Pulsatile Perfusion During Pediatric Cardiopulmonary Bypass. *Pediatr Res* 2011; 70: 181–185.

320. Andropoulos DB, Stayer SA, McKenzie ED, et al. Novel cerebral physiologic monitoring to guide low-flow cerebral perfusion during neonatal aortic arch reconstruction. *J Thorac Cardiovasc Surg* 2003; 125: 491–499.

321. Minagawa-Kawai Y, Mori K, Hebden JC, et al. Optical imaging of infants' neurocognitive development: Recent advances and perspectives. *Dev Neurobiol* 2008; 68: 712–728.

322. Ricci Z, Garisto C, Favia I, et al. Cerebral NIRS as a marker of superior vena cava oxygen saturation in neonates with congenital heart disease. *Paediatr Anaesth* 2010; 20: 1040–1045.

323. Spaeder MC, Klugman D, Skurow-Todd K, et al. Perioperative Near-Infrared

Spectroscopy Monitoring in Neonates with Congenital Heart Disease: Relationship of Cerebral Tissue Oxygenation Index Variability with Neurodevelopmental Outcome. *Pediatr Crit Care Med* 2017; 18: 213–218.

324. Zhang G, Katz A, Alfano RR, et al. Brain perfusion monitoring with frequency-domain and continuous-wave near-infrared spectroscopy: A cross-correlation study in newborn piglets. *Phys Med Biol* 2000; 45: 3143–3158.

325. Faber DJ, Aalders MCG, Mik EG, et al. Oxygen saturation-dependent absorption and scattering of blood. *Phys Rev Lett* 2004; 93: 028102-1.

326. Park Y, Best-Popescu CA, Dasari RR, et al. Light scattering of human red blood cells during metabolic remodeling of the membrane. *J Biomed Opt* 2011; 16: 011013.

327. Priestley MA, Golden JA, O’Hara IB, et al. Comparison of neurologic outcome after deep hypothermic circulatory arrest with alpha-stat and pH-stat cardiopulmonary bypass in newborn pigs. *J Thorac Cardiovasc Surg* 2001; 121: 336–343.

328. Sakamoto T, Hatsuoka S, Stock UA, et al. Prediction of safe duration of hypothermic circulatory arrest by near-infrared spectroscopy. *J Thorac Cardiovasc Surg* 2001; 122: 339–350.

329. Hagino I, Anttila V, Zurakowski D, et al. Tissue oxygenation index is a useful monitor of histologic and neurologic outcome after cardiopulmonary bypass in piglets. *J Thorac Cardiovasc Surg* 2005; 130: 384–392.

330. Mavroudis CD, Mensah-Brown KG, Ko TS, et al. Electroencephalographic Response to Deep Hypothermic Circulatory Arrest in Neonatal Swine and Humans. *Ann Thorac Surg*. Epub ahead of print 2018. DOI: 10.1016/j.athoracsur.2018.06.036.

331. Ko TS, Mavroudis CD, Baker WB, et al. Validation of diffuse optical spectroscopic measurement of cerebral oxygen metabolism in a piglet model of deep hypothermic circulatory arrest (DHCA). *Int Soc Opt Photonics* 2017; SPIE BiOS: Paper 10059-51.

332. Ko TS, Mavroudis CD, Baker WB, et al. Non-invasive optical neuromonitoring of the temperature-dependence of cerebral oxygen metabolism during deep hypothermic cardiopulmonary bypass in neonatal swine. *J Cereb Blood Flow Metab (in Rev*.

333. Liao SM, Culver JP. Near Infrared Optical Technologies to Illuminate the Status of the Neonatal Brain. *Curr Pediatr Rev* 2014; 10: 73–86.

334. Tobias J, Russo P, Russo J. Changes in near infrared spectroscopy during deep hypothermic circulatory arrest. *Ann Card Anaesth* 2009; 12: 17.

335. Abdul-Khaliq H, Troitzsch D, Schubert S, et al. Cerebral oxygen monitoring during neonatal cardiopulmonary bypass and deep hypothermic circulatory arrest. *Thorac Cardiovasc Surg* 2002; 50: 77–81.

336. Singer D. Neonatal tolerance to hypoxia: A comparative-physiological approach. *Comp Biochem Physiol - A Mol Integr Physiol* 1999; 123: 221–234.

337. Rogalska J, Caputa M. Hypometabolism as a strategy of survival in asphyxiated newborn mammals. *Res Signpost* 2011; 661: 117–145.

338. Pigula FA, Siewers RD, Nemoto EM. Hypothermic cardiopulmonary bypass alters oxygen/glucose uptake in the pediatric brain. *J Thorac Cardiovasc Surg* 2001; 121: 366–373.

339. Hunter CJ, Blood AB, Power GG. Cerebral metabolism during cord occlusion and hypoxia in the fetal sheep: a novel method of continuous measurement based on heat production. *J Physiol* 2003; 552: 241–51.

340. Cross KW, Tizard JP, Trythall DA. The gaseous metabolism of the newborn infant. *Acta Paediatr* 1957; 46: 265–285.

341. Mohr C, Brady JD, Rossi DJ. Young age and low temperature, but not female gender delay ATP loss and glutamate release, and protect Purkinje cells during simulated ischemia in cerebellar slices. *Neuropharmacology* 2010; 58: 392–403.

342. Mortola JP. How newborn mammals cope with hypoxia. *Respir Physiol* 1999; 116: 95–103.

343. Licht DJ, Wang J, Silvestre DW, et al. Preoperative cerebral blood flow is diminished in neonates with severe congenital heart defects. *J Thorac Cardiovasc Surg* 2004; 128: 841–849.

344. Salazar J, Coleman R, Griffith S, et al. Brain preservation with selective cerebral perfusion for operations requiring circulatory arrest: protection at 25 °C is similar to 18 °C with shorter operating times. *Eur J Cardio-thoracic Surg* 2009; 36: 524–531.

345. Simons J, Sood ED, Derby CD, et al. Predictive value of near-infrared spectroscopy on neurodevelopmental outcome after surgery for congenital heart disease in infancy. *J Thorac Cardiovasc Surg* 2012; 143: 118–125.

346. Rodriguez RA, Ruel M, Broecker L, et al. High flow rates during modified ultrafiltration decrease cerebral blood flow velocity and venous oxygen saturation in infants. *Ann Thorac Surg* 2005; 80: 22–28.

347. He J, Lu H, Young L, et al. Real-time quantitative monitoring of cerebral blood flow by laser speckle contrast imaging after cardiac arrest with targeted temperature management. *J Cereb Blood Flow Metab* 2017; 0271678X1774878.

348. Pastuszko P, Liu H, Mendoza-Paredes A, et al. Brain oxygen and metabolism is dependent on the rate of low-flow cardiopulmonary bypass following circulatory

arrest in newborn piglets. *Eur J Cardiothorac Surg* 2007; 31: 899–905.

349. Schultz S, Antoni D, Shears G, et al. Brain oxygen and metabolism during circulatory arrest with intermittent brief periods of low-flow cardiopulmonary bypass in newborn piglets. *J Thorac Cardiovasc Surg* 2006; 132: 839–844.

350. Cooper CE, Elwell CE, Meek JH, et al. The Noninvasive Measurement of Absolute Cerebral Deoxyhemoglobin Concentration and Mean Optical Path Length in the Neonatal Brain by Second Derivative Near Infrared Spectroscopy. *Pediatr Res* 1996; 39: 32–38.

351. Valabrègue R, Aubert A, Burger J, et al. Relation between cerebral blood flow and metabolism explained by a model of oxygen exchange. *J Cereb Blood Flow Metab* 2003; 23: 536–545.

352. Vazquez AL, Masamoto K, Kim SG. Dynamics of oxygen delivery and consumption during evoked neural stimulation using a compartment model and CBF and tissue PO2 measurements. *Neuroimage* 2008; 42: 49–59.

353. Hoge RD, Franceschini MA, Covolan RJM, et al. Simultaneous recording of task-induced changes in blood oxygenation, volume, and flow using diffuse optical imaging and arterial spin-labeling MRI. *Neuroimage* 2005; 25: 701–707.

354. Moler FW, Donaldson AE, Meert K, et al. Multicenter cohort study of out-of-hospital pediatric cardiac arrest. *Crit Care Med* 2011; 39: 141–9.

355. Maconochie IK, de Caen AR, Aickin R, et al. Part 6: Pediatric basic life support and pediatric advanced life support. 2015 International Consensus on Cardiopulmonary Resuscitation and Emergency Cardiovascular Care Science with Treatment Recommendations. *Resuscitation* 2015; 95: e147–e168.

356. Lopez-Herce J, Rodriguez A, Carrillo A, et al. The latest in paediatric resuscitation recommendations. *An Pediatr (Barc)* 2017; 86: 229.e1-229.e9.

357. Brissaud O, Botte A, Cambonie G, et al. Experts' recommendations for the management of cardiogenic shock in children. *Ann Intensive Care* 2016; 6: 1–16.

358. Scholkmann F, Kleiser S, Metz AJ, et al. A review on continuous wave functional near-infrared spectroscopy and imaging instrumentation and methodology. *Neuroimage* 2014; 85: 6–27.

359. Topjian AA, Nadkarni VM, Berg RA. Cardiopulmonary resuscitation in children. *Curr Opin Crit Care* 2009; 15: 203–208.

360. Chen Y, Tailor DR, Intes X, et al. Correlation between near-infrared spectroscopy and magnetic resonance imaging of rat brain oxygenation modulation. *Phys Med Biol* 2003; 48: 417–427.

361. Park Y, Diez-Silva M, Fu D, et al. Static and dynamic light scattering of healthy and malaria-parasite invaded red blood cells. *J Biomed Opt* 2010; 15: 020506.

362. Berg RA, Hilwig RW, Kern KB, et al. Simulated mouth-to-mouth ventilation and chest compressions (bystander cardiopulmonary resuscitation) improves outcome in a swine model of prehospital pediatric asphyxial cardiac arrest. *Crit Care Med* 1999; 27: 1893–9.

363. Zuercher M, Hilwig RW, Ranger-Moore J, et al. Leaning during chest compressions impairs cardiac output and left ventricular myocardial blood flow in piglet cardiac arrest. *Crit Care Med* 2010; 38: 1141–1146.

364. Duhaime A-C, Margulies SS, Durham SR, et al. Maturation-dependent response of the piglet brain to scaled cortical impact. *J Neurosurg* 2000; 93: 455–462.

365. Berg RA, Hilwig RW, Kern KB, et al. 'Bystander' chest compressions and assisted ventilation independently improve outcome from piglet asphyxial pulseless 'cardiac arrest'. *Circulation*. Epub ahead of print 2000. DOI: 10.1161/01.CIR.101.14.1743.

366. Meinke M, Müller G, Helfmann J, et al. Optical properties of platelets and blood plasma and their influence on the optical behavior of whole blood in the visible to near infrared wavelength range. *J Biomed Opt* 2007; 12: 014024.

367. Roggan A, Friebel M, Dörschel K, et al. Optical Properties of Circulating Human Blood in the Wavelength Range 400–2500 nm. *J Biomed Opt*. Epub ahead of print 1999. DOI: 10.1117/1.429919.

368. Asim K, Gokhan E, Ozlem B, et al. Near infrared spectrophotometry (cerebral oximetry) in predicting the return of spontaneous circulation in out-of-hospital cardiac arrest. *Am J Emerg Med* 2014; 32: 14–17.